2021

Dissecting the multi-functional role of heterogeneous nuclear ribonucleoprotein H1 in methamphetamine addiction traits

BOSTON UNIVERSITY

SCHOOL OF MEDICINE

Dissertation

DISSECTING THE MULTI-FUNCTIONAL ROLE OF HETEROGENEOUS NUCLEAR RIBONUCLEOPROTEIN H1 IN METHAMPHETAMINE ADDICTION TRAITS

by

QIU T. RUAN

B.S., Tufts University, 2014

Submitted in partial fulfillment of the

requirements for the degree of

Doctor of Philosophy

2021

Approved by

First Reader

Camron D. Bryant, Ph.D.
Associate Professor of Pharmacology and Psychiatry

Second Reader

Benjamin Wolozin, M.D., Ph.D.
Professor of Pharmacology and Neurology

“I have no special talents. I am only passionately curious.”

-Albert Einstein

DEDICATION

I would like to dedicate this work to my mother, Rui Lan, for her continuous love and support. I am extremely thankful for all the sacrifices my mom has made for me.

ACKNOWLEDGMENTS

I would like to thank the following people, without whom I would not have been able to complete this research.

I want to take a moment to express my gratitude to my boyfriend, Wesley, for being my rock throughout my PhD journey. Thank you for always being there for me when I need you.

I wish to thank my dissertation advisor, Dr. Camron Bryant, for providing guidance and constructive feedback in my research. I would not have been able to complete this research without your mentorship and patience.

To every members of my Dissertation Committee, Dr. Tsuneya Ikezu, Dr. Benjamin Wolozin, and Dr. Evan Johnson, thank you for keeping my research progress on track.

I wish to thank Dr. Neema Yazdani for laying the groundwork for my dissertation research and training me to take on the *Hnrnph1* project.

To past and present members of the Bryant Lab, especially Emily, Kristyn, and Jake, thank you for all the help throughout the past few years. I could not have asked for better lab mates.

I wish to thank our collaborators in the hnRNP H CLIP-seq project. To Dr. Joe Dougherty, thank you for hosting me in your lab and providing constructive feedback on my CLIP-seq manuscript. To Dr. Mike Rieger, thank you for training me in CLIP-seq.

I want to thank Dr. Pete Ash for helping me with troubleshooting many of my experiments.

I like to thank Dr. Lindsay Farrer for accepting me into the TTPAS training program so I can engage in trans-disciplinary research.

Lastly, I like to thank everyone in the Department of Pharmacology including Dr. Farb, Dr. Russek, Sara Johnson, Licia Holman, and Wanda Roberts for all their help and support throughout my PhD training.

DISSECTING THE MULTI-FUNCTIONAL ROLE

OF HETEROGENEOUS NUCLEAR RIBONUCLEOPROTEIN H1

IN METHAMPHETAMINE ADDICTION TRAITS

QIU RUAN

Boston University School of Medicine, 2021

Major Professor: Camron D. Bryant, Ph.D., Associate Professor of Pharmacology and Psychiatry

ABSTRACT

Both genetic and environment factors influence susceptibility to substance use disorders. However, the genetic basis of these disorders is largely unknown. We previously identified *Hnrnph1* (heterogeneous nuclear ribonucleoprotein H1) as a quantitative trait gene for reduced methamphetamine (MA) stimulant sensitivity. Mutation (heterozygous deletion of a small region in the first coding exon) in *Hnrnph1* also decreased MA reinforcement, reward, and dopamine release. 5'UTR genetic variants in *Hnrnph1* support reduced 5'UTR usage and hnRNP H protein expression as a molecular mechanism underlying the reduced MA-induced psychostimulant response. Interestingly, *Hnrnph1* mutant mice show a two-fold increase in hnRNP H protein in the striatal synaptosome with no change in whole tissue level. Proteome profiling of the synaptosome identified an increase in mitochondrial complex I and V proteins that rapidly decreased with MA in *Hnrnph1* mutants. In contrast, the much lower level of basal mitochondrial proteins in the wild-type mice showed a rapid,

MA-induced increase. Altered mitochondrial proteins associated with the *Hnrnph1* mutation may contribute to reductions in MA behaviors. hnRNP H1 is an abundant RNA-binding protein in the brain, involved in all aspect of post-transcriptional regulation. We examined both baseline and MA-induced changes in hnRNP H-RNA interactions to identify targets of hnRNP H that could comprise the neurobiological mechanisms of cellular adaptations occurring following MA exposure. hnRNP H post-transcriptionally regulates a set of mRNA transcripts in the striatum involved in psychostimulant-induced synaptic plasticity. MA treatment induced opposite changes in binding of hnRNP H to these mRNA transcripts between *Hnrnph*1 mutants versus wild-types. RNA-binding, transcriptome, and spliceome analyses triangulated on hnRNP H binding to the 3'UTR of *Cacna2d2,* an upregulation of *Cacna2d2* transcript, and decreased 3'UTR usage of *Cacna2d2* in response to MA in the *Hnrnph1* mutants. *Cacna2d2* codes for a presynaptic, voltage-gated calcium channel subunit that could plausibly regulate MA-induced dopamine release and behavior. The multi-omics datasets point to a dysregulation of mitochondrial function and interrelated calcium signaling as potential mechanisms underlying MA-induced dopamine release and behavior in *Hnrnph1* mutants.

PREFACE

Chapter II of this dissertation is adapted from Ruan et al. (2020), published in *The FASEB*. The work described was conducted by Qiu Ruan, Neema Yazdani, and Eric Reed.

Chapter III of this dissertation is adapted from Ruan and Yazdani et al. (2020), published in *Journal of Neuroscience*. The work described was conducted by Qiu Ruan and Neema Yazdani.

Chapter IV of this dissertation is adapted from a manuscript that is under peer review for publication. The work described was conducted by Qiu Ruan.

TABLE OF CONTENTS

LIST OF TABLES

LIST OF FIGURES

LIST OF ABBREVIATIONS

3’UTR	3’untranslated region
5’UTR	5’untranslated region
AC	adenylate cyclase
AMPAR	α-amino-3-hydroxy-5-methyl-4-isoxazolepropionic acid receptor
B6J	C57BL/6J
CaMKII	α-subunit of the calcium/calmodulin kinase II
CDS	coding sequence
CLIP-seq	crosslinking immunoprecipitation followed by sequencing
CNS	central nervous system
CPEB	cytoplasmic polyadenylation element binding factor
CPM	counts to million
CPP	conditioned place-preference
cTag	conditionally tagged
D2J	DBA/2J
DA	dopamine
DARPP-32	dopamine and cAMP-regulated phosphoprotein of 32 kDa
DAT	dopamine transporter
DOPAC	3,4-Dihydroxyphenylacetic acid
DRD1	dopamine receptor D1

ETC	electron transport chain
FMRP	fragile X mental retardation protein
GO	gene ontology
GTF	Gene Transfer Format
H1 MUT	*Hnrnph1* mutants
HEK	Human Embryonic Kidney
hnRNP A1	heterogeneous ribonucleoprotein A1
Hnrnph1	heterogeneous nuclear ribonucleoprotein H1
IHC	immunohistochemistry
KEGG	Kyoto Encyclopedia of Genes and Genomes
lncRNAs	long noncoding RNAs
MA	methamphetamine
mGluR	metabotropic glutamate receptor
miRs	microRNAs
MOR	mu opioid receptor
MSNs	medium spiny neurons
N2a	Neuro2a
NAc	nucleus accumbens
NLS	nuclear localization signal
NMDAR	N-methyl-D-aspartate receptor

Nova	neuro-oncological ventral antigen
OD	optical density
PBS	phosphate buffered saline
PKA	protein kinase A
PLP	proteolipid protein
PUDs	psychostimulant use disorders
qPCR	real-time quantitative PCR
qRRMs	quasi-RNA recognition motifs
QTG	quantitative trait gene
QTL	quantitative trait locus
QTVs	quantitative trait variants
RBP	RNA binding protein
RIP-seq	RNA-immunoprecipitation followed by sequencing
RNP	ribonucleoprotein
ROS	reactive oxygen species
SAL	saline
SNc	substantia nigra pars compacta
SNP	single nucleotide polymorphism
SUD	substance use disorder
TALENs	Transcription Activator-like Effector Nucleases

TH	tyrosine hydroxylase
Trf2	telomere repeat-binding factor
TRIBE	targets of RNA-binding protein identified by editing
VGCC	voltage-gated calcium channel
VMAT2	vesicular monoamine transporter 2
VTA	ventral tegmental area
WT	wild-type

CHAPTER I: INTRODUCTION

Molecular and Behavioral Response to Methamphetamine

Overview

The rate of overdose deaths involving psychostimulants with abuse potential [drugs such as methamphetamine (MA)], increased nearly five-fold from 2012 to 2018 in the U.S. (Hedegaard et al., 2020). MA is a highly addictive psychostimulant drug that induces neurotoxic effects and neurocognitive deficits following chronic administration. The widespread misuse of MA can destroy the social fabric of communities; thus, MA dependence presents a significant public health concern. After being a major drug of abuse in the 1970s and 1980s, MA has made a comeback as evident by the surge in overdose deaths due to MA. A major factor for its rise is the ease of manufacturing, thus, making MA highly accessible (Galbraith, 2015). While it is important to address the opioid crisis, the MA crisis that has fallen by the wayside should not be neglected. While there are medications available for treating opioid dependence (e.g. buprenorphine) and reversing opioid overdose (e.g. naloxone), there are currently no FDA-approved drugs to manage addiction to MA. There is an urgent need for effective therapeutics to mitigate the negative effects of MA, which will be discussed in the following section. Studies aimed to understand the relationship between sensitivity to initial drug effects and subsequent use in both humans and animal models suggest that the initial response to drugs often predict future use or abuse (Volkow et al., 2010; de Wit and Phillips, 2012). Because substance use disorders require drug exposure to manifest, understanding the underlying cellular and

molecular mechanisms of drug action and the rapid adaptations following acute administration will help inform novel therapeutic targets.

Methamphetamine: Mechanisms of Action

MA is a powerful synthetic amphetamine-type stimulant and frequent users of MA are more likely to become addicted to MA because of its better penetration in the brain (high lipid solubility) and longer duration of action (Nordahl et al., 2003; Won et al., 2013). MA is a substrate for monoamine transporters and competes with monoamines (mainly dopamine (DA), serotonin, and norepinephrine) and their respective transporters for reuptake (Rothman et al., 2001; Haughey et al., 2002; Adinoff, 2004). Once transported into the nerve terminal, MA enters synaptic vesicles via the vesicular monoamine transporter 2 (VMAT2) to and reverse its transport to promote efflux of monoamines into the cytosol (Fleckenstein et al., 2007; Siciliano et al., 2014). The elevated level of cytosolic monoamine causes reverse transport of monoamine into the synapse (Cruickshank and Dyer, 2009). In this way, MA elevates the extracellular monoamine by inducing synaptic vesicle depletion to increase intracellular monoamine and by promoting efflux through plasma membrane monoamine transporters. In addition, monoamine oxidase that is crucial for oxidative metabolism of monoamines is inhibited by MA (Sulzer et al., 2005), which further increases the synaptic level of monoamines for binding and stimulating postsynaptic monoamine receptors to shift neuronal and behavioral phenotypes.

Monoamine transporters, particularly dopamine transporters (DAT), are molecular targets that mediate abuse-related effects of psychostimulants such as amphetamine and MA (Koob, 1992; Howell and Negus, 2014). In early studies, amphetamine is reported to

reduce the cell surface level of DAT, resulting in accumulation of DAT in intracellular endosomes (Saunders et al., 2000; Chi and Reith, 2003; Sorkina et al., 2003). A mutation in DAT that impairs substrate transport but not substrate binding has no effect on amphetamine-induced DAT internalization when amphetamine is applied extracellularly (Kahlig et al., 2006). However, intracellular application of amphetamine leads to internalization of the uptake-impaired DAT, which indicates that DAT transport is not necessary for amphetamine-induced DAT internalization but rather the increase in intracellular amphetamine is the essential component for this regulation (Kahlig et al., 2006). Many of these earlier studies did not consider amphetamine-induced internalization of DAT is dependent upon the time of amphetamine exposure (Robertson et al., 2009). More recent studies indicate that the transient, rapid increase in DAT induced by amphetamine occurs within seconds and diminishes by 2.5 minutes (Johnson et al., 2005). Using a number of methods to tag and monitor endocytosis and recycling of DAT in DA neurons, the Amara lab has demonstrated that DAT internalized by DAT undergoes recycling and returns to neuronal surface (Hong and Amara, 2013).

Given that DA in the brain is important for the stimulant and rewarding effects of psychostimulants (Wise, 2004), the increase in DA induced by MA in key brain regions may largely account for the abuse potential of MA (Baumann et al., 2002). The major DA pathways include the mesolimbic, mesocortical, and nigrostriatal pathways (Wise, 2004) and DA release exerts different functional effects within these pathways including feelings of reward, decision making, and motor movement, respectively. The mesolimbic pathway comprises dopaminergic axonal projections originating in the DA-rich nucleus ventral

tegmental area (VTA) and projecting and terminating primarily in the nucleus accumbens (NAc) (Adinoff, 2004). Activation of the mesolimbic pathway by MA is accompanied by an increase in the extracellular concentration of DA in the NAc to mediate feeling of pleasure and reward (Juarez and Han, 2016). The VTA also provides dopaminergic innervation from the VTA to the prefrontal cortical regions (orbitofrontal cortex and anterior cingulate) known as the mesocortical pathway, which is known to play a role in inhibitory control and decision making (Gardner and Ashby, 2000). Lastly, the nigrostriatal pathway that originates in the zona compacta of the substantia nigra to the caudate putamen (or dorsal striatum) mediates motor activity (Bourdy et al., 2014). These neurons undergo MA-induced synaptic and neural circuit adaptations following acute and chronic MA exposure that ultimately lead to a transition into MA-dependent state. These three pathways and the initial action of drugs of abuse on these pathways are outlined in **Figure 1**.

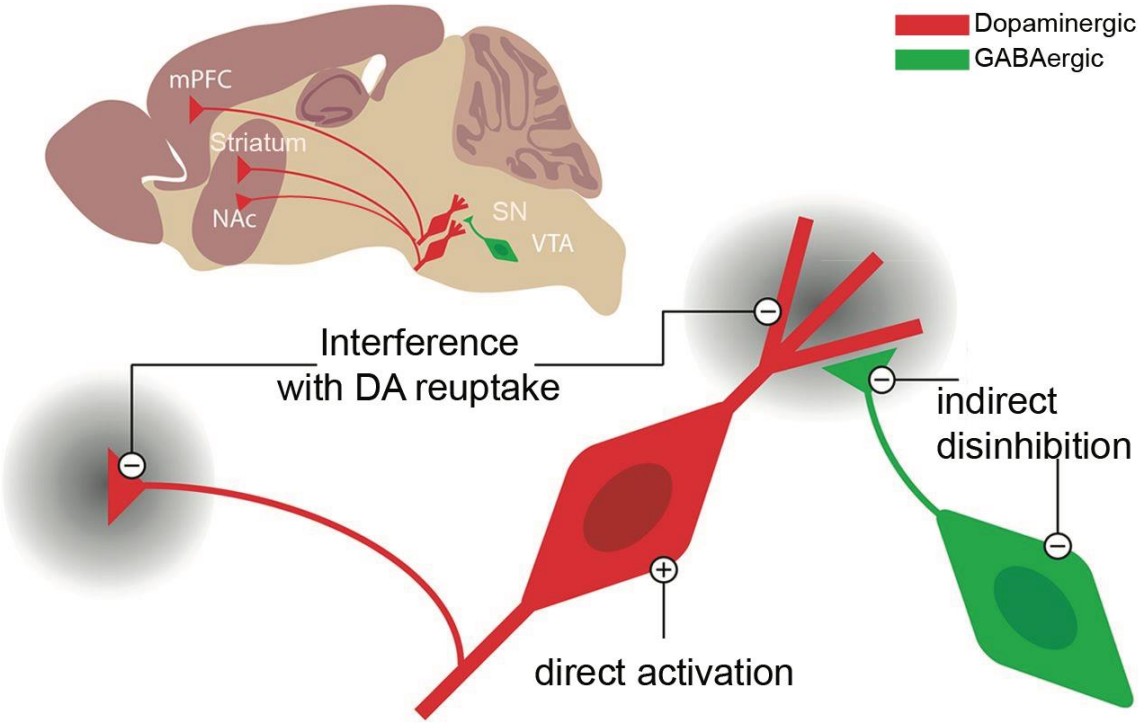

Figure 1. Initial Actions of Drugs of Abuse on the Mesocorticolimbic and Nigrostriatal Pathway.
Dopaminergic neuron projections from the VTA to the NAc and mPFC comprise the mesocorticolimbic system while dopaminergic neuron projections from the SNc to the striatum make up the nigrostriatal pathway. There are three ways for drugs of abuse to increase DA in these pathways: 1) direct activation of dopaminergic neurons; 2) indirect disinhibition of dopaminergic neuron by inhibiting GABAergic neurons; 3) interference of DA reuptake at the terminals. Psychostimulants like MA block reuptake of DA at synaptic terminals. Diagram is modified and adapted from Lüscher, 2013.

Dopamine Receptor Signaling

All drugs of abuse elicit their effect by activation of the mesolimbic reward pathways. MA reverses DAT to lead to a buildup of synaptic DA to activate dopamine receptors on target neurons (Drago et al., 1998; Tomkins and Sellers, 2001; Zhu and Reith, 2008). Through gene cloning procedures, pharmacological and genetic manipulation, five distinct dopamine receptor subtypes were isolated and structurally and functionally characterized and were divided into D1-like (D1, D5) or D2-like (D2, D3, D4) subgroups (Beaulieu and

Gainetdinov 2011; Missale et al. 1998; Rankin et al. 2009). All dopamine receptors are rhodopsin-like seven-transmembrane receptor (also known as G protein-coupled receptors because these receptors are coupled to G proteins for signal transduction) (Levey et al., 1993; Drago et al., 1998). Stimulation of brain dopamine receptors regulates locomotion, motivation, and working memory (Rankin et al., 2009).

The general property of D1-like dopamine receptor is the capability to activate adenylyl cyclase (AC). Activation of D1-like dopamine receptor is coupled to Gαs or Gαolf family of G proteins to stimulate cAMP production by AC, leading to increase in protein kinase A (PKA) activity. D1-class receptors are expressed at the highest level in the nigrostriatal, mesolimbic, and mesocortical areas and found almost exclusively on postsynaptic DA receptive cells such as GABAergic MSNs in the striatum (Beaulieu and Gainetdinov 2011). In general, activation of PKA by D1 signaling alters Ca^{2+} and K^{+} conductance to enhance excitatory glutamatergic input in MSNs shifting the cells into a more depolarized state (Surmeier et al., 2007). Activation of postsynaptic D1 receptors on postsynaptic neurons is required for manifestation of locomotor activity (Missale et al., 1998).

The most studied intracellular effect mediated by D1 dopamine receptor is the activation of the cAMP pathway (Hyman et al. 2006; Nishi et al. 2011). In striatal MSNs of the direct pathway, DA acting on D1 receptors activates AC for induction of the cAMP-PKA signaling cascade, whereby the increased level of cAMP leads to the activation of PKA. A major downstream target of this pathway is DARPP-32 (dopamine and cAMP-regulated phosphoprotein of 32 kDA), which is found on both D1-receptor-enriched

striatonigral neurons of the direct pathway and on D2-receptor-enriched striatopallidal neurons of the indirect pathway. Activated PKA phosphorylates DARPP-32 at Thr34, which in turn inhibits protein phosphatase-1 to control phosphorylation state of a cascade of downstream effectors including neurotransmitter receptors, ion channels and pumps, and transcription factors. The two other signaling cascades coupled to D1 receptor activation are 1) phospholipase and inositol 1,4,5-triphophate activation for increase in calcium to activate CaMKII (Ca^{2+}/calmodulin-dependent kinase II) and 2) Src family kinase/RAS/ERK signaling to induce histone H3 phosphorylation (Nishi et al. 2011). Collectively, all three distinct signaling pathways mediated by stimulation of D1 receptor lead to phosphorylation and activation of the cAMP-response element binding protein (CREB) in the nucleus for transcriptional activation of genes to alter the activity of the neurons which express those genes, ultimately leading to changes in synaptic plasticity.

The D2 class of DA receptor is coupled to Gαi or Gαo which inhibits AC causing a decrease in PKA activity (Surmeier et al., 2007). The reduction in PKA signaling alters Ca^{2+}, NA^{+}, and K+ conductance to decrease the glutamatergic innervation to prevent spiking. Unlike D1 receptors which are predominantly expressed postsynaptically, D2-like DA receptor including D2DAR and D3DAR are found both postsynaptically on DA target cells and presynaptically on dopaminergic neurons (Nagy et al., 1978; Sokoloff et al., 2006). The striatum, NAc and olfactory tubercle contain the highest levels of D2 DA receptor (Beaulieu and Gainetdinov 2011). Besides difference in expression level between D1 and D2 DA receptors, there is also difference in genomic organization where the D1 (and D5)

DA receptor genes have no introns in their coding sequence and genes that code for D2-class receptors contain various number of introns (Beaulieu and Gainetdinov 2011; Missale et al. 1998). The presence of introns allows for alternative splicing to generate DA receptor splice variant, and the most notable example is the differential splicing of the D2 dopamine receptor gene to give rise to two D2DAR isoforms with different localization and function.

The two alternative spliced isoforms of D2DAR are named D2S (D2-short) and D2L (D2-long), where D2S is generated by splicing of an 87-base-pair exon between introns 4 and 5 to yield a receptor product that is missing a stretch of 29 amino acids in the third intracellular loop (Nagy et al., 1978; Usiello et al., 2000). The two isoforms have distinct functions due to differences in anatomical, physiological and pharmacological properties. The D2S isoform is expressed on presynaptic dopaminergic neurons and functions as an autoreceptor to regulate DA synthesis and release in response to changes in extracellular dopamine concentration (Wolf and Roth, 1990; Missale et al., 1998; De Mei et al., 2009). The highest expression D2S is found in midbrain dopaminergic terminals (Fig. 1). As an autoreceptor, presynaptic D2S provides a negative feedback mechanism for regulating dopaminergic response. In condition of high synaptic dopamine level, in the case of dopamine transporter blockade by drugs of abuse, D2S becomes activated to slow the firing rate of presynaptic DA neurons and inhibit DA synthesis and release (De Mei et al., 2009). Thus, the main regulatory role of D2S is to counteract the effect of drugs of abuse. Due to its ability to exert feedback inhibition, dysregulation of D2S is highly implicated in the pathophysiology and vulnerability to drug abuse.

Several mechanisms have been proposed as to how D2S exerts auto-inhibition of DA synthesis and release. One of such mechanism is that D2S reduces phosphorylation of tyrosine hydroxylase (TH), which is an enzyme involved in the synthesis of catecholamine, resulting in decrease in dopamine synthesis (Lindgren et al., 2003). A reduced level of activated phosphorylated TH was found in D2R1/- mice (with knockout of both D2S and D2L isoform) but not in D2L-/- mice. In addition to modulating DA synthesis, D2S controls release of DA via regulation through protein-protein interaction for trafficking of DAT to the plasma membrane of nerve terminals (Lee et al. 2007). Disruption of D2S and DAT interaction leads to increased locomotor activity in mice, a behavior output similar to what has been observed in DAT knockout mice. Pharmacological studies have shown that a lower concentration of DA receptor agonist is needed for activation of the presynaptic D2-class autoreceptors compared to that of postsynaptic D2 receptors (Beaulieu and Gainetdinov 2011). For this reason, the same D2 dopamine receptor agonist can induce a biphasic effect where low dose can lead to decrease in locomotor activity and high dose results in increase in locomotor activity.

On the other hand, D2L is predominantly expressed on postsynaptic medium spiny neurons (MSNs). Activation of D2L inhibits adenylyl cyclase (and thus decrease in cAMP level and inhibition of PKA) to decrease DARPP-32 phosphorylation at Thr34 and also stimulates calcium-dependent PP2B to further dephosphorylate DARPP-32 (Bateup et al. 2008). D2L-mediated dephosphorylation is lost in MSNs of both D2L-/- and D2R-/- mice, demonstrating the involvement of the D2L isoform in postsynaptic regulation. At the postsynaptic site, there is also an cAMP-independent pathway mediated by activation of

D2L involving serine/threonine kinase AKT signaling. In a parallel pathway (in addition to PKA inactivation), D2L signaling recruits β-arrestin and PP2A to downregulate AKT phosphorylation and activity to result in inactivation of GSK3 (threonine/serine kinase 3) for regulation of dopaminergic associated behavior (Beaulieu et al. 2005).

Methamphetamine-Induced Hyperlocomotion

The rapid release of monoamines, mainly DA, from nerve terminals, is the early neurochemical event that drives the acute behavioral effects in response to MA, include motor stimulation, increased energy, alertness and active waking state (Hassan et al., 2016). The psychomotor stimulant theory of addiction states that the common action shared by addictive substances is their ability to cause psychomotor activation by stimulating dopaminergic fibers and their output projection as discussed in the previous sections (Wise and Bozarth, 1987). Behavioral studies involving manipulating DA levels established a role for DA in unconditioned behavior, such as locomotor activity (Costall and Naylor, 1975; Beninger, 1983). The onset of MA-induced locomotor activity correlates with the onset of DA efflux in the striatum and nucleus accumbens in the time-dependent manner (**Figure 2**) (Shimosato et al., 2003). Based on this observation, one can hypothesize that agents that bind to DAT, VMAT2, or DA receptors to antagonize or partially substitute for the effect of MA may be useful for treatment of MA addiction.

It is important to note that the neurocircuitry and molecular mechanisms underlying drug-induced locomotor activity are in part shared with those that mediate the reward and reinforcing properties of drugs of abuse (Wise and Bozarth, 1987; Di Chiara and Imperato,

1988; Deminiere et al., 1989). Thus, it is reasonable to hypothesize that common, shared genetic factors influence locomotor and addiction-relevant traits. In fact, our lab has observed such phenomenon with the gene, heterogeneous nuclear ribonucleoprotein (*Hnrnph1*), which we first mapped using forward genetics and validated for MA-induced locomotor activity (Yazdani et al., 2015), and we subsequently found plays a role in MA-induced reward, MA-induced reinforcement, and MA-induced change in extracellular level of DA in the NAc (Ruan et al., 2020a). More details about this gene will be covered later.

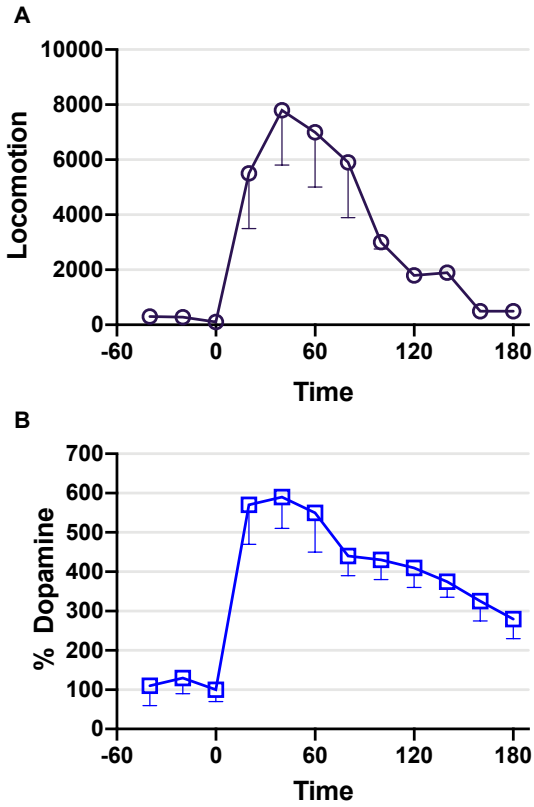

Figure 2. Effect of methamphetamine locomotion activation in mice.
MA increases locomotor activity **(A)** that is correlated with increase in DA release in the NAc **(B)**. These two plots are replotted from data generated in Shimosato et al. (2003) in which they performed a series of experiments to demonstrate that the onset of MA-induced locomotor activity correlates with the onset of dopamine release in nucleus accumbens in the time-dependent manner.

Genetic Factors that Drive Acute Drug Action of Addictive Drugs

Initial response to drugs can predict future use or misuse in both humans and model organisms (de Wit and Phillips, 2012), suggesting that understanding the initial actions of addictive drugs can yield potential therapeutic interventions in the treatment of addiction. Studies in humans and model organism demonstrated that there are individual differences in initial, acute responses to drugs of abuse (Deminiere et al., 1989), pointing out that the possibility of genetic factors influencing the initial response, and thus impacting

vulnerability to future use. For example, genetic variation can be found in a gene that affect the rate at which drugs are metabolized which affect one's sensitivity to the drug effects and risk for repeated use.

The use of longitudinal and laboratory-based studies in human demonstrated that subjects experiencing greater positive acute effects chose to consume the drug again when given the choice (de Wit and Phillips, 2012). The use of inbred mouse and rat strains to examine individual differences in sensitivity to initial drug effects (via locomotor activity assessment) in relation to likelihood of self-administrating drug also provided evidence that initial drug responses predict future use, where a greater acute locomotor activation was predictive of greater of self-administration (Deminiere et al., 1989; Piazza et al., 1989; Shabani et al., 2011). In fact, there are many shared genetic factors that influence initial sensitivity and subsequent drug intake (de Wit and Phillips, 2012).

Role of RNA-Binding Proteins in Addiction

Overview

RNA-binding proteins (RBPs) contain RNA binding domain and bind to RNAs and regulate every aspect of their life cycle including transcription, posttranscriptional editing, splicing, export into the cytoplasm, stability, translation, and finally degradation (Glisovic et al., 2008). RBPs bind to RNAs to form ribonucleoprotein (RNP) particles that permit spatiotemporal localization of the RNAs for translation in the proper location at the appropriate time (Tolino et al., 2012). mRNA trafficking and local protein synthesis allows neurons to meet constant synaptic demand and activity (Glock et al., 2017). Regulation of

mRNAs in neurons relies heavily on RBPs binding to cis-acting elements within the mRNAs for transport from cell body to distal axons and dendrites (Schuman, 1999; Czaplinski, 2014; Thelen and Kye, 2020). While there is an abundance of evidence implicating RBPs neurological diseases including autism, schizophrenia, amyotrophic lateral sclerosis, and neurodegeneration (Conlon and Manley, 2017; Zhou et al., 2018; Park et al., 2020), the role of RBPs in neuropsychiatric disorders like the addictions is less established. However, given the accumulating evidence that RBPs maintain proper synaptic function through regulating neuronal protein homeostasis (Sephton and Yu, 2015; Klein et al., 2016; Thelen and Kye, 2020), it is logical to hypothesize that RBPs play a role in synaptic plasticity that is important for all stages in the addiction cycle (Bryant and Yazdani, 2016), including rapid cellular adaptations induced by acute exposure as well as persistent changes in protein expression that mediate synaptic plasticity. Many RBPs regulate mRNA trafficking and local protein synthesis in synaptic plasticity (Ule and Darnell, 2006; Tolino et al., 2012; Thelen and Kye, 2020).

Function of RNA-Binding Proteins in Synaptic Plasticity: Implications for Addiction

Drug-induced synaptic plasticity refers to the neural circuit adaptations and the ability for the synapse to modify their synaptic strength following initial and repeated drug exposure in the establishment of addiction (Luscher and Malenka, 2011; Lüscher, 2013). Excitatory synaptic plasticity involves depolarization of neurons for activation of glutamate receptors and calcium influx for induction of long-term potentiation (Nestler, 2001). Post-transcriptional gene regulation by RBPs is necessary for activity-dependent synaptic plasticity (Schuman et al., 2006; Hörnberg and Holt, 2013; Mirisis and Carew, 2019). RBPs

exert diverse actions in the synapse, including alternative splicing to increase transcriptome and proteome diversity, and mRNA transport in response to neural activity (Glisovic et al., 2008; Fu and Ares, 2014), both of which will be explored in this section.

Transcriptomic studies indicate that the brain exhibits more alternative splicing than the other tissues (Yeo et al., 2004; Pan et al., 2008). Emerging evidence indicates an interplay between activity-dependent alternative splicing and synaptic plasticity (Thalhammer et al., 2020). Exon 19 of NMDA receptor 1 was shown be alternatively spliced in response to neuronal activity (Ehlers et al., 1995). The RBP neuro-oncological ventral antigen (Nova), acting in concert with heterogeneous ribonucleoprotein A1 and H and neuroblastoma apoptosis-related NAPOR represses exon 19 inclusion in the forebrain (Zhang et al., 2002; Han et al., 2005; Ule and Darnell, 2006). In addition, the identification Nova target RNAs via CLIP-seq (cross-linking immunoprecipitation followed by sequencing) revealed an RNA-network that was enriched for the synapse and axon guidance, suggesting this RBP to have a role in synaptic physiology (Ule et al., 2005b). Interestingly, many of the Nova target RNAs involved in synaptic plasticity exhibit alternative splicing patterns in the absence of Nova, suggesting the contribution of additional RBPs. Combination of CLIP-seq, other omic approaches, and electrophysiology like those employed in the study of Nova will be necessary for understanding the complexities of RBP-mediated splicing that regulate synaptic plasticity.

There are two ways in which temporal and spatial regulation of gene expression and protein synthesis are regulated for drug-induced neurotransmission. One, synaptic proteins are synthesized in the cell body and subsequently transported to the synapses

(Doyle and Kiebler, 2011). Second, localized mRNAs and components of the translational machinery are present at the dendrites, where local translation can take place on demand (Schuman et al., 2006; Fernandez-Moya et al., 2014). The latter requires the help of RBPs to actively transport mRNA transcripts from the cell body to the dendrites. Over the years, researchers have identified a handful of RBPs that are termed translational regulators of dendritic mRNAs that responds to synaptic activations. The cytoplasmic polyadenylation element binding factor (CPEB) is involved in NMDA-dependent long-term potentiation (Si et al., 2003; Alarcon et al., 2004). Specifically, CPEB functions to disinhibit translation in neuronal synapse to promote translations of mRNAs that are constitutively repressed (Huang et al., 2002). Following NMDAR stimulation in the synaptosome of primary neurons, CPEB is activated by the kinase Aurora and phosphorylated by CaMKII for dendritic localization and translational activation CaMKIIα, which in turn activates CPEB via phosphorylation, thus establishing a positive feedback loop (Atkins et al., 2005). In addition, NMDAR-activated CPEB also play a role in polyadenylation of a set of synaptic RNAs (Du and Richter, 2005).

In contrast, fragile X mental retardation protein (FMRP) mediates translational inhibition and plays a role in metabotropic glutamate receptor (mGluR)-dependent long-term depression (Huber et al., 2002). FMRP is implicated in an array of neuropsychiatric disorders including autism, ADHD, bipolar disorder, schizophrenia as well as the addictions (Fernández et al., 2013). inhibition of synthesis of cytoskeletal regulatory proteins (e.g., microtubule associated proteins) is required for proper synapse development (Comery et al., 1997; Nimchinsky et al., 2001). Stimulation of mGluRs localizes *Frm1*

(gene name for FMRP) mRNA to the dendrites followed by rapid translation of FMRP (McBride et al., 2005). Furthermore, there are many examples linking FMRP to psychostimulant neuroplasticity. In one example, deletion of FMRP disrupts cocaine-induced synaptic plasticity by increasing AMPA/NMDA receptor ratio and glutamatergic transmission (Smith et al., 2014). In another example demonstrating activity-dependent function of FMRP, DRD1 activation in prefrontal cortical neurons phosphorylates FMRP, resulting in synthesis of synaptic proteins needed for glutamate receptor trafficking (Wang et al., 2008, 2010).

The three RBPs discussed in this section are involved in activity-dependent synaptic plasticity either at the level of alternative splicing that is NMDAR-dependent (Nova), or mRNA trafficking and protein synthesis that is NMDAR-dependent (CPEB) or mGluR-dependent (FMRP). These examples shed light on the diverse function of RBPs in modulating different types of synaptic plasticity in response to neuronal stimulation. Following drug administration, these RBPs are required to coordinate splicing and translation in the VTA, which can have downstream consequences in neurotransmission in the striatum and prefrontal cortex. Besides FMRP playing a role in synaptic plasticity associated with psychostimulant addiction behaviors, evidence will be presented that another RBP, hnRNP H1, contributes to rapid presynaptic and postsynaptic cellular adaptations in response to MA administration that influences subsequent behavioral addiction traits and will be discussed below.

Role of RNA-Binding Proteins in Mitochondrial Function

The excessive amount of DA within the dopaminergic terminals and synaptic cleft caused by MA is oxidized to quinone or semi-quinone to generate reactive oxygen species, H_2O_2, OH^-, and $O2^-$ (LaVoie and Hastings, 1999; Baumann et al., 2002). The accumulation of these reactive oxygen species (ROS) leads to a series of oxidative stress reactions to promote organelle damage and protein misfolding and trigger cell death (Limanaqi et al., 2018). All these events converge to produce neurotoxicity within the DA terminals. The mitochondria, which generate energy through oxidative phosphorylation and ATP production, represent a major site of MA-induced ROS production in neurons (Dawson and Dawson, 2017). Multiple studies demonstrated that inhibition of the electron transport chain (ETC) and promotion of oxidative stress by MA can lead to mitochondrial dysfunction (Annepu and Ravindranath, 2000; Beer et al., 2004; Shin et al., 2017). Specifically, DA oxidation-generated ROS inhibit complexes I, II, III, IV and V of the ETC to lead to imbalance of oxidation and energy production (Burrows et al., 2000). The changes in mitochondrial enzymes in response to MA have been heavily investigated in recent years. Studies have found inhibition of striatal complex I activity after acute exposure to MA (Annepu and Ravindranath, 2000; Beer et al., 2004) and a decrease in striatal complex II activity with no change in complex I in response to rapid binge exposure to MA (Brown et al., 2005). MA treatment *in vitro* led to reduction in mitochondrial complex IV proteins in a time-dependent manner (Wu et al., 2007). All these studies shed light on the notion that MA can inhibit mitochondrial respiratory activity in neurons that

in turn promotes presynaptic toxicity in nerve terminals and impact synaptic ATP production needed for vesicle fusion, neurotransmitter release and recycling.

Mitochondria are abundant at the axons and dendrites and generate ATP for calcium buffering, vesicle release and recycling (Vos et al., 2010; Devine and Kittler, 2018). In addition, mitochondria are also present to synthesize ATP and regulate calcium needed for synaptic transmission and plasticity (Harris et al., 2012; Todorova and Blokland, 2017). Thus, maintaining mitochondrial function so that the mitochondria can respond to changes in synaptic activity requires coordinated regulation of the mitochondrial gene and protein expression (Schatton and Rugarli, 2018). Recent studies have identified a set of RBPs that regulate expression of mRNAs coding for mitochondrial proteins (a subset of these RBPs are highlighted in **Table 1**). RBPs transport mitochondrial RNAs from the nucleus (nuclear-coded mRNAs) to the mitochondria for organelle-coupled translation (Williams et al., 2014). In this way, RBPs chaperone these nuclear coded mRNAs toward the outer membranes of the mitochondria and recruit translation activators to initiate translation followed by transport into the mitochondrial for complex assembly (Béthune et al., 2019; Rossoll and Bassell, 2019).

The coordinated regulation of mitochondrial function by RBPs suggests that experimental targeting of these RBPs can modulate mitochondria to influence neurotransmission in response to drugs of abuse. Multi-omics approaches can be used to identify the consequences of dysfunction on the basal and drug-induced transcriptome and proteome of mitochondrial proteins and thus inform which RBPs may be important for regulating the localization and expression of specific sets of mitochondrial proteins.

Table 1. Examples of RBPs regulating mRNAs encoding mitochondrial proteins.
The content of this table is selected from (Schatton and Rugarli, 2018) to highlight the RBPs binding to different regions within their target RNA and biological effect on binding.

RBP	RNA sequence or motif	Molecular function	Mitochondrial target mRNAs	Cellular Localization
ZC3H14	poly(A) tail	pre-mRNA processing, maturation, nuclear export control	ATP5G1	nucleus (majority), cytoplasm
PINK1	5'-cap	Localized translation on OMM	mRNAs encoding OXPHOS subunits	mitochondrial surface
NONO	promoter-proximal introns, inverted repeats in 3'UTR	pre-mRNA processing, nuclear export control	mRNAs for mitochondrial metabolic enzymes	nucleus, paraspeckles
Lin28a	GGAGA(U) in loop structures present in 3'UTR or CDS	Translational activation	PDHA1, IDH3B, SDHA, NDUFB3, NDUFB8	nucleus, cytoplasm

Heterogenous Nuclear Ribonucleoprotein H1

Overview

The class of heterogeneous nuclear ribonucleoproteins (hnRNPs) is comprises 20 hnRNPs labeled from A through U (Dreyfuss et al., 1993) that possess multi-functional roles in RNA biogenesis and metabolism, ranging from transcription, splicing, and mRNA stability in the nucleus (Arhin et al., 2002; Han et al., 2010) and translation and degradation in the cytoplasm (Han et al., 2010; Uren et al., 2016). The use of fine-scale gene mapping with interval-specific congenic mouse lines identified *Hnrnph1*, (gene-coding for heterogeneous nuclear ribonucleoprotein H1 or hnRNP H1), as the quantitative trait gene (QTG) for sensitivity to MA-induced locomotor activity (Yazdani et al., 2015). Mice with a heterozygous deletion in the first coding exon of this gene showed reduced MA-induced behavioral responding and DA release (Ruan et al., 2020a). This mutation resulted in a two-fold increase in hnRNP H protein level in the synaptosome and an enrichment of proteins indicative of mitochondrial dysfunction (Ruan et al., 2020a). Besides hnRNP H1, genetic mutations in other genes encoding for RBPs including FMRP (Li et al., 2020), PTBP1 (Spellman and Smith, 2006), EFTUD2 (Lines et al., 2012), and SF3B4 (Bernier et al., 2012), have been implicated in neuropsychiatric disorders including the addictions, especially FRMP (Smith et al., 2014) as previously discussed. hnRNP H1 shares a 96% protein sequence homology with hnRNP H2 (Honoré et al., 1995) and there are no antibodies that have been demonstrated to distinguish between the two gene paralogs. Because hnRNP H1 and hnRNP H2 cannot be differentiated at the protein level, I will collectively refer to hnRNP H1 and hnRNP H2 as hnRNP H.

Structural Domains of hnRNP H1

hnRNP H1 contains three quasi-RNA recognition motifs (qRRMs) as RNA binding domains and two glycine-rich (GY and GYR) domains as illustrated in **Figure 3** (Dominguez and Allain, 2006; Van Dusen et al., 2010). While qRRM3 conforms to a canonical β-sheet structure, qRRM1 and qRRM2 are more structurally distinct and come together to form a more exposed RNA-binding surface that will allow the RBP to interact with the highly stable G-rich secondary structure within target RNAs (Dominguez and Allain, 2006). Deletion of the three qRRMs from *Hnrnph1* (a splice variant of the paralogue *Hnrnph3*) produces a truncated protein that cannot participate in RNA metabolism (Honoré, 2000), indicating the RNA binding property of hnRNP H1 is conferred by the qRRMs.

The two glycine-rich domains in hnRNP H1 are known to mediate protein interactions with other proteins, including other RBPs, to form multi-protein complexes needed for transcriptional and post-transcriptional (Van Dusen et al., 2010). The central GYR domain contains a nuclear localization signal (NLS) that allows hnRNP H1 to shuttle protein between the nucleus and cytoplasm. Van Dusen et al. (2010) discovered that the NLS within hnRNP H1 interacts with the import receptor Trn1 which facilitates the movement between the nucleus and cytoplasm. While hnRNP H1 is mainly nuclear restricted, activity-dependent translocation of hnRNP H1, e.g., in response to stress, can induce translocation of hnRNP H to the cytoplasm (Wall et al., 2020). These observations suggest that hnRNP H participates in RNA metabolism in both the nucleus and cytoplasm.

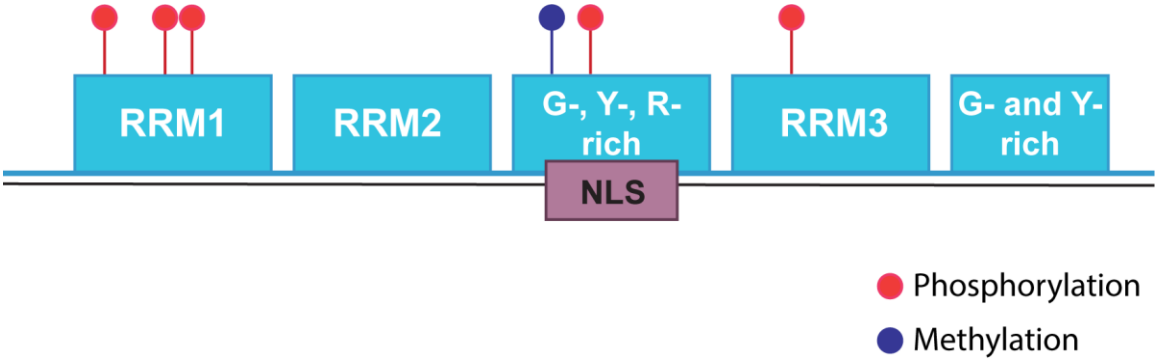

Figure 3. Domains and post translation modifications of hnRNP H1.
hnRNP H1 contains three RNA recognition domains, including RRM1, RRM2, and RRM3, which interact with RNAs during post-transcriptional regulation. The GYR and GY domains interact with other RBPs or proteins to form these multiprotein complexes. The NLS within the GYR domain allows hnRNP H1 to shuttle between the nucleus and cytoplasm. hnRNP H1 can be post-translationally modified at the level of phosphorylation and methylation. The signaling events that mediate this change are not well characterized.

Function of hnRNP H1 in the Central Nervous System and the Addictions

Whole exome sequencing identified variants in HNRNPH2 on the X chromosome that were associated with Bain type intellectual disability in a cohort of six females from independent families with neurodevelopmental disability (Bain et al., 2016). It is particularly interesting that variants are found within the NLS of *HNRNPH2*, in particular, the Arg206Trp mutation was found in four of the six subjects. Subsequently, in 2018 and 2020, two groups found the same pathogenic variant, Arg206Trp within *HNRNPH1* in patients showing Bain type syndromic neurodevelopmental disorder with a syndrome comprising developmental delay, intellectual disability, autism, hypotonia, and seizures (Pilch et al., 2018; Reichert et al., 2020). Breeding data from our lab indicated homozygous deletion of *Hnrnph1* is embryonic lethal. These observations implicate a role of hnRNP H1 in neurodevelopment, perhaps through transcriptional and post-transcriptional regulation

of mRNAs coding for proteins needed during development such as neuronal differentiation. Interestingly, transcriptome analysis found *Hnrnph1* to be downregulated during early stages of the oligodendrocyte differentiation process (Swiss et al., 2011; Wang et al., 2012).

While human genome-wide association studies have not identified *Hnrnph1* to be associated with the addictions, hnRNP H1 post-transcriptionally regulates genes involved in the addictions, including *Oprm1* (gene encoding for the mu opioid receptor or MOR) (Song et al., 2012; Xu et al., 2014) and glutamate NMDAR1 receptor (Han et al., 2005). The single-nucleotide polymorphism (SNP) (rs9479757) within the intron of the *OPRM1* gene was found in group of heroin addicts with the AG phenotype to be associated with mild addiction and the GG phenotype to be associated with more severe addiction (Xu et al., 2014). hnRNP H was found to bind to this G-containing SNP site to promote alternative splicing of nearby exon. Specifically, the G-to-A transition weakened the binding of hnRNP H, resulting in exon 2 skipping and increased expression of MOR protein (Xu et al., 2014). Identification of post-transcriptional regulators that bind to the 5'UTR of *OPRM1* via mass spectrometry detected the presence of hnRNP H1 and F (Song et al., 2012). Follow-up validation studies indicated that hnRNP H1 and F repress MOR translation though binding to the 5'UTR in a sequence-specific manner (Song et al., 2012). The studies from these two research groups provide evidence for the multi-functional roles of hnRNP H even when targeting the mRNA transcript of the same gene.

Activity-Dependent Function of hnRNP H1

hnRNPs are highly dynamic and respond to cellular cues and stimuli by changing RNA binding, subcellular localization, and protein interactions (Szostak and Gebauer, 2013; Hentze et al., 2018). hnRNPs can shuttle between the nucleus and cytoplasm and exert different regulatory effects on RNAs between the two compartments to support efficient recovery from cellular stress (Guil et al., 2006; Fukuda et al., 2009; Backlund et al., 2020). hnRNPs such as hnRNP A1 can associate with other RBPs in stress granules to sequester mRNAs in response to stress (Guil et al., 2006) and K (Fukuda et al., 2009). Stress granules are membrane-less organelles that are transiently formed to harbor translationally arrested mRNAs that might have accumulated in the cytoplasm in response to acute stress (Reineke and Neilson, 2019). The formation and decomposition of these stress granules are highly dynamic and complex, requiring over 100 RBPs (Aulas and Velde, 2015). Chronic stresses cause persistent formation of these stress granules, resulting in protein aggregations found in the pathophysiology of neurodegenerative diseases (Aulas and Velde, 2015; Wolozin and Ivanov, 2019). A recent study demonstrated that hnRNP H accumulates in the cytoplasm and localizes to the stress granules via its RRM3 domain in response to stress (Wall et al., 2020). Proteomic characterization of the stress granule composition also identified hnRNP H as a component of the stress granules, similar to hnRNP A1 and K (Markmiller et al., 2018). The association of hnRNP H with stress granule formation highlights the dynamic activity-dependent subcellular localization of hnRNP H in response to stress.

Our lab previously associated DRD1 activation with an increase in immunocytochemical staining but no change in protein level of hnRNP H in response to DRD1 agonist in primary rat cortical neurons, suggesting that potential post-translational modifications of hnRNP H and/or its association with other proteins or target RNAs could underlie this aberrant, DRD1-mediate change in hnRNP H staining (Ruan et al., 2018). Proteomic analyses to detect post-translational modifications in hnRNP H identified numerous phosphorylation residues and an arginine methylation site located downstream of the NLS (**Figure 3**) (Kim et al., 2002, 2014a). Activation of proteins for post-translational modification of hnRNP H (e.g., via kinase signaling cascades) can influence functional localization, RNA binding, and protein interactions.

Global Methods for Studying RNA-Binding Protein Interaction Networks

Overview

The transcriptional and post-transcriptional regulation of gene expression by RBPs are important for many biological processes. Characterizing RNA-binding preference of RBPs by assessing their target RNAs and binding site selection can reveal insights into their biological functions. UV-mediated crosslinking of protein-RNA complexes in biological samples is the most widely accepted strategy for genome-wide profiling and mapping of RBP-RNA interactions both *in vitro* and *in vivo* (Li et al., 2014; Nechay and Kleiner, 2020). Various variations of this prototypical method have been developed to improve the sensitivity, resolution, and efficiency (Lee and Ule, 2018; Sternburg and Karginov, 2020; Van Ende et al., 2020). computational methods and tools have been developed and are

continually updated to aid in the processing and analyzing the experimental data for binding site and binding target (Wang et al., 2015; Bottini et al., 2017; Uhl et al., 2017)

Crosslinking Immunoprecipitation Combined with RNA-Sequencing

Crosslinking immunoprecipitation followed by RNA sequencing (CLIP-seq) was first reported and performed by Dr. Robert Darnell's group to generate an RNA-binding map for Nova in the mouse brain (Licatalosi et al., 2008). This method provides a robust and unbiased means to identify functional protein-RNA interactions and define binding sites at single nucleotide resolution (Van Nostrand et al., 2016). In CLIP-seq, the use of UV irradiation at 254 nm activates the photo reactivity of nucleic acids to crosslink to protein and permits the capture of RBP-RNA complexes and defining the position of binding sites (Ule et al., 2005a). CLIP-seq can be applied to any type of samples, even post-mortem human tissue (Lee and Ule, 2018).

The following steps I will be describing are summarized from the Lee and Ule's (2018) review, which provides a comprehensive overview of core CLIP-seq steps. The next step following UV crosslinking includes cell lysis for purification of total cell and fractionated cells, which capture RBP-protein interactions in a cellular sub-compartmental manner (Sanford et al., 2008). Following this step is RNA fragmentation via limited RNase digestion, typically RNase I that cleaves nucleotides at random positions to minimize sequence bias of RNA fragmentation and produce RNA fragments of appropriate size for next-generation sequencing (Haberman et al., 2017) . The portion of RNA that is bound by the RBP is protected from RNase digestion. The following step is to capture the RBP-RNA complex with immunoprecipitation under stringent washing conditions to preserve only

the crosslinked RBP-protein contacts. Unlike RNA-immunoprecipitation followed by sequencing (RIP-seq), which does not require crosslinking and RNase and only identifies RNAs enriched in the IP, CLIP-seq can also detect the precise position of the binding sites, which is defined by the crosslinking site. The captured RBP-RNA complex is subjected to SDS-PAGE, membrane transfer, digestion of the RBP, and followed by RNA extraction to release the bound RNAs. Finally, sequencing adaptors are ligated to the extracted RNAs for next-generation sequencing. Each of these steps described here is subjected to optimization and variation to more accurately identify the mRNA transcripts interacting with RBPs *in vivo*.

Two parameters in CLIP-seq data need to be examined computationally, including sensitivity and selectivity (Chakrabarti et al., 2017). First, sensitivity refers to the number of unique cDNAs in the sequencing library (Chakrabarti et al., 2017). Duplicated cDNAs as a result of PCR amplification step can be identified using unique molecular identifiers (UMIs) in the cDNA during library preparation (Smith et al., 2017). Second, specificity refers to the identification of significant crosslinking events or peaks (Chakrabarti et al., 2017). Peak calling is an essential step in CLIP-seq analysis and determines the specific signal over background noise (Bottini et al., 2017). There are a number of publicly available peak calling programs that use different statistical models. The selection of a suitable peak calling program depends on the CLIP protocol used to produce the dataset (Chakrabarti et al., 2017) and might require literature search to compare the utility of the available peak calling programs. If possible, the addition of a control condition such as knockout or knockdown, can help to identify false positive peaks (Bottini et al., 2017).

After a list of significant peaks are identified, the next step is to characterize the RBP-RNA interactions by closer examination of the peaks. The regulatory role of the RBP on transcription and post-transcription regulated can be evaluated by quantifying the distribution of the peaks across mRNA subregions, including the 5'UTR, 3'UTR, intron, and coding sequence (CDS). The signatures of the peak-associated binding sequences signatures can be detected via *de novo* motif discovery programs such as MEME (Bailey et al., 2009) and Homer (Heinz et al., 2010). The output from these programs includes a list of sequence enriched in the CLIP peaks from the peak calling program. To gain insight into the molecular and biological functions of the RBP, target RNAs that are associated with the peaks are subjected to pathway and gene ontology (GO) enrichment analysis to determine whether the RBP regulates a subset of targets with a particular biological relevance. By coupling CLIP-seq datasets with other omic datasets including transcript expression, alternative splicing, and protein expression profile, the functional impact of the RBP on the target RNAs can be assessed. A multi-omics approach can also narrow down the RBP-RNA interactions that warrant validation and testing for functional relevance, e.g., at the cellular or behavioral level.

Besides performing genome-wide functional validation at the genome-wide scale like with RNA-seq and/or mass spectrometry, CLIP-seq experiments can be validated by candidate approach, which involving picking only the most significant targets or a set of targets that are enriched for a relevant biological pathway or function (Thomson et al., 2011). The type of validation experiments can be performed at the level of physical interaction and functional output (Bottini et al., 2017). Interaction between an RBP and

mRNA transcript of interest can be validated using *in vitro* electrophoretic mobility shift assays, which involve the incubation of a candidate RBP with a radiatively labeled 32-P RNA fragment containing the binding site identified through CLIP-seq followed by electrophoresis using a polyacrylamide gel to observe a shift if the RBP binds to the RNA fragment (Fillebeen et al., 2014). For *in vivo* method of validation in cell or tissue, RNA-immunoprecipitation with an RBP-specific antibody followed by a northern blot or qPCR can be used to verify whether the RBP "pulls down" or associates with the mRNA transcripts of interest (Gagliardi and Matarazzo, 2016). In terms of functional validation, knockdown/knockout or overexpression of the RBP followed by quantification of gene expression, mRNA stability, or splicing of the target RNAs can be performed to characterize the impact of RBP-RNA interaction(s) on transcription and post-transcription regulation of the target RNAs (Bottini et al., 2017). The type of validation study that is chosen often depends on the experimental questions that researchers are trying to answer.

Incorporation of Transcriptome-Wide Profiling by RNA-seq

With the advances in CLIP-seq technologies, the detection of binding peaks for a given RBP have become quite precise and sensitive and can detect thousands of binding events. Given that interactions between an RBP to an mRNA transcript can be transient, how do we parse out those RBP binding peaks that have functional relevance from those that do not? The coupling of transcriptome profiling by RNA-seq with CLIP-seq would allow us to provide one proximal level of functional consequence. A R-based program recently developed by the Keleş Lab (Chen and Keleş, 2020), called SURF, permits integrative analysis of CLIP-seq and RNA-seq datasets to detect differential alternative transcriptional

regulation events followed by the association of the these events to the CLIP peaks associated with the RBP. The incorporation of transcript information also allows permits normalization of CLIP peaks so that there is no bias toward those transcripts that are more highly expressed in the cells (Ule et al., 2005a). In summary, incorporating RNA-seq with the CLIP-seq analysis pipeline streamlines the follow-up validation procedure and facilitates verification of differential transcription and e.g., differential exon usage indicative of splicing.

Other Methods

CLIP-seq relies on crosslinking and immunoprecipitation to identify RNA interactions with a given RBP, and both of these procedures have limitations. Antibodies for the endogenous or epitope-tagged protein for immunoprecipitation might not always be available or feasible. UV-crosslinking is often insufficient to capture all RBP-RNA interactions and sometimes captures transient interactions that are not biologically meaningful (Riley and Steitz, 2013). The RBP binding events identified through CLIP-seq are “averaged” across a heterogenous population of cells, meaning that CLIP-seq fails to account for differences in transcriptional and post-transcriptional states between tissues and cell types (Lin and Miles, 2019). Cell type-specific profiling of the RBP-RNA interactome can be achieved through conditionally tagged (cTag) CLIP technology, which involves knocking in an extra copy of the RBP’s last coding exon fused with GFP sequence downstream of the last coding exon that is flanked by loxP sites (**Figure 4**) (Hwang et al., 2017; Ule et al., 2018). In this way, when crossed with a cell type specific Cre driver line, the endogenous last coding exon is excised and replaced by the GFP-tagged exon for cell

type specific tagging of the RBP for CLIP experiments with a GFP antibody. This technique is highly useful when there is no specific antibody for the RBP.

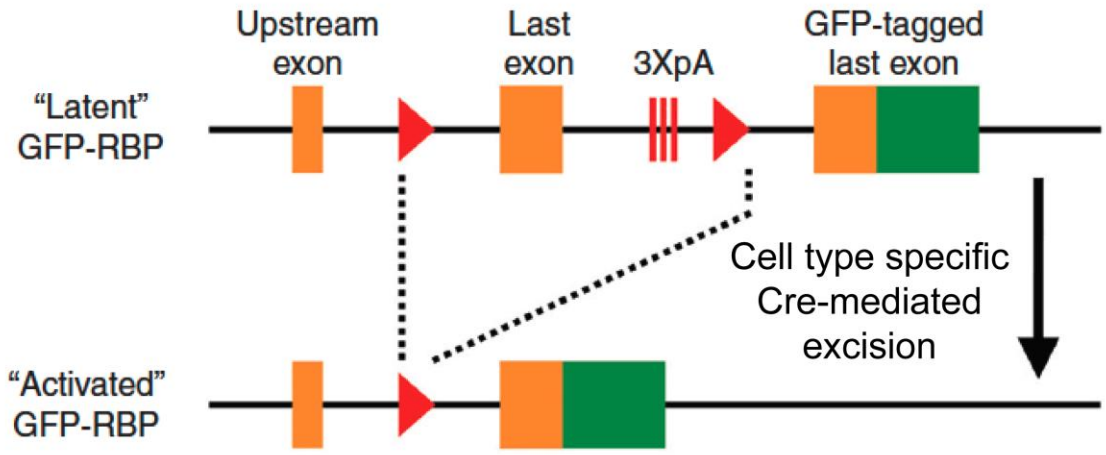

Figure 4. Schematics for cTag-CLIP.
The latent GFP-tagged RBP contains an extra copy of the last exon fused with GFP and loxP sites flanking the endogenous last exon. Cell type specific Cre-mediated excision of the endogenous last exon results in the expression of the GFP-tagged RBP. The GFP tagged to the last exon of the RBP can be used to identify and isolate RBP in a cell-type specific manner when used with Cre driver mouse line or even promoter-specific AAV-Cre viral vector. The diagram is adapted from Ule et al., 2018.

There are other techniques for profiling RBP-RNA interactions that do not require crosslinking and immunoprecipitation. TRIBE (targets of RNA-binding protein identified by editing) has been developed, which entails the fusion of an RBP to the catalytic domain of an RNA-editing enzyme that converts adenosine to inosine (McMahon et al., 2016). RNA-seq is then performed to identify transcripts with edited sites as RNA targets (McMahon et al., 2016). The RBP binding sites are defined by the location of the adenosine-to-inosine converted sites along the mRNA transcripts. In this way, no antibody and crosslinking are required, and more importantly, TRIBE allows for cell type- specific

capturing of RNA targets by restricting the expression of the fusion protein to a particular cell type. Another technique, called RNA-tagging, utilizes a very similar strategy as TRIBE, in that a poly-U polymerase (which adds U nucleotides to the 3' end of RNAs) is fused to the RBP and is capable of adding U nucleotides to the 3' end the mRNA transcripts which recruits binding of the RBP (Lapointe et al., 2015). The binding sites are defined by the covalent marks left on the RNA by the RBP, and RNA targets are defined by the U-tagged mRNA transcripts. The strength of RNA-tagging compared to CLIP-seq is the ability to parse out transient and non-productive binding events because the time the RBP is bound to the RNA is reflected by the number of U's added by poly-U polymerase.

The major downside to these alternative techniques is the need for gene editing of the RBP which could disrupt its endogenous function and its interactions with target RNAs. With this said, the versatility and advantages offered by cTAG-CLIP, TRIBE, and RNA Tagging as well as other similar techniques should be considered when deciding on experimental technique used to study RBP binding targets.

RNA Binding Targets of Heterogenous Nuclear Ribonucleoprotein H1

Overview

Alternative splicing is the process by which exons or introns are differentially included/excluded to produce distinct mRNAs from the same pre-mRNAs to increase protein diversity (Martinez-Contreras et al., 2007). It was established very early on that the hnRNP class of RBPs bind in sequence-specific manner onto mRNAs to define and control splice site selection (Matunis et al., 1994; Wurtz et al., 1996). Basic mechanistic principles

can be gleaned from studying hnRNP proteins splicing function over the years that also apply to hnRNP H1. First, binding of hnRNP to an exon often blocks splicing by preventing the binding of spliceosome components, resulting in exon retention (Martinez-Contreras et al., 2007). Interestingly, the bound hnRNP can also propagate along an mRNA to occlude binding of spliceosome components to bind to inhibit splicing of adjacent sites (Zhu et al., 2001). Second, binding of hnRNP to an intron often inhibits intron splicing by blocking functional interaction between splicing factors, resulting in intron retention (Spellman and Smith, 2006). Third, cooperative interactions of multiple bound hnRNP proteins loop out portions of mRNAs to promote exon skipping when bound to exon or stimulate intron exclusion (Martinez-Contreras et al., 2006). Genome-wide analysis following hnRNP H knockdown in cell lines indicated a large number of alternative splicing events to be influenced by hnRNP H (Katz et al., 2010; Huelga et al., 2012; Wang et al., 2012; Uren et al., 2016). In this section, I will describe a few notable neural splicing targets of hnRNP H that have been reported in the literature to highlight the different splicing strategies employed by hnRNP H.

Non-Receptor Tyrosine Kinase c-Src

c-Src is highly expressed in neural cells and is important for controlling neural development and function (Yagi, 1994). Analysis of *c-Src* splicing indicated inclusion of the N1 exon in neurons, and such an exon exclusion event requires an intronic splicing enhancer sequence downstream of the N1 exon (Black, 1992). UV crosslinking-linking combined with gel mobility assay identified several proteins that bind to the intronic splicing enhancer sequence: hnRNP F, KH-type splicing regulatory protein, and hnRNP H

(Min et al., 1995, 1997; Chou et al., 1999). Furthermore, immunoprecipitation with an anti-hnRNP H antibody demonstrated binding of hnRNP H to the *c-Src* mRNA after the assembly of spliceosome (Chou et al., 1999). Closer examination of the sequence composition around the intronic enhancer sequence of *c-Src* indicated G-rich elements that have been proposed to promote tight binding of hnRNP H (Matunis et al., 1994). In considering the splicing strategies of hnRNP proteins, the association of hnRNP H with other proteins nearby *c-Src* exon 1 supports the looping-out model of splicing for exon skipping.

Acetylcholinesterase Isoforms

The enzyme acetylcholinesterase hydrolyzes and clears the neurotransmitter, acetylcholine, from synaptic cleft to terminate synaptic transmission (Soreq and Seidman, 2001). The 3' end of acetylcholinesterase pre-mRNA undergoes alternative splicing to different isoforms containing different C-terminal ends, with each isoform showing tissue-specific expression (Massoulié et al., 1998). hnRNP H contributes to splicing of the particular acetylcholinesterase isoform that is predominately expressed in neurons (Nazim et al., 2016). There are two polyadenylation sites (proximal and distal) within the exon that undergoes alternative splicing that can signal the start of polyadenylation and two 3' splice sites (proximal and distal) (Massoulié et al., 1998). hnRNP H binds to the G-runs upstream of the distal 3' splice site and activates this site to generate the splice isoform that contains the distal polyadenylation site. Tissue-specific splicing of acetylcholinesterase relies on the competitive regulation of hnRNP H and another protein CstF64 (Nazim et al., 2016). In tissue where there is low amount of hnRNP H, the binding of CstF64 predominates and

activates the proximal polyadenylation site upstream of hnRNP H binding site to generate non-neuronal specific isoforms of acetylcholinesterase. This example indicates that hnRNP H binding near 3’ end of genes can determine both the splice site and the polyadenylation site.

NMDA R1 receptor

Exon 19 of the NMDA R1 receptor mRNA transcript is an example of neuron-region-specific exon that is alternatively spliced by hnRNP H (Han et al., 2005). This exon is included in the forebrain and skipped in the hindbrain (Wang and Grabowski, 1996; Zhang et al., 2002). NMDA R1 receptor plays an important role in impacting drug-induced synaptic plasticity and exon 19 inclusion promotes the trafficking of NMDA R1 receptors to the synapse (Ehlers et al., 1995; Mu et al., 2003). The control mechanisms underlying exon 19 inclusion versus exclusion are determined by the motif pattern surrounding or within this exon (Han et al., 2005). The presence of two exonic UAGG motifs and one intronic GGGG motif proximal to the 5’ splice site promotes binding of hnRNP A1 to the UAGG motif (for exon skipping) and hnRNP H to the GGGG motif (for exon inclusion), where binding of one RBP disrupts the binding of the other to produce different isoforms (Han et al., 2005) . This competitive binding of hnRNP A1 and H at the 5’ splice site of exon 19 of the NMDA R1 receptor mRNA transcript determines the type of isoform that is generated to regulate excitatory neurotransmission and signaling.

Proteolipid Protein (PLP) and Telomere Repeat-Binding Factor (Trf2)

hnRNP H has been shown to regulate mRNA transcripts coding for genes necessary for neuronal cells differentiation and neuron development (Wang et al., 2007; Grammatikakis et al., 2016b). The PLP/DM20 ratio (both of which are myelin proteins) regulates oligodendrocyte differentiation process and brain development (Hobson et al., 2006; Wang et al., 2006). Differentiated oligodendrocytes contain a higher level of PLP whereas oligodendrocyte progenitor cells have a higher level of DM20, which is an isoform of PLP containing a truncated exon 3 of PLP (Gudz et al., 2002), suggesting that the alternative splicing of these two myelin proteins to be tightly controlled. Wang et al. (2007) showed that hnRNP H and F synergistically and selectively bind to the G-rich 5' splice site in exon 3 of PLP to promote alternative splicing and generate DM20. More specifically, knocking down hnRNP H and F increased in the PLP/DM20 ratio, demonstrating a decrease in hnRNP H and F expression might be necessary for the initiation of oligodendrocyte differentiation. Another group of researchers also found that hnRNP H plays an inhibitory role in neuronal cell differentiation and regulates the alternative splicing of exon 8 of the neuronal differentiation factor, TRF2 (Grammatikakis et al., 2016b). There are two isoforms of *TRF2* mRNA transcripts: TRF2-S (truncated exon 7) and TRF2-L (full length exon 7), where TRF2-S promotes transcription of neural genes in neurogenesis and TRF2-L inhibits their expression and is expressed at high level in undifferentiated neurons (Grammatikakis et al., 2016a). In fact, the alternative splicing mechanism of TRF2 exon 7 by hnRNP H is similar to that of PLP and exon 3, where hnRNP H binds to the 5' splice site within exon 7 to promote alternative splicing.

The main conclusions that can be drawn from the review of different splicing events mediated by hnRNP H include: 1) the presence of G-rich motif near the splice site can enhance binding of hnRNP H; 2) cell-specific, brain-region-specific and/or time-specific expression of hnRNP H drive the expression of different mRNA isoforms; 3) hnRNP H shows both competing and cooperative association with other hnRNP proteins to regulate splicing, as demonstrated by interaction with hnRNP F and A1 in the above examples.

Genome-Wide Characterization of hnRNP H RNA-interactome

Overview

hnRNP H proteins contribute to multiple aspect of RNA metabolism. Dissecting this multi-functional aspect of its functions and identifying its diverse range of RNA-binding targets require high-throughput analyses combining RNA-seq, RIP-seq, CLIP-seq, and proteomics. These omics analyses can yield new insight into the hnRNP H RNA-binding interactome and its role in splicing, gene expression, mRNA stability, and translation. In this section, I will provide a detailed description and summary of each approach.

Knockdown of hnRNP H on Splicing and Gene Expression

In the first genome-wide analysis of splicing events and gene expression regulated by hnRNP H in oligodendrocyte progenitor cells, Wang et al. (2012) performed gene- and exon-level transcriptome analysis to examine splicing events and gene expression in oligodendrocytes treated with siRNA to knock down expression of hnRNP H compared to untreated cells. Two major splicing events were found: exon inclusion and exon skipping.

Out of those exons that showed alternative splicing, 67% of them contained nearby G tracts. The density, length, and proximity of the G tracts to the 5' splice spice correlated with the splicing enhancer function of hnRNP H. Knocking down of hnRNP H resulted in differentially expressed genes that are involved in the transition from oligodendrocyte progenitor cells to oligodendrocyte, possibly through interacting with G runs in the 3'UTR of the mRNAs by affecting message stability (Wang et al., 2012). In summary, this study implicated the role of hnRNP H on splicing and gene expression in oligodendrocyte.

Cooperative Interaction of hnRNP H with other RNA Binding Proteins

In another high-throughput study, splicing-sensitive microarrays, CLIP-seq, and RNA-seq were used to understand the mechanisms of how six major hnRNP proteins (Al, A2/B1, F, H1, M, and U) coordinate alternative splicing in human cells (Huelga et al., 2012). In their analysis, hnRNP H was found to bind both flanking intronic and exonic regions that were alternatively spliced. The sequence motifs for hnRNP H were most enriched for G-rich sequences. A fundamental finding from this study was these hnRNP proteins cooperate with each other to regulate alternative splicing events.

Impact of hnRNP H Binding on Gene Expression, Splicing, and Protein Expression

The most extensive high-throughput analyses for understanding hnRNP H1 function was conducted by Uren et al. (2016) in HeLA cells, where they identified 1086 target transcripts associated with hnRNP H using RIP-seq and CLIP-seq and assessed the impact of hnRNP H binding on gene expression and splicing on those targets using RNA-seq and protein expression using shot-gun proteomics. The TGGG tetrameter was identified as the most

prevalent component of hnRNP H binding motif. There was a strong enrichment of hnRNP H1 targets for spliceosome-associated genes, supporting hnRNP H as having a major role in the regulation of splicing. In addition, the data also supported hnRNP H regulation of mRNA decay (as corroborated by RNA decay assay) and polyadenylation (length of 3'UTR was altered as a result of hnRNP H knockdown).

To date, genome-wide characterization of hnRNP H1 RNA-interactome has only been performed in cell lines and not in CNS tissue. Given the ubiquitous expression of hnRNP H1 in the brain and brain-region specific as well as cell type specific alternative splicing of neural genes by hnRNP H1 previously discussed, *in vivo* CLIP-seq analyses in specific brain regions and cell types are necessary for understanding the multi-functional roles of hnRNP H1 in transcriptional and post-transcriptional regulation of gene expression.

Dissertation Research Specific Aims

The genetic factors underlying risk for psychostimulant addiction remain largely unknown. Our lab mapped and validated *Hnrnph1* as a QTG for reduced MA stimulant sensitivity. Mice heterozygous for a 16 bp deletion in the first coding exon of *Hnrnph1* also showed reduced MA-induced reward and reinforcement, and a decrease in MA-induced DA release. The combined results indicate reduced addiction liability in H1 MUT mice. Thus, understanding the cellular and molecular mechanisms underlying reduced MA addiction liability in *Hnrnph1* mutants could provide novel insight into strategies for psychostimulant addiction treatments as well as stimulant therapeutics. hnRNP H1 is an RNA binding protein that regulates every aspect of post-transcriptional gene regulation.

The objective of my dissertation research is to understand the mechanism of hnRNP H1 dysfunction in MA-induced DA release and behavior through multi-omics data integration including proteome, transcriptome, and hnRNP H1 RNA-interactome. These are my specific aims:

Aim 1: Identify the functional variants within the 5'UTR region of *Hnrnph1* underlying reduced sensitivity to psychostimulant effect of methamphetamine.

Aim 2: Identify the striatal synaptosome proteome associated with decreased methamphetamine behavior and increased synaptic hnRNP H in *Hnrnph1* mutant versus wild-type mice.

Aim 3: Evaluate the effect of methamphetamine on hnRNP H RNA-binding targets and hnRNP H-mediated gene expression and splicing in *Hnrnph1* mutant versus wild-type mice.

CHAPTER II: 5'UTR variants in *Hnrnph1* support reduced 5' UTR usage and hnRNP H protein for reduced methamphetamine sensitivity

Adapted from Ruan et al., 2020, *The FASEB Journal*

ABSTRACT

We previously identified a 210 kb region on chromosome 11 (50.37-50.58 Mb, mm10) containing two protein-coding genes (*Hnrnph1, Rufy1*) that was necessary for reduced MA-induced locomotor activity in C57BL/6J congenic mice harboring DBA/2J polymorphisms. We have since shown that *Hnrnph1* mutants also exhibit reduced MA-induced reward, reinforcement, and DA release. However, the quantitative trait variants that modulate *Hnrnph1* function at the molecular level are not known. Nine single nucleotide polymorphisms and seven indels distinguish C57BL/6J from DBA/2J within *Hnrnph1*, including four variants within the 5' untranslated region. Gene-level transcriptome analysis of striatal tissue from 114 kb congenics versus *Hnrnph1* mutants identified a nearly perfect correlation of fold-change in expression for those differentially expressed genes that were common to both mouse lines, indicating functionally similar effects on the transcriptome and behavior. Exon-level analysis (including noncoding exons) revealed decreased 5'UTR usage of *Hnrnph1* and immunoblot analysis identified a corresponding decrease in hnRNP H protein in 114 kb congenic mice. Molecular cloning of the *Hnrnph1* 5'UTR containing all four variants (but none of them individually) upstream of a reporter induced a decrease in reporter signal in both HEK293 and N2a cells, thus identifying a set of QTVs underlying molecular regulation of *Hnrnph1*.

INTRODUCTION

Psychostimulant use disorders (PUDs), including MA and cocaine dependence, are a serious public health concern in the United States. While the opioid epidemic crisis continues to garner warranted attention, there has been much less focus on the recent steep surge in PUDs as evidenced by the steep increase in PUD-related deaths, especially MA-related deaths (Fogger, 2019). This public health concern is particularly problematic, given that there are no FDA-approved treatments for PUDs. Both genetic and environmental factors contribute to PUDs (Pierce et al., 2018), yet genome-wide association studies to date have identified very few genetic factors (Jensen, 2016). One notable example was the identification of a genome-wide association between *FAM53B* and cocaine dependence in humans (Gelernter et al., 2014). This finding was particularly interesting in the context of a mouse forward genetic study of psychostimulant addiction traits that identified a *trans*-expression quantitative trait locus (QTL) originating from a locus containing *Cyfip2* and *Hnrnph1* that influenced *Fam53b* expression and was associated with cocaine intravenous self-administration (Dickson et al., 2015). This is one of the first examples demonstrating a direct correspondence between genome-wide genetic association, functional changes in gene expression, and trait-relevant behaviors (cocaine self-administration) between rodents and humans. Thus, this example highlights the power and translational relevance of systems genetics in mice in the study of substance use disorder (SUD)-relevant traits.

There are several advantages to using rodent forward genetics in studying the genetic basis of molecular and behavioral traits relevant to SUDs, including the ability to control allelic frequency, genetic background, the environment, the amount and length of

drug exposure, the sample size, the collection of the appropriate tissue at the appropriate time points, and the ability to both map and validate causal functional variants *in vivo* within the same animal species. While there are clear limitations to modeling the genetic basis of psychiatric disease traits in rodents, it is important to point out studies in which there have been promising successes. In addition to the translational link of *Fam53b* with cocaine addiction traits in mice and humans (Gelernter et al., 2014; Dickson et al., 2015), there are multiple other recent examples of forward genetic discoveries in rodents that have yielded a high likelihood for translation to humans. A missense SNP in *Taar1* (trace amine-associated receptor 1) was mapped in mice for the aversive properties of MA self-administration, body temperature (Harkness et al., 2015) and toxicity (Shi et al., 2016; Miner et al., 2017; Reed et al., 2018) and genetic variants in *TAAR1* in humans were associated with drug craving in methamphetamine dependence (Shi et al., 2016; Loftis et al., 2019) . *CNIH3* (Cornichon Family AMPA Receptor Auxiliary Protein 3) was identified as a GWAS hit for opioid dependence in humans that was corroborated with a forward genetic study of morphine physical dependence in mice (Nelson et al., 2016). Whole genome sequencing plus QTL analysis and functional validation identified *Grm2* (mGlu2 receptor) in escalation of alcohol consumption in rats (Zhou et al., 2013). A mouse strain survey correlating gene expression with behavior found a link between glyoxylase 1 (*Glo1*) and anxiety-like behavior that was confirmed via viral knockdown and overexpression (Hovatta et al., 2005). A *cis*-eQTL and copy number variant containing *Glo1* was subsequently discovered to segregate in outbred mice and is fixed in several classical inbred strains, thus revealing a genetic and molecular mechanism linking *Glo1* expression

with anxiety-like behavior (Williams et al., 2009). *Glo1* metabolizes methylglyoxal which, in light of mouse preclinical studies, was found to act as an agonist for the GABA-A receptor and exert anxiolytic-like effects (Distler et al., 2012; McMurray et al., 2016). Increasing methylglyoxal levels preclinically reduced alcohol drinking (McMurray et al., 2017; de Guglielmo et al., 2018), induced a rapid antidepressant-like response (McMurray et al., 2018), and reduced seizures (Distler et al., 2014). To summarize, mouse forward genetic studies have led to the identification and/or corroboration of several promising therapeutic targets for SUDs and other psychiatric disorders.

A major focus of our lab is to use discovery-based forward genetics to identify novel genetic factors underlying heritable differences in sensitivity to the locomotor stimulant response to drugs of abuse, including opioids as well as psychostimulants such as MA. The neurocircuitry and neurochemical mechanisms underlying drug-induced locomotor activity are in part shared with those that mediate the addictive properties of drugs of abuse (Wise and Bozarth, 1987; Di Chiara and Imperato, 1988; Deminiere et al., 1989); thus, a reasonable hypothesis is that a subset of shared, polymorphic genetic factors influence both sets of complex behavioral traits. Examples from our lab that support this hypothesis include casein kinase 1-epsilon which influences opioid- and MA-induced locomotor activity (Bryant et al., 2009, 2012) and opioid conditioned place preference (Goldberg et al., 2017) as well as *Hnrnph1* which we first mapped and validated for MA-induced locomotor activity (Yazdani et al., 2015) and subsequently found to influence MA-induced extracellular DA in the NAc, MA-induced reward, and MA-induced reinforcement (Ruan et al., 2020a).

With regard to *Hnrnph1*, QTL mapping in an F2 cross first identified a locus containing *Hnrnph1* on chromosome 11 whereby the DBA/2J (D2J) allele was associated with reduced MA-induced locomotor activity (Parker et al., 2012). An interval-specific congenic approach was employed in C57BL/6J (B6J) mice carrying various introgressed regions on chromosome 11 from the DBA/2J strain (Iakoubova et al., 2001) to fine map the QTL. We detected a fortuitous recombination event that revealed a 210 kb region on chromosome 11 (50.37 - 50.58 Mb) that was necessary for reduced sensitivity in the locomotor stimulant response to MA (Yazdani et al., 2015). Replacement of this polymorphic region with the background C57BL/6J allele completely eliminated the MA-induced behavioral phenotype, thus demonstrating that this region was necessary for reduced MA-induced locomotor activity (Yazdani et al., 2015). The 210 kb region contains two protein-coding genes – *Hnrnph1* and *Rufy1*. Introduction of a heterozygous deletion within the first coding exon of each gene provided strong support for *Hnrnph1* (and not *Rufy1*) as a QTG underlying reduced MA sensitivity (Yazdani et al., 2015) and we subsequently expanded the phenotypic repertoire of the *Hnrnph1* mutants to include a reduction MA reinforcement, MA reward and MA-induced dopamine release (Ruan et al., 2020a).

Although the combined published evidence supports *Hnrnph1* as a QTG for MA sensitivity, to date, we have only demonstrated that inheritance of the 210 kb region polymorphic region containing *Hnrnph1* and *Rufy1* is *necessary* for the reduction in MA-induced behavior. In order to demonstrate that this region is also *sufficient*, in the present study, we backcrossed and screened for congenic mice capturing only *Hnrnph1* and *Rufy1*

and we identified a founder containing a 114 kb introgressed region. Following the observation of reduced MA-induced locomotor activity in 114 kb congenic mice, we assessed the striatal transcriptome at both the gene- and exon-level and compared these results to the transcriptome of *Hnrnph1* mutants (H1 MUT) in order to provide further support for *Hnrnph1* as a QTG and to identify the quantitative trait variant(s) (QTV)s. Upon discovering decreased usage of the 5'UTR in *Hnrnph1* in 114 kb congenic mice as a potential molecular mechanism underlying the QTL and QTG, we validated decreased 5'UTR expression via real-time quantitative PCR (qPCR) by targeting the adjacent exon junction and the specific 5'UTR noncoding exon. We then identified decreased protein expression of hnRNP H in 114 kb congenic mice as a potential downstream functional consequence of reduced 5'UTR usage. Finally, to validate candidate QTV(s), we cloned the 5' UTR of *Hnrnph1* containing either the individual *Hnrnph1* 5'UTR variants, or the combined set of all four 5' UTR variants fused to a luciferase reporter gene and tested the effect on reporter expression in two different cell lines. The results identify a set of 5' UTR variants within *Hnrnph1* that likely represent the QTVs underlying molecular regulation of *Hnrnph1* and behavior.

RESULTS

Positional cloning of a 114 kb interval that is necessary for reduced MA sensitivity

In backcrossing the congenic line "Line 4a" that captured a QTL for reduced MA-induced locomotor activity and contained a heterozygous introgressed region from the D2J strain that spanned 50Mb to 60Mb, we monitored for recombination events at rs254771403 (50,486,998 bp, mm10). We identified a crossover event that defined 114 kb congenic region that influenced MA sensitivity. There are two protein coding genes within this 114 kb region - *Hnrnph1* and *Rufy1* (**Figure 5A**). 114 kb congenic mice homozygous for the D2J allele within this region on an otherwise isogenic B6J background displayed no difference in saline-induced locomotor activity, compared to their wild-type homozygous B6J littermates (**Figure 5B-C**). In response to an acute dose of MA on Day 3, 114 kb congenic mice showed reduced locomotor activity relative to B6J (**Figure 5D**). Again, in response to a second dose of MA on Day 4, the 114 kb congenic mice showed reduced MA-induced locomotor activity compared to B6J wild-type littermates **(Figure 5E)**. No genotypic difference in MA-induced locomotor activity were observed on Day 5 after the third MA injection (**Figure 5F**) which is potentially explained by a ceiling effect on sensitization at this dose.

In examining changes in summed locomotor activity across days, both 114 kb and B6J mice showed habituation to the testing apparatus as indicated by a reduction in saline-induced locomotor activity from Day 1 to Day 2 (**Figure 5G**). 114 kb congenic mice showed greater sensitization to repeated doses of MA from Day 3 to Day 5 (**Figure 5G**), due to their initially lower level of acute-MA-induced locomotor activity on Day 3

compared to B6J wild-types. In comparing summed locomotor activity over 60 min across the five days, the 114 kb congenic mice showed a significant reduction in MA-induced locomotor activity compared to B6J wild-type littermates on Day 4 (**Figure 5G**). Taken together, these results indicate that 114 kb congenic mice are less sensitive to the locomotor stimulant response to MA.

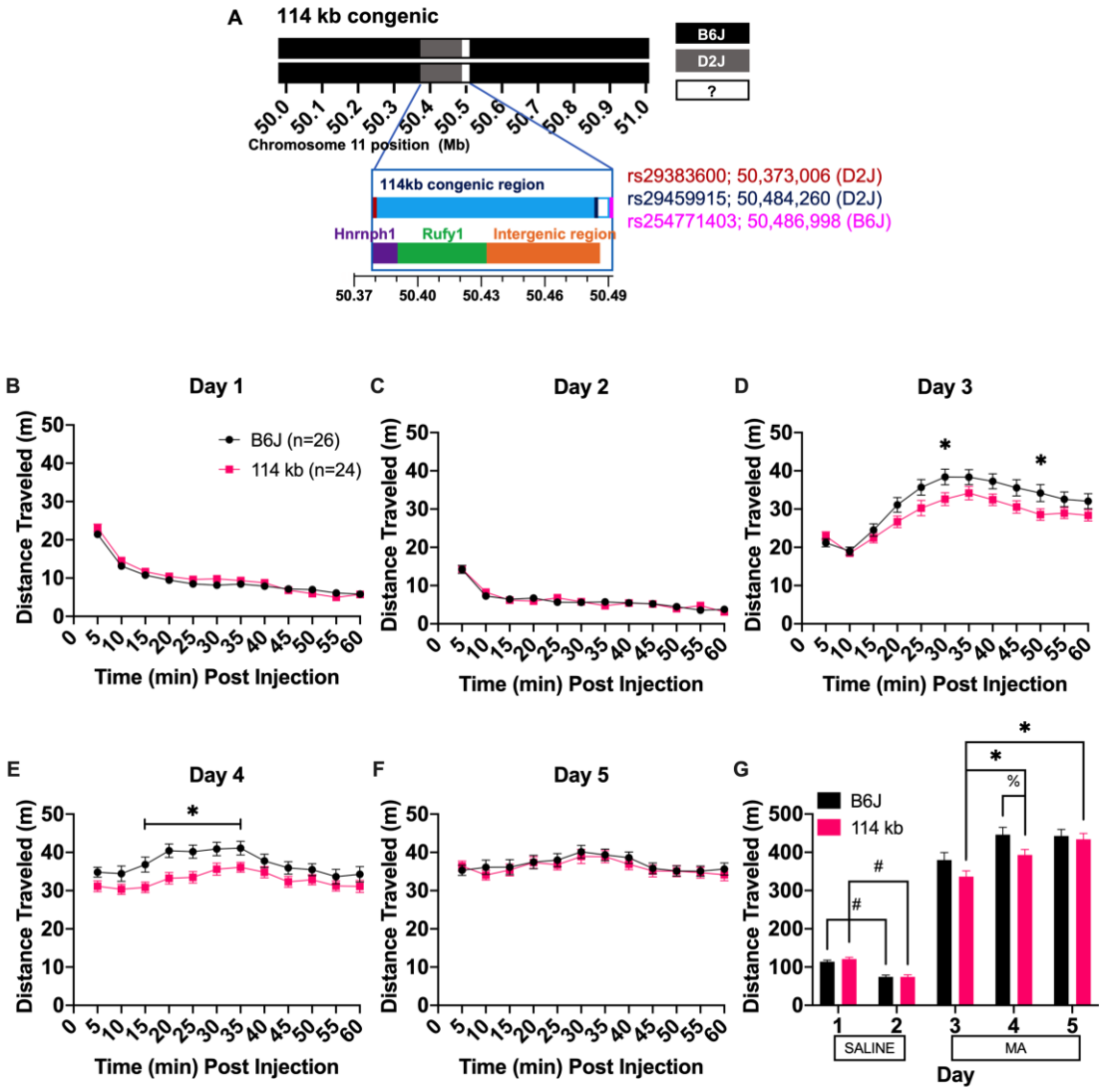

Figure 5. MA-induced locomotor activity in the 114 kb congenic mice.
(A): Congenic mice containing an introgressed 114 kb region on chromosome 11 from the D2J strain on an isogenic B6J background were identified via backcrossing and screening for a recombination event at rs254771403 (50,486,998 bp; mm10) while monitoring for the retention of polymorphic rs29383600 (50,373,006 bp; mm10) and polymorphic rs29459915 (50,484,260 bp; mm10), and. Mice were then backcrossed again to B6J to generate additional heterozygotes for intercrossing (heterozygous-heterozygous breeding) which yielded heterozygous offspring as well as offspring homozygous for the 114 kb region (homozygous D2J) and wild-type homozygous B6J littermates. Behavioral analysis and results are shown for the homozygous genotypes. The 114 kb region contains two protein-coding genes: *Hnrnph1* and *Rufy1*. Mice were injected on Days 1 to 2 with saline (i.p.; panels B and C) and on Days 3, 4, and 5 with 2 mg/kg MA (panels D, E, and F). Locomotor activity was video-recorded for 60 min on each day and is presented in 5-min bins over 60 min. (B,C): No genotypic differences were observed in distance traveled in response to a saline injection on Day 1 [mixed ANOVA: $F(1,46)_{\text{Genotype}} = 1.48$, $p = 0.229$; $F(11,506)_{\text{Genotype x Time}} = 1.48$,

p = 0.133] or Day 2 [mixed ANOVA: $F(1,46)_{Genotype}$ = 0.003, p = 0.958; $F(11,506)_{Genotype\ x\ Time}$ = 1,29, p = 0.227]. A main effect of Sex was detected for both Days 1 and 2 [$F(1,46)_{Day1}$ = 10.52, p = 0.002; $F(1,46)_{Day2}$ = 9.83, p = 0.003]. However, there was no significant Genotype x Sex interaction for Day 1 or Day 2 [$F(1,46)_{Day1}$ = 0.32, p = 0.576; $F(1,46)_{Day2}$ = 2.32, p = 0.134]. (D): Locomotor activity on Day 3 in response to MA is shown in 5-min bins over 60 min. 114 kb congenic mice showed reduced acute MA-induced locomotor activity relative to B6J wild-type littermates [mixed ANOVA: $F(1,46)_{Genotype}$ = 3.41, p = 0.071; $F(11,506)_{Genotype\ x\ Time}$ = 2.80, p = 0.002; unpaired t-test for each 5-min bin: $t(48)_{30min}$ = 2.17, *p = 0.035; $t(48)_{50min}$ = 2.05, *p = 0.045]. A main effect of Sex was also detected [F(1,46) = 4.32, p = 0.043], however, there was no significant Genotype x Sex interaction [F(1,46) = 2.74, p = 0.104]. (E): MA-induced locomotor activity on Day 4 is shown in 5-min bins over 60 min. 114 kb congenic mice showed reduced MA-induced locomotor activity relative to B6J mice [mixed ANOVA: $F(1,46)_{Genotype}$ = 5.40, p = 0.025; $F(11,506)_{Genotype\ x\ Time}$ = 1.96, p = 0.031; unpaired t-test for each 5-min bin: $t(48)_{15min}$ = 2.43, *p = 0.019; $t(48)_{20min}$ = 3.10, *p = 0.003; $t(48)_{25min}$ = 2.90, *p = 0.006; $t(48)_{30min}$ = 2.22, *p = 0.031]. A main effect of Sex was also detected [F(1,46) = 7.33, p = 0.009] but no significant Genotype x Sex interaction [F(1,46) = 2.05, p = 0.159]. (F): MA-induced locomotor activity is shown for Day 5 in 5-min bins over 60 min. 114 kb congenic mice showed no difference in MA-induced locomotor activity compared to B6J [mixed ANOVA: $F(11,506)_{Genotype\ x\ Time}$ = 0.59, p = 0.841]. A main effect of Sex was detected [F(1,46) = 6.09, p = 0.017], however, there was no significant Genotype x Sex interaction [F(1,46) = 0.39, p = 0.535]. (G): Locomotor activity summed over 60 min is shown for Days 1 and 2 (saline) and on Days 3, 4, and 5 (MA). In examining habituation via changes in locomotor activity in response to saline injections on Day 1 versus Day 2, both B6J and 114 kb showed similar degree of habituation [mixed ANOVA: $F(1,46)_{Genotype}$ = 0.47, p = 0.496; $F(1,46)_{Day}$ = 225.51, p < 2E-16; $F(1,46)_{Genotype\ x\ Day}$ = 1.35, p = 0.252; unpaired t-test for each day: $t(50)_{Day\ 1}$ = 6.34, #p = 3.26E-04; $t(46)_{Day\ 2}$ = 6.64, #p = 1.55E-04]. In examining sensitization of MA-induced locomotor activity across Day 3, Day 4, and Day 5, 114 kb congenic mice showed increased locomotor sensitization relative to B6J [mixed ANOVA: $F(1,46)_{Genotype}$ = 2.74, p = 0.105; $F(2,92)_{Day}$ = 65.71, p < 2E-16; $F(2,92)_{Genotype\ x\ Day}$ = 5.03, p = 0.009]. Only the 114 kb congenic mice showed an increase in MA-induced locomotor activity across the three MA treatment days [Bonferroni's multiple comparison tests (adjusted for 3 comparisons in 114 kb congenics and B6J group separately): Day 3 versus D4: $t(50)_{B6J}$ = 2.40, p = 0.120; t(46)114 kb = 2.76, *p = 0.050; Day 3 versus D5: $t(50)_{B6J}$ = 2.45, p = 0.108; $t(46)_{114\ kb}$ = 4.52, *p = 2.57E-04; Day 4 versus D5: $t(50)_{B6J}$ = 0.12, p = 0.999; $t(46)_{114\ kb}$ = 1.92, p = 0.368]. In addition, 114 kb congenic mice showed reduced MA-induced locomotor activity compared to B6J mice on Day 4 when compared across all five days [mixed ANOVA: $F(4,184)_{Genotype\ x\ Day}$ = 3.96, p = 0.004; unpaired t-test for each day: $t(48)_{Day4}$ = 2.16, %p = 0.036]. A main effect of Sex was detected [F(1,46) = 9.17, p = 0.004] but there was no significant Genotype x Sex interaction [F(1,46) = 2.14, p = 0.150]. Data are represented as the mean ± S.E.M.

Acute MA-induced locomotor activity and sensitization in 114 kb congenic mice

Next, we examined MA-induced locomotor activity while accounting for individual differences in baseline locomotion in response to saline on Day 2 (**Figure 6A-C**), as well as MA-induced locomotor sensitization (**Figure 6D-F**), via differences in MA-induced locomotor activity between MA treatment days. When accounting for non-drug locomotor activity, we again found that 114 kb congenic mice showed less acute MA-induced locomotor activity relative to B6J mice (**Figure 6A**), as well as after repeated exposure to MA (**Figure 6B-C**). After two MA injections (comparing Day 4 versus Day 3 activity), 114 kb congenic mice showed a significant decrease in locomotor sensitization early post-injection (**Figure 6D**). After three MA injections (comparing between Day 5 and Day 3), 114 kb congenic mice showed a significant increase in locomotor sensitization, starting at 20 min post-MA (**Figure 6E**). Again, when comparing Day 5 versus Day 4, 114 kb congenic mice also showed significantly greater MA locomotor sensitization relative to B6J mice (**Figure 6F**). The more delayed, greater sensitization in 114 kb congenic mice during the later MA injections is likely due to their initially lower MA response which takes longer to sensitize.

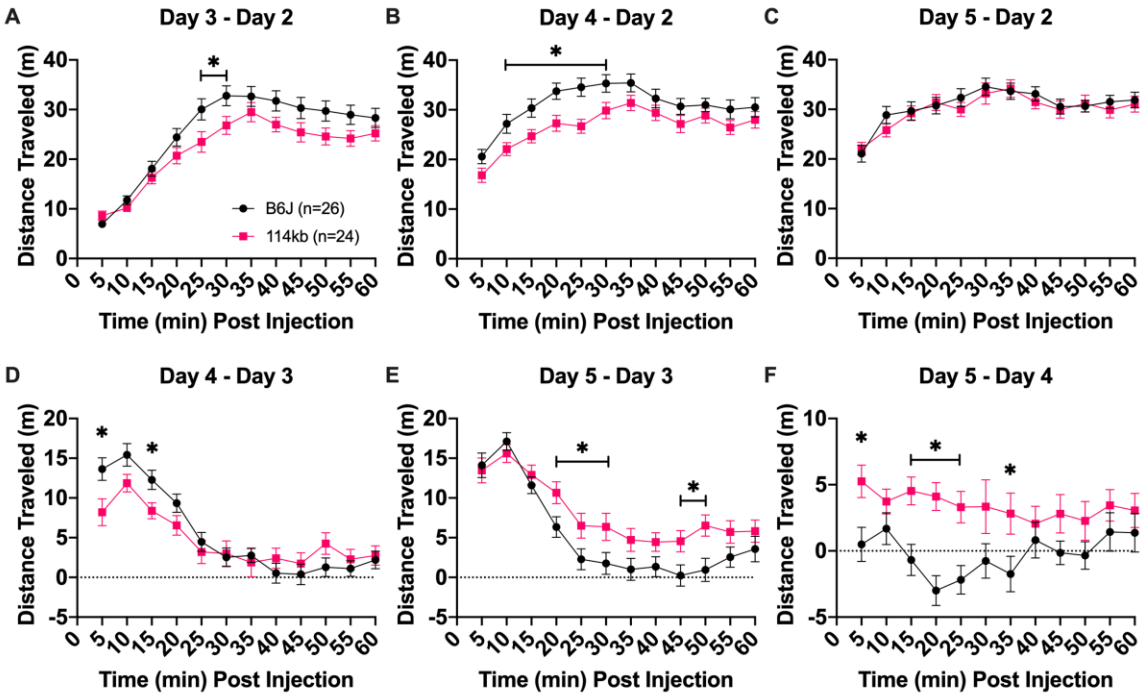

Figure 6. Normalized MA-induced locomotor activity and locomotor sensitization in 114 kb congenic mice.

Mice were injected (i.p.) with saline on Days 1 to 2 and with 2 mg/kg MA on Days 3, 4, and 5. Locomotor activity was recorded for 60 min. (A): Day 3 – Day 2 distance traveled represents the acute locomotor response to MA while accounting for individual differences in non-drug, saline-induced locomotor activity. 114 kb congenic mice showed less acute MA-induced locomotor activity relative to B6J wild-type littermates [mixed ANOVA: $F(1,46)_{Genotype} = 3.43$, $p = 0.070$; $F(11,506)_{Genotype \times Time} = 2.36$, $p = 0.008$; unpaired t-test for each 5-min bin: $t(48)_{25min} = 2.30$, $^*p = 0.033$; $t(48)_{30min} = 2.18$, $^*p = 0.035$]. (B): Day 4 – Day 2 distance traveled represents the locomotor response to the second, repeated dose of MA while accounting for individual differences in non-drug, saline-induced locomotor activity. 114 kb congenic mice showed less MA-induced locomotor activity relative to B6J [mixed ANOVA: $F(1,46)_{Genotype} = 5.25$, $p = 0.027$; $F(11,506)_{Genotype \times Time} = 1.76$, $p = 0.058$; unpaired t-test for each 5-min bin: $t(48)_{10min} = 2.15$, $^*p = 0.037$; $t(48)_{15min} = 2.47$, $^*p = 0.017$; $t(48)_{20min} = 2.80$, $^*p = 0.007$; $t(48)_{25min} = 3.34$, $^*p = 0.002$; $t(48)_{30min} = 2.24$, $^*p = 0.030$]. (C): Day 5 – Day 2 distance traveled represents locomotor response to the third, repeated dose of MA while accounting for individual differences in saline locomotor activity. No genotypic difference in locomotor activity was observed in response to the third dose of MA [mixed ANOVA: $F(1,46)_{Genotype} = 0.17$, $p = 0.680$; $F(11,506)_{Genotype \times Time} = 0.92$, $p = 0.523$]. (D): Day 4 – Day 3 distance traveled is shown to represent locomotor sensitization from the first to the second MA injection. 114 kb congenic mice showed a decrease in locomotor sensitization during the first 15 min [mixed ANOVA: $F(1,46)_{Genotype} = 0.47$, $p = 0.495$; $F(11,506)_{Genotype \times Time} = 3.09$, $p = 4.92e\text{-}5$; unpaired t-test for each 5-min bin: $t(48)_{5min} = 2.47$, $^*p = 0.017$; $t(48)_{15min} = 2.47$, $^*p = 0.017$]. (E): Day 5 – Day 3 distance traveled is shown to indicate the degree of sensitization observed following the third MA injection relative to the first MA exposure. 114 kb congenic mice showed an increase in locomotor sensitization relative to B6J

[mixed ANOVA: F(1,46)Genotype = 5.35, p = 0.025; F(11,506)Genotype x Time = 1.95, p = 0.032; unpaired t-test for each 5-min bin: t(48)20min = 2.30, p = *0.026; t(48)25min = 2.07, *p = 0.044; t(48)30min = 2.11, *p =0.040; t(48)45min = 2.27, *p = 0.028; t(48)50min = 2.80, p = 0.007]. (F): D5 – D4 distance traveled is shown to indicate which genotype continued to sensitize from the second MA injection to the third MA injection. Again, 114 kb congenic mice showed increased locomotor sensitization relative to B6J [mixed ANOVA: F(1,46)Genotype = 8.50, p = 0.006; F(11,506)Genotype x Time = 1.75, p = 0.061; unpaired t-test for each 5-min bin: t(48)5min = 2.67, *p = 0.010; t(48)15min = 3.28, *p = 0.002; t(48)20min = 4.59, *p = 3.17E-05; t(48)25min = 3.43, *p = 0.001; t(48)35min = 2.24, *p = 0.030]. No main effect of Sex was detected for any locomotor sensitization measures (panels A-F) [F(1,46)Sex < 0.8, all p's > 0.3]. Data are represented as the mean ± S.E.M.

Transcriptome analysis of the striatum identifies differential usage of the Hnrnph1 5'UTR in 114 kb congenic mice

To further understand the molecular mechanism of the 114 kb congenic region in reducing MA sensitivity, we performed both differential gene expression and differential exon usage analysis on RNA-seq data collected from the striatum of naïve 114 kb and their B6J wild-type littermates. We identified 69 differentially expressed genes ($p < 0.001$; **Table 2**). Enrichr analysis of these 69 genes for pathway and gene ontology (GO) terms identified enrichment for several terms potentially related to MA-induced DA release and behavior, including circadian entrainment, cholinergic synapse, cAMP signaling pathway, long-term potentiation, and regulation of synaptic transmission (**Table 3**).

Table 2. Differentially expressed genes in the striatum of 114 kb congenic mice.
This table shows the 69 genes that are differentially expressed in the striatum of 114 kb congenic mice relative to the B6J wild-type littermates ($p < 0.001$).

Gene	logFC	AveExpr	t	p value	Adjusted p value	B
Baiap3	-0.534	4.730	-5.500	1.14E-06	0.0162	5.180
Hap1	-0.302	7.192	-5.065	5.36E-06	0.0271	3.919
Wdr6	-0.348	5.830	-5.047	5.72E-06	0.0271	3.856
Zcchc12	-0.225	7.100	-4.726	1.75E-05	0.0623	2.815
Trpc4	-0.562	3.444	-4.556	3.13E-05	0.0713	1.838
Tmem130	-0.270	7.087	-4.545	3.26E-05	0.0713	2.237
Prkcd	-0.524	4.363	-4.523	3.51E-05	0.0713	2.076
Trp53inp2	0.183	8.099	4.399	5.33E-05	0.0857	1.752
Wnk1	0.123	8.451	4.347	6.35E-05	0.0857	1.578
Scd1	0.184	7.767	4.338	6.55E-05	0.0857	1.568
Zic1	-0.630	4.393	-4.317	7.03E-05	0.0857	1.482
Cacng5	-0.454	3.203	-4.291	7.65E-05	0.0857	1.005
Col6a3	-0.892	2.255	-4.259	8.51E-05	0.0857	0.249
Kcnj2	0.201	6.042	4.259	8.53E-05	0.0857	1.378
Ecel1	-0.187	5.713	-4.203	0.000102	0.0857	1.220
Fos	0.994	2.801	4.201	0.000103	0.0857	0.773
Lbhd2	-2.694	-0.765	-4.196	0.000105	0.0857	-1.978
Magel2	-0.704	1.965	-4.186	0.000108	0.0857	0.001
Zic2	-0.692	2.885	-4.118	0.000136	0.0986	0.386
Osbpl8	0.115	8.486	4.099	0.000144	0.0986	0.808
Qk	0.152	8.422	4.097	0.000145	0.0986	0.805
Gatm	0.193	7.062	4.056	0.000166	0.1074	0.730
Nrp2	-0.391	3.477	-4.005	0.000196	0.1127	0.423
Itm2c	-0.089	10.023	-4.001	0.000198	0.1127	0.461
Ezr	-0.170	6.308	-3.982	0.000211	0.1127	0.537
Zic4	-0.971	1.787	-3.980	0.000213	0.1127	-0.702
Ermn	0.240	6.924	3.978	0.000214	0.1127	0.502
Zcchc18	-0.103	8.156	-3.954	0.000231	0.1175	0.381
Pnmal2	-0.226	7.963	-3.925	0.000253	0.1216	0.300
Fth1	0.169	10.805	3.922	0.000256	0.1216	0.196
Dlx1	-0.701	3.098	-3.895	0.000279	0.1252	-0.051
Icam5	-0.104	8.147	-3.891	0.000283	0.1252	0.195
Sept7	0.107	8.420	3.883	0.000290	0.1252	0.162
Pcdh8	-0.391	3.388	-3.853	0.000319	0.1337	0.027
Ttll7	0.104	7.896	3.840	0.000332	0.1346	0.055
Rasd1	-0.842	1.393	-3.830	0.000344	0.1346	-1.180
Tspan2	0.175	7.668	3.824	0.000350	0.1346	0.019
Slc22a17	-0.120	9.192	-3.810	0.000366	0.1371	-0.082
Gpm6b	0.091	10.728	3.777	0.000406	0.1378	-0.233
Tppp	0.091	9.176	3.775	0.000409	0.1378	-0.184
Cadm2	0.134	7.765	3.764	0.000423	0.1378	-0.161
Gprasp1	-0.102	9.355	-3.762	0.000426	0.1378	-0.230

Adcy1	0.111	8.611	3.761	0.000426	0.1378	-0.201
Npas4	0.694	4.629	3.758	0.000431	0.1378	-0.052
Rapgef4	0.146	9.876	3.744	0.000451	0.1378	-0.299
Tro	-0.103	7.983	-3.744	0.000451	0.1378	-0.233
Grin2a	0.232	4.844	3.736	0.000462	0.1378	-0.111
Scn5a	-0.522	2.614	-3.734	0.000465	0.1378	-0.572
Maged1	-0.152	8.935	-3.694	0.000526	0.1528	-0.410
Kcna2	0.109	8.165	3.684	0.000543	0.1547	-0.410
Ano3	0.105	9.169	3.668	0.000571	0.1594	-0.493
Slit1	-0.361	4.198	-3.652	0.000601	0.1645	-0.361
Oip5os1	0.146	6.009	3.621	0.000661	0.1747	-0.483
Lpgat1	0.090	8.070	3.620	0.000663	0.1747	-0.589
Ptprd	0.143	7.600	3.602	0.000700	0.1812	-0.619
Ngb	-0.792	1.543	-3.596	0.000714	0.1815	-1.419
Rgs7bp	0.118	9.071	3.589	0.000729	0.1821	-0.716
Camk4	0.101	9.316	3.583	0.000744	0.1825	-0.743
Thsd7a	0.117	7.467	3.561	0.000793	0.1892	-0.728
Hipk2	0.191	5.988	3.560	0.000798	0.1892	-0.651
Pnck	-0.209	5.758	-3.542	0.000843	0.1968	-0.686
Camk2n1	0.106	10.768	3.519	0.000904	0.2022	-0.979
Ret	-0.589	2.081	-3.516	0.000911	0.2022	-1.307
Zeb2	0.142	6.285	3.512	0.000922	0.2022	-0.798
Bcas1	0.185	8.413	3.507	0.000937	0.2022	-0.920
Samd5	0.260	3.992	3.507	0.000937	0.2022	-0.747
S100b	0.206	7.036	3.498	0.000964	0.2033	-0.884
Gpc3	-0.594	1.672	-3.495	0.000971	0.2033	-1.579
Gpi1	-0.136	9.102	-3.488	0.000991	0.2045	-1.003

Table 3. Pathway and gene ontology analysis of differential gene expression in 114 kb congenic mice.

This table shows the top 5 KEGG pathways (A) and the top 5 Gene Ontology (GO) biological processes (B) pathways when considering the 69 differentially expressed genes ($p < 0.001$) between 114 kb congenic and B6J mice

(A): KEGG Pathways			
Name	**p value**	**Overlap**	**Genes**
Oxytocin signaling pathway	1.92E-04	5/154	Camk4, Fos, Adcy1, Kcnj2, Cacng5
Circadian entrainment	3.82E-04	4/99	Grin2a, Rasd1, Fos, Adcy1
Cholinergic synapse	6.29E-04	4/113	Camk4, Fos, Adcy1, Kcnj2
cAMP signaling pathway	8.10E-04	5/211	Grin2a, Camk4, Fos, Adcy1, Rapgef4
Long-term potentiation	1.71E-03	3/67	Grin2a, Camk4, Adcy1
(B): GO Biological Processes			
Name	**p value**	**Overlap**	**Genes**
peptidyl-threonine phosphorylation (GO:0018107)	1.92E-04	4/68	Pnck, Wnk1, Prkcd, Hipk2
regulation of non-motile cilium assembly (GO:1902855)	3.82E-04	2/6	Sept7, Hap1
peptidyl-threonine modification (GO:0018210)	6.29E-04	4/89	Pnck, Wnk1, Prkcd, Hipk2
regulation of synaptic transmission, GABAergic (GO:0032228)	8.10E-04	2/11	Npas4, Hap1
brain development (GO:0007420)	1.71E-03	4/119	Grin2a, Zic2, Zic1, Hap1

Exon-level analysis of coding and noncoding exons (e.g., 5'UTR noncoding exons) identified 35 genes exhibiting differential exon usage (**Table 4A-B**), which is defined as the proportion of total normalized reads per gene that are counted within an exon bin for that gene. Enrichr analysis of the 35 genes for pathway analysis identified an enrichment of dopaminergic synapse and amphetamine addiction involving *Ppp3ca*, *Calm2* and *Mapk2* as well as calcium signaling and long-term potentiation involving *Ppp3ca* and *Calm2* (**Figure 7**). Notably, *Hnrnph1* (the first protein-coding gene within the 114 kb congenic interval) was one of the top genes exhibiting differential exon usage (**Table 4A**), providing direct evidence at the exon level that one or more functional variants within *Hnrnph1* regulates exon usage and ultimately underlies differences in MA behavior. Note that *Hnrnph1* did not show a significant difference in overall gene-level transcript levels ($\log_2$FC = 0.016; t(14) = 0.70; p = 0.49; adjusted p = 0.99). Thus, any subsequent downstream functional changes that we report are not mediated by overall *Hnrnph1* transcript levels, but instead, by transcripts with alternative exons (either coding or noncoding; see Table 6). It should also be noted that we did not identify a significant difference in gene expression or in exon usage of *Rufy1* (the second protein-coding gene within the interval), thus limiting functional effects of D2J variants at the mRNA level to *Hnrnph1* and further supporting the candidacy of *Hnrnph1* as a QTG underlying MA behavior (Yazdani et al., 2015).

Table 4. Genes exhibiting differential exon usage in 114 kb congenic mice.
The table shows 35 genes exhibiting differential exon usage in striatal tissue from 114 kb congenic mice relative to their B6J wild-type littermates ($p < 0.001$). Differential exon usage was detected using either an F-test (A) or a Simes test (B) in limma (Ritchie et al., 2015).

(A): F-test (p < 0.001)					
Gene	**Fstat**	**Fstat_P**	**Fstat_FDR**	**Simes_P**	**Simes_FDR**
Ppp3ca	2.87	5.12E-07	0.0092	1.30E-09	2.30E-05
Cdhr4, Ip6k1, Uba7, Gm20661, Gm20662	1.65	1.36E-06	0.012	0.0015	1
Hnrnph1	2.19	7.50E-06	0.045	0.0055	1
Mrps14	4.92	2.67E-05	0.1	4.10E-05	0.19
Pfdn5, Myg1	2.1	2.89E-05	0.1	0.028	1
Scn3a	2.14	4.26E-05	0.13	0.002	1
Chn2	2.53	5.58E-05	0.14	0.026	1
Myo5b	1.89	7.13E-05	0.16	0.036	1
Mapk9	2.33	1.20E-04	0.21	0.022	1
Calm2	3.6	1.30E-04	0.21	0.0024	1
Hnrnpm, March2	1.83	1.40E-04	0.21	0.014	1
Cdc42bpa	1.75	1.40E-04	0.21	0.18	1
Arrdc1	2.11	1.90E-04	0.26	0.21	1
Igbp1	3.98	3.50E-04	0.43	0.014	1
Sptbn1	1.84	3.60E-04	0.43	0.017	1
Tm4sf1	3.64	4.30E-04	0.49	0.018	1
Ptpn5	1.94	5.60E-04	0.6	0.2	1
(B): Simes (p < 0.001)					
Gene	**Fstat**	**Fstat_P**	**Fstat_FDR**	**Simes_P**	**Simes_FDR**
Ppp3ca	2.87	5.12E-07	0.0092	1.30E-09	2.30E-05
Tspan32	2.96	0.0013	1	2.27E-05	0.19
Mrps14	4.92	2.67E-05	0.1	4.09E-05	0.19
Txn2	1.59	0.048	1	4.13E-05	0.19
Map2	1.6	0.0018	1	1.50E-04	0.53
Map4, Mtap4	1.57	0.007	1	1.80E-04	0.54
Slc8a3	2.88	0.0011	1	2.20E-04	0.57
Alpk3	1.76	0.052	1	3.80E-04	0.81
Jaml	2.74	0.006	1	4.10E-04	0.81
Dph1, Ovca2	1.29	0.15	1	4.90E-04	0.87
Rab21	2.69	0.15	1	5.40E-04	0.89
Usp24	0.83	0.86	1	9.70E-04	1

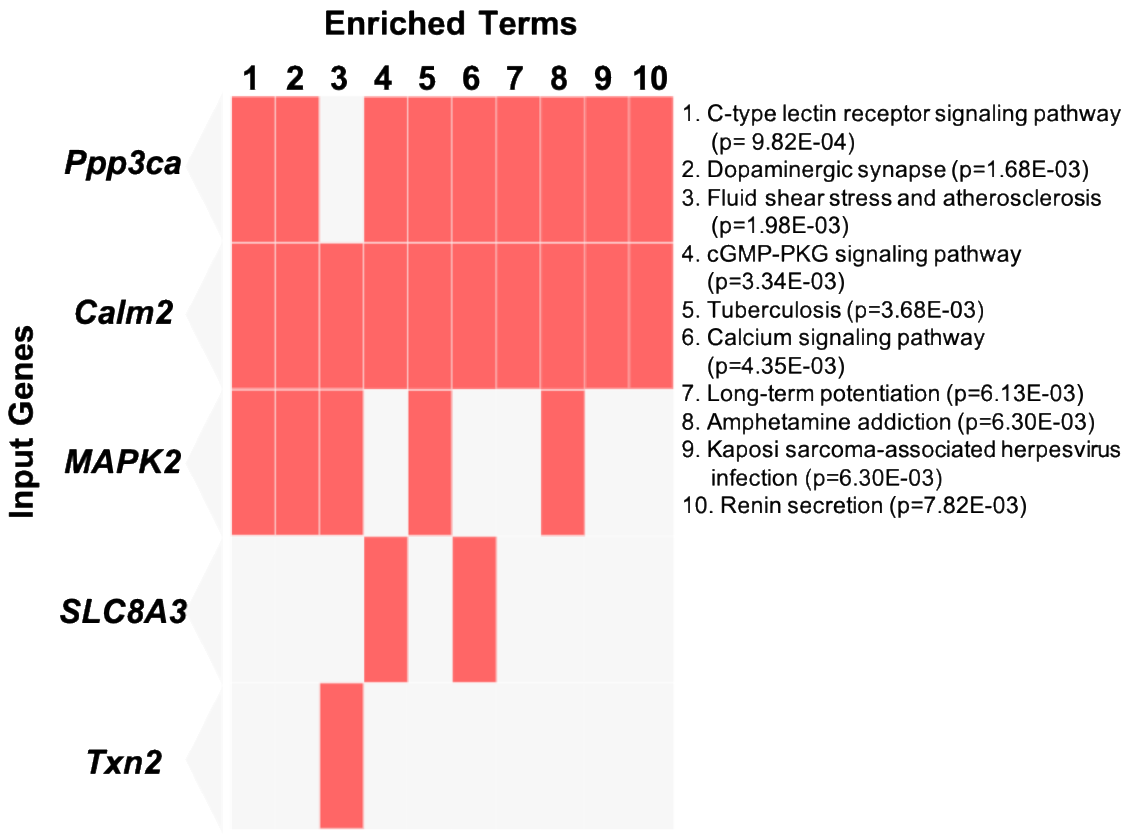

Figure 7. Pathway analysis of the top genes with differential exon usage.
We identified 35 genes showing differential exon usage between 114 kb and B6J mice ($p < 0.001$). The top 10 enriched KEGG pathways along with the five genes overlapping with each of these pathways are shown in the clustergram. The enriched pathways are shown in columns and input genes are shown in the rows and cells (in orange) in the matrix to indicate if a gene is associated with a pathway.

We previously showed that mice heterozygous for a 16-bp deletion within the first coding exon of *Hnrnph1* (refer to as the H1 MUT mice) were less sensitive to the stimulant, rewarding, and reinforcing properties of MA and showed a reduction in MA-induced extracellular DA level in the NAc (Yazdani et al., 2015; Ruan et al., 2020a). To directly compare the functional effects of inheriting the deletion versus the 114 kb congenic region on gene expression and exon usage, we identified 21 overlapping genes that were differentially expressed in the striatum between 114 kb congenic mice and H1 MUT mice relative to their B6J wild-type littermates (**Figure 8A**), which was significantly greater than what would be expected by chance (Fisher's exact test: p = 9.31E-23). In addition, there were 10 overlapping genes between H1 MUT and 114 kb congenic mice that showed differential exon usage, relative to their B6J littermates (**Figure 8B**). Again, this overlap was significantly greater than what would be expected by chance (Fisher's exact test: p = 2.96E-07). Finally, in correlating differential expression for the 21 shared differentially expressed genes between 114 kb congenic mice and H1 MUT mice, we found a nearly perfect relationship between the magnitude and direction of change in gene expression (**Table 5 and Figure 9**). These results suggest functionally similar effects of the 114 kb region and the H1 MUT allele on their overlapping, convergent transcriptome.

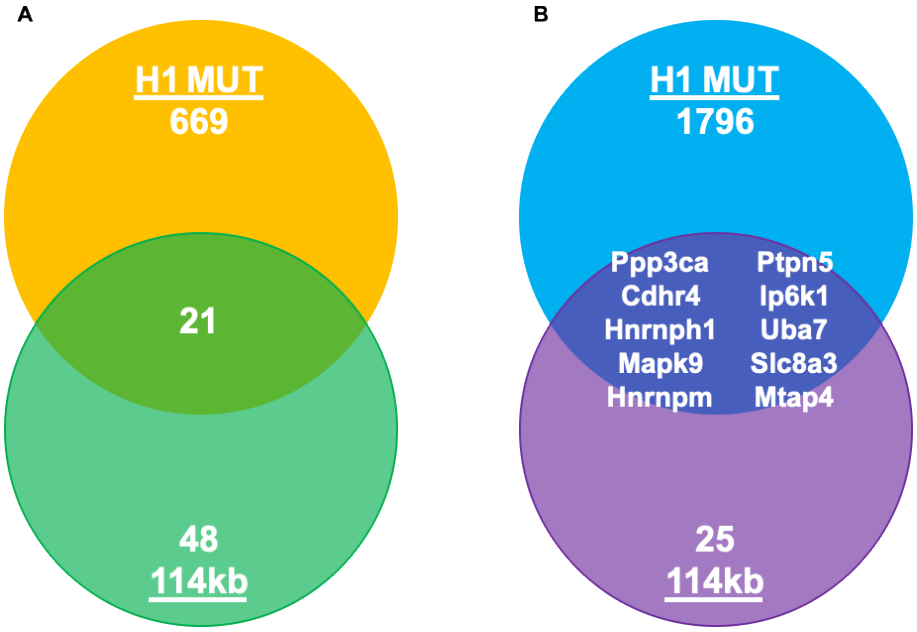

Figure 8. Overlap in differentially expressed genes and genes exhibiting differential exon usage between 114 kb congenic mice and H1 MUT mice.
(A): Venn diagram showing the number of differentially expressed genes (DEGs) in 114 kb ($p < 0.001$) versus H1 MUT mice ($p < 0.001$). The 21 DEGs that were shared between the two are significantly greater than what would be expected by chance (Fisher's exact test: $p = 9.31E-23$) as it represents nearly ½ of the 48 total DEGs identified in 114 kb congenic mice. (B): Venn diagram shows the number of non-overlapping and overlapping genes with differential exon usage in 114 kb congenic mice ($p < 0.001$) versus H1 MUT mice ($p < 0.001$). Ten genes showed differential exon usage in both the 114 kb congenic mice and the H1 MUT mice which is significantly greater than chance (Fisher's exact test: $p = 2.96E-07$) and include *Ppp3ca*, *Cdhr4*, *Hnrnph1*, *Mapk9*, *Hnrnpm*, *Ptpn5*, *Ip6k1*, *Uba7*, *Slc8a3*, and *Mtap4*.

Table 5. Correlation of differential expression between 114 kb congenic and H1 MUT mice. Table showing the log_2FC values for the 21 overlapping genes in the 114 kb and H1 MUT. The change in gene expression (up/down) is relative to B6J wild-type littermates.

Gene	114 kb log_2FC	H1 MUT log_2FC
Magel2	-0.704	-0.857
Dlx1	-0.701	-0.686
Zic2	-0.692	-0.811
Zic1	-0.630	-0.897
Trpc4	-0.562	-0.786
Prkcd	-0.524	-0.528
Wdr6	-0.348	-0.420
Hap1	-0.302	-0.380
Zcchc12	-0.225	-0.297
Pnck	-0.209	-0.353
Ecel1	-0.187	-0.596
Zcchc18	-0.103	-0.154
Camk4	0.101	0.311
Ano3	0.105	0.212
Kcna2	0.109	0.247
Osbpl8	0.115	0.129
Thsd7a	0.117	0.303
Rgs7bp	0.118	0.335
Wnk1	0.123	0.220
Cadm2	0.134	0.192
Oip5os1	0.146	0.369

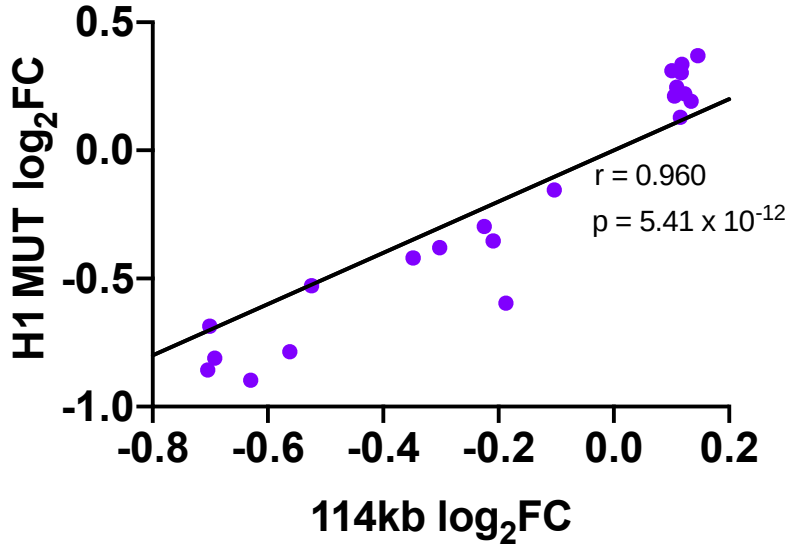

Figure 9. Correlation of differential expression between 114 kb congenic mice and H1 MUT mice.

The direction and the magnitude of change in gene expression relative to B6J wild-type were nearly identical between the 114 kb congenics and H1 MUT mice for every gene [Pearson correlation: r = 0.960, R^2 = 0.922, p = 5.41E-12].

The physical positions and exon numbers comprising differential exon usage of *Hnrnph1* in 114 kb relative to B6J mice are shown in **Table 6**. Note that fewer normalized reads were mapped to the junction comprising exon 3 and exon 4 in 114 kb congenic mice versus B6J **(**$\log_2$FC = -0.484 = 1.4-fold decrease; **Table 6**). Additionally, a greater number of normalized reads mapped to the junction comprising exons 6 and 7, as well as the junction comprising exons 7 and 8 in the 114 kb congenic mice relative to B6J (**Table 6**). It is important to note that *Hnrnph2* (homolog of *Hnrnph1*) did not show differential exon usage in our analysis (F = 1.330, Fstat p = 0.198, Fstat FDR = 1 and Simes p = 0.38, Simes FDR = 0.998). To validate differential exon usage of *Hnrnph1*, we performed qPCR with primers flanking those exons exhibiting significant differential exon usage. Out of the three exon junctions, 114 kb congenic mice showed less usage of exons 3 to 4, but no difference in the other two exon junctions (**Figure 10A**). To further validate the specific exons exhibiting differential usage, we designed primers to target exon 3 (5'UTR noncoding exon) and exon 4 (first coding exon) separately. Less usage of the 5'UTR noncoding exon was detected in the 114 kb congenic mice (**Figure 10B**), with no change in the first coding exon (**Figure 10C**). Exons 1 to 3 are noncoding exons that comprise the 5'UTR of *Hnrnph1* (see Figure 12). Thus, we conclude that 114 kb congenic mice show a reduced number of *Hnrnph1* transcripts that include this 5'UTR exon.

Table 6. Differential exon usage of *Hnrnph1* in 114 kb congenic mice.
Table showing the four exon positions of *Hnrnph1* that display differential exon usage in 114 kb congenic mice relative to B6J wild-type littermates with $p < 0.05$ using the Simes test. Exon usage was defined as the proportion of total normalized reads per gene that were counted within an exon bin for that gene.

Position (mm10)	Corresponding exon junction	log_2FC	p value	FDR
chr11:50,377,719-50,377,750	3-4	-0.484	0.018	1
chr11:50,380,191-50,380,825	6-7	0.137	0.001	1
chr11:50,381,598-50,382,137	7-8	0.094	0.017	1
chr11:50,382,138-50,382,536	7-8	0.167	3.80E-04	1

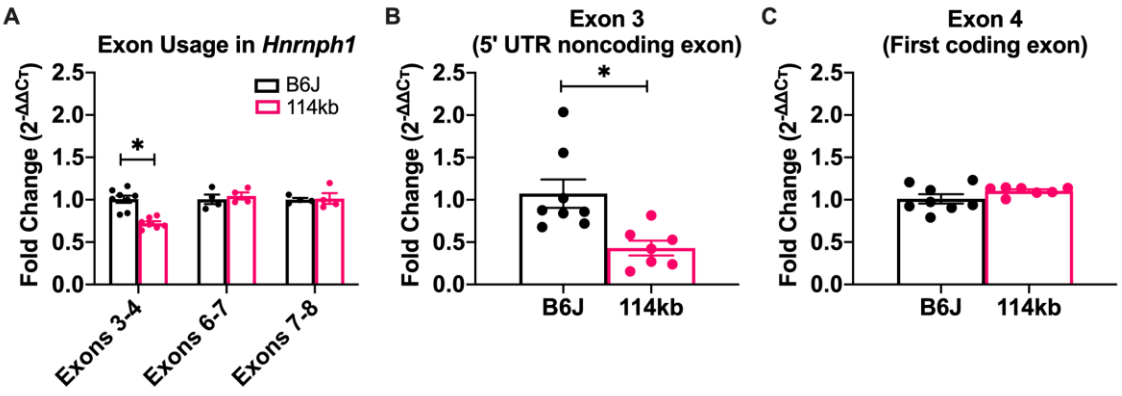

Figure 10. Decreased 5'UTR noncoding exon 3 usage of *Hnrnph1* in striatal tissue of 114 kb congenic mice.
Hnrnph1 was one of the top-ranked genes showing differential exon usage as indicated via the proportion of total normalized reads counted within an exon bin between 114 kb congenic mice versus B6J wild-type littermates. To validate differential exon usage, we conducted a set of qPCR experiments targeting the exon junction or the individual exons. Primer sequences, as well as the exon junctions or individual exons they target are provided in Supplemental Table 1. (A) Decreased usage of the junction comprising exons 3 and 4 was detected in 114 kb congenic mice [unpaired t-test for each exon junction: $t(13)_{exon\ 3\text{-}4} = 5.65$, *p = 7.9e-5; $t(6)_{exon\ 6\text{-}7} = 0.58$, p = 0.585; $t(6)_{exon\ 7\text{-}8} = 0.20$, p = 0.846]. (B-C) To further test specific exons, primers targeting either exon 3 or 4 of *Hnrnph1* were used to demonstrate that 114 kb congenic mice showed decreased usage of the 5' UTR noncoding exon 3 [unpaired t-test: t(13) = 3.25, *p = 0.006] but no difference in the first coding exon, exon 4 [unpaired t-test: t(13) = 1.53, p = 0.150]. Data are represented as the mean ± S.E.M.

Reduced hnRNP H protein expression in the striatum of 114 kb congenic mice

Three different antibodies for detecting and quantifying hnRNP H protein expression between 114 kb congenic mice and B6J wild-type litters were used and all samples analyzed are shown in **Figure 11A**. A significant decrease in hnRNP H immunoreactivity was detected with all three antibodies in the 114 kb congenic mice as indicated by total protein stain normalized densitometry values (**Figure A1**) that were in turn normalized to averaged B6J values to illustrate fold-change ($p = 0.003, 0.014, 0.01$; **Figure 11B-D**). Thus, *Hnrnph1* variants in 114 kb congenic mice are associated with both a decrease in *Hnrnph1* 5' UTR usage and decrease in hnRNP H protein expression.

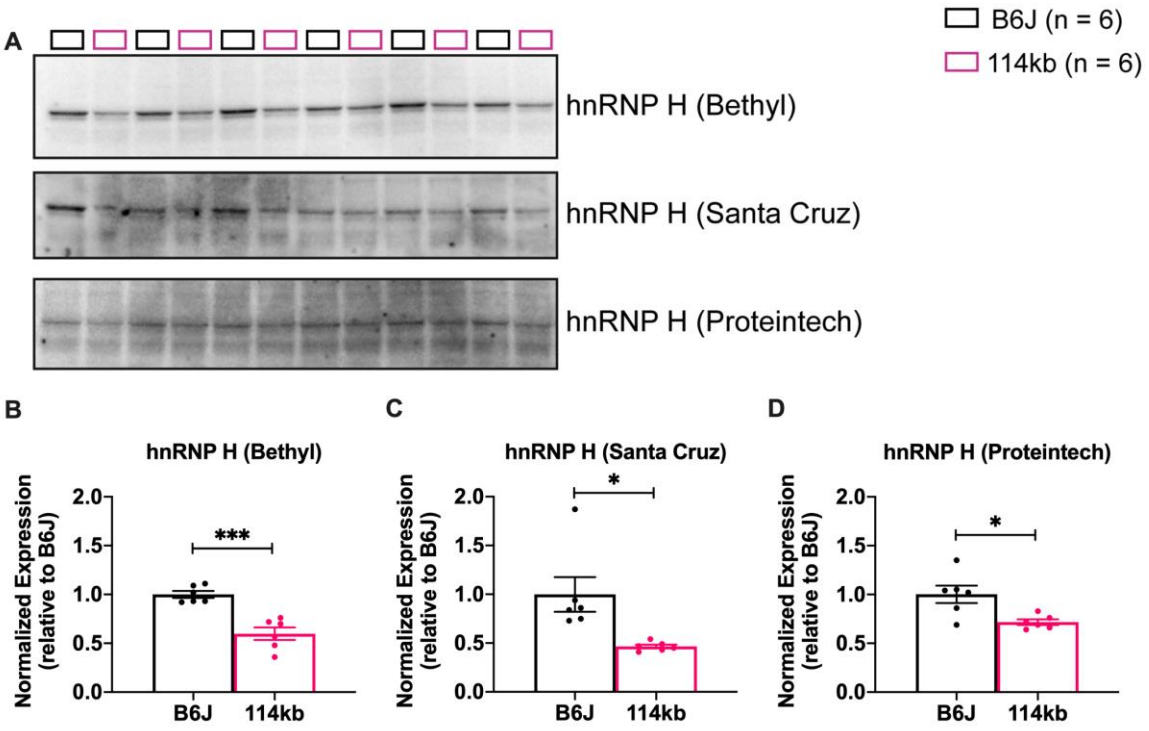

Figure 11. Decrease in hnRNP H protein expression in the striatum of 114 kb congenic mice. The striatum (left and right whole striatum) were dissected from the mice and protein lysates were extracted for protein quantification of hnRNP H using three anti-hnRNP H antibodies from three different companies. (A): Immunoblots showing hnRNP H protein expression in the striatum of 114 kb congenics and B6J mice. Three antibodies specific for hnRNP H were used. The hnRNP H antibody from Bethyl recognizes the C-terminus of the protein and the one from Santa Cruz recognizes the N-terminus. The epitope site for the antibody from Proteintech is unknown. (B-D): Quantification of the immunoblots shown in A showing a significant decrease in hnRNP H protein expression in the 114 kb congenic mice relative to the B6J mice when assessed with all three anti-hnRNP H antibodies [unpaired t-test: $t(10)_{Bethyl} = 5.06$, ***p = 0.003; $t(10)_{Santa\ Cruz} = 2.99$, *p = 0.014; $t(10)_{Proteintech} = 3.02$, *p = 0.013]. The expression values for hnRNP H were normalized to total protein staining by ponceau S as a loading control (See Appendix Figure A1 for ponceau S staining images and densitometry quantification values). The normalized values were normalized to the average of B6J expression values to examine fold-change in expression relative to B6J wild-type. Data are represented as the mean ± S.EM.

Identification of a set of 5' UTR functional variants in Hnrnph1 that decrease translation using a luciferase reporter assay

Three SNPs and one indel between D2J and B6J are located within the 5' UTR noncoding exons and introns (**Figure 12 and Table 7**). Given that the 5' UTR contains a promoter element for translational regulation, we employed a luciferase reporter system to assay the strength of the *Hnrnph1* promoter in the presence of one or all four of the 5' UTR variants in both Human Embryonic Kidney (HEK) 293T and Neuro2a (N2a) cells. We engineered a *Hnrnph1:luc2* construct by cloning 2956 bp of the B6J *Hnrnph1* promoter into the pGL4.17[luc2/Neo] promoter-less vector (**Figures A2 and 13A**). The 2956-bp promoter increased firefly luminescence compared to the pGL4.17[luc2/Neo] vector, and this increase in signal showed a cell number dependency (**Figure A3**). Using site-directed mutagenesis, we constructed 4 *Hnrnph1* promoters each possessing its own D2J variant within the 5' UTR (**Table A1**). In HEK293T cells, none of the four promoters with a single D2J variant showed a significant difference between the wild-type B6J *Hnrnph1* promoter in driving luciferase expression (**Figure 13B**). However, when all four D2J variants were introduced into the promoter, there was a significant reduction in luciferase activity compared to the B6J promoter ($p = 5.68E-11$; **Figure 13C**). The findings were subsequently replicated in N2a cells ($p = 1.19E-06$; **Figure 13D-E**).

Taken together, these results identify a set of functional 5' UTR variants within *Hnrnph1* that are associated with a decrease in usage of the 5' UTR noncoding exon 3, a decrease in hnRNP H protein expression, and that reduce *Hnrnph1* 5' UTR driven translation.

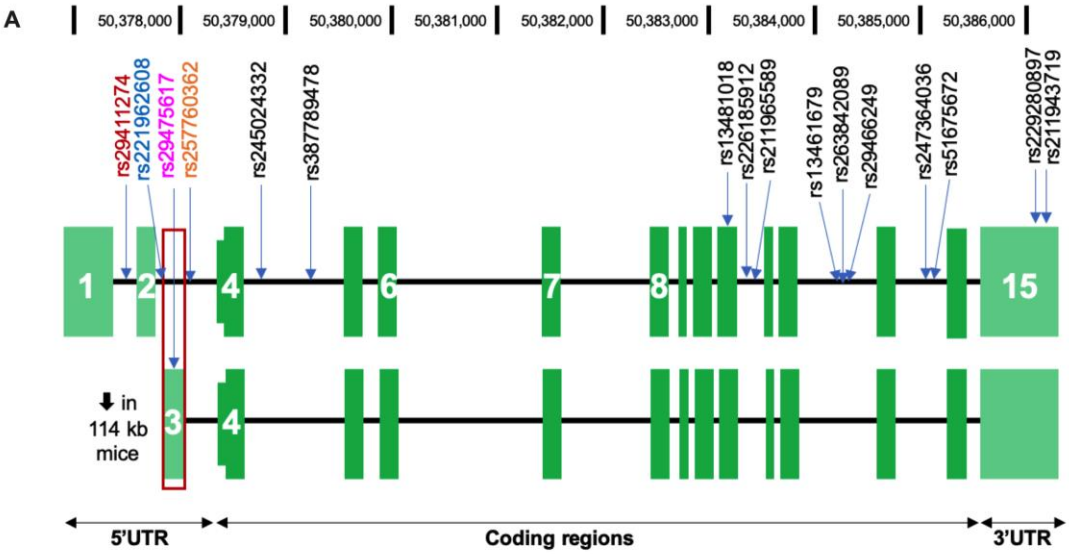

B

```
CTTCGCGCCCCTGGCAGTCTCAGCCTTCCCTCGCGAGGCGCCGCACACCG 50,377,024
AGCGCCTCTCGTGCAAGGGCGAGGGGTTCGTAGAGTGCGAGTCCGTTAGG 50,377,074
CAAAGTGGGGTACAGGACTAGCTCGGGCACTGGCAGCCCATGTGGGTCGG 50,377,124
GACTGACCCCCTAAAGCGGGCAGGTAAGGGGACTGGTCCCAGGCGCCCCA 50,377,174
CGGAGATCGGGGATTTGGGCGCAGGGGGCGGGGCGGTACCCAGAGGAGGT 50,377,224
TTGGCACAACCCGGCCCTCCAGCTCCTACGCGTTCTGAGGAGAAAGGGCA 50,377,274
TGGCTTCCTTTTCTTCGTGGTGTCTTTCAAAACCGACAGGAGCGCGGATG 50,377,324
AAAAGCTGCGGATTAAGGGTAGAACTACCGCCCCTGCAAACCTGAACGAA 50,377,374
CTCTGGATTACTACCCAGTCCCTGCGGGGAGCTGATTAGCGCCATTCCCC 50,377,424
TCCCCCACTCCGGCGGGTAGGTCTAGAGAACGGTTTGAAGGTAGCCGCAT 50,377,475
GCGCATTAAGTAAAACAAGAAACCGCTGAGACGCCAAGCGCAATAATTGC 50,377,524
AAAAAGGCGCAGGCGCAGAAAGAAAAAAAAAAAACAACCAAAAACACCTC 50,377,574
GGTCAGTTTATGAAGAGGGCTGAGCCCAAACGCATGCGTGTAATAATAGG 50,377,624
ACGGCGGGAGAGAGCTCGGGGTTTCTTAATACGCATGCGTCCAATCTCTC 50,377,674
TGTGACGCAAGTGGGGCGGGGCCGGCAACAGGGTGCGCGTGCGCAGAGCT 50,377,724
TGCTGGAAGGGCTTTATTTAGCCTGCGCAGGCGCCCGCTTATCATTTCTC 50,377,774
CTCAGCCACGCCGAGGCTTTTTGTGGAGGTGAGTGACTTTCCGTCTTCGA 50,377,824
CTGCTGCCCGAGCTCTCCACGGACACCTCTTTGGGTGACGATTGCTTGTC 50,377,874
GCTGAGCTTAGGTTCTAACCTGAGGGGCCGTGGCAGGCGCAGGCTGCCCC 50,377,924
TGGGAGCCGCGAGTGTCTCGCCGGCGTGGCAGCGCCGCCTAGGCCTGCAG 50,377,974
```

Figure 12. *Hnrnph1* variants between the B6J and D2J parental strains.
(A): Schematic representation of the position of SNPs and indels in *Hnrnph1* with the exon numbers listed. The exon with decreased usage in 114 kb congenic mice is boxed in red. (B): Genomic sequence for part of the *Hnrnph1* 5' UTR with positions of the three noncoding exons highlighted in green and positions of the 4 variants.

Table 7. SNPs and indels in *Hnrnph1* between B6J and D2J.
A query for *Hnrnph1* genetic variants (SNPs plus indels) between the B6J and D2J parental strains was conducted using the Sanger database query tool (mm10, REL-1505). The variants highlighted in orange are located in close proximity to the 5' UTR noncoding exon 3 and were cloned and tested for functional significance in the luciferase reporter assay.

Position (mm10)	dbSNP	C57BL/6J	DBA/2J	Type
50,377,288	rs29411274	T	C*	SNP; intron variant
50,377,546	rs221962608;rs224352813	GA	G*	Indel; intron variant
50,377,795	rs29475617	T	G*	SNP; 5'UTR variant
50,377,937	rs257760362	G	C*	SNP; intron variant
50,378,499	rs245024332	T	C*	SNP; intron variant
50,379,377	rs387789478;rs233140941	GTT	GT*	Indel; intron variant
50,383,262	rs13481018	C	T*	SNP; synonymous variant
50,383,443	rs226185912	ATG	A*	Indel; intron variant
50,383,487	rs211965589	T	TA*	Indel; intron variant
50,384,116	rs13461679	G	A*	SNP; intron variant
50,384,175	rs263842089	T	TAGATG*	Indel; intron variant
50,384,378	rs29466249	A	T*	SNP; intron variant
50,385,052	rs247364036	GTT	G*	Indel; intron variant
50,385,066	rs51675672	G	T*	SNP; intron variant
50,386,305	rs229280897	T	t/c*	SNP; 3'UTR variant
50,386,341	rs211943719;rs240064076	CTT	CTTT*	Indel; 3'UTR variant

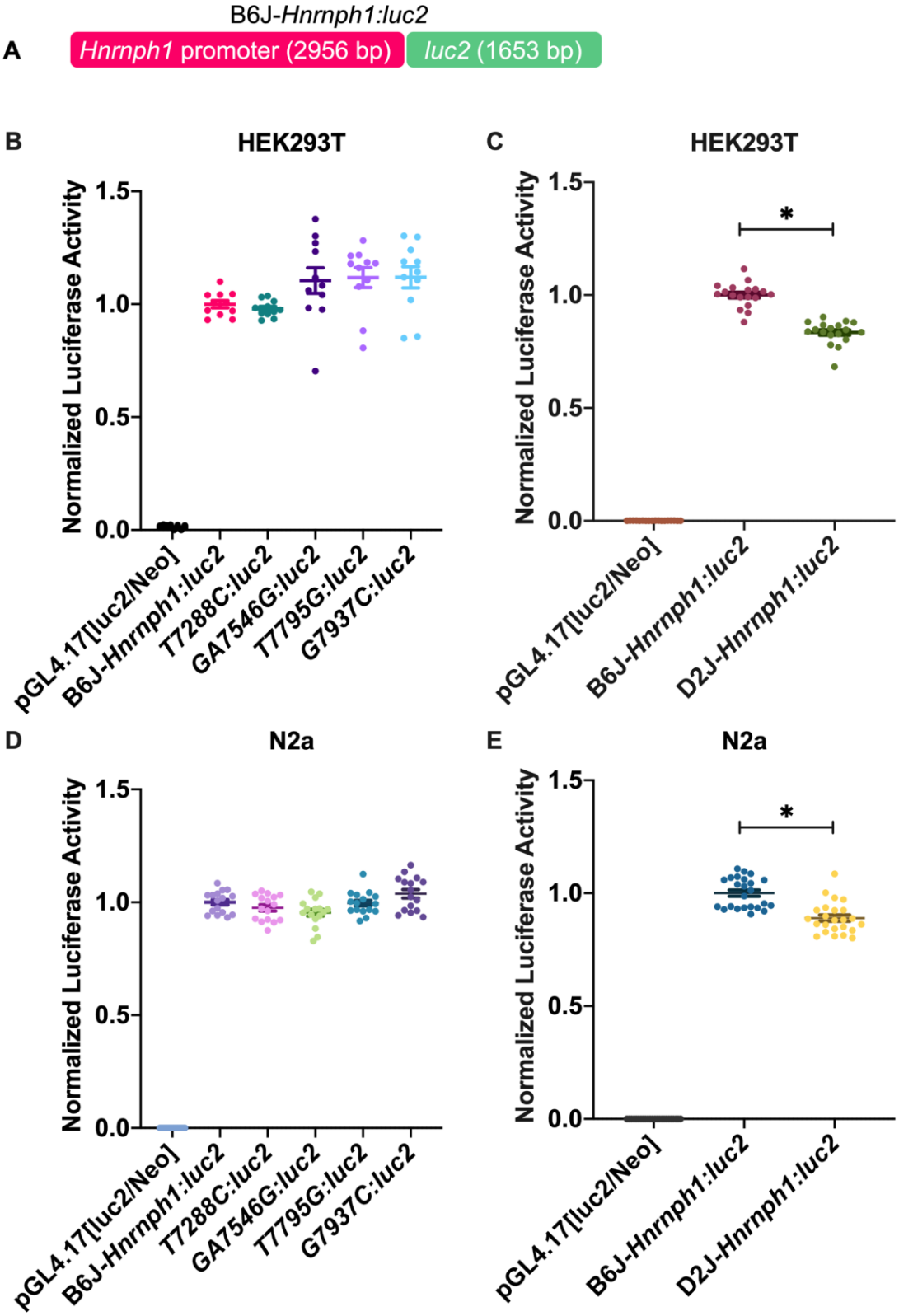
A
B6J-Hnrnph1:luc2
Hnrnph1 promoter (2956 bp)
luc2 (1653 bp)
B
HEK293T
Normalized Luciferase Activity
1.5
1.0
0.5
0.0
pGL4.17[luc2/Neo]
B6J-Hnrnph1:luc2
T7288C:luc2
GA7546G:luc2
T7795G:luc2
G7937C:luc2
C
HEK293T
*
Normalized Luciferase Activity
pGL4.17[luc2/Neo]
B6J-Hnrnph1:luc2
D2J-Hnrnph1:luc2
D
N2a
Normalized Luciferase Activity
pGL4.17[luc2/Neo]
B6J-Hnrnph1:luc2
T7288C:luc2
GA7546G:luc2
T7795G:luc2
G7937C:luc2
E
N2a
*
Normalized Luciferase Activity
pGL4.17[luc2/Neo]
B6J-Hnrnph1:luc2
D2J-Hnrnph1:luc2

Figure 13. Luciferase reporter assay for the *Hnrnph1* promoter in HEK293T and N2a cells to test the functional effect of 5' UTR variants.

Firefly luciferase was used as a reporter to assess the activity of B6J-*Hnrnph1:luc2* versus promoters containing individual 5' UTR variants from the D2J strain. *Renilla* luciferase was used as an internal control reporter. (A): Schematic representation of the *Hnrnph1:luc2* reporter construct that was transfected to HEK293T (B and C) or N2a (D and E) cells. (B): Single D2J variants were engineered within the 5' UTR of the *Hnrnph1* promoter and had no effect on the luciferase reporter signal in HEK293T cells [one-way ANOVA comparing B6J-*Hnnrph1:luc2* against the single D2J variants: $F(4,50) = 3.03$, $p = 0.025$; Dunnett's multiple comparison test with comparing each of the four variants with the *B6J-Hnnrph1:luc2* control group: $D_{Dunnett(T7288C)} = 0.36$, $p = 0.988$; $D_{Dunnett(GA7546G)} = 1.88$, $p = 0.199$; $_{DDunnett(T7795G)} = 2.11$, $p = 0.125$; $D_{Dunnett(G7937C)} = 2.14$, $p = 0.117$]. Data points represent the normalized luciferase signal from 2 independent replicates. (C): Engineering of all four D2J variants (D2J-*Hnrnph1:luc2*) in the promoter of *Hnrnph1* decreased luciferase luminescence relative to B6J-*Hnrnph1:luc2* in HEK293T cells [unpaired t-test, $t(34) = 9.39$, $*p = 5.68E\text{-}11$]. Data points represent the normalized luciferase signal from 3 independent replicates. (D): Singly engineered D2J variants within the promoter had no effect on luciferase reporter signal in N2a cells [one-way ANOVA comparing B6J-*Hnnrph1:luc2* against the single D2J variants: $F(4,75) = 4.42$, $p = 0.003$; Dunnett's multiple comparison test with comparing each of the four variants with the *B6J-Hnnrph1:luc2* control group: $D_{Dunnett(T7288C)} = 1.18$, $p = 0.584$; $D_{Dunnett(GA7546G)} = 2.20$, $p = 0.100$; $D_{Dunnett(T7795G)} = 0.18$, $p = 0.999$; $D_{Dunnett(G7937C)} = 1.79$, $p = 0.229$]. Data points represent the normalized luciferase signal from 2 independent replicates. (E): Engineering all four D2J variants (D2J-*Hnrnph1:luc2*) within the *Hnrnph1* promoter decreased luciferase luminescence relative to the B6J-*Hnrnph1:luc2* promoter in N2a cells [unpaired t-test, $t(46) = 5.59$, $*p = 1.19E\text{-}06$]. Data points are normalized luciferase signal from 3 independent replicates. Data are represented as the mean ± S.E.M.

DISCUSSION

The 114 kb region containing two protein genes (*Hnrnph1, Rufy1*) was not only necessary (Yazdani et al., 2015), but was also sufficient to cause a decrease in sensitivity to the locomotor stimulant response to MA (**Figure 5**). Our prior work strongly implicated *Hnrnph1* and not *Rufy1* as the QTG responsible for the reduction in MA-induced locomotor activity (Yazdani et al., 2015) and we subsequently expanded the behavioral repertoire of H1 MUT mice to include reduced MA-induced reinforcement, reward, and DA release (Ruan et al., 2020a). Our exon-level transcriptome analysis and comparative differential gene expression analysis between the 114 kb congenics and H1 MUT mice further supports *Hnrnph1* as the QTG underlying the reduction in MA-induced behavior (**Figure 8 and Table 4**). Decreased usage of the 5' UTR noncoding exon 3 of *Hnrnph1* in 114 kb congenic mice was independently validated via qPCR (**Figure 10**). Approximately 13% of genes in the mammalian transcriptome show differences in 5' UTR splicing of their transcripts (Carninci et al., 2005). Inheritance of the *Hnnrph1* 5'UTR variants (along with the other *Hnrnph1* variants; **Table 7**) were associated with a decrease in striatal hnRNP H protein expression (**Figure 11**). We identified a set of four variants within and flanking the 5' UTR that decreased reporter expression in two different cell lines (**Figure 13**), thus identifying a set of QTVs underlying molecular regulation of *Hnrnph1* and likely MA behavior.

Identification of QTGs and QTVs is extremely rare in mammalian forward genetic studies, in particular for behavior (Yalcin and Flint, 2012), and especially when considering the identification of noncoding functional variants. In the recent identification of a noncoding functional variant underlying a *cis*-expression QTL, Mulligan and colleagues

took advantage of the reduced genetic complexity of closely related C57BL/6 substrains (Bryant, 2011; Bryant et al., 2020) to deduce and validate an intronic variant in *Gabra2* (alpha-2 subunit of the GABA-A receptor) near a splice site that drastically reduced transcript and protein expression and modulated behavior (Mulligan et al., 2019). Correction of the single base deletion in C57BL/6J to the wild-type C57BL/6N allele via CRISPR/Cas9-mediated gene editing restored *Gabra2* transcript and protein levels to a normal level, thus identifying the QTV (Mulligan et al., 2019). The vast majority of other examples that successfully identified both the QTG and the QTV involve functional coding mutations, including *Cyfip2* (Kumar et al., 2015), *Grm2* (Zhou et al., 2013) , and *Taar1* (Stafford et al., 2019). With regard to *Hnrnph1*, a human candidate gene association study identified a functional intronic variant in *OPRM1* (mRNA target of hnRNP H) that affected binding to hnRNP H to regulate splicing and was associated with the severity of heroin addiction (Xu et al., 2014).

Less than one-third of genes analyzed in human cell lines showed a direct correlation between mRNA level and protein expression (Vogel et al., 2010; Araujo et al., 2012). Furthermore, *cis*-expression QTL analysis at both the mRNA and protein level in Diversity Outbred mice indicated the presence of genetic variants that regulate protein levels without affecting overall transcript levels (Chick et al., 2016). In support, our gene-level transcriptome analysis did not identify *Hnrnph1* as a differentially expressed gene; however, exon-level analysis identified decreased 5'UTR noncoding exon usage of *Hnrnph1* in 114 kb congenic mice (**Figure 10 and Table 6**) that was associated with decreased hnRNP H protein expression (**Figure 11**). Genetic variants within *cis*-regulatory

elements located in the 5'UTR and 3'UTR of genes and *trans*-regulatory factors that bind to these elements (e.g. RBPs) can perturb translation or overall protein abundance (Chatterjee and Pal, 2009; Vogel et al., 2010; Araujo et al., 2012; Dvir et al., 2013; Kim et al., 2014b). In our study, we identified an association between decreased 5'UTR usage and decreased hnRNP H protein expression in 114 kb congenic mice. The GC content, secondary structure, and length of the 5' UTR can affect translational efficiency (Jackson et al., 2010; Araujo et al., 2012). Thus, the altered GC content within the 5'UTR of *Hnrnph1* in 114 kb congenic mice could inhibit translation by changing the thermal stability of secondary stem loop structure (Araujo et al., 2012). Because the length of the 5'UTR determines the amount of energy needed for the ribosome to reach the AUG start site (Chatterjee and Pal, 2009), a change in length of the 5'UTR in *Hnrnph1* caused by the set of 114 kb variants could also alter protein synthesis. Also, a change in binding sites for RBPs to regulate translation could contribute to reduced hnRNP H protein in 114 kb congenic mice (Dassi, 2017; Steri et al., 2018). RBPs recognizes specific motifs in the 5'UTRs, and thus, a change in the sequence of these motifs induced by these variants could alter the association of RBPs with the translation machinery at the 5' UTR of *Hnrph1* to control expression. The RBPDB database (Cook et al., 2011) indicates that several RBPs are predicted to bind to the 5'UTR of *Hnrnph1*, though notably not hnRNP H itself (**Table A3**).

The hnRNP family of RBPs act in concert to regulate RNA metabolism and gene expression of other RBPs (Huelga et al., 2012). Downregulation of hnRNP H protein in 114 kb congenic mice (**Figure 11**) could affect complexing of hnRNP H with other RBPs

to regulate expression and in turn, alter recruitment of RBPs involved in splicing of the 5'UTR of *Hnrnph1*. As an example, hnRNP A1 is predicted to bind to the 5' UTR of *Hnrnph1* (Cook et al., 2011) and this RBP is known to cooperate with hnRNP H in mediating gene splicing (Fisette et al., 2010). Thus, although *Hnrnph1* is not predicted to be a direct target of hnRNP H, reduced hnRNP H protein could alter the expression of and coordination with other RBPs to regulate 5'UTR usage of *Hnrnph1*.

To summarize, we provide further causal behavioral and molecular evidence for *Hnrnph1* as a QTG for MA sensitivity by demonstrating that inheritance of a small, 114 kb chromosomal region was not only *necessary* (Yazdani et al., 2015) but also *sufficient* to induce the behavioral phenotype. We provide functional evidence for a set of four QTVs within the 5'UTR that could plausibly reduce 5'UTR usage and the amount of hnRNP H protein; however, demonstrating that these four variants are sufficient alone to induce these functional effects on *Hnrnph1* molecular regulation and behavior would require the generation of a mouse model containing only these four variants. The relatively subtle effect of the 114 kb region on behavior raises the question of whether modeling these variants *in vivo* is worth the effort – convergent evidence provides strong evidence that we have identified a set of QTVs underlying functional molecular and behavioral changes. Future studies involving cell type-specific knockdown of *Hnrnph1* using the Cre-loxP system will efficiently and more selectively model the effects of reduced hnRNP H protein expression on MA-induced behavior.

MATERIALS AND METHODS

Generation of B6J.D2J 114 kb congenic mice

All procedures involving mice were conducted in accordance with the Guidelines for Ethical Conduct in the Care and Use of Animals and were approved by the Institutional Animal Care and Use Committee at Boston University (#AN-15326). The founder 114 kb congenic mouse was identified by monitoring the distal single nucleotide polymorphism (SNP) sites of offspring generated via backcrossing heterozygous congenic mice from Line 4a carrying one copy of a ~11 Mb introgressed interval from the D2J strain to the background B6J strain (Yazdani et al., 2015). We monitored for retention of the most proximal D2J SNP that was just upstream of *Hnrnph1* (rs29383600; 50,373,006 bp; mm10) and this SNP defined the proximal end of the 114 kb interval. We previously genotyped several purported SNP markers proximal to rs29833600 that were monomorphic until 49,873,463 bp (mm10), which was catalogued by Sanger as a B6J/D2J polymorphic marker and that we genotyped as homozygous for B6J (Yazdani et al., 2015). Because we were unable to identify any polymorphisms between 49,873,463 bp (mm10) and rs29383600, we defined the proximal interval of this smaller congenic with the marker rs29383600 (50,373,006 bp). The remainder of the genome is isogenic for B6J as determined by several other markers on chromosome 11 and by a medium-density genotyping array containing 882 informative SNP markers from our previous study (Yazdani et al., 2015).

We also simultaneously monitored for the detection of a recombination event (i.e., the observation of a homozygous B6J genotype) at a second marker located just distal to *Rufy1* (rs254771403; 50,486,998 bp; mm10). Following detection of a recombination event

at rs254771403, we then genotyped at an additional upstream proximal marker at rs29459915 (50,484,260 bp; mm10) that was also downstream of *Rufy1* and found retention of the D2J allele at this locus. Thus, the new remarkably smaller congenic interval was conservatively defined by a region spanning proximal rs29383600 (50,373,006 bp) and distal rs254771403 (50,486,498 bp), yielding a 114 kb interval. Thus, we named this new congenic, "114 kb".

PCR primers were designed to amplify a ~200 bp amplicon that contained and flanked each SNP. The PCR products were run on a 1.5% agarose gel and visualized for band specificity. Single bands were excised according to their predicted fragment size and gel-purified (Promega Wizard SV Gel and PCR Clean-Up System, Cat A9281), and prepared for Sanger sequencing (Genewiz, Cambridge, MA, USA). Mice homozygous for the 114 kb region (referred to as 114 kb) and B6J littermates were generated via heterozygous-heterozygous 114 kb breeders. To avoid genetic drift, heterozygous 114 kb breeders were maintained by mating heterozygous male offspring with C57BL/6J females purchased from The Jackson Laboratory in Bar Harbor, ME, USA. Mice were SNP-genotyped using genomic DNA extracted from tail biopsies and two Taqman SNP markers: rs29383600 (50.37 Mb) and rs29459915 (50.48 Mb) (ThermoFisher Scientific, Waltham, MA, USA).

Methamphetamine-induced locomotor activity in 114 kb congenic mice

Both female and male littermates (56-100 days old at the start of the experiment), were phenotyped for MA-induced locomotor activity. Mice were housed in same-sex groups of 2 to 4 mice per cage in standard shoebox cages and housed within ventilated racks under

standard housing conditions. Colony rooms were maintained on a 12:12 h light–dark cycle. The estimated sample size required to detect a significant effect (Cohen's d = 0.72), with 80% power ($p < 0.05$) was n = 25 per genotype based on the previously published phenotype in the larger congenics capturing a QTL for reduced MA-induced locomotor activity (Yazdani et al., 2015). Mice were tested for baseline locomotor activity on Days 1 and 2 over 60 min and then administered MA (2 mg/kg, i.p.) on Days 3, 4, and 5 and were video-recorded for distance traveled over 60 min using Anymaze (Stoelting Co., Wood Dale, IL, USA) as previously described (Yazdani et al., 2015). Data are presented in six, five-min bins or as the summed distance traveled over 60 min for each of the five days of injections.

Transcriptome analysis followed by gene set enrichment analysis

Striatum punches were harvested bilaterally from 114 kb congenic mice homozygous for the congenic region (n = 8) and B6J wild-type littermates (n = 8) and processed for total RNA extractions (Yazdani et al., 2015). RNA samples were bioanalyzed (RIN > 8) and cDNA library was prepared using the Illumina TruSeq Standard mRNA LT (100 bp paired-end reads). The 16 samples were multiplexed and sequenced over three lanes on Illumina HiSeq 2500. The data is available on the NCBI GEO database under accession number GSE76929. FastQ files were aligned to the mouse mm10 reference genome using TopHat (Trapnell et al., 2012). HTSeq python framework (Anders et al., 2015) was used to compute the read counts per gene followed by limma (Ritchie et al., 2015) to integrate counts and detect differentially expressed genes. For differential analysis, a linear model was used to compare gene expression between genotypes with "Cage" included as a covariate.

Furthermore, between-technical replicate correlation was accounted for using the duplicateCorrelation(), limma function (Smyth et al., 2005). An α level of $p < 0.001$ was employed. For gene set enrichment analysis of the 69 differentially expressed genes that meet the significant cutoff, Enrichr (Chen et al., 2013; Kuleshov et al., 2016) was used to determine the enrichment of top Kyoto Encyclopedia of Genes and Genomes (KEGG) pathway terms and gene ontology (GO) terms.

Differential exon usage analysis followed by gene set enrichment analysis

For differential usage of exons using limma (Ritchie et al., 2015), reads were aligned to the Ensembl-annotated genome that contains extensive annotation of coding and non-coding exons and quantified using DEXSeq (Anders et al., 2012) with a requirement of one read count per exon bin and a minimum of at least 10 reads across all replicates. Similar to differential analysis, for each gene, a linear model was used to detect differential exon usage between genotypes with "Cage" included as a covariate and between-technical replicate correlation was accounted for using the duplicateCorrelation() limma function (Smyth et al., 2005). Differential exon usage was defined as the proportion of total normalized reads per gene that are counted within an exon bin for that gene. Statistical significance was evaluated using gene-level tests, including an F test that reflects a consensus signal across a gene and is highly powered to detect differential exon usage when more than one signal is observed across multiple exons per gene. We also report the results from a Simes multiple testing procedure that assesses all exons within a gene which is more powered to detect differential exon usage when a single strong signal is observed. An α level of $p < 0.001$ was employed for both the F-test and the Simes test. The 35

significant genes exhibiting differential exon usage between the 114 kb and B6J were analyzed for pathway enrichment using Enrichr (Chen et al., 2013; Kuleshov et al., 2016) for KEGG pathway enrichment analysis. A clustergram was used for visualization of the overlapping genes of the top enriched pathways.

Real-time quantitative PCR (qPCR) validation

For qPCR validation of exon usage, oligo-dT primers were used to synthesize cDNA from total RNA using the same samples that were used in RNA-seq analysis using SYBR Green (ThermoFisher Scientific, Waltham, MA, USA; Cat# 4309155). The qPCR primers used for exon usage in *Hnrnph1* are shown in **Table A2.** Each sample was run in triplicate, averaged, and normalized to its own expression level using *GAPDH* as a housekeeping gene. Differential exon usage was reported as the fold-change in 114 kb congenic mice relative to B6J littermates using the $2^{-(\Delta\Delta C_T)}$ method (Schmittgen and Livak, 2008).

SDS-PAGE and Western blot

Whole striata (left and right sides) were homogenized using a hand-held homogenizer in RIPA buffer supplemented with Halt protease and phosphatase inhibitor cocktail (Thermo Fisher Scientific, Waltham, MA, USA; Cat# 78840) followed by sonication. 30 μg of protein was heated in a 70°C water bath for 10 min before loading into a 4 – 20% Criterion TGX precast Midi protein gel (Bio-Rad, Hercules, CA, USA; Cat# 5671094) for SDS-PAGE followed by wet transfer to a nitrocellulose membrane. After the transfer, all membranes were stained with ponceau S solution (0.1% ponceau S in 1% (v/v) acetic acid) for 1 minute and quickly de-stained in water to remove non-specific staining. The

membranes were then imaged and densitometry analysis for total protein per lane was quantified in ImageJ2 (Rueden et al., 2017). The membrane was then blocked with 5% milk for 1 h and probed with primary antibodies. hnRNP H protein expression was evaluated using three different antibodies: 1) C-term specific hnRNP H antibody (1:100,000, Bethyl, Montgomery, TX, USA; Cat #A300-511A); 2) N-term specific hnRNP H antibody (1:20,000, Santa Cruz, Dallas, TX, USA; Cat# sc-10042); and 3) hnRNP H1 antibody (1:10,000, Proteintech, Rosemont, IL, USA; Cat# 14774-1-AP). The secondary used for the Bethyl and Proteintech antibodies was donkey anti-rabbit HRP (1:10,000, Jackson ImmunoResearch Laboratories, West Grove, PA; Cat# 711-035-152) and the secondary used for the Santa Cruz one was bovine anti-goat HRP (1:10,000, Jackson ImmunoResearch Laboratories, West Grove, PA; Cat# 805-035-180). All membranes were imaged via enhanced chemiluminescence photodetection. For quantification analysis of protein expression, total protein stains were used as loading controls in normalization for immunoblotting quantification (Aldridge et al., 2009; Gilda and Gomes, 2013).

Cell culture and transfection

HEK-293T cells were grown in DMEM, high glucose with L-glutamine (Gibco, Waltham, MA, USA; Cat# 11965-092), supplemented with 10% fetal bovine serum (Gibco, Waltham, MA, USA; Cat# 26140-079), and 1% penicillin-streptomycin (Gibco, Waltham, MA, USA; Cat# 15140-122). N2a neuron-like cells were grown in 1:1 ratio of DMEM, high glucose with L-glutamine (Gibco, Waltham, MA, USA; Cat# 11965-092) to Opti-MEM (GibCO, Waltham, MA, USA; Cat# 31985-070), supplemented with 5% fetal bovine serum (Gibco, Waltham, MA, USA; Cat# 26140-079), and 1% penicillin-streptomycin (Gibco, Waltham,

MA, USA; Cat# 15140-122). Cells were split every 3 to 4 days and were grown at 37°C in an atmosphere of 5% CO_2.

For HEK293T, cells were seeded in 6-well plate at a density of 2.5 x 10^5 cells per well 24 hours prior to transfection and would be about 90% confluent at the time of transfection. For N2A (given they grow faster than HEK293T cells), cells were seeded in 6-well plate at a density of 2 x 10^5 cells per well. A suspension of plasmids, Lipofectamine 3000 and P3000 reagents (ThermoFisher Scientific, Waltham, MA, USA; Cat# L3000008) in Opti-MEM medium was pre-incubated at room temperature for 15 min before being added to each well of the 6-well plates. The cells were co-transfected with 1 μg of the experimental firefly luciferase construct and 0.2 μg internal pRL control plasmid expressing *Renilla* luciferase driven by the CMV promoter (Promega, Madison, WI, USA; Cat# E2261). 24 hours after transfection, HEK293T cells were detached with 0.25% of Trypsin-EDTA (ThermoFisher Scientific, Waltham, MA, USA; Cat# 25200056) and counted and re-seeded at a density of 2.5 x 10^4 cells per well in 96-well plate. N2a cells were re-seeded at a density of 2 x 10^4 cells per well in 96-well plate. Cells were allowed to grow for approximately 48 h before measurement of luciferase activity as described below.

Luciferase reporter assay

We cloned the B6J *Hnrnph1* promoter sequence (Chr11: 50,375,375 to 50,378,330; mm10) starting at 2956 bp upstream of the annotated transcription start site for *Hnrnph1*. This sequence was amplified from B6J genomic DNA extracted from spleen tissue using iProof High-Fidelity PCR kit (BIO-RAD, Hercules, CA, USA; Cat# 172-5330) with the following primers containing *XhoI* and *HindIII* restriction enzyme sites in the sense and antisense

primers respectively: sense (5'-GATTCTCGAGGCTCCCGTGATCAGATACAG-3') and anti-sense (5'-GTAAAGCTTCGTCCCTTCGGTGGTCCTGGC- 3'). The sequence was subsequently cloned into the multiple cloning site of pGL4.17[luc2/Neo] (Promega, Madison, WI, USA; Cat# E6721) with restriction enzymes *XhoI* and *HindIII,* placing the *Hnrnph1* promoter was inserted upstream of firefly luciferase luc2 coding sequence.

To identify variants within *Hnrnph1* between D2J and B6J mice, we used the whole genome sequence dataset (35, 36) and the online Sanger variant query tool (REL-1505 - GRCm38) to identify a total of 16 variants including three SNPs and one idel (insertion/deletion) located in the 5'UTR of Hnrnph1 (see Table 7). To replace B6J variants with D2J variants within the 5'UTR of *Hnrnph1,* we conducted site-directed mutagenesis using the B6J *Hnrnph1:luc2* construct as a template (Agilent QuikChange II, Santa Clara, CA, USA; Cat# 200521) to generate four luciferase reporter lines, each containing a single D2J variant. To introduce the three SNPs and the single indel all together into the 5' UTR of *Hnrnph1,* multi-site directed mutagenesis was performed by using the *GA7546G:luc2* construct with rs221962608 SNP variant as the template (Agilent, Santa Clara, CA, USA; Cat# 200514). The mutagenic primers are provided in **Table A1.**

To account for background fluorescence signal, untransfected cells were used to subtract out background signal from the 96-well plate. Negative control cells were transfected with the promoter-less plasmid pGL4.17[luc2/Neo]. The Dual-Glo luciferase assay system (Promega, Madison, WI, USA; Cat# E2920) was used to measure luciferase activity. The growth medium was removed first and cells were then washed with PBS. Cell lysates were prepared by adding 50 µl of 1X passive lysis buffer to each well to lyse the

cells by shaking the plate on rocker for 15 min. 20 µl of lysate from each well was transferred to wells of white opaque 96-well microplate (Corning, Corning, NY, USA; Cat# 3610). Dual-Glo LARII reagents (100 µl) were added into each well and the firefly luminescence was measured with SpectraMax i3x microplate reader after 15 min. An equal amount (100 µl) of Stop & Glo reagent was then added to the wells and Renilla luminescence was measured after 15 min.

Firefly and Renilla luciferase signal values were subtracted from the average background signal first. The background-adjusted firefly luciferase activity (FLA) for each sample was normalized to the background-adjusted internal control Renilla luciferase activity (RLA) to correct for differences in transfection efficiency and cell death. Relative luciferase activity for each experimental construct is expressed as the fold increase over the B6J *Hnrnph1:luc2* control:

$$Normalized\ luciferase\ activity = \frac{\left(\frac{FLA}{RLA}\right)_{Experimental}}{\left(\frac{FLA}{RLA}\right)_{\text{B6J } Hnrnph1:luc2\ control}}$$

Experimental design and statistical analyses

All data are presented as means of replicates from each experiment ± S.E.M. For experiments in which two conditions were compared, a two-tailed unpaired t-test was used to analyze the data unless otherwise specified. For the behavioral experiments in which multiple factors were evaluated, ANOVA was used and significant interactions were deconstructed along the relevant factor to examine main effects and group differences followed up with t-tests. For the qPCR validation and luciferase report assay analyses in

which multiple factors were evaluated, ANOVA was used and significant interactions were deconstructed with Dunnett's post hoc test for multiple comparisons. Statistical α level for t-test, ANOVA, and post-hoc tests were set to 0.05. The data comprising MA-induced locomotor activity were analyzed in R (http://www.R-project.org/). All other data analyses were performed in GraphPad Prism (Version 8.3.0).

CHAPTER III: A mutation in *Hnrnph1* that decreases methamphetamine-induced reinforcement, reward, and DA release and increases synaptosomal hnRNP H and mitochondrial proteins

Adapted from Ruan et al., 2020, *Journal of Neuroscience*

ABSTRACT

Individual variation in the addiction liability of amphetamines has a heritable genetic component. We previously identified *Hnrnph1* as a quantitative trait gene underlying decreased MA-induced locomotor activity in mice. Here, we showed that mice (both females and males) with a heterozygous mutation in the first coding exon of *Hnrnph1* (H1 MUT) showed reduced MA reinforcement and intake and dose-dependent changes in MA reward as measured via conditioned place preference. Furthermore, H1 MUT mice showed a robust decrease in MA-induced extracellular DA in the NAc with no change in baseline extracellular DA, striatal whole tissue DA, DA transporter protein, DA uptake, or striatal MA and amphetamine metabolite levels. Immunohistochemical and immunoblot staining of midbrain dopaminergic neurons and their forebrain projections for tyrosine hydroxylase did not reveal any major changes in staining intensity, cell number, or forebrain puncta counts. Surprisingly, there was a two-fold increase in hnRNP H protein in the striatal synaptosome of H1 MUT mice with no change in whole tissue levels. To gain insight into the mechanisms linking increased synaptic hnRNP H with decreased MA-induced DA release and behaviors, synaptosomal proteomic analysis identified an increased baseline abundance of several mitochondrial complex I and V proteins that rapidly decreased at 30 min post-MA administration in H1 MUT mice. In contrast, the much lower level of basal

synaptosomal mitochondrial proteins in wild-type mice showed a rapid increase. We conclude that H1 MUT decreases MA–induced extracellular DA in the NAc, reward, and reinforcement and induces dynamic changes in basal and MA-induced synaptic mitochondrial function.

INTRODUCTION

Addiction to psychostimulants including MA is a major public health concern in the United States, with an estimated 535,000 individuals currently meeting the criteria for MA dependence (Lipari et al., 2016). Despite the prevalence of MA addiction, there is currently no FDA-approved treatment, in part because the neurobiological mechanisms underlying MA addiction are still not clear. Variation in sensitivity to the locomotor stimulant response to psychostimulants is a heritable trait and can sometimes predict differences in drug self-administration in rodents (Hooks et al., 1991; Yamamoto et al., 2013) because shared neurocircuits and neurochemical mechanisms underlie these behaviors. We recently used QTL mapping, positional cloning and gene editing via Transcription Activator-like Effector Nucleases (TALENs) to identify *Hnrnph1* as a quantitative trait gene for MA sensitivity in mice (Yazdani et al., 2015). *Hnrnph1* encodes an RBP that is expressed throughout the brain, and is a part of a subfamily of hnRNPs that includes hnRNP H1, hnRNP H2 and hnRNP F that possess structurally unique quasi-RNA recognition motifs (Honoré et al., 1995). hnRNP H1 regulates all aspects of RNA metabolism, including pre-mRNA splicing through binding at specific intronic sites, mRNA stability and translational regulation via binding to the 5'UTR and 3'UTR, and poly-adenylation control (Chou et al., 1999; Arhin et al., 2002; Katz et al., 2010; Witten and Ule, 2011; Wang et al., 2012; Song et al., 2017).

We previously demonstrated that *Hnrnph1* polymorphisms and heterozygous deletion in the first coding exon of *Hnrnph1* affect behavioral sensitivity to acute MA-induced locomotor stimulation; however, the effects on MA reward and reinforcement are

unknown. Additionally, the neurobiological mechanism(s) underlying the mutational effects of *Hnrnph1* on MA-induced behaviors remain to be established. *Hnrnph1* mRNA is ubiquitously expressed throughout the adult mouse brain (Lein et al., 2007). While the protein expression of hnRNP H1 appears to be nuclear-restricted, studies assessing hnRNP H1 protein in the brain are limited (Kamma et al., 1995; Honore et al., 1999; Van Dusen et al., 2010). With regard to CNS function, hnRNP H family proteins are described as master regulators of neuron and oligodendrocyte differentiation via alternative splicing control (Wang et al., 2007; Grammatikakis et al., 2016b). Whole-exome sequencing identified coding variants in human *HNRNPH1* and *HNRNPH2* (located on the X chromosome) associated with severe neurodevelopmental disorders (Bain et al., 2016; Pilch et al. 2018), implicating a crucial role of the hnRNP H protein family in neurodevelopment.

The purpose of the present study was three-fold. First, in order to expand beyond MA locomotor stimulant sensitivity, we examined the effect of the *Hnrnph1* mutation on oral MA reinforcement and intake via operant-conditioning and MA reward via conditioned place-preference (CPP). This mutation comprises a small, frameshift deletion in the first coding exon of *Hnrnph1* (H1 MUT) that causes reduced MA-induced locomotor activity (Yazdani et al., 2015). To gain insight into the neurobiological mechanisms underlying behavioral differences in MA sensitivity, we examined drug-induced extracellular DA level via *in vivo* microdialysis, DA content of striatal tissue, and DA clearance from striatal tissue. Second, because we previously implicated *Hnrnph1* polymorphisms in dopaminergic neuron development, we assessed the effect of H1 MUT on tyrosine hydroxylase (TH) levels in cell bodies and processes of the mesolimbic

pathway via immunoblotting and immunohistochemistry. Finally, to gain insight into neural dysfunction in H1 MUT mice at the protein level that could underlie behavioral and neurochemical deficits, we examined the synaptosomal proteome of the striatum between the H1 MUT and wild-type (WT) mice at baseline and in response to MA.

RESULTS

Characterization of Hnrnph1/2 and hnRNP H protein expression in H1 MUT mice

Hnrnph1 mutant mice (H1+/- or H1 MUT) were generated using TALENs targeting the first coding exon of Hnrnph1 (exon 4, UCSC Genome Browser). Deletion of a small region in the first coding (exon 4) in *Hnrnph1* leads to a premature stop codon and transcription of a truncated mRNA message. The mice were genotyped using a restriction enzyme based assay (**Figure 14A**; Yazdani et al., 2015). Gene expression via qPCR with primers specific for exons 6 – 7 (not targeting the deleted exon 4) detected a 50% increase of *Hnrnph1* transcript in the H1 MUT (heterozygous for deletion) relative to WT (Yazdani et al., 2015) and a 1.5-fold increase in the H1-/- (homozygous for deletion) (**Figure 14B**) with no change in gene expression of *Hnrnph2* (**Figure 14C**, Yazdani et al., 2015). At the protein level, there was no change in hnRNP H protein expression in H1 MUT or H1-/- embryonic stage brain tissue homogenate (**Figure 14D-G**). Because hnRNP H1 and H2 have 96% amino acid sequence homology, there is no commercially available antibody that can differentiate the two proteins. Quantitative analysis of protein peptide from an hnRNP H immunoprecipitation mass spectrometry study identified no difference in peptide level unique to hnRNP H1 between the H1 MUT mice compared to that of WT (**Figure 15A-B**). Because we previously detected a decrease in transcription of exon 4 in the H1 MUT mice (Yazdani et al. and **Figure 14B**), we hypothesized that there would be a decrease in the level of Peptide 3 (GLPWSCSADEVQR) which contains amino acid residues encoded by the deleted region in exon 4 of Hnrnph1. Indeed, there was a decrease in the level of Peptide 3 in H1 MUT mice, although this result did not reach statistical significance (**Figure 15A-**

B). No genotypic difference was observed in unique peptides associated with hnRNP H2 (**Figure 15C-D**).

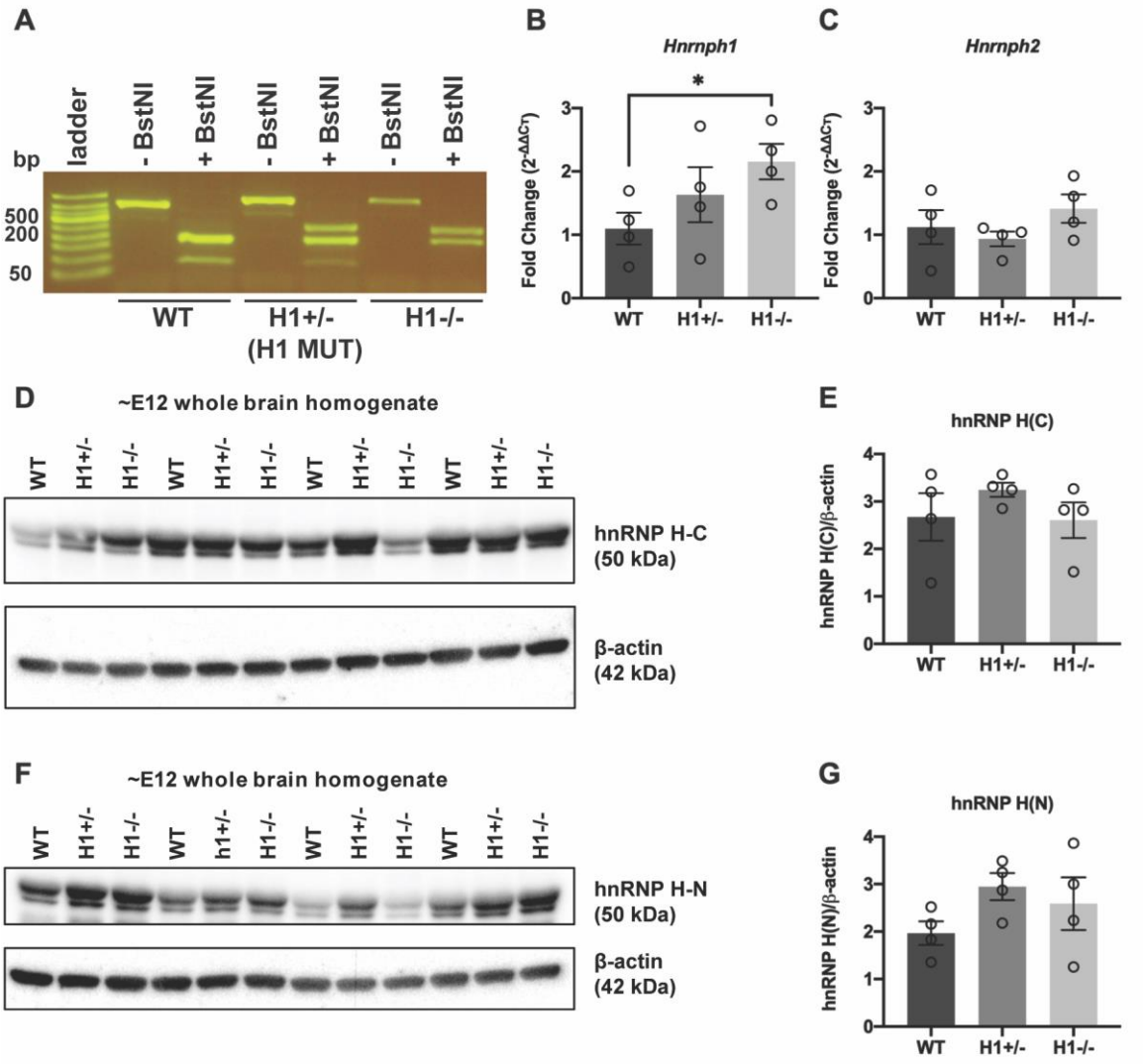

Figure 14. ***Hnrnph1*** **whole brain mRNA and hnRNP H whole body protein expression in WT, H1 MUT, and H1-/- mice. H1-/- mice and WT littermates were generated by intercrossing H1 MUT and H1 MUT.**

Embryos were harvested at E12 for genotyping using a restriction enzyme-based assay. (A): A PCR amplicon capturing the deleted region was digested with BstNI. WT mice had two copies of two BstNI restriction sites, and thus, restriction digest produced three fragments (58 bp, 157 bp, and 153 bp) corresponding to two bands on the gel. H1-/- mice had two copies of a single BstNI restriction sites, and thus, restriction digest produced two fragments (153 bp and 198 bp). H1 MUT mice possessed one copy of each of the two BstNI restriction sites and one copy of a single BstNI restriction site, and thus, restriction digest produced 5 fragments (58 bp, 153 bp, 153 bp, 157 bp, and 198 bp) corresponding to three bands on the gel. (B): There was a gene dosage-dependent

increase in the transcript level *Hnrnph1* in H1 MUT and H1-/- mice. The 1.5-increase in *Hnnph1* transcript level in H1 MUT mice replicated our previously observation (Yazdani et al. 2015). The > 2-fold increase in *Hnrnph1* transcript level in H1-/- with two copies of the mutation provides further functional support for increased expression of the mutant transcript (one-way ANOVA, $F(2,9) = 2.55$, $p = 0.133$; pairwise comparison between WT versus H1-/-: $t(6) = -2.82$, $^*p = 0.031$). (C): There was no genotypic difference in *Hnrnph2* transcript level. (D-G): Protein expression of hnRNP H in WT, H1 MUT, and H1-/- mice. There was no significant genotypic difference in hnRNP H protein expression using an antibody targeting the C-terminus of hnRNP H (D-E) or the N-terminus of hnRNP H (F-G) (one-way ANOVA, C-terminus: $F(2,9) = 0.89$, $p = 0.440$; N-terminus: $F(2,9) = 1.64$, $p = 0.250$). n = 4 per genotype.

A

	hnRNP H1 unique peptide sequence
1	MMLGAEGGEGFVVK
2	MLGAEGGEGFVVK
3	GL**PWSCS**ADEVQR
4	SNNVEMDWVLK
5	GAYGGGYGGYDDYNGYNDGYGFGSDR
6	YGDGGSTFQSTTGHCVHMR
7	VTGEADVEFATHEDAVAAMSK
8	YVELFLNSTAGASGGAYEHR

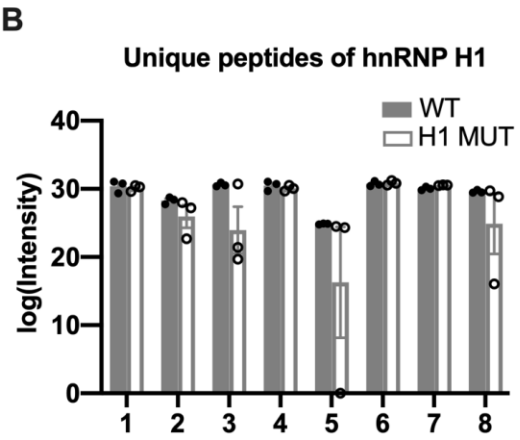

C

	hnRNP H2 unique peptide sequence
1	ATENDIYNFFSPLNPMR
2	GAYGGGYGGYDDYGGYNDGYGFGSDR
3	GLPWSCSAEEVMR
4	SNSVEMDWVLK
5	VTGEADVEFATHEDAVAAMAK
6	YGDGGSSFQSTTGHCVHMR

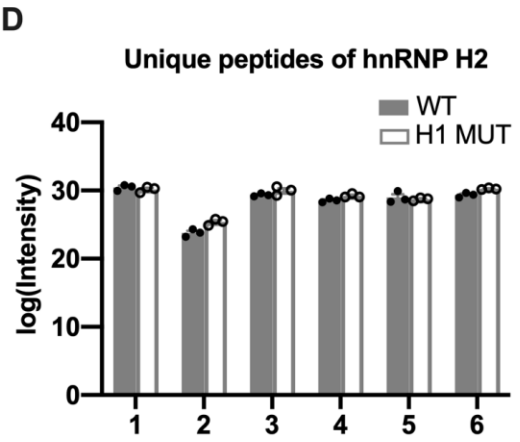

Figure 15. Quantification of hnRNP H1 and hnRNP H2 protein peptide sequences from mass spec of hnRNP H immunoprecipitates from H1 MUT and WT striatum.
A separate cohort of mice were used for this study. Co-immunoprecipitation was used to pull down hnRNP H and associated proteins. Using the "Similarity" function in the Scaffold software, peptides exclusive to hnRNP H1 or hnRNP H2 were identified and quantified. (A): A list is shown for the peptides that are unique to hnRNP H1. (B): Quantification of peptides unique to hnRNP H1. There was a trend for a decrease in peptide GLPWSCSADEVQR in the striatum of H1 MUT versus

WT mice (unpaired t-test for each individual peptide, Peptide 1: t(4) = -0.45, p = 0.673; Peptide 2: t(4) = -1.39, p = 0.236; Peptide 3: t(4) = -1.94, p = 0.125; Peptide 4: t(4) = -0.85, p = 0.445; Peptide 5: t(4) = -1.06, p = 0.351; Peptide 6: t(4) = 0.46, p = 0.672, Peptide 7: t(4) = 2.21, p = 0.091, Peptide 8: t(4) = -1.07, p = 0.346;). Amino acids PWSCS within this peptide are encoded by the deleted region (GCCCTGGTCCTGCTCC) in exon 4 of *Hnrnph1* in the H1 MUT mice. (C): Table outlining the peptides that are unique to hnRNP H2. (D): Quantification of hnRNP H2 unique peptides. No significant change in unique peptides of hnRNP H2 was observed between WT and H1 MUT mice (unpaired t-test for each individual peptide, Peptide 1: t(4) = -0.83, p = 0.454; Peptide 2: t(4) = 0.86, p = 0.441; Peptide 3: t(4) = 1.56, p = 0.197; Peptide 4: t(4) = 0.95, p = 0.396; Peptide 5: t(4) = -0.516, p = 0.633; Peptide 6: t(4) = -0.07, p = 0.950)

Oral MA self-administration

We previously demonstrated a robust reduction in sensitivity to the locomotor stimulant response to MA in H1 MUT mice (Yazdani et al., 2015). To more directly test MA-induced motivated behaviors, we investigated MA reinforcement and intake in H1 MUT mice using an oral MA self-administration paradigm as conducted previously in C57BL/6J mice (Szumlinski et al., 2017). This study showed that mice allocated the majority of their nose-poking behavior toward the MA-reinforced hole, indicating drug reinforcement. H1 MUT mice presented fewer active nose-pokes at the 160, 200, 300 and 400 mg/L MA doses compared to WT mice (**Figure 16A**), with no difference in non-specific, inactive nose-pokes across a range of MA concentrations (80-400 mg/L) (**Figure 16B**). Consistent with their lower level of MA reinforcement, H1 MUT mice also consumed less MA (intake; mg/kg/day) at the 200, 300 and 400 mg/L concentrations (**Figure 16C)**. No interactions between Sex and Genotype were observed for any measure during self-administration testing. The genotypic differences in high-dose MA intake did not relate to bitter taste sensitivity as quinine intake in the home cage was equivalent between H1 MUT and WT mice (data not shown; refer to Ruan et al., 2020a).

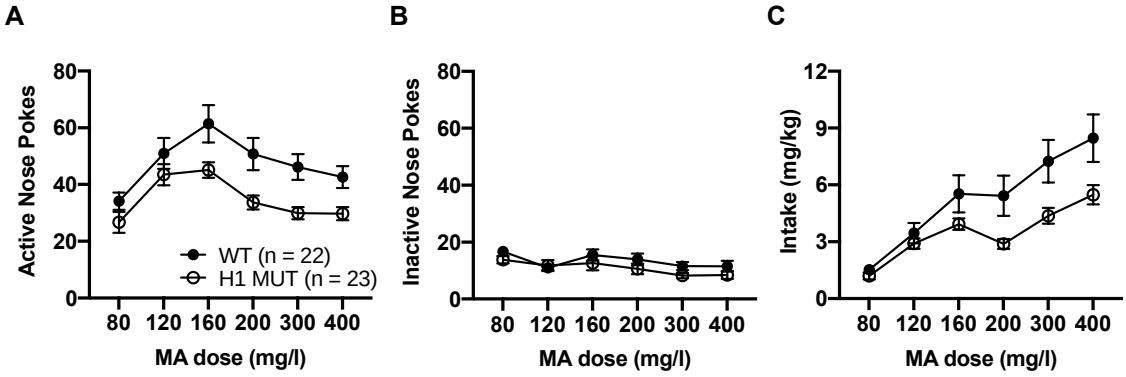

Figure 16. Oral MA self-administration in H1 MUT mice.
H1 MUT mice were less sensitive than WT to the reinforcing effect of MA. H1 MUT and WT mice were provided access to 80, 120, 160, 200, 300 and 400 mg/L of MA for a time period of five days per dose. (A): The average total active nose-pokes emitted during five, 1 h, sessions varied as a function of MA Dose with H1 MUT showing less active nose pokes at MA doses 160, 200, 300, and 400 mg/l (mixed effects ANOVA, $F(1,41)_{Genotype} = 6.33$, $p = 0.02$; $F(5,205)_{Dose} = 23.93$, $p < 0.0001$; $F(5,205)_{Genotype \times Dose} = 1.58$, $p = 0.166$; unpaired t-tests for 80 and 120 mg/L, p's > 0.65; for 160-400 mg/L, p's < 0.03; unpaired t-test at each dose for WT versus H1 MUT: for 160-400 mg/L, *p's < 0.03). (B): The average total inactive nose-pokes emitted during the five, 1 h, sessions varied as a function of MA Dose with no genotypic difference between H1 MUT and WT (mixed effects ANOVA, $F(1,41)_{Genotype} = 0.76$, $p = 0.39$; $F(5,205)_{Dose} = 5.84$, $p < 0.0001$; $F(5,205)_{Genotype \times Dose} = 1.27$, $p = 0.28$). (C): H1 MUT mice consuming less MA than WT mice at 200, 300, and 400mg/l doses of MA (mixed effects ANOVA, $F(1,41)_{Genotype} = 6.85$, $p = 0.01$; $F(5,205)_{Dose} = 52.11$, $p < 0.0001$; $F(5,205)_{Genotype \times Dose} = 4.47$, $p < 0.0001$; unpaired t-tests for 80 -160 mg/L, p's > 0.12; for 200 - 400 mg/L, *p's < 0.03). n = 23 (10 females, 13 males) for H1 MUT and n = 22 (9 females, 13 males) for WT.

The blunted escalation of oral MA intake observed at high MA concentrations (≥ 200 mg/L) in H1 MUT mice initially trained to respond for 80 mg/L MA prompted us to determine if the *Hnrnph1* mutation would blunt the acquisition of oral MA self-administration when 200 mg/L MA served as the reinforcer. However, we were unable to detect any genotypic difference in MA intake and active nose-pokes when mice were trained at this higher MA concentration (data not shown; refer to Ruan et al., 2020a). These results indicate that the *Hnrnph1* mutation interferes with the transition from low to high-

dose MA self-administration, without altering the reinforcing effects of MA during acquisition.

MA-conditioned reward

To further investigate why H1 MUT mice showed less oral self-administration of MA, we assessed MA reward via CPP. When mice were tested in a MA-free state (Day 8), the genotypic difference in the time spent in the MA-paired side between Day 8 and varied with MA doses (**Figure 17A**). H1 MUT mice showed lower CPP to 0.5 mg/kg MA but higher CPP to 2 mg/kg MA compared to the WT mice (**Figure 17A**;). Similar non-significant effects were observed during drug state-dependent CPP whereby H1 MUT mice exhibited lower and higher CPP at 0.5 mg/kg and 2 mg/kg MA doses, respectively (**Figure 17B**). No sex differences or interactions were observed for any measure during MA-CPP testing. The dose-dependent difference in CPP indicates that H1 MUT showed a reduced sensitivity to the rewarding effect of low-dose MA and that a higher MA dose was required to elicit CPP in H1 MUT mice.

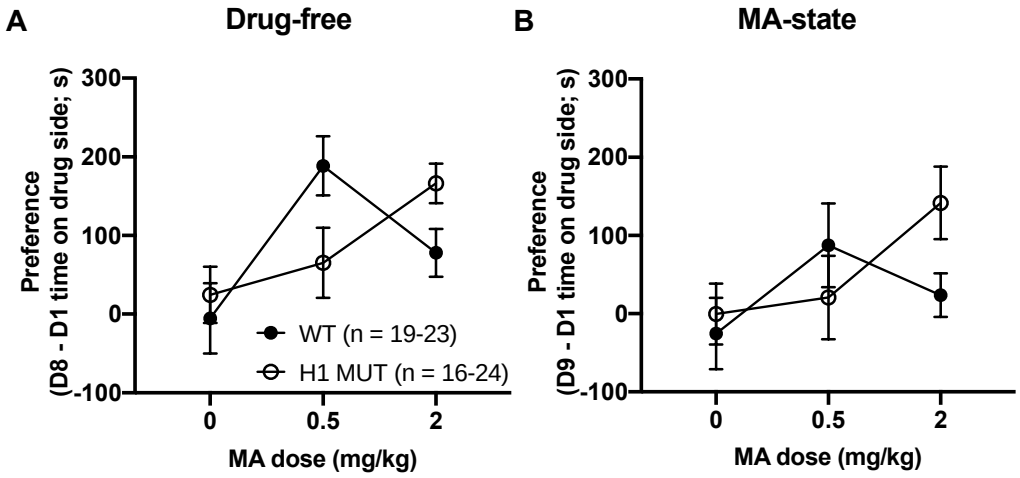

Figure 17. MA-induced CPP in H1 MUT mice.
H1 MUT mice were less sensitive than WT to the rewarding effect of MA. **(A):** Genotypic differences in the time spent in the MA-paired side between Day 8 and 1 (preference, s) were observed at 0.5 mg/kg and 2 mg/kg MA doses. H1 MUT mice showed lower preference at 0.5 mg/kg and higher preference at 2 mg/kg in comparison to WT (two-way ANOVA, $F(2,121)_{interaction} = 3.92$; $p = 0.023$; $F(1,121)_{Genotype} = 0.07$, $p = 0.788$; $F(2,121)_{Dose} = 6.15$, $p = 0.003$; unpaired t-test; 0.5 mg/kg: $t(45) = -2.13$, $p = 0.039$; 2 mg/kg: $t(45) = 2.18$, $p = 0.036$). **(B):** In examining state-dependent CPP following a challenge dose of MA that was the same dose administered during training, a similar pattern of results (although no significant) was observed with H1 MUT showing lower and higher preference at 0.5 and 2 mg/kg, respectively, compared to WT wo-way ANOVA, $F(2,121)_{interaction} = 1.86$; $p = 0.160$; $F(1,121)_{Genotype} = 0.23$, $p = 0.634$; $F(2,121)_{Dose} = 2.08$, $p = 0.129$. n = 24 (16 females, 8 males), 22 (14 females, 8 males) and 16 (9 female, 7 males) at 0, 0.5 and 2 mg/kg MA for H1 MUT; n = 23 (9 female, 14 males), 23 (12 female, 11 males) and 19 (7 female, 12 males) at 0, 0.5 and 2 mg/kg MA for WT.

We also identified significant genotypic differences in MA-induced locomotor activity in the confined one-half of the CPP box during CPP training on Days 3 and 5 (data not shown; refer to Ruan et al., 2020a). H1 MUT mice traveled less distance at 60 min post-2 mg/kg MA injection on Day 3 and 5 (data not shown; refer to Ruan et al., 2020a). During state-dependent CPP (following the two previous MA exposures) on Day 9 when mice had twice as much open access space, we observed a decrease in MA-induced locomotor activity in H1 MUT mice (data not shown; refer to Ruan et al., 2020a). This result was similar to the previously published results in the same-sized open arena minus

the CPP divider and floor textures in response to a single, acute MA dose of 2 mg/kg (Yazdani et al., 2015). Furthermore, note that we later demonstrate replication of reduced MA-induced locomotor activity in H1 MUT mice using the same three-day protocol from the original publication (Yazdani et al., 2015) prior to tissue harvesting for mass spectrometry analysis (see **Figure 24** and later description of the results). There was no genotypic difference in the striatal level of either MA or its metabolite amphetamine at 30 min i.p. post injection of MA (**Figure 18**). Thus, differences in transport or metabolism of MA are unlikely to explain the decrease in MA-induced behavior in H1 MUT mice at 30 min post-MA.

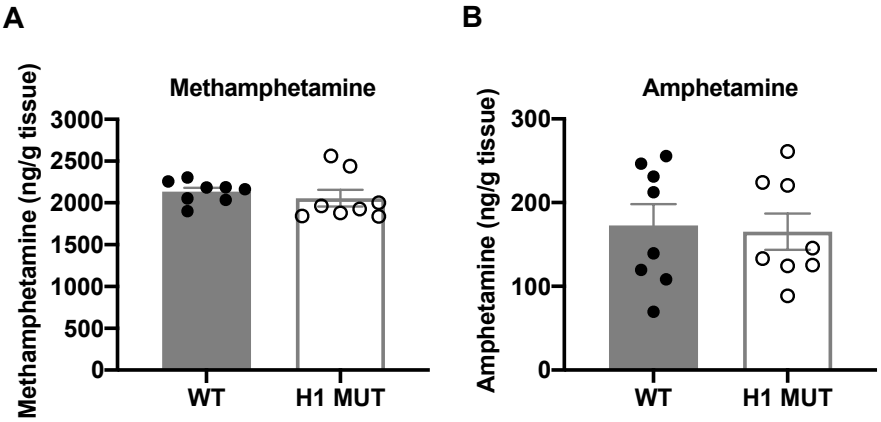

Figure 18. Concentration of MA and amphetamine in the striatum at 30 min post-MA injection in H1 MUT mice.
On Days 1 and 2, mice were injected (i.p.) with saline and placed into apparatus for 1 h. On Day 3, mice were injected (i.p.) with 2 mg/kg MA and placed into apparatus for 30 min followed by subsequent removal of the striatum. **(A):** No genotypic difference was detected in the striatal concentration of MA. **(B):** Also, no genotypic difference was detected in the striatal concentration of amphetamine. Unpaired t-test, $t(14) = -0.72, -0.22$, $p = 0.480, 0.826$ for MA and amphetamine respectively; WT: $n = 8$ and H1 MUT: $n = 8$.

MA-induced extracellular DA in NAc of H1 MUT mice

Because H1 MUT mice showed reduced MA self-administration and reward, we next examined basal extracellular DA and MA-elicited extracellular DA using *in vivo* microdialysis in the NAc, a brain region and neurochemical event that are necessary for MA reinforcement and reward (Prus et al., 2009; Keleta and Martinez, 2012; Bernheim et al., 2016). Linear regression analysis of no net-flux *in vivo* microdialysis in the NAc indicated no significant change in either DA release/reuptake (data not shown; refer to Ruan et al., 2020a) or basal extracellular DA content or (data not shown; refer to Ruan et al., 2020a). Following administration of 0.5 mg/kg MA (i.p.), WT mice exhibited an increase in extracellular DA whereas H1 MUT mice showed a decrease in extracellular DA below baseline (**Figure 19A**). Administration of 2 mg/kg MA (i.p.) induced an increase in DA within the NAc of both genotypes but H1 MUT mice again showed markedly lower MA-induced extracellular DA levels, in particular from 100 to 180 min post-MA (**Figure 19B**). Consistent with the genotypic differences in extracellular DA levels, for both the 0.5 and 2 mg/kg MA doses, H1 MUT mice also showed a lower level of 3,4-Dihydroxyphenylacetic acid (DOPAC, metabolite of DA) compared to WT mice (**Figure 19C-D**).

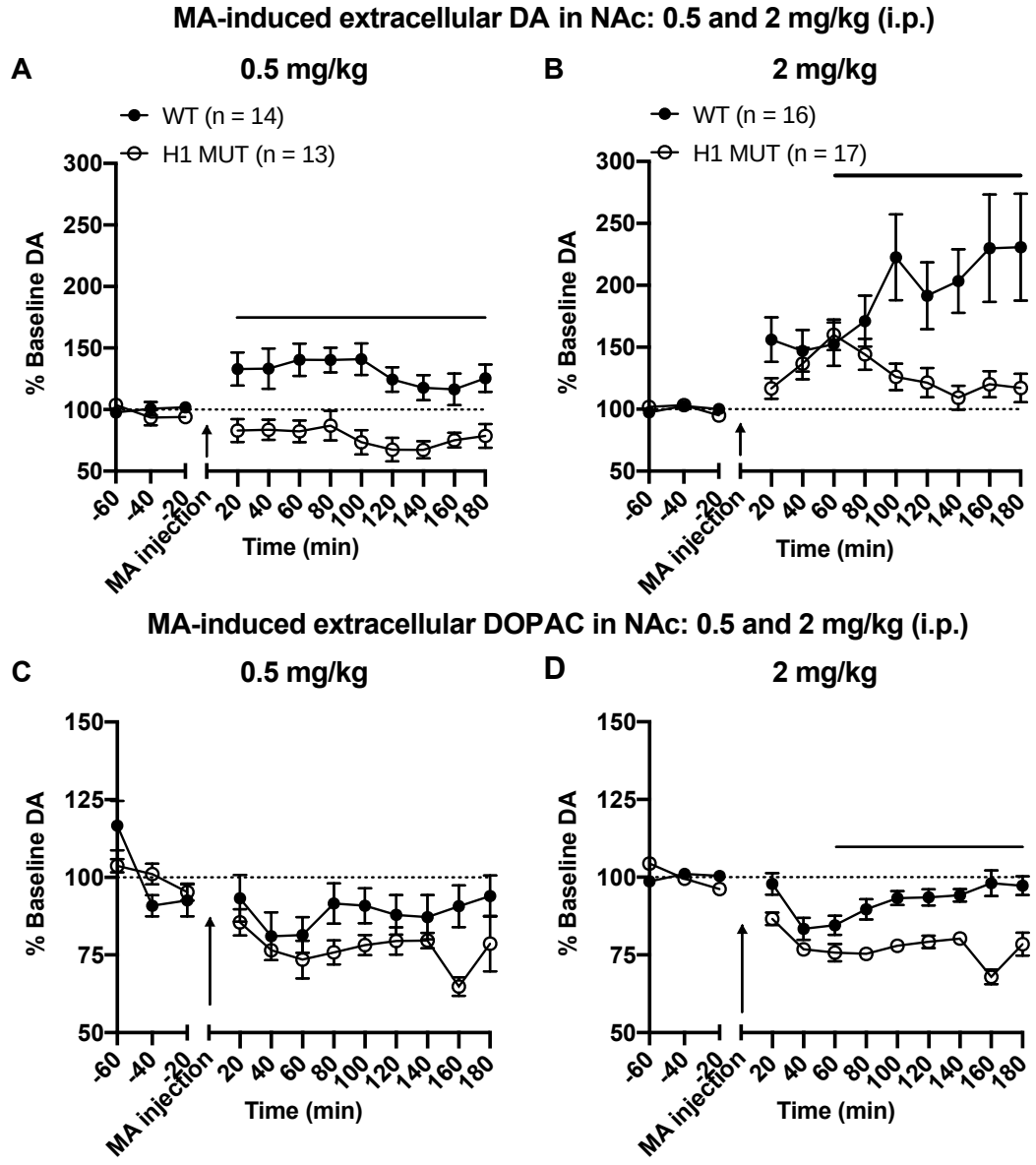

Figure 19. *In vivo* microdialysis of MA-induced extracellular DA in NAc of H1 MUT mice. H1 MUT mice showed blunted MA-induced DA and DOPAC levels compared to WT. Mice were probed on the contralateral side, perfused with artificial cerebrospinal fluid (aCSF), and administered a MA challenge of either 0.5 mg/kg or 2 mg/kg (i.p., black arrow) after a 1 h baseline period. **(A-B):** The capacity of MA to elevate DA in the NAc was blunted in the H1 MUT mice, in a manner that varied with the dose of MA administered. **(A):** The 0.5 mg/kg MA dose elicited an increase in extracellular DA in in WT but not in H1 MUT mice, with H1 MUT mice exhibiting significantly lower extracellular DA levels than WT mice at all time-points post-injection (mixed effects ANOVA, $F(1,25)_{Genotype} = 18.57$, $p < 0.0001$; $F(11,275)_{Time} = 1.63$, $p = 0.09$; $F(11,275)_{Genotype \times Time} = 4,71$, $p < 0.0001$; unpaired t-tests for time = -60 to 0 min, $t(25) < 0.60$, p's > 0.60; for time = 20 to 180 min, $t(25) > 2.25$, *p's < 0.033). **(B):** The 2 mg/kg MA dose elicited an increase in extracellular DA in both genotypes; however, the temporal patterning and the magnitude of this

rise was distinct between H1 MUT and WT mice. H1 MUT mice exhibited lower DA levels compared to WT mice during the first 20 min post-injection, as well as during the second half of testing (mixed effects ANOVA, $F(1,31)_{Genotype} = 6.41$, $p = 0.02$; $F(11,341)_{Time} = 8.29$, $p < 0.0001$; $F(11,341)_{Genotype\ X\ Time} = 5.58$, $p < 0.0001$; unpaired t-tests, for time -60 to 0 and 40 min, $t(31) < 1.5$, p's > 0.15; for time 20, 60-180 min, $t(31) > 2.0$, * p's < 0.05). **(C-D):** MA dose-dependently reduced NAc extracellular DOPAC levels; however, irrespective of MA Dose or Sex, this reduction was, overall, greater in H1 MUT versus WT mice. **(C):** 0.5 mg/kg MA induced a lowering of extracellular DOPAC, relative to baseline levels, with H1 MUT mice exhibiting significantly lower DOPAC 80 min post-injection (mixed effects ANOVA, $F(1,28)_{Genotype} = 1.50$, $p = 0.23$; $F(11,308)_{Time} = 13.33$, $p < 0.0001$; $F(11,308)_{Genotype\ X\ Time} = 2.76$, $p = 0.002$; unpaired t-tests, for all times but 160 min, $t(28) < 1.90$, p's > 0.08; for time = 160 min, $t(28) = 2.37$, * $p = 0.03$). **(D):** 2 mg/kg MA induced a lowering of extracellular DOPAC in both genotypes; however, the effect was amplified in H1 MUT mice. Relative to WT animals, H1 MUT mice exhibited lower DA levels during the first 20 min post-injection, as well as during the second half of testing (mixed effects ANOVA, $F(1,25)_{Genotype} = 24.09$, $p < 0.0001$; $F(11,275)_{Time} = 29.04$, $p<0.0001$; $F(11,275)_{Genotype\ X\ Time} = 10.42$, $p < 0.0001$; unpaired t-tests, for time -60 to 0 and 40 min, $t(25) < 1.6$, p's > 0.10; for time 20, 60-180 min, $t(25) > 2.0$, *p's < 0.05). n=13 (7 females, 6 males) at 0.5 and n=17 (10 females, 7 males) at 2.0 mg/kg MA for H1 MUT; n=14 (8 females, 6 males) at 0.5 mg/kg MA and 17 (10 females, 7 males) at 2 mg/kg MA for WT.

In examining glutamate levels, no net flux microdialysis study revealed no difference in basal extracellular level of glutamate (data not shown; refer to Ruan et al., 2020a). Acute administration of 0.5 mg/kg or 2 mg/kg MA did not induce much effect on extracellular glutamate levels, nor was there any genotypic differences in glutamate levels (data not shown; refer to Ruan et al., 2020a). To summarize, H1 MUT mice showed a significantly blunted MA-induced DA release in the NAc in the absence of any significant difference in baseline DA levels and in the absence of any significant differences in glutamate neurotransmission. No sex differences or interactions were observed. These results point toward a MA-induced deficit in DA release as a plausible functional mechanism underlying the deficit in the MA-induced behavioral responses in H1 MUT mice.

To further investigate the possible causes of the decreased capacity of MA to increase extracellular DA in H1 MUT mice, we quantified basal striatal tissue levels of biogenic amines in drug-naïve H1 MUT and WT mice. No genotypic difference was detected in the amount of DA and DOPAC (**Figure 20A**), or in the levels of other biogenic amines, including HVA, 3-MT, 5-HT, etc. (**Figure 20A**). We also tested whether H1 MUT impacts the function of DAT by examining DAT-mediated DA uptake in synaptosomes prepared from whole striatal tissue. However, no difference in basal DAT function was detected (**Figure 20B**). In addition, there was no change in the protein level of DAT in the total striatal brain lysate in H1 MUT compared to WT mice (**Figure 20C-D**). An increase in DAT protein level was detected in the female mice (**Figure 20C-D**). There was also no effect of MA on DAT protein level in the synaptosome of either H1 MUT or WT mice (**Figure 20E-F**).

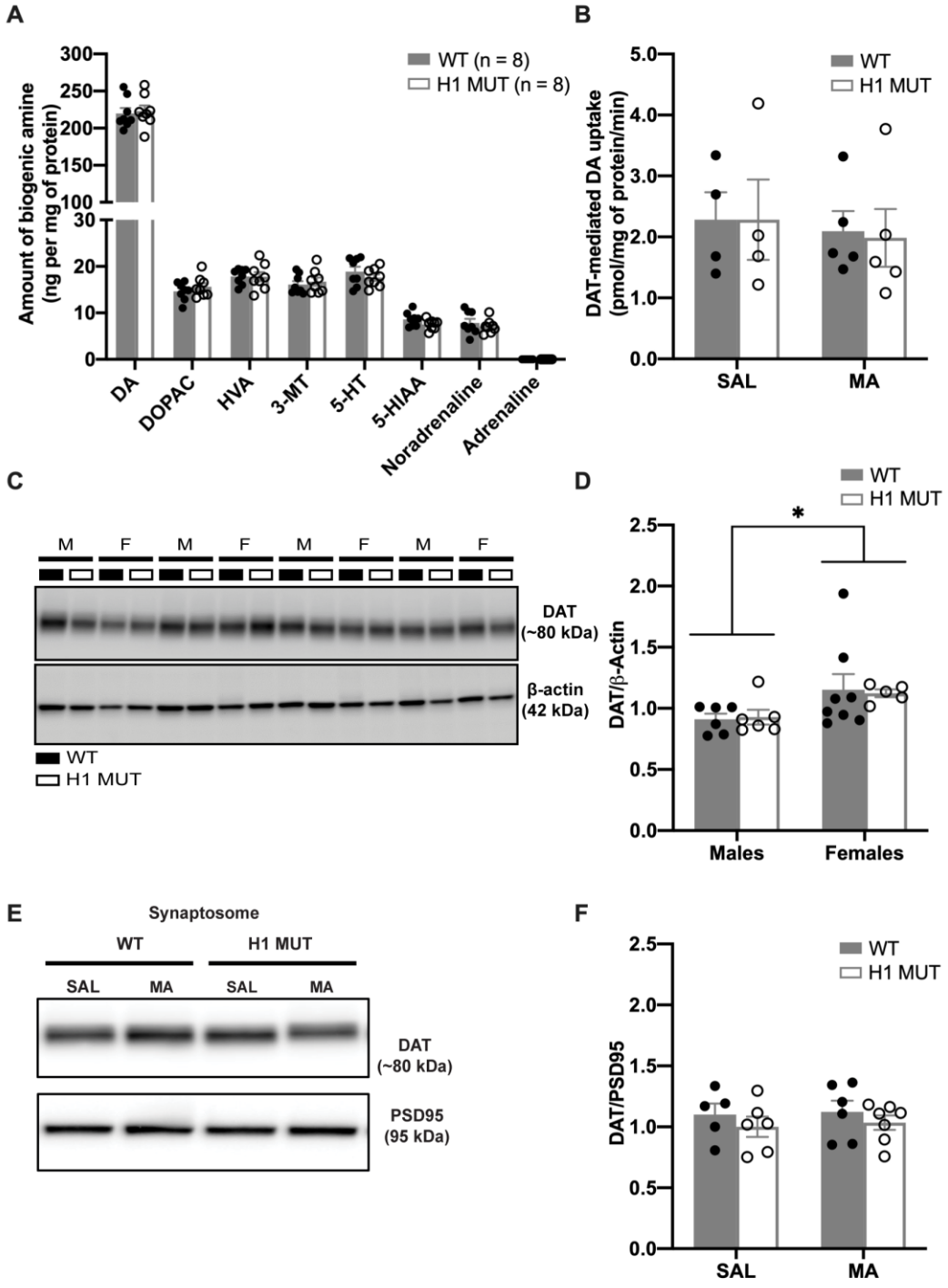

Figure 20. DA content and uptake and DAT levels in the striatum of H1 MUT mice.
No changes in DA or in DAT were detected at baseline in the striatum of H1 MUT mice compared to WT mice. **(A)** Measurement of biogenic amine content in the striatum showed no difference in the level of DA between H1 MUT and WT mice. H1 MUT also exhibited no change in the levels

of other biogenic amines unpaired t-test, DA: t(14) = -0.30, p = 0.766; DOPAC: t(14) = -0.93, p = 0.372). n = 8 per genotype. **(B)** DAT-mediated DA uptake in the striatum of H1 MUT mice. Striatum was harvested at 2 h post-saline or MA injection for DA uptake assay, based on the time course of the microdialysis data. There was no genotypic difference in the rate of DA uptake in response to saline (SAL) or MA (two-way ANOVA, $F(1,14)_{interaction} = 0.01$, p = 0.911; $F(1,14)_{Genotype} = 0.02$, p = 0.903; $F(1,14)_{Treatment} = 0.26$, p = 0.619). n = 4 per group. **(C-D):** Immunoblot for DAT level in the striatum. Representative immunoblot for DAT shown in **(C)** with quantification shown in **(D)**. There was no change in DAT protein level in the striatum of H1 MUT relative to WT mice (unpaired t-test, t(23) = 0.32, p = 0.750). WT: n = 14 and H1 MUT: n = 11. There was a main effect of Sex that was explained by females showing a higher level of DAT compared to that of male mice (two-way ANOVA, $F(1,21)_{Sex} = 5.74$, p = 0.026, $F(1,21)_{Genotype} = 0.12$, p = 0.730; $F(1,21)_{interaction} = 0.07$, p = 0.800; unpaired t-test, females versus males t(23) = 2.53, *p = 0.019.) Females: n = 13 and Males: n = 12. **(E):** Immunoblot showing DAT protein level the striatal synaptosome at 30-min post saline (SAL) or MA treatment. **(F):** The striatal synaptosome of H1 MUT mice did not show any change in DAT relative to WT mice after SAL or MA treatment (two-way ANOVA, $F(1,20)_{Genotype} = 0.031$, p = 0.86; $F(1,20)_{Treatment} = 0.037$, p = 0.85; $F(1,20)_{interaction} = 1.24$, p = 0.28). WT SAL: n = 5, WT MA: n = 6, H1 MUT SAL: n = 6, and H1 MUT MA: n = 7.

TH expression in the mesolimbic and nigrostriatal brain regions of H1 MUT mice

In our previous transcriptome analysis of congenic mice that captured *Hnrnph1* polymorphisms and decreased MA behavioral sensitivity, we identified a decrease in expression of *Nurr1* (*Nr4a2*), a transcription factor critical for dopaminergic neuron development (Yazdani et al., 2015). Thus, we hypothesized that dysfunctional mesolimbic and nigrostriatal DA pathways at the neuroanatomical level could underlie decreased MA-induced behaviors and DA release in H1 MUT mice. We tested this hypothesis by examining changes in the number of neurons and the number of projections from neurons in the dopaminergic mesolimbic and nigrostriatal pathways, which mediate reward and motor activity, respectively (Adinoff 2004). Diagrams outlining the different brain regions assessed are presented in **Figure A4**. We first examined co-expression of hnRNP H (there are currently no commercially available antibodies for differentiating between hnRNP H1 and hnRNP H2) and tyrosine hydroxylase (TH; the rate-limiting enzyme for the synthesis

of DA; Daubner et al., 2011). Results showed that hnRNP H and TH were co-expressed in the same midbrain TH neurons of the ventral tegmental area (VTA) and substantia nigra pars compacta (SNc) at a similar level in both genotypes (**Figure 21A**). hnRNP H immunostaining was primarily nuclear whereas TH immunostaining was cytoplasmic. We next examined expression of TH in the dopaminergic neurons of the mesolimbic and nigrostriatal circuit (**Figures 21 and 22)**. TH DAB immunohistostaining in the VTA and SNc of the midbrain (**Figure 21B**) indicated no significant genotypic differences in TH optical density (OD) (**Figure 21C)**. There was also no genotypic difference in the number (**Figure 21D**) or diameter (**Figure 21E**) of TH-positive neuron of the VTA and SNc. Immunoblot analysis indicated no significant difference in TH protein level in the midbrain (**Figures 21F-G**).

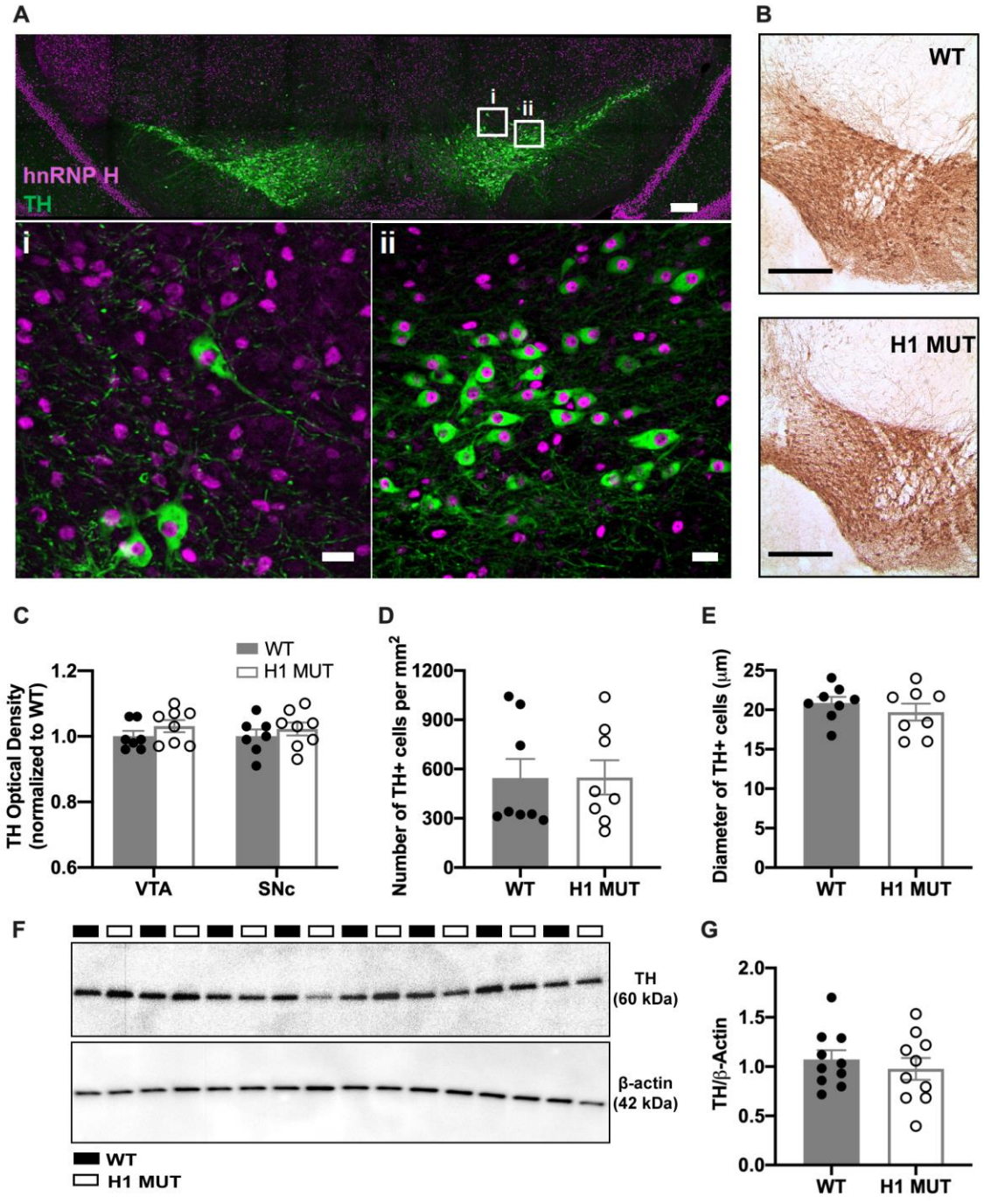
A
hnRNP H
TH
i
ii
B
WT
H1 MUT
C
WT
H1 MUT
TH Optical Density (normalized to WT)
1.2
1.0
0.8
0.6
VTA
SNc
D
Number of TH+ cells per mm2
1200
900
600
300
0
WT
H1 MUT
E
Diameter of TH+ cells (μm)
25
20
15
10
5
0
WT
H1 MUT
F
TH (60 kDa)
β-actin (42 kDa)
WT
H1 MUT
G
TH/β-Actin
2.0
1.5
1.0
0.5
0.0
WT
H1 MUT

Figure 21. TH levels in the midbrain of H1 MUT mice.
No difference in TH level was detected in the VTA between H1 MUT and WT mice. **(A):** Immunofluorescent staining of hnRNP H (*magenta*) and TH (*green*) was conducted in coronal midbrain sections (Bregma: -3.28 mm to -3.64 mm) containing the VTA dopaminergic neurons in adult H1 MUT and WT mice. Higher magnification images in panels (***i***) and (***ii***) demonstrate nuclear expression of hnRNP H across all TH-positive dopaminergic neurons that we examined. Scale bars represent 200 μM (*top*) and 20 μM (*bottom)*. **(B):** Representative image showing immunohistochemical DAB staining of TH in coronal sections of the midbrain region (Bregma: -3.28 mm to -3.64 mm). Scale bars represent 1 mm. **(C-E):** Immunohistochemical DAB staining of TH in the midbrain regions revealed no genotypic difference between the H1 MUT and WT mice in **(C)** TH optical density (unpaired t-test, VTA: $t(13) = -1.29$, $p = 0.220$; SNc: $t(13) = -0.75$, $p = 0.466$; WT: n = 7 and H1 MUT: n = 8), in **(D)** number of TH-positive cells (unpaired t-test, $t(14) = 0.02$, $t = 0.985$; n = 8 per genotype), or in **(E)** the diameter of TH-positive cells ($t(14) = 0.88$, $p = 0.395$; n = 8 per genotype). **(F-G):** Immunoblot for TH protein level in the midbrain. Representative immunoblot for TH shown **(F)** and quantification **(G)**. There was no change in TH protein level in the midbrain region of H1 MUT relative to WT mice (unpaired t-test, $t(18) = 0.67$, $p = 0.510$; n = 10 per genotype).

TH DAB immunostaining in the striatum indicated no change in TH OD in the dorsal striatum between H1 MUT and WT mice (**Figures 22A-C**). However, a small, but statistically significant increase in TH OD was observed in the ventral striatum (which includes the NAc) of the H1 MUT mice (**Figures 22D-F**). To measure TH-positive puncta as an indirect estimate of the number of DA terminals in the striatum, we performed stereology under higher magnification (**Figure A5A**) and detected no difference in the number of TH-positive puncta between the H1 MUT and WT mice in the dorsal striatum or in the ventral striatum (**Figure A5B**). Immunoblot analysis indicated no significant difference in TH protein level in the whole striatum (**Figures 22G-H**). Taken together, analysis of the dopaminergic mesolimbic and nigrostriatal DA circuit did not provide strong evidence for changes in the expression of TH within cell bodies or terminals or changes in the number of TH-positive terminals that could explain behavioral differences in H1 MUT mice.

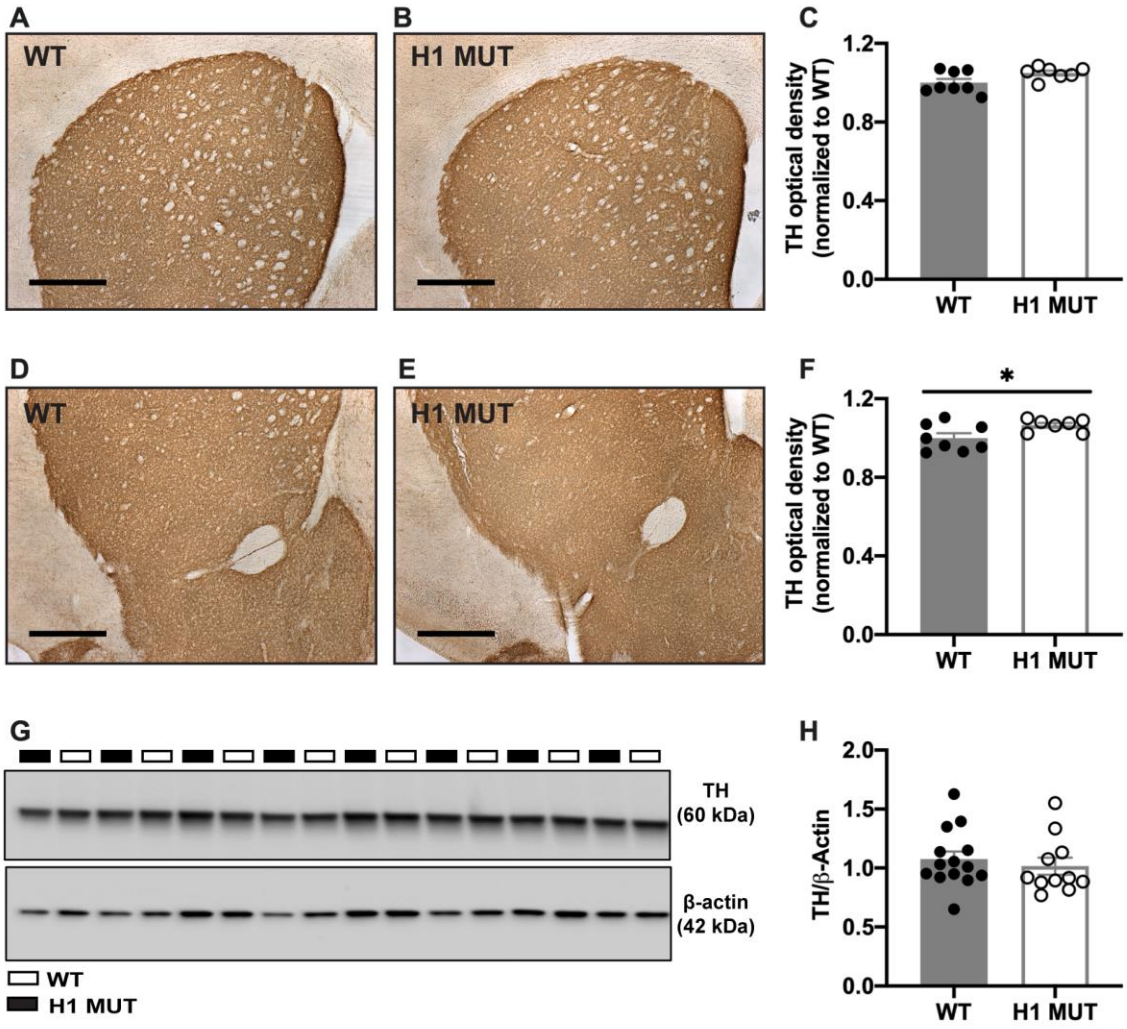

Figure 22. TH levels in striatum of H1 MUT mice.
No difference in TH level was detected in the striatum between the H1 MUT versus WT mice. **(A-F):** Representative images showing immunohistochemical DAB staining on coronal sections of striatum (Bregma: 1.18 mm to 0.86 mm). **A-C:** dorsal striatum. **D-F:** ventral striatum which includes NAc. Scale bars represent 1 mm. Optical density (OD) analysis revealed a nonsignificant increase in TH OD in the dorsal striatum (unpaired t-test, $t(13) = 2.07$, $p = 0.10$) and a small but significant increase in TH intensity in the ventral striatum (unpaired t-test, $t(13) = 2.30$, $^*p = 0.040$) of H1 MUT compared to WT mice. WT: n = 8 and H1 MUT: n = 7. **(G-H):** Immunoblot for TH protein level in the striatum. Representative immunoblot for TH shown in **(G)** with quantification shown in **(H)**. There was no change in TH protein expression in the striatum of H1 MUT compared to WT mice (unpaired t-test, $t(23) = 0.62$, $P = 0.540$). WT: n = 14 and H1 MUT: n = 11.

An important message gleaned from the above results is that the behavioral and neurochemical deficits exhibited by H1 MUT mice appear to manifest only under the influence of MA. In further support of this notion, a screen of WT and H1 MUT mice in a behavioral test battery (data not shown; refer to Ruan et al., 2020a) did not detect any genotypic differences in sensorimotor-gating, anxiety-like behaviors, depressive-like behaviors, or in sensorimotor coordination. The null results from this behavioral battery, combined with the lack of genotypic differences in saline-induced locomotion/response to a novel environment, and in various indices of basal DA transmission in the striatum argue for an active, MA-induced cell biological mechanism linking *Hnrnph1* dysfunction to MA behavior.

MA-induced changes in total and synaptic level of hnRNP H

The above neuroanatomical studies failed to support a neuroanatomical hypothesis of reduced neurodevelopment of DA projection pathways that could underlie reduced MA-induced DA release and behavior in H1 MUT mice. Thus, to further explore the possibility of a synaptic, MA-induced cell biological mechanism that could underlie H1 MUT behavior, we next examined changes in the synaptic localization of hnRNP H which is potentially relevant for understanding how H1 MUT could alter MA-induced DA release. Surprisingly, we identified a two-fold *increase* in hnRNP H protein level in the striatal synaptosome of H1 MUT mice, regardless of treatment (**Figures 23A-B**). In contrast, there was no significant genotypic difference in hnRNP H protein level in bulk striatal tissue in response to saline or MA (**Figures 23C-D**), indicating a change in localization rather than total hnRNP H protein in H1 MUT mice.

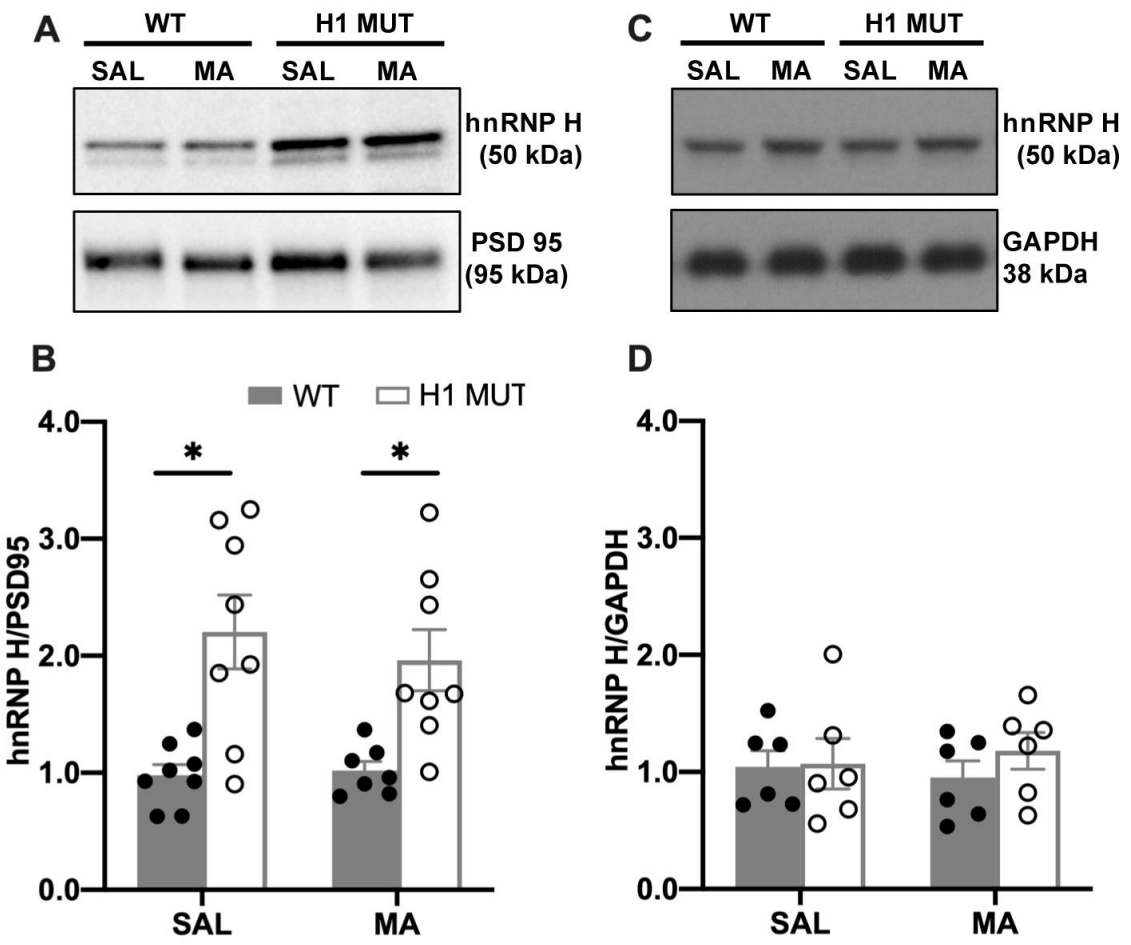

Figure 23. MA-induced changes in hnRNP H protein expression in striatal tissue and striatal synaptosomes of H1 MUT mice.

An increase in hnRNP H protein level was detected in the striatal synaptosome of H1 MUT versus WT mice but no change in hnRNP H protein from total striatal tissue. **(A-B):** Representative immunoblot for hnRNP H protein level in the striatal synaptosome at 30min post-saline (SAL) or post-MA treatment **(A)** and quantification **(B)**. A genotypic difference in hnRNP H protein level was detected in the striatal synaptosome of H1 MUT and WT mice. Collapsing across Treatment, an increase in hnRNP H protein was noted in the striatal synaptosome of H1 MUT versus WT mice regardless of Treatment (two-way ANOVA, $F(1,27)_{Genotype} = 24.36$, $p = 3.63E\text{-}5$; $F(1,27)_{Treatment} = 0.23$, $p = 0.636$; $F(1,27)_{interaction} = 0.41$, $p = 0.528$; WT ($n = 15$) versus H1 MUT ($n = 16$): unpaired t-test, $t(29) = -5.51$, $^*p = 2.176E\text{-}5$). This finding was subsequently validated in multiple replications. **(C-D):** Representative immunoblot for *total* hnRNP H protein level in the striatum at 30-min post-SAL or post-MA **(C)** and quantification **(D).** There was no change in total striatal level of hnRNP H relative to WT mice after SAL or MA treatment (two-way ANOVA, $F(1,20)_{Genotype} = 0.60$, $p = 0.450$; $F(1,20)_{Treatment} = 0.01$, $p = 0.952$; $F(1,27)_{interaction} = 0.37$, $p = 0.548$). $n = 6$ per group.

To identify changes in the levels of other synaptic proteins that could mechanistically link the robust increase in synaptic hnRNP H with decreased MA-induced DA release and behavior, we examined genotypic differences in the synaptosomal proteome in the striatum of H1 MUT and WT mice treated with MA versus saline using LC-MS/MS. At the behavioral level, H1 MUT showed reduced MA-induced locomotor activity only in response to MA on Day 3 (**Figure 24C**). In contrast, no difference in locomotor activity was detected between WT and H1 MUT in response to saline (**Figures 24A-B**).

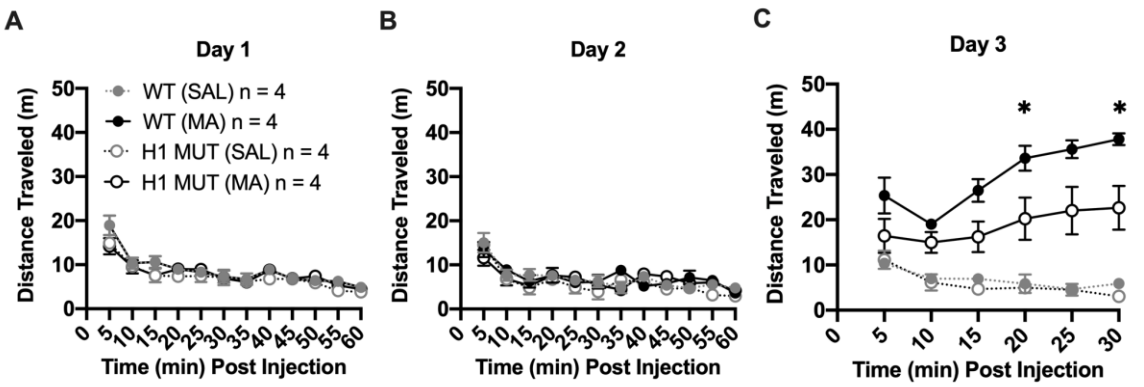

Figure 24. MA-induced locomotor activity in H1 MUT and WT mice that were used for harvest of striatal synaptosome for proteomic analysis.
On Days 1 and 2, mice were injected (i.p.) with saline (SAL) and placed into apparatus for 1 h. On Day 3, mice were injected (i.p.) with 2 mg/kg MA and placed into apparatus for 30 min followed by immediate sacrifice and removal of the striatum. **(A-B):** Locomotor activity on Day 1 **(A)** and Day 2 **(B)** for 1 h in 5-min bin. No genotypic difference in total distance traveled was observed in response to a SAL injection (i.p.) on Day 1 or Day 2 (mixed effects ANOVA, Day 1: $F(1,12)_{Genotype} = 2.40$, $p = 0.147$; $F(1,12)_{Treatment} = 0.203$, $p = 0.660$; $F(1,12)_{Genotype \times Treatment} = 0.17$, $p = 0.684$; $F(11,132)_{Time} = 1.89$, $p = 0.046$; $F(11,132)_{Genotype \times Treatment \times Time} = 1.19$, $p = 0.301$; Day 2: $F(1,12)_{Genotype} = 1.27$, $p = 0.283$; $F(1,12)_{Treatment} = 0.466$, $p = 0.508$; $F(1,12)_{Genotype \times Treatment} = 0.21$, $p = 0.656$; $F(11,132)_{Time} = 0.45$, $p = 0.930$; $F(11,132)_{Genotype \times Treatment \times Time} = 1.32$, $p = 0.219$). **(C):** Locomotor activity on Day 3 for 30 min in six, 5-min bins. In response to MA (2 mg/kg, i.p.), H1 MUT showed less distance traveled compared to WT (mixed effects ANOVA, $F(1,12)_{Genotype} = 8.54$, $p = 0.013$; $F(1,12)_{Treatment} = 77.42$, $p = 1.4E\text{-}6$; $F(1,12)_{Genotype \times Treatment} = 5.85$, $p = 0.032$; $F(5,60)_{Time} = 1.83$, $p = 0.120$; $F(5,60)_{Genotype \times Treatment \times Time} = 1.23$, $p = 0.305$; unpaired t-test for WT versus H1 MUT post MA at each 5-min bin, $t(6) = -1.63, -1.67, -2.44, -2.46, -2.41, -3.01$, $p = 0.154, 0.147, 0.050, 0.049, 0.052, 0.023$ for 5-, 10-, 15-, 20-, 25-, and 30-min time point respectively).

Overall, proteomic analysis for the main effect of Genotype identified a highly enriched upregulation of mitochondrial proteins in the H1 MUT striatal synaptosome regardless of treatment (**Figure 25A**). Enrichment analysis for the set of top differentially expressed proteins (absolute $\log_2$FC > 0.2; $p < 0.05$) between H1 MUT and WT mice revealed a highly significant enrichment for mitochondrial respiratory chain complex I assembly (**Table 8**). In examining MA-induced changes in synaptic proteins in H1 MUT versus WT mice, we again identified an enrichment for alterations in metabolic processes involving components of mitochondrial complex I and V (**Figures 25B and A6, Table 9**). Interestingly, in response to MA, there was a decrease in the level of mitochondrial proteins in the H1 MUT mice, but an increase in the WT mice (**Figure 26**). The findings were independently validated with a separate cohort of mice, which also pointed to a trending, non-significant pattern of an increase in expression of all three mitochondrial proteins in saline-treated H1 MUT mice and a trending, non-significant decrease in all three mitochondrial proteins in response to MA (**Figure 27**).

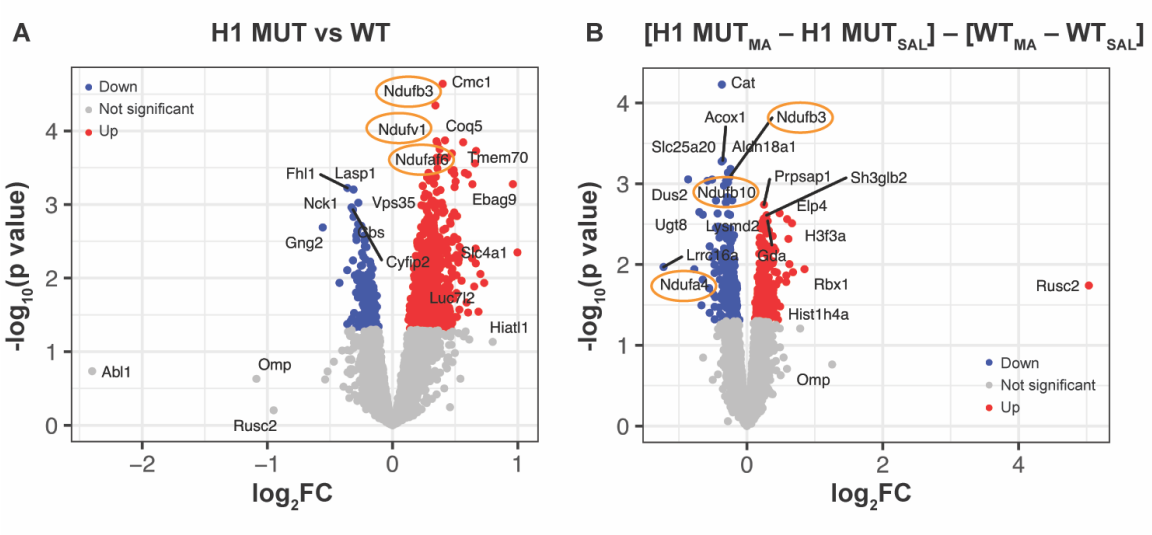

Figure 25. Proteomic analysis of the striatal synaptosome in H1 MUT mice.
On Days 1 and 2, mice were injected (i.p.) with saline (SAL) and placed into apparatus for 1 h. On Day 3, mice were injected (i.p.) with 2 mg/kg MA and placed into the apparatus for 30 min and then whole striatum was rapidly harvested via free form dissection. Locomotor activity for all three days is shown in Figure 20. The LIMMA package was used for differential analysis with Genotype and Treatment as factors. A ranked list was generated from the analysis and the fgsea R package was used to perform pre-ranked analysis, with proteins filtered for absolute $log_2FC > 0.2$ and $p < 0.05$. **(A):** Proteomic analysis was performed to identify differences in protein abundance in the striatal synaptosome of H1 MUT versus WT mice. The volcano plot shows the top differentially expressed proteins in the H1 MUT versus WT striatal synaptosome. Proteins that are part of the mitochondrial respiratory complex I are circled in orange. **(B):** Proteomic analysis was performed to examine Genotype x Treatment interactions in protein abundance in the striatal synaptosome of H1 MUT versus WT mice. This analysis accounted for baseline differences by examining the difference of the difference between the H1 MUT and WT in response to MA: ($H1\ MUT_{MA} – H1\ MUT_{SAL}$) – ($WT_{MA} – WT_{SAL}$). The volcano plot shows the top differential expressed proteins between the H1 MUT versus WT striatal synaptosome in response MA. Proteins that are part of the mitochondrial respiratory complex I are circled in orange. Network and pathway analysis in Figure 21-1 also detected an enrichment of proteins involved in metabolic processes in the H1 MUT and WT striatal synaptosome in response to MA (normalized to baseline).

Table 8. Differentially expressed proteins in H1 MUT vs WT.

GO Term	p value	FDR	Proteins
mitochondrial respiratory chain complex I assembly	2.1E-12	1.4E-09	SAMM50, NDUFB10, NDUFAF6, NDUFB3, NDUFA1, NDUFAF2, NDUFV3, NDUFV1
Complex I biogenesis	1.7E-11	1.6E-09	NDUFB10, NDUFAF6, NDUFB3, NDUFA1, NDUFAF2, NDUFV3, NDUFV1
Respiratory electron transport	2.3E-11	1.6E-09	NDUFB10, NDUFAF6, NDUFB3, NDUFA1, NDUFAF2, NDUFV3, NDUFV1, COX5A

Table 9. Differentially expressed proteins in [H1 MUT $_{(MA)}$ − H1 MUT $_{(SAL)}$] − [WT$_{(MA)}$ − WT$_{(SAL)}$].

GO Term	p value	FDR	Proteins
Metabolic pathways	4.2E-10	1.7E-08	NDUFB10, NDUFB3, ATP5A1, MBOAT2, HSD17B4, ATP5F1, ATP5O, AGPAT1, UGT8, GANAB, MTHFD1L, ACOX1, AGPS, NDUFS1, ALDH18A1
Parkinson's disease	3.6E-09	7.0E-08	NDUFB10, NDUFB3, ATP5A1, NDUFS1, VDAC1, ATP5F1, ATP5O
mitochondrial ATP synthesis coupled proton transport	4.1E-06	1.2E-3	ATP5A1, SLC25A20, ATP5F1, ATP5O

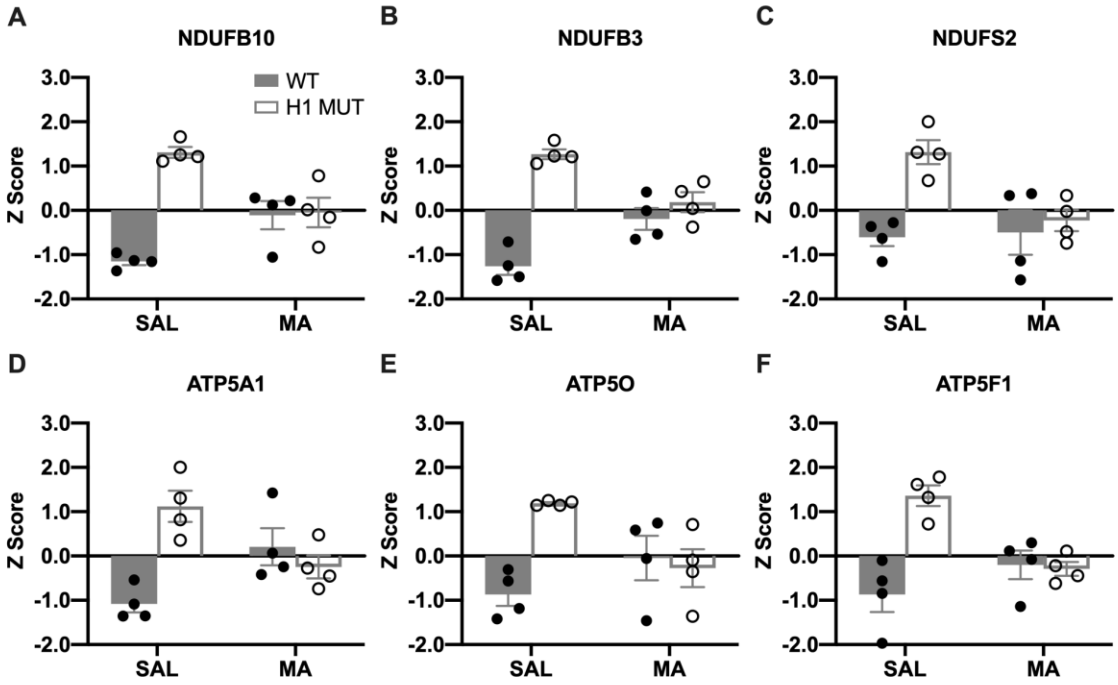

Figure 26. Protein expression profiles of select mitochondrial proteins in the striatal synaptosome of H1 MUT and WT mice from the proteomic dataset.
The protein abundance for the mitochondrial proteins are shown for the four groups: WT (SAL), H1 MUT (SAL), WT (MA) and H1 MUT (MA). Opposing Genotype x Treatment effects on protein levels are shown for the mitochondrial complex I components **(A-C)** and complex V ATPase subunits **(D-F)**. MA administration induced a decrease in protein expression of these subunits in H1 MUT mice and an increase in WT mice.

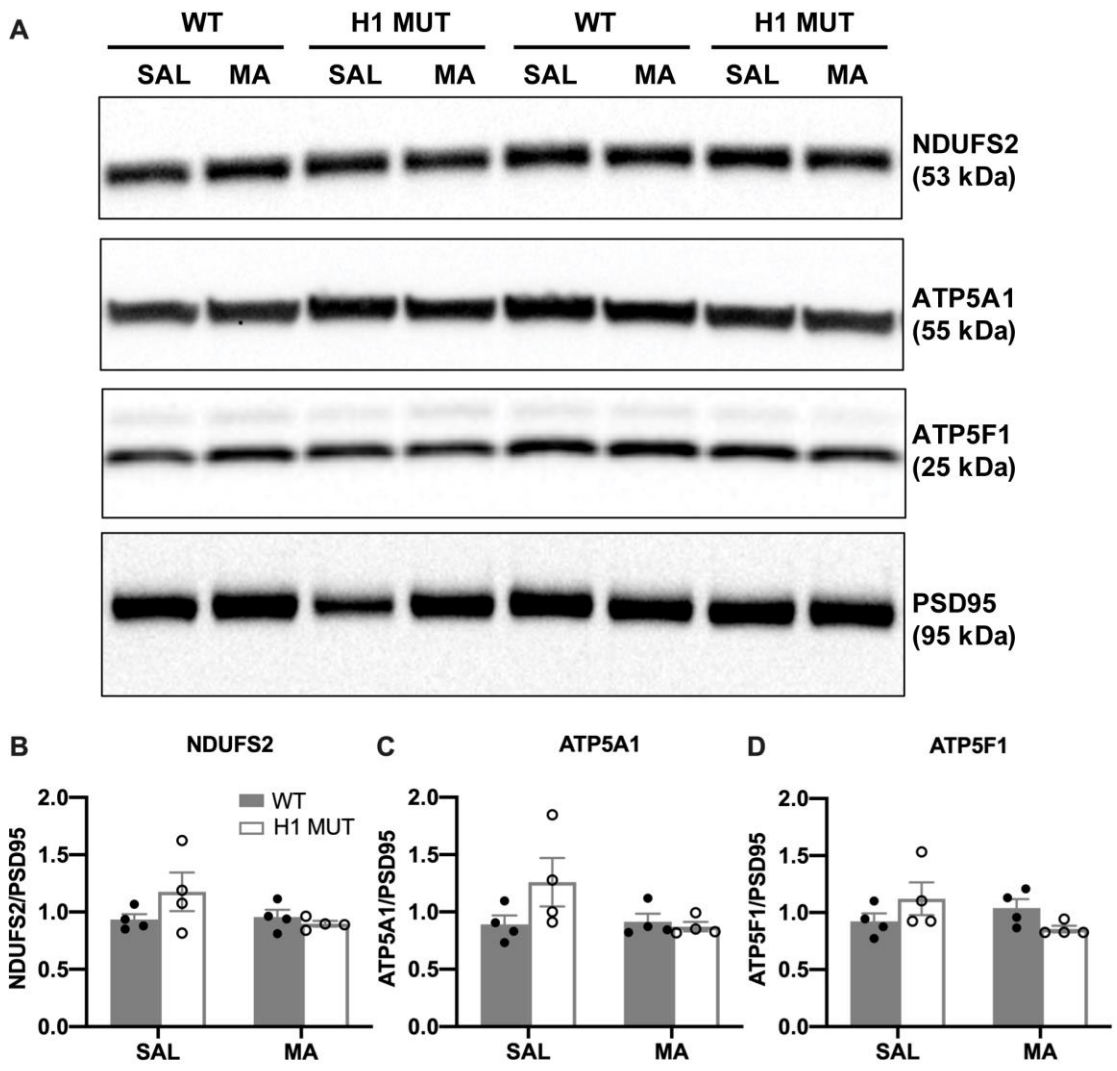

Figure 27. Immunoblots of select mitochondrial proteins in the synaptosome of H1 MUT and WT mice.

Three mitochondrial proteins (NDUFS2, ATP5A, and ATP5F1) were selected for independent validation of mass spectrometry results in a separate sample cohort via immunoblot. **(A):** Immunoblots for NDUFS2, ATP5A1 and ATP5F1. **(B-D):** Quantification of protein expression of three select mitochondrial proteins. All three proteins show the same trend as the mass spectrometry results depicted in Figure 9 where an increase in expression was detected in SAL-treated H1 MUT versus SAL-treated WT mice (unpaired t-test, NDUFS2: $t(6) = -1.39$ $p = 0.107$; ATP5A1: $t(6) = -1.64$, $p = 0.077$; ATP5F1: $t(6) = -1.24$, $p = 0.131$). n = 4 per genotype per dose.

DISCUSSION

Here, we extend a role for *Hnrnph1* in MA reinforcement and reward (**Figure 28**). A heterozygous frameshift 16 bp deletion of the first coding exon of *Hnrnph1* reduced MA oral operant self-administration and MA-induced CPP (**Figures 16-17**) and induced a robust reduction in MA-induced DA release in the NAc (**Figure 19**). This DA anomaly occurred without any differences in 1) basal extracellular DA; 2) basal DA content within striatal tissue (**Figure 20A**); 3) DA uptake (**Figure 20B**); 4) the number or staining of midbrain DA neurons within the mesolimbic and nigrostriatal dopaminergic circuits (**Figure 21**) or 5) any robust changes in the number of forebrain striatal puncta originating from these neurons (**Figure 22**). The combined results suggested an alternate mechanism underlying the decrease in MA-induced extracellular DA level and behavior in H1 MUT mice**.** In further support of a MA-induced cell biological mechanism, there was no effect of H1 MUT on spontaneous locomotion, anxiety- and depressive-like behaviors, or sensorimotor function.

H1 MUT mice showed less MA-CPP at 0.5 mg/kg but greater CPP at 2 mg/kg than WT mice (**Figure 17**). One interpretation is that MA-CPP exhibits an inverted U-shaped dose-response curve (Uhl et al., 2014) in WT and that H1 MUT shifts this curve to the right, yielding reduced sensitivity to positive and negative reinforcing effect of MA at lower versus higher doses. Consistent with this interpretation, H1 MUT mice exhibited blunted operant oral MA reinforcement. The combined data are consistent with H1 MUT mice self-administering less MA because they are less sensitive to the physiological and interoceptive effects of MA due to a reduced MA-induced extracellular DA in the NAc.

H1 MUT mice exhibited a blunted DA response to 0.5 and 2 mg/kg MA. This effect on MA-induced extracellular level could not be explained by alterations in total DA levels (**Figure 20A**), or in DAT levels or function at the presynaptic membrane (**Figures 20B-F**). An alternative explanation to DAT dysfunction is that the *Hnrnph1* mutation somehow decreases MA binding to DAT, limiting its entry into presynaptic dopaminergic neuronal terminals and decreasing DA release. Future studies are necessary to examine MA binding to DAT in H1 MUT mice.

Our findings support a dopaminergic mechanism underlying reduced MA reward and reinforcement in H1 MUT mice. Nevertheless, we acknowledge the potential involvement of additional neurotransmitter systems and brain regions. We did not identify any difference in basal or MA-induced changes in extracellular glutamate levels in the NAc of H1 MUT mice. While MA reward is generally attributed to an increase in DA release in the NAc (Segal and Kuczenski, 1997; Adinoff, 2004), MA also increases release of norepinephrine and serotonin by targeting their respective transporters that could modulate the locomotor stimulant and/or rewarding response to psychostimulants such as MA (Haughey et al., 2002; Rothman et al., 2001; Zaniewska et al., 2015). Future studies are warranted to address these other neurotransmitters in MA-induced behavioral dysfunction in H1 MUT mice as well as the possibility that H1 MUT has a pleiotropic influence on behavioral (e.g., cognitive, antidepressant) and neurochemical responses to drugs targeting other membrane transporters such as NET and SERT. For example, phosphorylation of the RBP hnRNP K increases expression of SERT protein via changes in binding to the distal polyadenylation element of the transporter (Yoon et al., 2013).

The two-fold increase in hnRNP H protein in the striatal synaptosome of H1 MUT mice with no change in total hnRNP H protein was surprising. This finding was observed in multiple replication studies and suggests a redistribution of hnRNP H protein to the synapse in H1 MUT mice. We performed LC-MS/MS analyses on striatal synaptosomes following 2 mg/kg MA (i.p.) to further understand the effect of increased synaptosomal hnRNP H on global changes in protein expression and the underlying cell biological mechanisms. We identified a higher abundance of several mitochondrial proteins, in particular, complex I of the mitochondrial respiratory chain in H1 MUT mice. The mammalian complex I consists of 38 nuclear DNA-encoded subunits (Sharma et al., 2009) and our proteomic analysis identified 8 out of the 38 subunits that showed higher expression in H1 MUT mice (**Figures 25-27**). Proteomics has been widely used to study the effects of MA on protein expression in the brain tissues of animals (Liao et al., 2005; Faure et al., 2009; Bosch et al., 2015). Iwazaki et al. (2006) used two-dimensional gel electrophoresis proteomics and found that a single low dose of MA (1 mg/kg) administration in rats induced differential expression of proteins involved in mitochondria/oxidative metabolism. Furthermore, chronic exposure of 1 mg/kg MA induced locomotor sensitization and neurotoxicity along with a downregulation of numerous striatal proteins indicating mitochondrial dysfunction and an oxidative response (Iwazaki et al., 2007; Chin et al., 2008).

Recent studies showed postsynaptic dendritic mitochondrial fission and fusion processes mediate cellular and behavioral plasticity, spine and synapse formation, and synaptic function (Li et al., 2004; Oettinghaus et al., 2016; Chandra et al., 2017; Divakaruni

et al., 2018). Dynamin-related protein (Drp1), a GTPase involved in mitochondria fission, has been shown to regulate addiction-relevant behavior during early cocaine abstinence (Chandra et al., 2017), with inhibition of mitochondrial fission blunting cocaine-seeking and locomotor sensitization. While the results of our synaptosomal proteome dataset did not reveal any mitochondrial fission and fusion mediators, it is still possible that changes in mitochondrial proteins in the post-synaptic dendrites contribute to behavioral differences. Future studies will isolate potential pre- versus postsynaptic mechanisms.

Most mitochondrial proteins are nuclear-encoded and must be transported to mitochondria for organelle-coupled translation (Williams et al., 2014). RBPs play a critical role in targeting mRNAs to membrane-bound organelles such as mitochondria. RBPs interact with mRNAs and chaperone them toward mitochondrial outer membranes where they are translated (Gerber et al., 2004; García-Rodríguez et al., 2007; Eliyahu et al., 2010; Gehrke et al., 2015). RBPs recognize and bind mitochondria-targeting RNA elements to form higher-order units called mRNA ribonucleoprotein (RNP) complexes consisting of mRNAs and associated RBPs (Béthune et al., 2019; Rossoll and Bassell, 2019). The robust increase in hnRNP H protein in the striatal synaptosome accompanied by the increase in several complex I subunits suggests a novel function for hnRNP H in targeting mRNAs encoding for subunits of mitochondrial complex I to the mitochondria, thus, regulating local translation (**Figure 28**). Once the mRNAs are transported nearby the mitochondria, hnRNP H could coordinate with other RBPs to form an RNP complex to stabilize mRNAs to the mitochondrial membrane where translational activators initiate translation. An example of a RBP with such function is Puf3pm that binds to *ATP2* mRNA encoding

mitochondrial components of the F_1F_0 ATPase and localizes to the outer mitochondrial membrane (García-Rodríguez et al., 2007). Future studies involving CLIP-seq will identify target mRNAs bound to hnRNP H and determine the degree of enrichment for mRNAs encoding mitochondrial complex I subunits.

Mitochondria are abundant at the synapse where they generate ATP for Ca^{2+} buffering, vesicle release, and recycling (Vos et al., 2010; Devine and Kittler, 2018). Mitochondria consist of five oxidative phosphorylation complexes (I through V) (Mimaki et al., 2012; Sharma et al., 2009). Complex I is the first enzyme of the respiratory chain and initiates electron transport continuing to complex II through IV to generate redox energy for Complex V to produce ATP. The increase in Complex I subunits in H1 MUT mice could increase Complex I activity and synaptic ATP production to support vesicle fusion, DA release, and DA transport back into the cells via DAT and Na+/K+ ATPase to counteract MA-induced DA release. We found a Genotype by Treatment effect on protein levels of F_0F_1 ATP synthase subunits (Atp5a1, ATP5f1 and Atp5o) of Complex V (**Figure 26**) in the synaptosomal proteome whereby MA decreased these ATP synthase subunits in H1 MUT mice which could decrease ATP production in response to MA in H1 MUT mice and affect extracellular DA levels.

Besides binding and targeting RNAs to the mitochondria for translation, hnRNP H, like other RBPs, could bind and target proteins via its glycine-rich domain in an activity-dependent manner (Tiruchinapalli et al., 2008). In an animal model for frontotemporal dementia, ploy(GR) aggregates (resulting from hexanucleotide repeats in *C9ORF72)* bind to mitochondrial complex V protein ATP5A1 to increase its ubiquitination and degradation

through the proteasome pathway, thus disrupting mitochondrial function (Choi et al., 2019). The higher level of synaptosomal hnRNP H protein in H1 MUT mice could increase binding to mitochondrial complex I and V proteins (e.g., via the glycine-rich domain) to prevent degradation, yielding higher protein levels at baseline (**Figures 25 and 26**). MA administration could then decrease hnRNP H-protein interactions in H1 MUT mice, thus decreasing synaptic mitochondrial proteins and synaptic function.

Taken together, the opposing effects of MA treatment on synaptic abundance of mitochondrial complex I proteins between H1 MUT and WT mice could represent a mechanism underlying blunted MA-induced extracellular DA level in the NAc of H1 MUT mice. Future studies will focus on the interaction between hnRNP H and mRNA encoding mitochondrial complex I and V subunits at the protein-RNA and protein-protein level (pre- and postsynaptically) and determine whether disruption of such interactions can alter ATP production and extracellular DA level in the NAc.

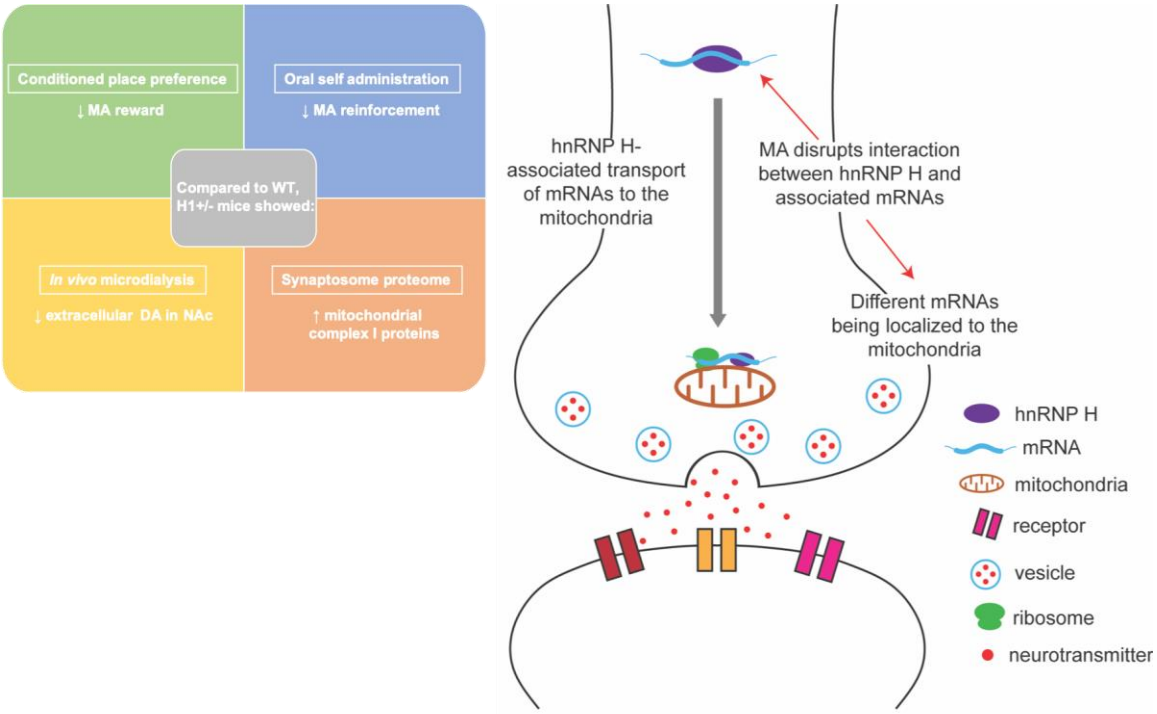

Figure 28. Proposed model linking increased synaptic mitochondria with a decrease in MA-induced DA release and behaviors.
Compared to WT mice, H1 MUT mice showed reduced MA-induced extracellular DA in the NAc and reduced sensitivity to the locomotor stimulant, rewarding, and reinforcing effects of MA. In addition, H1 MUT mice show an increase in hnRNP H protein in the striatal synaptosome, with no change in total hnRNP H. This increased localization of synaptosome hnRNP H is associated with an increase in complex I mitochondrial proteins. RBPs such as hnRNP H chaperone mRNAs to membrane-bound organelles such as the mitochondria for translation and subsequent assembly in the mitochondria. In the absence of MA, hnRNP H binds to mRNA transcripts encoding mitochondria proteins and transports them to the surface of the mitochondria. MA administration disrupts hnRNP H-RNA interactions which results in fewer mitochondrial mRNAs being transported to the mitochondria for translation.

MATERIAL AND METHODS

Mice

Experimental mice were generated by mating H1 MUT males with C57BL/6J females purchased from The Jackson Laboratory in Bar Harbor, ME USA (for studies in Boston University) or in Sacramento, CA USA (for studies in UC Santa Barbara). Offspring were genotyped as previously described (Yazdani et al., 2015). Unless otherwise indicated, both female and male littermates (56-100 days old at the start of the experiment), were used in the studies. Mice were housed in same-sex groups of 3-5 in standard mouse cages and housed within ventilated racks under standard housing conditions. All procedures conducted in mice were approved by the Boston University, UC Santa Barbara and Virginia Commonwealth University Animal Care and Use Committees. All experiments were conducted in strict accordance with the Guide for the Care and Use of Laboratory Animals. Colony rooms were maintained on a 12:12 h light–dark cycle.

Genotyping of H1 MUT and H1-/- mice

The genotyping protocol for the H1+/- or H1 MUT mice is published in Yazdani et al. (2015). For genotyping of H1-/- embryo tissue, an *Hnrnph1* forward primer (GATGATGCTGGGAGCAGAAG) and reverse primer (GGTCCAGAATGCACAGATT G) were designed to target upstream and downstream of the deleted region in exon 4 of *Hnrnph1*. Genomic DNA was used to amplify a 204-bp PCR product using DreamTaq Green PCR Mastermix (ThermoScientific) followed by overnight restriction enzyme digest with BstNI (New England Biolabs).

Hnrnph1 and Hnrnph2 RT-qPCR for mouse embryo tissue

Oligo-dT primers were used to synthesize cDNA from total RNA to examine mRNA expression and qPCR for evaluating gene expression were performed using Taqman SYBR Green (ThermoFisher Scientific Cat# 4309155). The primer sequences used for evaluating expression of *Hnrnph1* (targeting exons 6 and 7 were ACGGCTTAGAGGACTCCCTTT and CGTACTCCTCCCCTGGAAGT. The primer sequences used for quantifying expression of *Hnrnph2* (targeting exons 1 and 2) were TAGCCGTTTGAGGGAAGAAG and CCCTGTTAGAGTTTCTTCCAGGTA. The house keeping gene used was *Hprt* (targeting exons 7 and 9) with following primer sequence: GCTGGTGAAAAGGACCTC T and CACAGGACTAGAACACCTGC.

Oral MA self-administration

The procedures for MA operant-conditioning were similar to those recently described (Lominac et al., 2016). Testing was conducted in operant chambers equipped with 2 nose-poke holes, 2 cue lights, a tone generator, and a liquid receptacle for fluid reinforcement (Med Associates Inc.). Mice were not water-restricted at any point during oral MA self-administration procedures. The vehicle for MA was filtered tap water**.** Under a fixed-ratio 1 (FR1) schedule of reinforcement, mice were trained daily to self-administer MA during 1 h sessions where a single active nose poke response resulted in delivery of 20 µl of liquid MA into the receptacle, with a 20s illumination of the cue light, and the sounding of the tone. During the 20s period, further responding resulted in no programmed consequences. Inactive hole responses were recorded but had no consequences, serving to gauge the selectively of responding in the MA-reinforced hole. Mice were initially trained to nose-

poke 80 mg/l MA, with the concentration of MA progressively increased over weeks (120, 160, 200, 300 and 400 mg/l MA; five days per dose). Upon the completion of each daily session, the volume of MA remaining in the receptacle was determined by pipetting and was subtracted from the volume delivered to calculate MA intake (Lominac et al., 2016).

Conditioned place preference (CPP)

Mice were trained for 1 h each day in Plexiglas activity boxes within sound-attenuating chambers (40 cm length x 20 cm width x 45 cm tall; divided into two sides with different plastic floor textures for CPP). Mice were recorded from above using infrared cameras (Swan) and tracked with ANY-maze (RRID:SCR_014289). The CPP paradigm was described in Kirkpatrick and Bryant (2015). On training Days 2-5, mice were injected with either saline (Days 2 & 4) or MA (Days 3 & 5; saline, 0.5 or 2 mg/kg, i.p.) and confined to either the saline- or MA-paired side for 1 h.

Stereotaxic surgery

The procedures to implant indwelling microdialysis guide cannulae bilaterally over the NAc of mice were described previously (Lominac et al., 2014, 2016). Mice were anesthetized under 1.5–2% isoflurane with 4% oxygen as a carrier gas, mounted in a Kopf stereotaxic device with tooth and ear bars adapted for mice. The mouse skull was exposed, leveled, and holes were drilled based on coordinates from Bregma for the NAC (AP: +1.3 mm, ML: ±1 mm, DV: −2.3 mm), according to the mouse brain atlas of Paxinos and Franklin (2001). The guide cannulae were lowered bilaterally such that the tips of the cannulae were 2 mm above the NAc. The skull was then prepared for polymer resin

application and the guide cannulae were secured to the skull with dental resin. Post-surgery, mice were injected subcutaneously (s.c.) with warm saline and 250 µl of 2.5 mg/ml Banamine (Henry Schein Animal Health) and allowed to recover on a heating pad. Post-operative care was provided for four days, during which mice were injected with 250 µl of 2.5 mg/mL Banamine s.c. daily for the first two days. Mice were allowed a minimum 1-week recovery prior to *in vivo* microdialysis assessments.

In vivo microdialysis & HPLC analysis

Conventional microdialysis was conducted using a within-subjects design to examine saline and acute MA-induced DA release (0.5 or 2 mg/kg, i.p.), using procedures similar to those described previously (Lominac et al., 2014, 2016). Microdialysis probes were inserted unilaterally and perfused with artificial cerebrospinal fluid for 3 h (2 µl/min), allowing for neurotransmitter equilibration. For DA no net-flux analysis, DA was infused at 0, 2.5 nM, 5 nM, and 10 nM, and dialysate was collected in 20-min intervals for 1h/concentration. On a subsequent day, mice were probed on the contralateral side, and following the 3 h equilibration period and 1 h of baseline dialysate collection, mice were injected i.p. with either 0.5 or 2.0 mg/kg MA and dialysate was collected in 20-min intervals for 3 h post-injection. HPLC analysis of DA was conducted as described previously (Lominac et al., 2014). Cannulae placement was determined on Nissl-stained coronal sections and only mice exhibiting correct placement within the NAc were included in analyses.

Quantification of baseline monoamine neurotransmitters

Drug-naïve striatum were harvested from H1 MUT and WT littermates and flash-frozen on dry ice. The dissected tissue was sent to Vanderbilt University Neurotransmitter Core for the quantification of monoamine neurotransmitters using HPLC wth electrochemical detection.

DAT-mediated DA uptake

SAL or MA (2.0 mg/kg) was administered interperitoneally in a volume of 10 ml/kg. After 2 h post-administration (2 h was chosen based on the microdialysis results), mice were decapitated, and DAT-specific [^{3}H]DA uptake from synaptosome preparations was conducted as described previously (Kivell et al., 2014). Mice were rapidly decapitated, and striatal regions were dissected from the brain and collected in 10 volumes (wt/vol) of prechilled 0.32 M sucrose buffer (0.32 M sucrose in 5 mM HEPES, pH 7.5). The striatal tissue was homogenized and centrifuged at 1000 x g for 15 min at 4˚C. The supernatant was centrifuged at 12,000 x g for 20 min, and the pellet was suspended in 0.32 M sucrose buffer. Striatal synaptosomes (30 µg) were incubated in a total volume of 0.3 ml of Krebs-Ringer-HEPES (KRH) buffer consisting of 120 mM NaCl, 4.7 mM KCl, 2.2 mM $CaCl_2$, 10 mM HEPES, 1.2 mM $MgSO_4$, 1.2 mM KH_2PO_4, 5 mM Tris, 10 mM D- glucose, pH 7.4 containing 0.1 mM ascorbic acid, and 0.1 mM pargyline at 37˚C for 10 min with or without DAT- specific blocker GBR12909 (50 nM). Following incubation, 5 nM [^{3}H]DA (63.2 Ci/mmol-dihydroxyphenylethylamine [2,5,6,7,8-3H]; PerkinElmer) and further incubated for additional 5 min. Uptake of DA was terminated with the addition of 500 nM DAT blocker GBR12909. The samples were filtrated over 0.3% polyethylenimine coated GF-B

filters on a Brandel Cell Harvester (Brandel Inc.), and washed rapidly with 5 ml cold PBS. Radioactivity bound to the filter was counted using a liquid scintillation counter. DAT mediated [^{3}H]DA uptake was determined by subtracting total accumulation of [^{3}H]DA (absence of GBR12909) and in the presence of GBR12909. Uptake assays were performed in triplicates.

Immunohistochemistry

For immunohistochemistry (IHC), drug-naïve H1 MUT and WT mice were anesthetized with pentobarbital, and transcardially perfused with phosphate buffered saline (PBS) followed by 4% paraformaldehyde in PBS at room temperature. Next, brains were dissected and processed for tyrosine hydroxylase (TH) 3-3'-diaminobenzidine (DAB) IHC and analysis as previously described (Burke et al., 1990; Hutson et al., 2011), or double immunofluorescent IHC for hnRNP H and TH colocalization. For DAB IHC, coronal slices were blocked with 4% normal goat serum and then incubated for 48 h at 4°C with anti-hnRNP H (1:50,000, Bethyl Cat# A300-511A, RRID:AB_203269) or tyrosine hydroxylase (TH) (1:500, Santa Cruz Cat# sc-14007, RRID:AB_671397), and processed for DAB staining and analyzed as previously described (Hutson et al., 2011). For co-staining studies with hnRNP H and TH, tissues were blocked with superblock (ThermoFisher Scientific Cat# 37515), and incubated with anti-hnRNP H (Santa Cruz Cat# sc-10042, RRID:AB_2295514) and TH (1:500, Santa Cruz Cat# sc-14007, RRID:AB_671397) for 48 hours at 4°C. Next, tissues were incubated with donkey anti-rabbit Alexa Fluor 488 (1:500, Molecular Probes Cat# A-21206, RRID:AB_141708) and donkey anti-goat Alexa Fluor 633 (1:500, Molecular Probes Cat# A-21082, RRID:AB_141493), washed, and then

coated with ProLong Diamond Antifade Mountant (ThermoFisher Scientific Cat#P36961), mounted onto slides, and imaged on the Leica SPE Confocal microscope.

TH puncta quantification in the striatum

Entire coronal slices of rostral, medial, and caudal striatum were imaged at 40x magnification using a Nikon Eclipse 600 microscope. A 225,000 μm^2 grid was overlaid onto these images using Image J and every 3rd field of view within the striatum was graded. Number of puncta within a field of view was graded in ImageJ by subtracting out background signal, creating binary images from these files, and then counting puncta meeting roundness and diameter criteria (roundness <0.6, diameter 1-45 μm). Averages puncta densities for ventral, dorsal, and total striatum were calculated. Grading of the puncta was performed in Image J. The image was duplicated into a 1,000,000-pixel area followed by brightness/contrast adjustment and background subtraction. The threshold was set to 106. A binary image was then generated for puncta measurement. Roundness was set to 0.6-1 and size was set to 5 – 200 pixels.

Dissection of mouse brain regions: striatum and midbrain

Live, rapid decapitation was used to avoid the effects of anesthesia or CO2 asphyxiation on gene expression. Immediately followed live-decapitation using large, sharpened shears with an incision just posterior from the ears, the mouse brain was removed quickly with forceps and transfer to a cold surface. The striatum has a somewhat darker appearance than the surrounding cortex. To dissect the dorsal and ventral striatum, fine-tip forceps were used to separate the midline of the brain and then the cortex and hippocampus were

removed to reveal the striatum. To dissect the midbrain, a razor blade was used to make a rostral cut where the cerebral aqueduct begins and another caudal cut just before the start of the cerebellum.

Methamphetamine-induced locomotor activity followed by tissue harvesting

On Days 1 and 2, all mice received a SAL injection (10 ml/kg, i.p.) and were recorded for locomotor activity in Plexiglas chambers (40cm length x 20 cm width x 45 cm height) for 1 h. On Day 3, mice receive either saline or MA (2 mg/kg, i.p.; Sigma Aldrich) and were recorded for locomotor activity for 30 min and the whole striatum was harvested as described above at 30 min post-injection. Whole striata (left and right sides) were flash frozen in ethanol/dry ice bath and stored at -80^{o}C for long-term storage. Four cohort of animals were run in this behavioral paradigm for tissue collection: 1) hnRNP H immunoprecipitation followed by mass spec; 2) synaptosome mass spec and hnRNP H immunoblot; 3) validation studies for mitochondrial protein immunoblots; 4) measurement of MA concentration in MA-treated striatal tissues. The mice that were used for hnRNP H immunoprecipitation were all MA-treated on Day 3.

Quantification of MA metabolites MA-treated whole striatal tissue

Whole striata (left and right sides) were flash frozen in ethanol/dry ice bath and stored at -80^{o}C. Tissue were then shipped on dry ice to University of Utah Health Science Center for MA and amphetamine metabolite quantification as previously described (Slawon et al., 2002; DeYoung et al., 2016).

Preparation of synaptosomes

Striatal tissue collection from saline- or MA-treated mice was performed as described above. The tissues were subsequently processed to obtain synaptosomes using a Percoll (Sigma Aldrich Cat# 1644) gradient fractionation method, which was adapted from Dunkley et al. (Dunkley et al., 2008). Whole striata (left and right hemisphere) were placed in 1 ml sucrose homogenization buffer (2 mM HEPES, pH7.4, 320 mM Sucrose, 50 mM EDTA, 20 mM DTT) supplemented with protease and phosphatase inhibitor (ThermoFisher Scientific Cat# 78440). The brain tissues were lightly homogenized using a handheld motorized pestle. The homogenate for each sample was then centrifuged for 2 min at 3000 rcf and the supernatant (S1) was collected. The pellet (P1) was then resuspended in 500 µl of sucrose homogenization buffer and re-spun for 3 min at 3000 rcf. The supernatant (S1') was collected and combined with S1 and then centrifuged for 15 min at 9200 rcf. The supernatant S2 was then removed and the pellet (P2) was re-suspended in 500 µl of sucrose homogenization buffer and loaded onto a Percoll density gradient consisting of 23%, 10%, and 3% Percoll (1 ml each) in Polycarbonate centrifuge tubes (13 x 51 mm; Beckman Coulter Cat# 349622). The gradients were then centrifuged for 15 min at 18,700 rcf. The distinct band between the 10% and 23% Percoll was collected as the synaptosome. The synaptosome fraction was then washed to 5 mL with 1X HBM buffer, pH 7.4 (140 mM NaCl, 5 mM KCl, 5 mM $NaHCO_3$, 1.2 mM NaH_2PO_4, 1 mM $MgCl_2$-$6H_2O$, 10 mM glucose, 10 mM HEPES) to dilute out the Percoll by centrifuging for 12 min at 18700 rcf. The pellet was then re-suspended in 100 µl of HBM buffer to yield the final synaptosme fraction and BCA assay was used to determine protein concentration. A total

of 30 μg of synaptosome was loaded per sample for SDS-PAGE and Western blotting as described below.

SDS-PAGE and Western Blot

Brain tissues were homogenized using hand-held homogenizer in RIPA buffer with Halt™ Proteatase & Phosphotase inhibitor cocktail (ThermoFisher Scientific Cat# 78840). For each sample, 30 μg of protein was heated in a 70ºC water bath for 10 min prior to loading into into a 4-15% Criterion TGX precast Midi protein gel (Bio-Rad) for SDS-PAGE followed by wet transfer to nitrocellulose membrane. The membrane was then blocked with 5% milk for 1 h and probed with primary antibodies. For evaluating TH expression in brain tissues, overnight incubuation of the membrane at 4°C with anti-TH (1:50,000, Santa Cruz Cat# sc-14007, RRID:AB_671397) was performed followed by 1 h incubation with donkey anti-rabbit HRP (1:10,00, Jackson ImmunoResearch Labs Cat# 711-035-152, RRID:AB_10015282). For evaluating hnRNP H protein expression in mouse embryo tissues and in striatal synaptosome, the following antibodies were used: hnRNP H (C-term: 1:50,000, Bethyl Cat# A300-511A, RRID:AB_203269; N-term: 1:50,000, Santa Cruz Cat# sc-10042, RRID:AB_2295514) followed by 1 h incubation with the appropriate secondary antibodies. For vadilation of mitochondrial protein expression following MA treatment, the following priamry antibodies were used: ATP5A1 (1:2000, Abcam Cat# ab14748, RRID:AB_301447); ATP5F1 (1:5000, Proteintech Cat# 15999-1-AP, RRID:AB_2258817); and NDUFS2 (1:5000; abcam ab192022). We used the following loading controls: anti-β-actin (1:20,000, Sigma-Aldrich Cat# A2228, RRID:AB_476697);

anti-GAPDH (1:20,000; Millipore Cat# MAB374, RRID:AB_2107445), and PSD95 (1:10,000, Cell Signaling Technology Cat# 3450, RRID:AB_2292883).

Mouse brain tissue processing for SDS-PAGE and DAT immunblotting was modified from Staal et al., 2007. Briefly, tissue was triturated using a 20-22 gauge needle in RIPA buffer (10 mM Tris, pH 7.4, 150 mM, NaCl, 1 mM EDTA, 0.1% SDS, 1% Triton X-100) supplemented with Halt^{TM} Proteatase & Phosphotase inhibitor cocktail (ThermoFisher Scientific Cat# 78840). 30 μg of protein of each sample was allowed to rotate at room temperature prior to SDS-PAGE instead of heating the sample at high temperature. For evaluating DAT expression in whole striatal tissue and striatal synaptosome, we conducted overnight incubation anti-DAT (1:2000; Millipore Cat# MAB369, RRID:AB_2190413) followed by 1 h incubation with goat anti-rat (1:500, Jackson ImmunoResearch Labs Cat# 112-035-003, RRID:AB_2338128).

All processed membranes were imaged via enhanced chemiluminescence photo-detection. Densitometry analysis in Image J was used for quantification.

hnRNP H immunoprecipitation

Following the three-day locomotor paradigm assessing acute locomotor sensitivity in H1 MUT versus WT mice as described above, striata were dissected from the mice at 30 min post-injection of MA or saline. Striatum was dissected from WT or H1 MUT mice and frozen on dry ice and stored at -80^{o}C. Striatal tissues were then homogenized using a microcentrifuge pestle in ice-cold RIPA buffer (50 mM Tris-HCl, pH 6.8, 150 mM NaCl, 5 mM EDTA, 1% Triton X-100, 0.1% SDS, 0.5% sodium deoxycholate) supplemented with protease and phosphatase inhibitor cocktails (ThermoFisher Scientific Cat#

78840) and incubated overnight at 4^{o}C with gentle agitation. Lysates were centrifuged at 10,000 rpm for 15 min at 4^{o}C, and the supernatant fraction was saved for protein quantification via BCA assay. 1 mg of striatal lysates was pre-cleared for 1 h with 80 ul Protein G Sepharose coated beads (ThermoFisher Scientific Cat# 101243) and then centrifuged at 4^{o}C for 5 min at 1000 rpm. The pre-cleared lysates (supernatant) were then incubated overnight with 10 μg of rabbit anti-hnRNP H (Bethyl Cat# A300-511A, RRID:AB_203269) or control normal rabbit IgG antibody (Millipore Cat# NI01-100UG, RRID:AB_490574). The next day, 80 μl of Protein G Sepharose coated beads were added to the antibody-lysate mixture, and incubated for an additional 2 h. The beads were then washed 4 times in 1 ml lysis buffer, resuspended and centrifuged for 1 min at 1000 rpm each time. The beads were eluted by adding 60 μl of non-reducing SDS buffer and heating at 95^{o}C for 10 min. hnRNP H immunoprecipitates were eluted in non-reducing SDS buffer as described above. 50 μl of each sample was separated by SDS-PAGE at 100 V for 30 min (~2 cm) on a Novex Bolt 4-12% Bis-Tris gel. The gel was then washed 3 times in deionized H_2O and stained with Simply Blue Coomassie SafeStain (ThermoFisher Scientific Cat# LC6060). The gel was then cut at ~160 kDa to exclude the prominent non-reduced IgG band. Individual gel lanes were then separately excised and stored in pre-washed microcentrifuge tubes at 4^{o}C prior to shipping to the UMass Worchester Proteomics and Mass Spectrometry facility for analysis by OrbiTrap liquid chromatography tandem mass spectrometry.

TMT Labeling, High pH reverse phase HPLC fraction, followed by LC-MS/MS

Following the three-day locomotor paradigm assessing acute locomotor sensitivity in H1 MUT versus WT mice as described above, striata were dissected from the mice at 30 min post-injection. Synaptosomes were isolated following the procedure outlined above for proteomic characterization. Samples were resuspended in 8 M urea for 30 min, followed by the addition of 5 mM DTT for 1 h. Lodoacetamide was then add to the samples that were incubated in the dark for 30 min. The urea concentration was diluted below 1 M with the addition of 50 mM of ammonium bicarbonate. The samples were then digested with trypsin (50:1, protein to enzyme ratio) overnight at 37^{o}C and terminated with the addition of formic acid to 1%. The samples were desalted with a C18 tip. Peptide was determined by Pierce Quantitative Colorimetric Assay (ThermoFisher Scientific Cat# 23275), then 100 µg of peptide was resuspended in 0.1 M triethylammonium bicarbonate (TEAB) and incubated with the TMT plex isobaric labeling for 1 h at room temperature. To quench the reaction, 5% hydroxylamine was added to each sample and incubated for 15 min. Each sample was combined at equal amount and cleaned with C18 tips. One mg of labeled peptides was fractioned using a Waters XBridge BEH C18 (3.5µm, 4.6 ×250mm) column on an Agilent 1100 HPLC system. 48 fractions were collected and combined to 12 fractions and then dried. A C18 Acclaim PepMap 100 pre-column (3µm, 100 Å, 75µm × 2cm) hyphenated to a PepMap RSLC C18 analytical column (2µm, 100 Å, 75µm × 50cm) was used to separate peptide mixture. LC-MS/MS analyses were completed using an EASY nLC 1200 system coupled to a Q Exactive HF-X mass spectrometer. Full MS spectra were collected at a resolution of 120,000 with an AGC of 3×10^6 or maximum injection time of

50 ms and a scan range of 350 to 1650 m/z. MS2 scans were performed at 45,000 resolution and using 32% total normalized collision energy. Source ionization parameters were optimized with the spray voltage at 2.1 kV, dynamic seclusion was set to 45 s.

Proteomics Data Analysis and Pathway Enrichment Results

The acquired data was searched by MaxQuant against the UniProt mouse proteome data base with standard settings (fragment ion mass tolerance of 20ppm, maximum missed cleavage of 2, oxidation as variable modification, false discovery was 1%, only protein groups identified with at least 2 or more peptides). The intensity data were filtered and normalized using R (RRID:SCR_001905) and the LIMMA package (RRID:SCR_010943) was used for differential analysis with Genotype and Treatment as factors. A ranked list was generated from the analysis and the fgsea R package was used to perform pre-ranked analysis, with proteins filtered for absolute log2FC > 0.2 and $p < 0.05$. Enrichment results for the comparisons were visualized using Cytoscape (RRID:SCR_003032) and EnrichmentMap (RRID:SCR_016052), with nodes representing pathways and edges representing overlap genes. Pathways were clustered and annotated with themes using AutoAnnotate (Reimand et al., 2019).

Experimental design and statistical analyses

Characterization of *Hnrnph1/2* gene expression and hnRNP H protein expression in H1 MUT mice: For gene expression analysis of *Hnrnph1/2* via qPCR, each sample was run in triplicate and averaged. Differential gene expression was reported as the fold-change in H1 MUT and H1-/- relative to WT littermates using the $2^{-(\Delta\Delta C_T)}$ method (Livak and Schmittgen,

2001). To examine genotypic differences in transcript and protein expression among WT, H1 MUT and H1-/-, one-way ANOVA was conducted. To examine genotypic difference in level of peptides unique to either hnRNP H1 or hnRNP H2, two-tailed unpaired t-test was performed for each peptide with the exception of Peptide 3 for hnRNP H1, where we employed a one-tailed unpaired t-test based on *a priori* results published in Yazdani et al. (2015) indicating a decrease in exon 4 usage of *Hnrnph1* in the H1 MUT versus WT. Thus, we hypothesized that Peptide 3, which is encoded by part of exon 4, would also be decreased in the H1 MUT mice.

Oral self-administration: To determine the effects of the H1 MUT upon MA reinforcement and intake, an operant-conditioning procedure was employed and the data for the mean number of active nose-pokes, inactive nose-pokes and MA intake compared between WT and H1 MUT mice. This comparison was evaluated using mixed model ANOVA with the between-subjects factors of Genotype and Sex and the within-subjects factor of MA concentration (80, 120, 160, 200, 300 and 400 mg/L). In a follow-up study, WT and H1 MUT mice were trained to self-administer the 200 mg/L MA concentration over the course of 14 days. The data for this study were analyzed using mixed model ANOVA with Genotype and Sex as between-subjects factors and Day as the repeated measure (Day 1 to 14). To interrogate potential genotypic differences in bitter tastant sensitivity, the dose-response function for quinine intake was determined in a separate cohort of mice and the data were analyzed using a mixed model ANOVA with between-subjects factors of Genotype and Sex and repeated measures on the Quinine Concentration factor (0.003, 0.01, 0.03, 0.1, 0.3 and 0.6 mg/ml).

In vivo microdialysis: To relate genotypic differences in behavior to changes in extracellular DA and glutamate within the NAc, we conducted a series of *in vivo* microdialysis experiments. The first series of experiments employed no net-flux microdialysis procedures and the ensuing dose-response data were analyzed by linear regression to determine the extraction fraction/clearance of the neurotransmitter (determined by the slope of the regression) and the basal neurotransmitter content (determined by x=0 from the regression). The extraction fraction and content were analyzed by an univariate ANOVA with the between-subjects factors of Sex and Genotype. The second series of experiments examined the time-course of MA-induced changes in extracellular DA, DOPAC and glutamate. The average baseline neurotransmitter content for the 60 min prior to MA injection was analyzed using an univariate ANOVA along the between-subjects factors of Genotype and Sex. Mice were slated to receive one of two MA doses (0.5 mg/kg and 2.0 mg/kg) and the data for each neurotransmitter were expressed as a percent change from the average baseline and analyzed using a mixed model ANOVA with Genotype and Sex as between-subjects factors and repeated measures on the Time factor (12, 20-min, bins), separately for each MA dose.

Conditioned place preference (CPP): To examine genotypic differences in MA reward, we assessed MA-CPP by quantifying the change in time spent on drug-paired side on Day 8 minus Day 1 or on Day 9 minus Day 1. Preference was analyzed using a three-way ANOVA with Genotype, Sex, and Treatment (saline, 0.5 mg/kg MA, and 2 mg/kg MA) as between-subjects factors. Because this analysis indicated genotype and dose-dependent change in MA-CPP, we ran two-tailed unpaired t-tests at each dose to identify genotypic

differences in MA-CPP. To assess potential genotypic differences in MA-induced locomotor activity in the smaller arena containing the textured floor that comprised the MA-CPP side (Days 2, 3, 4, and 5) as well as in the entire arena (Days 1, 8 and 9), we analyzed distance traveled in 5-min bin using a mixed effects ANOVA with Genotype, Sex, and Treatment (saline, 0.5 mg/kg, or 2 mg/kg MA) as between-subjects factors and repeated measures on Time (12, 5-min bins), separately for each day. Two-tailed unpaired t-tests were used to determine the sources of main effects of Genotype and Treatment and interactions with Time.

Behavioral test battery: To determine the effects of Genotype upon sensorimotor function and affect, WT and H1 MUT mice were subjected to a behavioral test battery consisting of PPI, the novel object test, marble-burying, light-dark shuttle-box, Porsolt swim test, and motor coordination on a rotarod. The data generated from these assays were analyzed using two-tailed unpaired t-tests.

Quantification of DA content and MA metabolites and DAT-mediated DA uptake: To determine whether there was a genotypic difference in DA content at baseline and MA metabolite after MA injection, a two-tailed unpaired t-test was performed. In examining whether there in an MA-induced change on DAT-mediated DA uptake between WT and H1 MUT mice, a two-way ANOVA with Genotype and Treatment (saline and MA) as between-subjects factors was used.

MA-induced locomotor activity assessment prior to tissue collection for mass spectrometry: To replicate the reduction in MA-induced locomotor activity in H1 MUT mice that we previously observed under identical conditions (Yazdani et al., 2015), we examined total

distance traveled in 5 min-bin, separately for Days 1, 2, and 3 via mixed effects ANOVA with Genotype, Sex, and Treatment (saline and 2 mg/kg MA) as between-subjects factors and Time as the repeated-measures factor. Two-tailed unpaired t-tests were used to determine sources of the main effects of Genotype and interactions with Time.

Immunoblotting and IHC: To examine the effect of Genotype on TH protein expression via immunoblotting and IHC, two-tailed unpaired t-test was performed on loading control-normalized data between WT and H1 MUT. To determine whether there was an effect of Sex on DAT protein expression, two-way ANOVA with Genotype and Sex as between-subjects factors was conducted. Two-tailed unpaired t-tests were used to determine sources of the main effects of Sex and interactions with Genotype. To examine MA-induced changes in protein expression including DAT, hnRNP H and mitochondrial proteins, two-way ANOVA with Genotype and Treatment as between-subjects factors was conducted. For hnRNP H expression in the synaptosome, the significant main effect of Genotype was followed up with two-tailed unpaired t-tests to examine differences between WT and H1 MUT.

For all behavioral studies, we used an effect size of Cohen's $d = 0.9$ to guide our sample size based on genotypic differences in MA-induced locomotor activity at 30 min post-MA in our previously published data from H1 MUT mice (Yazdani et al., 2015). We used G*Power 3 (Faul et al., 2007) to calculate a sample size of $n = 16$ per genotype required for 80% power ($p < 0.05$). All behavioral studies utilized both male and female mice. All data are presented as means of replicates from each experiment ± SEM. In summary, for experiments in which two conditions were compared, a two-tailed unpaired

t-test was used to analyze the data unless otherwise specified. For experiments in which multiple factors were evaluated, ANOVA was used and significant interaction was deconstructed along the relevant factor to examine main effects and group differences followed-up using t-tests. Statistical p value threshold for t-test and ANOVA was set to 0.05. The data comprising oral self-administration in vivo microdialysis were analyzed in SPSS (Version 21). All other data were analyzed in R (RRID:SCR_001905).

Data and Code Availability

All related data and materials are available upon request. The mass spectrometry proteomics data are available in MassIVE under proteome exchange accession number PXD014813.

CHAPTER IV: The dynamic, methamphetamine-induced hnRNP H interactome reveals synaptic RNA-binding targets associated with reduced DA release and behavior

ABSTRACT

The genetic factors underlying risk for psychostimulant addiction remain largely unknown. We previously identified *Hnrnph1* as a QTG with a set of 5'UTR functional variants underlying reduced MA behavioral sensitivity and hnRNP H protein expression. Mice with a heterozygous frameshift deletion in the first coding exon (containing the first RNA recognition motif) of *Hnrnph1* (H1 MUT) showed reduced MA-induced behaviors and DArelease. H1 MUT also showed a two-fold increase in synaptosomal localization of hnRNP H and proteomic evidence for mitochondrial dysfunction. To inform the mechanism linking hnRNP H dysfunction with reduced methamphetamine-induced DA release and behavior, we surveyed RNA targets of hnRNP H via cross-linking immunoprecipitation coupled with high-throughput sequencing (CLIP-seq) in striatal tissue at baseline and at 30 min post-MA (2 mg/kg, i.p.). hnRNP H mostly bound introns of target mRNA transcripts, confirming its role in splicing. MA treatment induced opposite changes in hnRNP H binding to mRNAs between H1 MUT versus WT, including 3'UTR targets in mRNAs enriched for synaptic proteins involved in DA release and psychostimulant-induced excitatory synaptic plasticity. RNA-binding, transcriptome and spliceome analyses triangulated on an upregulation of *Cacna2d2* transcript and decreased 3'UTR usage in response to MA in H1 MUT mice. *Cacna2d2* codes for a presynaptic, voltage-gated calcium channel subunit that could regulate MA-induced DA release and

behavior. Our study provides new insight into the rapid methamphetamine-induced cell biological adaptations that are regulated by hnRNP H and likely other RNA-binding proteins working in concert to modulate synaptic transmission. (Yazdani et al., 2015)(Yazdani et al., 2015)(Yazdani et al., 2015)(Yazdani et al., 2015)

INTRODUCTION

MA is a highly addictive psychostimulant with strong abuse potential and neurotoxic effects on the central nervous system (Kish, 2008; Galbraith, 2015; Yazdani et al., 2015). In the United States, the drug overdose death rate involving psychostimulants increased nearly 5-fold from 2012 through 2018 and continues to rise (Hedegaard et al., 2020). There are currently no FDA-approved treatments for MA dependence. Understanding the cell biological mechanisms and adaptations underlying MA's psychostimulant properties will inform new therapeutic avenues. MA-induced DA release in the striatum is mediated through displacement of DA from synaptic vesicles through VMAT2 and the reverse transport of DA into the synapse through the DAT (Fleckenstein and Hanson, 2003; Siciliano et al., 2014). This increased DA release induced by MA contributes to the abuse potential of MA (Baumann et al., 2002). However, the rapid cell biological adaptations following MA administration, and their consequences on neurotransmission are not fully understood.

Genetic factors play a major role in risk for developing substance use disorders, including addiction to psychostimulants such as MA (Goldman et al., 2005; Ducci and Goldman, 2012). We identified *Hnrnph1* as a QTG for MA stimulant sensitivity in mice (Yazdani et al., 2015) and have since identified a set of quantitative trait variants within the 5'UTR associated with both decreased hnRNP H protein and MA-induced behavior (Ruan et al., 2020a). Furthermore, mice heterozygous for a 16 bp deletion within the first coding exon of *Hnrnph1* (H1 MUT) showed reduced sensitivity to MA-induced locomotor activity, reward, and reinforcement and reduced MA-induced extracellular DA in the

ventral striatum (Ruan et al., 2020a). Synaptosomal proteomic analysis of the striatum following MA administration identified opposite changes in the localization of several mitochondrial proteins in H1 MUT compared to WT mice, suggesting synaptic mitochondrial dysfunction as a cell biological mechanism underlying reduced MA-induced DA release and addiction-related behaviors (Ruan et al., 2020a).

RBPs such as hnRNP H1 (coded by *Hnrnph1*) regulate each step of the RNA life cycle from processing to localization to degradation (Darnell, 2013; Hentze et al., 2018). In human genetic studies, coding mutations in *HNRNPH1* and the gene paralog *HNRNPH2* are associated with severe neurodevelopmental disorders comprising mental retardation and intellectual disability (Pilch et al., 2018; Reichert et al., 2020). Increasing evidence links RBPs to substance use disorders, including FMRP and the family of hnRNPs (Bryant and Yazdani, 2016). Deletion of FMRP disrupts DA neuron development and alters psychostimulant-induced neuroplasticity and behavior (Fulks et al., 2010; Fish et al., 2013; Smith et al., 2014). Alternative splicing of exon 2 and transcriptional regulation of *Oprm1* (mu opioid receptor, MOR) is mediated through the binding of hnRNP H and recruitment of other hnRNPs to its intronic AGGG sequence (Xu et al., 2014). Translation repression of MOR is mediated through binding of hnRNP H and F at its 5'UTR (Song et al., 2012). Song et al. also demonstrated that morphine can increase expression of hnRNP K and poly(C)-binding protein 1 to upregulate MOR expression through binding of the two RBPs to its 5'UTR (Song et al., 2017). Thus, RBPs are critical for regulating RNA metabolism relevant to normal brain development and substance use disorders.

Hnrnph1 codes for an RBP that is expressed throughout the brain and belongs to the hnRNP H/F subfamily of hnRNP RBPs that engage in several aspects of RNA processing including pre-mRNA splicing, mRNA stability, transcriptional and translational regulation, and polyadenylation control (Honoré et al., 1995; Arhin et al., 2002; Han et al., 2010; Geuens et al., 2016; Uren et al., 2016). During cellular stress, RBPs including hnRNP H (Markmiller et al., 2018; Wall et al., 2020), hnRNP A1 (Guil et al., 2006), and hnRNP K (Fukuda et al., 2009) localize to stress granules in the cytoplasm to sequester mRNAs from being translated. The highly dynamic formation of stress granules induced by cellular stress suggests that the interaction of hnRNP H with its RNAs can change rapidly in response to environmental stimuli, including stress-induced signaling. Based on the multifunctional role of hnRNP H and our observations of reduced MA-induced DA release and behavior in H1 MUT mice (Yazdani et al., 2015; Ruan et al., 2020), we hypothesized that acute MA treatment would alter hnRNP H binding to transcripts coding for proteins that control MA-induced dopaminergic synaptic transmission, including those regulating DA release and clearance (Joffe et al., 2014), intracellular release of calcium (Uramura et al., 2000), and formation of reactive oxidative species (Hedges et al., 2018). We further hypothesized that disruption of this RBP in H1 MUT mice would impact basal gene expression, splicing, and function of its target RNAs and that acute MA treatment would perturb hnRNP H-RNA interactions differently in H1 MUT versus WT mice.

To address these critical questions, we dissected the *in vivo* mRNA targets of hnRNP H at baseline and in response to acute, systemic MA administration by assessing hnRNP H mRNA binding via CLIP-seq in the striatum. Complementary to this goal, we

conducted parallel bulk RNA-seq from the same samples which allowed us to determine the relationship between hnRNP H binding and transcriptional regulation in H1 MUT versus WT mice. This 2 x 2 design permits the ability to identify baseline differences in RNA-binding targets as a function of H1 MUT as well as the dynamic, MA-induced hnRNP H interactome and how this is also affected by H1 MUT. Genotype x Treatment interactions in the MA-induced interactome could reveal the dysregulated dynamic, downstream changes in cell biological signaling that lead to functional reductions in MA-induced DA release and behavior.

RESULTS

H1 MUT mice showed reduced MA-induced locomotor activity relative to WT

H1 MUT and WT mice were subjected to a 3-day behavioral protocol to assess MA-induced locomotor activity prior to tissue collection on Day 3. Performing CLIP specifically in the striatum required a large quantity of tissue. For this reason, we pooled striata (left and right) from four mice (2 females and 2 males per pooled sample) for each condition (**Tables A4 and A5**). The data reported here represent the averaged locomotor activity from four mice per replicate for each of the four conditions listed. On the saline (SAL)-treated Days (Day 1 and Day 2), both WT and H1 MUT mice showed no significant difference in locomotor activity (**Figure 29A-B**). On Day 3, after an acute dose of MA at 2 mg/kg, H1 MUT mice showed reduced locomotor activity compared to WT (**Figure 29C**) (Yazdani et al., 2015; Ruan et al., 2020a). Importantly, there was no significant genotypic difference in response to SAL on Day 3 (**Figure 29C**), indicating that the genotypic difference was specific to MA treatment. The striatum was harvested from each mouse at 30 min post-injection on Day 3 for CLIP-seq processing.

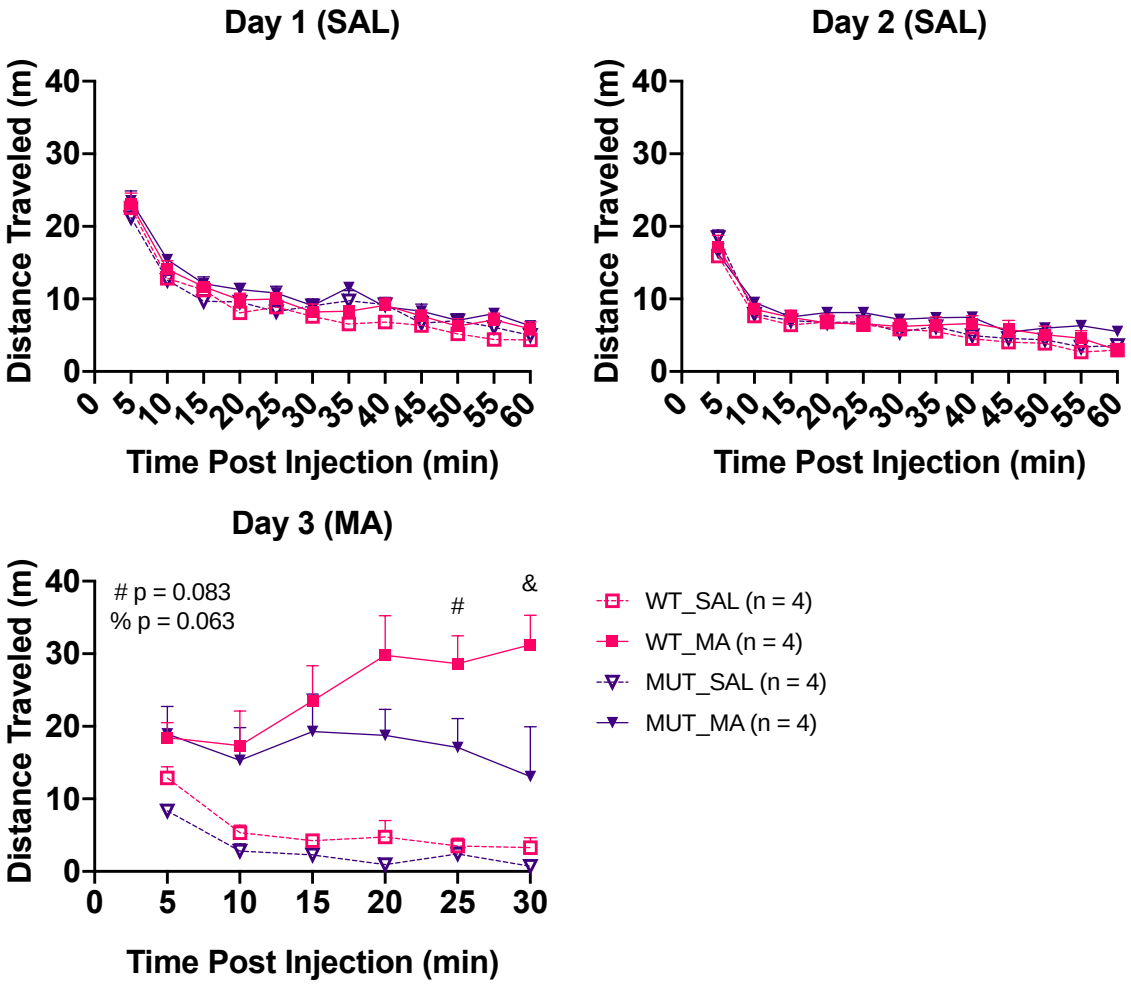

Figure 29. MA-induced locomotor activity in H1 MUT versus WT mice.
On Days 1 and 2, mice were injected (i.p.) with saline (**SAL**) and placed into testing apparatus for 1 h. On Day 3, mice were injected (i.p.) with 2 mg/kg methamphetamine (**MA**) and placed into testing apparatus for 30 min followed by immediate sacrifice and removal of the striatum. **(A-B):** Locomotor activity on Day 1 **(A)** and Day 2 **(B)** for 1 h in 5-min bins. There was no genotypic difference in total distance traveled in response to SAL on Day 1 or Day 2 [Day 1: $F(11,616)_{\text{Genotype x Treatment x Time}} = 0.841$, $p = 0.599$; Day 2: $F(11,616)_{\text{Genotype x Treatment x Time}} = 1.181$, $p = 0.296$]. **(C):** MA-induced locomotor activity on Day 3 for 30 min in 5-min bins. 30 min post MA injection, mice were sacrificed and striatum from each mouse was dissected and harvested. H1 MUT showed less locomotor activity compared to WT [$F(5,280)_{\text{Genotype x Treatment x Time}} = 7.354$, $p = 1.70e\text{-}06$]. There was also a significant decrease in total distance traveled in H1 MUT relative to WT in response to SAL on Day 3 at 0 – 5 min bin $F(1,30) = 6.687$, $^{\%}p = 0.015$; and a significant decrease in distance traveled in H1 MUT relative to WT in response to MA on Day 3 at 10 – 15 min bin [$F(1,30) = 5.163$, $^{*}p = 0.030$, 15 – 20 min bin [$F(1,30) = 5.259$, $^{*}p = 0.029$], 20 – 25 min bin [$F(1,30) = 5.187$, $^{*}p = 0.030$], and 25 – 30 min bin [$F(1,30) = 5.895$, $^{*}p = 0.021$]. No effect of Sex or interaction of Sex with other factors was detected for any of the measure reported. n = 8 per Sex per Genotype per Treatment.

hnRNP H binding sites contain G-rich binding motifs, with enrichment in the intronic regions

To our knowledge, there are no *in vivo* CLIP studies reported for hnRNP H in whole brain tissue or in specific brain regions. Accumulating evidence from our lab indicates a role of hnRNP H in MA addiction liability (Ruan et al., 2020). Defining a set of RNA targets regulated by hnRNP H would inform key mechanisms modulating these MA-induced behavioral responses. To identify the *in vivo* hnRNP H targets, we performed CLIP in the striatum of H1 MUT versus mice, both at baseline (SAL) and in response to MA with an antibody specific for hnRNP H. We previously validated the antibody to be specific for the C-terminus of hnRNP H via immunoabsorption with a blocking peptide for the epitope (Ruan et al., 2018). Here, we show that the antibody was able to specifically pull down hnRNP H at approximately 50 kDa with no signal detected at this size using rabbit IgG (**Figure A7A**; Lane 6 versus Lane 3). In addition, it is important to note that we used stringent lysis and wash conditions according to the CLIP protocols previously reported (Van Nostrand et al., 2016). We subsequently determined that 20 μg of hnRNP H antibody was the optimal amount needed by visual inspection of the band intensity at 50 kDa which was greater at 20 μg versus 10 μg antibody but similar at 20 and 30 μg antibody (**Figure A7B**).

Performing CLIP with anti-hnRNP H antibody in H1 MUT and WT mice followed by RNase digestion and radiolabeling of nucleic acid across four different RNase concentrations indicated RNA-specific pulldown. As expected, treatment with increasing concentrations of RNase fragmented the CLIP samples into different sizes (**Figure 30A**;

from left to right, Lanes 3 – 6), with higher concentrations of RNase more readily digesting the RNA into smaller fragments. As we decreased the concentrations of RNase used for RNA fragmentation, a higher level of RNA was detected (Figure 30A; from left to right, Lanes 3 – 6), indicating the hnRNP H CLIP was RNA-dependent. Longer incubation of CLIP samples with RNase resulted in lower amount of RNA, providing further support that hnRNP H CLIP was RNA-dependent, with 3-min digestion time being the most optimal (**Figure A7C**). Negative controls included immunoprecipitation (IP) from uncrosslinked sample (Lane 1) and IP using rabbit IgG from WT striatal tissues (Lane 2). No RNA was detected in the negative control samples (**Figure 30A**; Lanes 1 and 2), indicating the need for UV-crosslinking for RNA pull down and demonstrating the specificity of hnRNP H pull down. We chose a region approximately 30 – 70 nucleotides in size (50 – 80 kDa) for RNA extraction in order to capture the targets of hnRNP H *in vivo* (**Figure 30A**). We collected 3 replicates of CLIP samples from pools of striata of 4 mouse brains per condition (**Table A5**). For the negative control, we performed IgG mock IP from pools of striatum of 4 mouse brains per condition. The cDNA libraries generated from the CLIP samples of the IgG IPs did not yield any detectable PCR bands using gel electrophoresis, even after 28 PCR cycles (**Figure A8A**). However, for the CLIP samples, DNA bands corresponded to the correct size of the cDNA library (> 150 bp) were detected after 18 PCR cycles. For this reason, none of the four IgG cDNA libraries were subjected to sequencing. To account for differences in RNA abundance, we subjected the same samples used in CLIP for total RNA-seq and measured starting transcript abundance, which permitted normalization (**Figure A8B**).

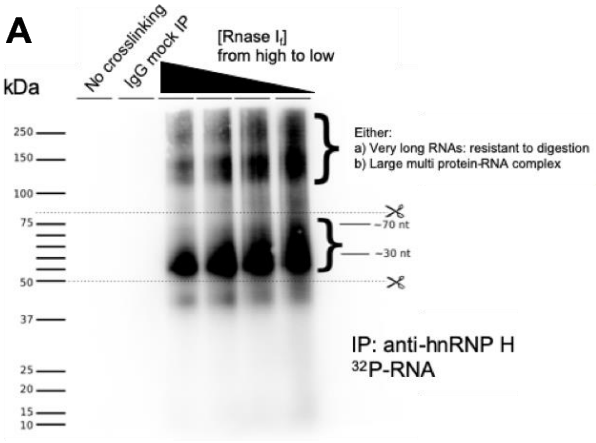

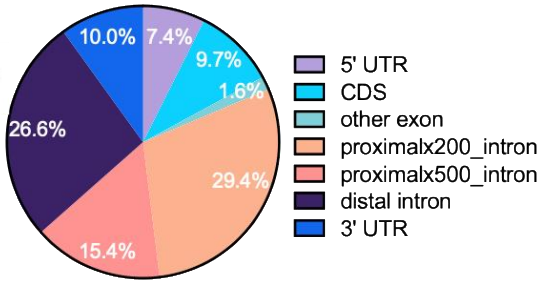

C

Rank	Motif	p value	% of targets
1		1E-129	14.21%
2		1E-108	5.78%
3		1E-102	20.44%
4		1E-101	46.28%
5		1E-71	3.00%

D hnRNP H-associated targets with G-rich motif in WT_SAL

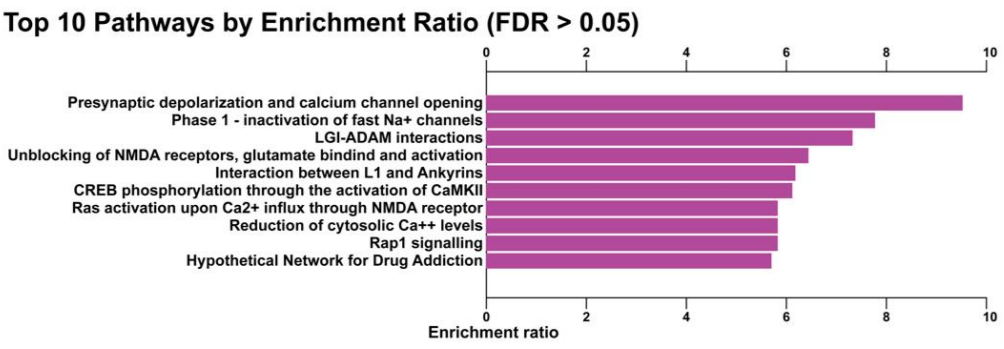

Figure 30. hnRNP H binding sites in untreated saline WT mice are enriched for introns and G-rich binding motifs.
eCLIP-seq revealed transcriptome-wide striatal target RNAs associated with hnRNP H in untreated saline WT mice. Peak calling of both uniquely and multi-mapped reads was performed using CLAM (Zhang and Xing, 2017). **(A):** CLIP and ^{32}P labeling of hnRNP H-bound RNA. CLIP conditions are shown for each lane: no crosslinking, IgG mock IP, and four different RNase I_f concentrations from high to low. An increasing amount of RNA was pulled down as the concentration of RNase I_f was decreased. The scissors denote the region above the molecular weight of hnRNP H (50 kDa) that was isolated for sequencing. The region runs from 50 to 80 kDa, which corresponds to 30 to 70 bp for RNA length. The larger bands observed above 100 kDa could represent very long RNAs that are resistant to digestion or large hnRNP H-associated protein-protein complexes bound to RNAs. **(B):** hnRNP H binds primarily to introns of target RNAs. More than 60% of hnRNP H CLIP sites are intronic. The pie chart shows the relative distribution of CLIP sites in 5'UTR, coding sequences (CDS), introns, and 3'UTR. Proximal introns indicate less than 200 (proximalx200_intron) or 500 (proximalx500_intron) nucleotides from the 5' or 3' splice sites with the remainder annotated as distal introns. Unannotated exons are referred to as "other exons". **(C):** Poly-G runs is the prevalent component of the hnRNP H binding motif. *De novo* motif discovery of hnRNP H CLIP sites was performed using Homer (Heinz et al., 2010). **(D):** hnRNP H RNA-binding targets containing G-rich motifs in their binding sites are most highly enriched for "presynaptic depolarization and calcium channel opening" pathway. Pathway enrichment analysis of hnRNP H RNA-binding targets with the poly-G motif was performed in WebGestalt (Liao et al., 2019) using the over-representation analysis methods. The top 10 pathways with FDR > 0.05 are shown, sorted from high to low enrichment ratio. The hnRNP H RNA-binding targets containing G-rich motifs associated with these pathways are listed in **Table A7.**

To define the targets of hnRNP H, we first focused the analysis on the WT_SAL (WT treated with SAL) condition. Specific sites of hnRNP H were identified using Peakcaller subcommand in CLAM (Zhang and Xing, 2017) to perform peak calling throughout the whole genome. The peak calling process was done on a gene-by-gene basis by breaking down each gene into 100 nucleotide bins and looking for enrichment of mapped reads over control (or total RNA-seq mapped reads) and specifying a negative-binomial model on observed read counts. Importantly, CLAM can call peaks using the combination of uniquely- and multi-mapped reads for inclusion of RNA binding sites that are repetitive elements (Zhang and Xing, 2017). We then annotated the peaks to their corresponding genomic regions. An example trace of a peak associated with the *Oprm1*

gene in the intron is shown in **Figure A9**. hnRNP H was shown to bind to *Oprm1* for transcriptional and translation regulation (Song et al., 2012; Xu et al., 2014). hnRNP H-associated peaks were defined as significantly enriched ($p < 0.05$ and peak signal intensity > 1.5) in CLIP samples over input RNA-seq samples. Analysis of the peaks across the gene subregions revealed enriched binding of hnRNP H in introns, comprising about 70% of total distribution (**Figure 30B**). This finding is consistent with previous characterization of hnRNP H in HeLa cells (Huelga et al., 2012; Uren et al., 2016), supporting successful isolation of hnRNP H-bound RNAs in mouse striatal tissue.

De novo motif discovery of significant hnRNP H-associated binding sites using the Homer database (Heinz et al., 2010) detected the top over-represented motif to be G-rich (**Figure 30C**). Closer examination of the highly enriched motifs around hnRNP H CLIP sites in 5'UTR, coding region sequence (CDS), introns, and 3'UTR detected these poly-G run to be more prevalent in intronic regions (**Table A6**). Previous individual and genome-wide studies of hnRNP H-RNA interactions in cultured cells identified binding sites containing the tetramer (T/G)GGG (Lefave et al., 2011; Uren et al., 2016), poly-G runs of various lengths (Katz et al., 2010; Russo et al., 2010), or poly-G stretches interspersed or terminated by A (Huelga et al., 2012). Our data supports poly-G tracts as a prevalent component of the hnRNP H binding motif, with particular enrichment of the motif in the intronic regions. These poly G-stretches in the introns have been shown to enhance hnRNP H binding (Han et al., 2005) and the length of the poly-G tracts was shown to positively correlate with splicing (Katz et al., 2010). The consistency of our CLIP-seq findings on the characteristics of hnRNP H binding sites with those previously reported validated our

results and supported our experimental protocol and analyses for successful isolation of hnRNP H-associated targets in mouse striatal tissue. To determine whether these hnRNP H binding targets harboring the G-rich motif share any common biological and molecular pathways, we performed pathway enrichment analysis and found these targets to be most enriched for "presynaptic depolarization and calcium channel opening," comprising of subunits of calcium channels encoded by *Cacna1a, Cacnb4, Cacna1e, Cacng4, Cacna1b, Cacng2, and Cacnb2* (**Table A7**), all of which are important for neurotransmission (Dolphin, 2012). Another RBP that binds to mRNA transcripts that encode for ion channels is FMRP (Darnell et al., 2011). Our findings implicate another RBP, hnRNP H, in binding to introns of calcium channel subunit transcripts to post-transcriptionally regulate gene expression at the level of splicing to adaptively modulate neurotransmission (**Table A8**).

hnRNP H regulates gene networks important for synaptic function

To determine whether hnRNP H regulates a subset of targets in the striatum, pathway and gene ontologies (GO) analyses were performed to examine the biological and molecular functions of hnRNP H targets. Gene sets along with the associated genes are organized into an enrichment map network as depicted in **Figure 31**. Gene sets are connected to one another depending on the number of shared genes, where groups of highly related gene sets are clustered together. The enrichment map network revealed a clear overrepresentation of gene sets related to synaptic function (**Figure 31**). The top five enriched gene sets include transmission across chemical synapse, neuronal system, axon guidance, muscle contraction, and mRNA processing (nodes indicated in asterisk **Figure 31**). This finding indicates that

hnRNP H post-transcriptionally regulates pre-mRNAs and mRNAs encoding for proteins for modulating synaptic function that plausibly contribute to the neural mechanism underlying hnRNP H dysfunction in reducing acute response to MA.

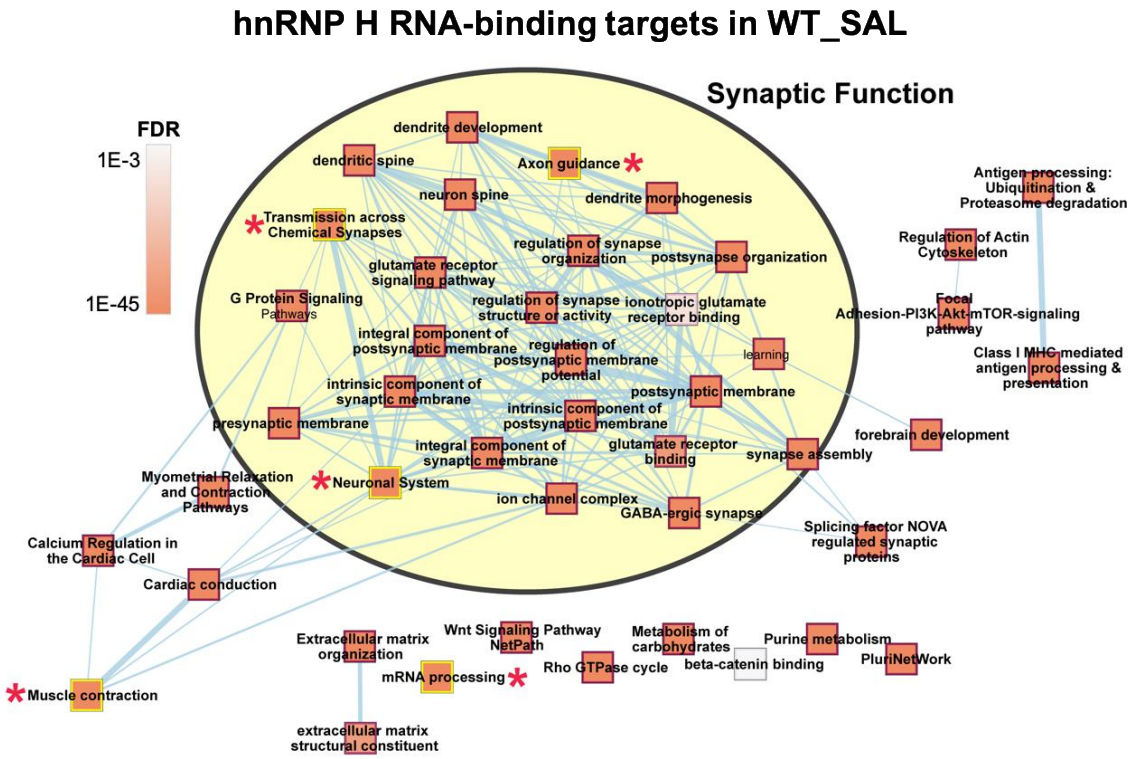

Figure 31. hnRNP H RNA-binding targets in untreated saline WT mice are enriched for synaptic function.
A list containing all hnRNP H targets meeting the CLAM peak signal threshold cutoff of greater than 1.5 was used as the input for gene ontology and pathway analysis using g:Profiler (Raudvere et al., 2019). The top 10 gene ontology (molecular function, cellular component and biological process) as well Reactome and WikiPathways were selected for visualization and clustering of gene-set enrichment as a network in the EnrichmentMap Cytoscape App (Merico et al., 2010). Gene sets are organized into a network enrichment map as shown. Each square (node) represents a gene set and each edge represents mutual overlaps. The five nodes indicated in asterisk represent the top five most enriched gene sets by p-value. A majority of gene sets are annotated for synaptic functions, as indicated by the asterisks.

Hnrnph1 mutation and MA treatment induce changes in targets of hnRNP H

In order to test the hypothesis that hnRNP H, like other RBPs, can respond to cellular stimuli, we examined both baseline and MA-induced changes in hnRNP H1-RNA interactions to identify targets of hnRNP H1 that could comprise neurobiological mechanisms of the acute behavioral response and potentially the long-term cellular adaptations occurring from repeated drug exposure. To date, dynamic RNA-protein interaction studies that examine the effect of exposure to drugs of abuse such as MA on changes in RNA-binding are lacking. We also want to determine whether the heterozygous 16-bp deletion (part of the first RNA recognition motif in *Hnrnph1*) affects hnRNP H1 binding that can account for the difference in acute behavioral response observed between H1 MUT and WT. Thus, in addition to examining MA perturbation on the hnRNP H RBP interactome, we also examined differential RNA binding in H1 MUT mice versus WT and its potential interaction with drug treatment. Comparing changes in binding across the subregions of the mRNA transcript would tell us whether MA and the *Hnrph1* mutation impact splicing function (via binding to introns) or mRNA stability and/or translation (via binding to 3'UTRs).

In using the 2 x 2 design to analyze the read distribution separately across the 3'UTR, introns, CDS, and 5'UTR for each of the four conditions, we again discovered over-representation of binding sites for intronic regions of the mRNA transcripts across all four conditions (**Figure 32A**). In comparison to the hnRNP H binding events at steady state (those detected in WT_SAL), changes in hnRNP H binding at 3'UTR and introns due to MA treatment and Genotype were more variable compared to binding in the CDS and

5’UTR than would be expected by chance (**Table A9**). The variation detected for the proportion of intronic binding across the four conditions indicated signaling events shifted the binding of hnRNP H to its intronic targets that can disrupt splicing of mRNA transcripts. In response to MA, WT mice showed an increase in the percentage of 3’UTR binding sites whereasH1 MUT mice showed the exact opposite, namely, a decrease in the percentage of 3’UTR binding sites in response to MA. The shift in the proportion of binding events at the 3’UTR suggested that MA-induced signaling events altered hnRNP H-dependent post-translational regulation at the level of mRNA stability, polyadenylation site usage, and translation. Thus, the binding interaction of these 3’UTRs and intronic targets to hnRNP H warranted further investigation.

The opposite change in the percentage of 3’UTR targets between H1 MUT and WT in response to MA prompted us to look more closely at the hnRNP H RNA-interactome. By plotting changes in hnRNP H-associated CLIP peaks in the WT against H1 MUT in response MA relative to SAL, a negative correlation was identified (**Figure 32B**). An hnRNP H CLIP peak with increased binding in the WT in response to MA was more likely to show decreased binding in the H1 MUT. This negative correlation potentially indicates that the heterozygous deletion in the H1 MUT exerts a dominant negative effect on hnRNP H1 function, especially in response to MA. Thus, the hnRNP H shift in binding depends on both MA and Genotype and those CLIP peaks that show Genotype x Treatment interaction would show a stronger negative correlation (**Figure 32B**, points highlighted in magenta).

Our CLIP-seq dataset defined more than 1000 mRNAs transcripts responsible for Genotype and MA effects (**Figure A10A-B**). To narrow on the list to those that are most relevant for the neural mechanisms driving reduced MA-induced dopamine release and behavior in H1 MUT mice, we focused on the ones that show Genotype x Treatment interaction. These targets are enriched for pathways associated with psychostimulant-induced synaptic plasticity including "amphetamine addiction," "long-term potentiation," and "dopaminergic synapse" (**Figure 32C and Table A10A**). The targets are found to be in cellular components of "ATPase complex", "myelin sheath," "neuron spine", and "nuclear chromatin", all of which are involved in the cellular adaptations underlying exposure to drug of abuse (**Figure 32D and Table A10B**). Furthermore, the enrichment map network of top over-represented pathways and GO terms for these targets revealed clustering of nodes associated with synaptic function (**Figure A10C**). The post-transcriptional regulation of the mRNA transcripts for these targets (most of which are important for synaptic transmission in response drugs of abuse) by hnRNP H to could be part of the neural mechanisms responsible for driving the MA phenotypic difference between H1 MUT and WT mice.

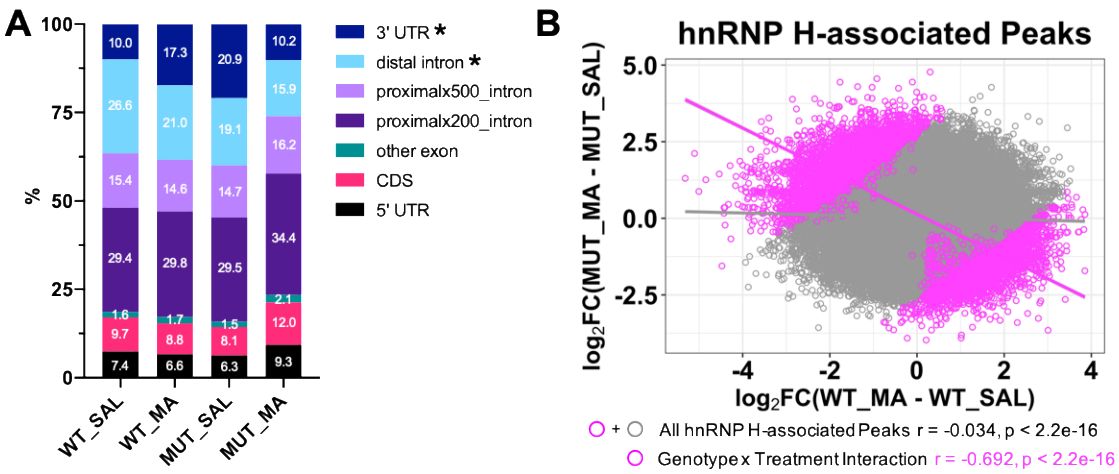
A
100
75
50
25
0
%
10.0
26.6
15.4
29.4
1.6
9.7
7.4
17.3
21.0
14.6
29.8
1.7
8.8
6.6
20.9
19.1
14.7
29.5
1.5
8.1
6.3
10.2
15.9
16.2
34.4
2.1
12.0
9.3
WT_SAL
WT_MA
MUT_SAL
MUT_MA
3' UTR *
distal intron *
proximalx500_intron
proximalx200_intron
other exon
CDS
5' UTR
B
hnRNP H-associated Peaks
log2FC(MUT_MA - MUT_SAL)
5.0
2.5
0.0
-2.5
-4
-2
0
2
4
log2FC(WT_MA - WT_SAL)
All hnRNP H-associated Peaks r = -0.034, p < 2.2e-16
Genotype x Treatment Interaction r = -0.692, p < 2.2e-16

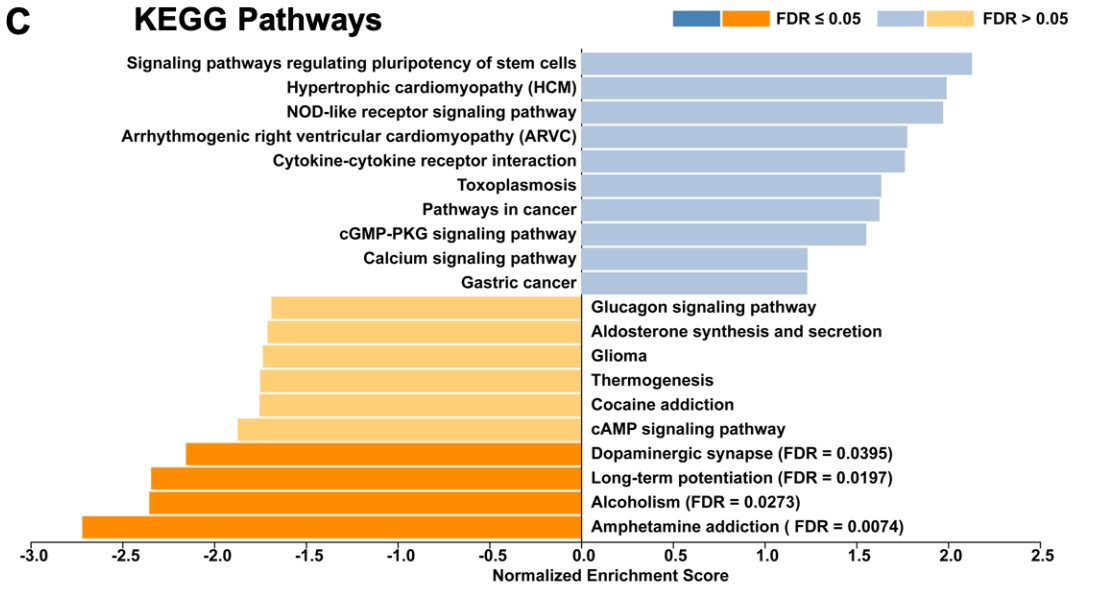
C
KEGG Pathways
FDR ≤ 0.05
FDR > 0.05
Signaling pathways regulating pluripotency of stem cells
Hypertrophic cardiomyopathy (HCM)
NOD-like receptor signaling pathway
Arrhythmogenic right ventricular cardiomyopathy (ARVC)
Cytokine-cytokine receptor interaction
Toxoplasmosis
Pathways in cancer
cGMP-PKG signaling pathway
Calcium signaling pathway
Gastric cancer
Glucagon signaling pathway
Aldosterone synthesis and secretion
Glioma
Thermogenesis
Cocaine addiction
cAMP signaling pathway
Dopaminergic synapse (FDR = 0.0395)
Long-term potentiation (FDR = 0.0197)
Alcoholism (FDR = 0.0273)
Amphetamine addiction (FDR = 0.0074)
-3.0
-2.5
-2.0
-1.5
-1.0
-0.5
0.0
0.5
1.0
1.5
2.0
2.5
Normalized Enrichment Score

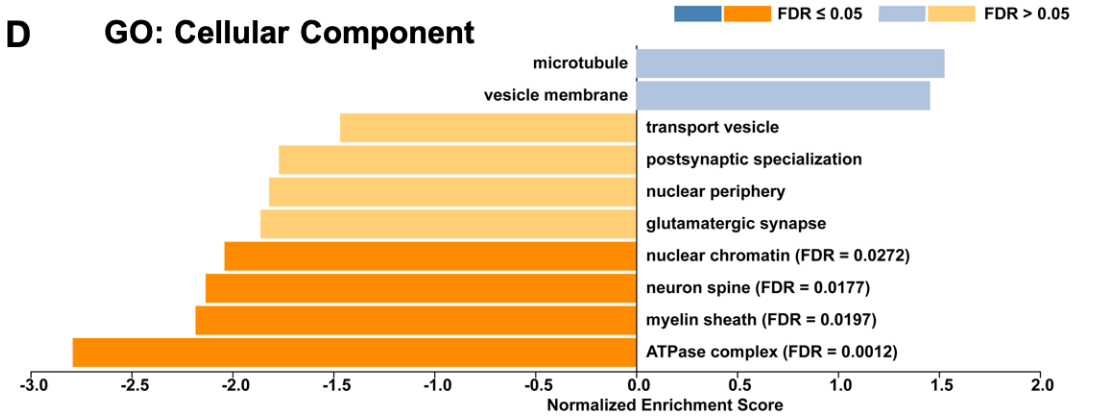
D
GO: Cellular Component
FDR ≤ 0.05
FDR > 0.05
microtubule
vesicle membrane
transport vesicle
postsynaptic specialization
nuclear periphery
glutamatergic synapse
nuclear chromatin (FDR = 0.0272)
neuron spine (FDR = 0.0177)
myelin sheath (FDR = 0.0197)
ATPase complex (FDR = 0.0012)
-3.0
-2.5
-2.0
-1.5
-1.0
-0.5
0.0
0.5
1.0
1.5
2.0
Normalized Enrichment Score

Figure 32. hnRNP H RNA-binding targets showing a Genotype x Treatment interaction are enriched for pathways and cellular components involved in drug-evoked synaptic plasticity. CLIP-seq analysis revealed transcriptome-wide striatal RNA targets associated with hnRNP H in untreated SAL or MA-treated H1 MUT versus WT mice. Peak calling in CLAM (Zhang and Xing, 2017) was performed separately for each of the four conditions. For differential analysis, peak calling was also performed using CLAM (Zhang and Xing, 2017) on the merged bam file across all conditions followed by read counts against the identified peaks and differential analysis of peak intensity. **(A):** In comparison to untreated saline WT mice (WT_SAL), only the percentages of hnRNP H binding events associated with 3'UTR and introns were significantly different from those detected in WT_SAL (See chi-square tests in **Table A7**). The percentage that comprised 3'UTRs varied between Genotype and Treatment with an increase in response to MA versus SAL in WT mice and a decrease in response to MA versus SAL in H1 MUT mice (chi-square test: *$p < 0.001$). All of the intron binding events (including distal introns and proximal introns) also varied significant from WT_SAL (chi-square test: all p's < 0.001, with the exception of MUT_SAL vs WT_SAL where $p = 0.453$ for proximalx200_intron). The relative distribution of hnRNP H binding sites over the gene elements for each of the four conditions in the 2 x 2 (Genotype x Treatment) experimental design is shown. WT_MA = WT treated with MA; MUT_SAL = H1 MUT treated with SAL; and MUT_MA = H1 MUT treated with MA. **(B):** An hnRNP H CLIP peak with increased binding in WT mice in response to MA is more likely to show decreased binding in H1 MUT mice. The plot shows a negative correlation between log_2FC(WT_MA vs WT_SAL) and log_2FC(MUT_MA vs MUT_SAL) (Pearson's correlation coefficient $r = -0.034$, $p < 2.2e-16$). The hnRNP H CLIP peaks showing Genotype x Treatment interaction (highlighted in magenta) showed a much stronger negative correlation (Pearson's $r = -0.692$, $p < 2.2e-16$). Each data point corresponds with a hnRNP H-associated CLIP peak. **(C):** Strong enrichment scores for the "amphetamine addiction", "alcoholism", "long-term potentiation", and "dopaminergic synapse" pathways were detected for those hnRNP H RNA-binding targets showing decreased binding to hnRNP H in the H1 MUT versus WT in response to MA relative to SAL. The hnRNP H RNA-binding targets associated with these pathways are listed in **Table A10A.** GSEA analysis was performed in WebGestalt (Liao et al., 2019) on a ranked list (based on log_2FC) of hnRNP H targets showing Genotype x Treatment interaction. **(D):** Strong enrichment for "ATPase complex", "myelin sheath", "neuron spine" and "nuclear chromatin" cellular components were detected for those hnRNP H RNA-binding targets showing decreased binding to hnRNP H in the H1 MUT versus WT in response to MA relative to SAL. The hnRNP H RNA-binding targets associated with these cellular components are listed in **Table A10B**.

3'UTR and intronic targets of hnRNP H show consistent enrichment for pathways involved in excitatory and psychostimulant-induced synaptic plasticity

Hnrnph1 binding events comprising the intron and 3'UTRs both showed Genotypic and MA-induced changes compared to the untreated WT_SAL condition (**Figure 32A**). We reasoned that targets showing a MA Treatment x Genotype interaction in hnRNP H binding

at the introns and 3'UTRs are potential mechanistic targets that warrant further investigation and validation. We subsetted the hnRNP H-interactive CLIP peaks into separate subgenic regions (5'UTR, 3'UTR, intron, or CDS). Subsetting the binding events allowed us to characterize the impact of changes in binding on specific types of hnRNP H-dependent post-transcriptional regulation by MA and the *Hnrnph1* mutation. Do the 3'UTR and intron targets also show this dominant negative relationship in their association to hnRNP H in response to MA between H1 MUT and WT? Which subset of subgenic targets are enriched for pathways associated with the synaptic functions that we previously identified?

We examined binding of hnRNP H across transcripts by plotting normalized $\log_2$CPM (counts per million) mapped reads to subgenic regions (**Figure 33**). The row of each heatmap represents a binding site sorted by p value from smallest to largest, where those with a p-value of less than 0.01 are shown in the heatmap. Interestingly, a distinct pattern was observed for the 3'UTR targets with opposing changes in the dynamics of hnRNP H binding in response to MA treatment between WT and H1 MUT. In response to MA relative to SAL, hnRNP H showed increased 3' UTR binding in WT but decreased 3' UTR binding in H1 MUT. Again, this was the same dominant negative relationship that was observed previously reported in **Figure 32B**. In plotting $\log_2$FC[WT_MA – WT_SAL] versus $\log_2$FC[MUT_MA – MUT_SAL] for each of these subgenic regions separately, a negative correlation was also detected for 3'UTR as well as 5'UTR, CDS, and introns. However, this dominant negative association with hnRNP H was most pronounced for the top, high confidence 3'UTR targets (**Figure 33**). Even at steady state with no MA

administration (WT_SAL versus MUT_SAL), increased binding of hnRNP H to these 3'UTR targets was detected.

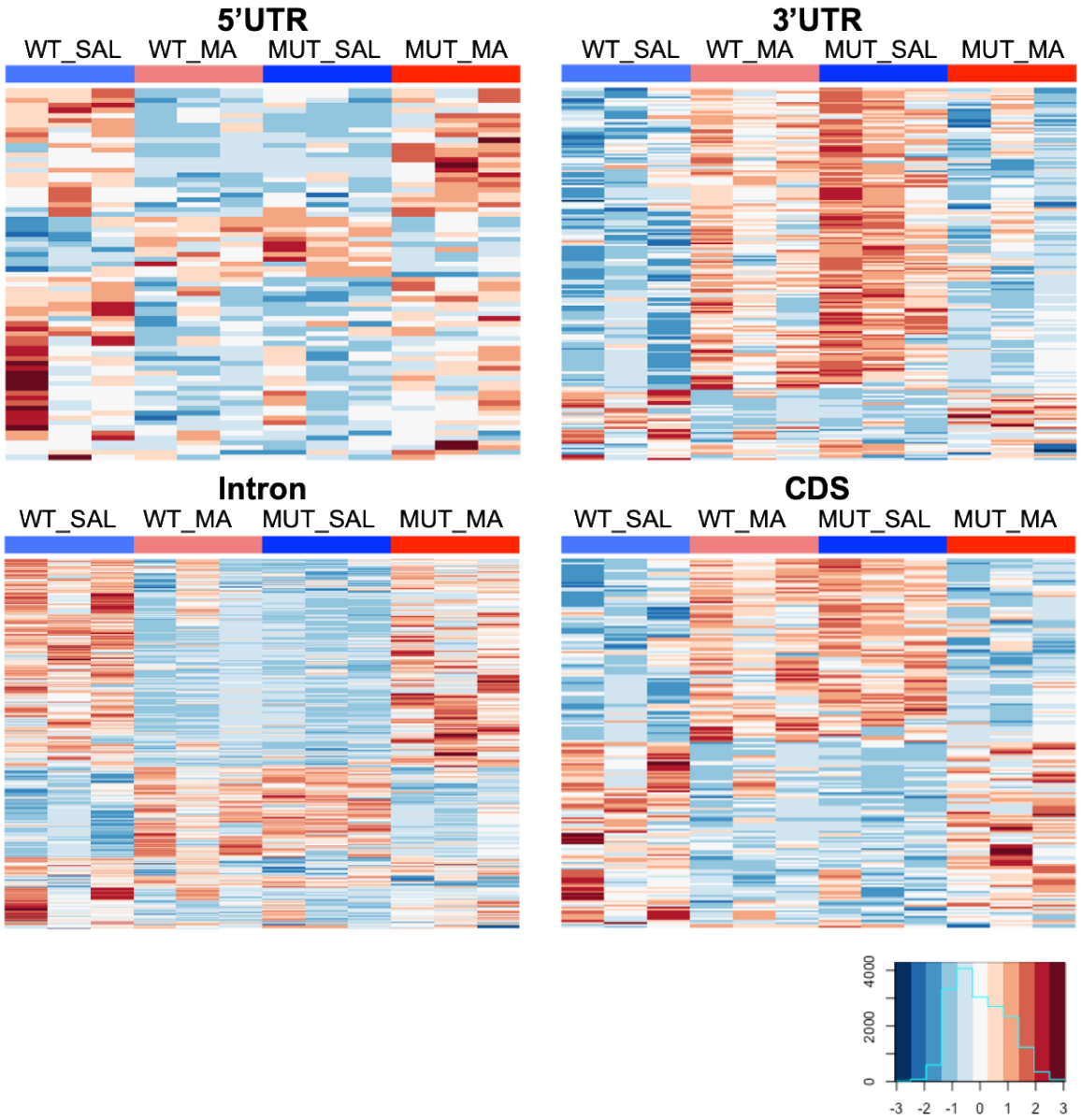

Figure 33. 3'UTR targets showed opposing changes in binding to hnRNP H between H1 MUT and WT in response to MA.
Genotype x Treatment-associated hnRNP H CLIP peaks, divided into 4 gene elements: 5'UTR, 3'UTR, intron, and CDS. Heatmaps show normalized $\log_2$CPM (count-per-million) read counts for significant peaks demonstrating a Genotype x Treatment interaction ($p < 0.05$). The interaction is expressed as $(MUT_{MA} - MUT_{SAL}) - (WT_{MA} - WT_{SAL})$. Relative to WT mice, a broad increase in binding of hnRNP H to the 3'UTR regions of RNA-binding targets under SAL (or basal) condition that decreases with MA treatment is detected in the H1 MUT mice.

To gain additional mechanistic insight into the 3'UTR targets showing a Genotype x Treatment interaction in binding, we performed separate KEGG pathway enrichment analysis for each type of subgenic binding site. Interestingly, only the 3'UTR targets showed significant enrichment for pathways associated with psychostimulant-induced synaptic plasticity (**Table 10**), whereas the 5'UTR and CDS targets did not show significant enrichment for any pathways. Some of these 3'UTR targets, including *Gnas, Prkcb, Gria2, Grin2a,* and *Calm2* are involved in "dopaminergic synapse" and other 3'UTR targets including *Atp6v1b2, Atp60C, Slc6a1, Slc1a3, and Slc1a2* are involved in "synaptic vesicle cycling." Closer examination of targets linked to "synaptic vesicle cycling" (**Figure A11A**) and "dopaminergic synapse" (**Figure A11B**) pointed to an opposing change in hnRNP H binding as a function of Genotype and MA treatment, just as we previously observed in the heatmap for 3'UTR targets in **Figure 33**. The binding of RBPs to 3'UTRs of transcripts provides a rapid means for mRNA translation at sites distance from the cell body such as the synapse (Mayr, 2017; Harvey et al., 2018). Thus, in response to MA exposure, hnRNP H could plausibly regulate rapid changes in levels of proteins coded by genes involved in synaptic function via changes in 3'UTR binding to mRNA transcripts. Intronic targets also showed very similar enriched pathways as those found for 3'UTR targets, thus implicating hnRNP H in splicing of transcripts coding for proteins involved in synaptic function as well (**Table 11**). Thus far, our CLIP-seq data provided evidence for hnRNP H interacting with G-rich motifs within mostly introns and 3'UTRs of mRNAs to drive post-transcriptional gene regulation in response to MA. However, the functional impact (both the at level of gene expression and splicing) on these

mRNA transcripts have yet to be characterized.

Table 10. KEGG Enrichment analysis of dynamic hnRNP H 3'UTR targets.
The table shows those 3'UTR RNA targets responding to the interaction of Genotype and Treatment. The interaction is expressed as $(MUT_{MA} - MUT_{SAL}) - (WT_{MA} - WT_{SAL})$ with $p < 0.01$.

Pathway	Adjusted p	RNA targets
Long-term potentiation	1.36E-06	*Braf, Prkcb, Grm5, Ppp3r1, Hras, Gria2, Gnaq, Grin2a, Calm2*
Glutamatergic synapse	5.69E-06	*Gnas, Prkcb, Slc38a1, Grm5, Ppp3r1, Gria2, Gnaq, Grin2a, Slc1a3, Slc1a2*
Long-term depression	7.15E-05	*Gnas, Braf, Prkcb, Hras, Gria2, Gnaq, Ppp2r1b*
Salivary secretion	2.87E-04	*Gnas, Prkcb, Atp1b1, Atp1b2, Gnaq, Calm2, Vamp2*
Dopaminergic synapse	9.51E-04	*Gnas, Prkcb, Ppp2r5b, Gria2, Gnaq, Ppp2r1b, Grin2a, Calm2*
Aldosterone synthesis and secretion	9.51E-04	*Gnas, Prkcb, Pde2a, Atp1b1, Atp1b2, Gnaq, Calm2*
Amphetamine addiction	9.51E-04	*Gnas, Prkcb, Ppp3r1, Gria2, Grin2a, Calm2*
Gastric acid secretion	1.24E-03	*Gnas, Prkcb, Atp1b1, Atp1b2, Gnaq, Calm2*
Synaptic vesicle cycle	1.31E-03	*Atp6v1b2, Slc6a1, Slc1a3, Atp6v0c, Vamp2, Slc1a2*
Cocaine addiction	1.31E-03	*Gnas, Rgs9, Gria2, Cdk5r1,Grin2a*

Table 11. KEGG Enrichment analysis of dynamic hnRNP H intronic targets.
The table shows those intronic RNA targets responding to the interaction of Genotype and Treatment. The interaction is expressed as $(MUT_{MA} – MUT_{SAL}) – (WT_{MA} – WT_{SAL})$ with $p < 0.01$.

Pathway	Adjusted p	RNA targets
Oxytocin signaling pathway	1.31E-11	*Prkag2, Itpr1, Prkcb, Rock1, Cacnb2, Plcb1, Adcy5, Cacng2, Ryr2, Ppp1cb, Ppp3ca, Kcnj4, Camk1d, Ppp3r1, Cacna2d4, Cacna2d3, Cacna1d, Ppp1r12c, Camk4, Elk1, Camk2a, Map2k2, Cacna1c, Cacnb4, Gnas, Cacng8, Prkag1, Ppp3cb, Cacnb1, Hras, Rock2, Adcy6, Calm2, Plcb4*
Long-term potentiation	6.66E-09	*Itpr1, Prkcb, Gria1, Grin2b, Plcb1, Grin2a, Ppp1cb, Ppp3ca, Ppp3r1, Camk4, Camk2a, Map2k2, Cacna1c, Grin2d, Gria2, Ppp3cb, Hras, Calm2, Plcb4*
Glutamatergic synapse	7.93E-09	*Itpr1, Prkcb, Gria1, Grin2b, Plcb1, Adcy5, Grm4, Grin2a, Slc1a3, Ppp3ca, Gng7, Dlgap1, Ppp3r1, Grik5, Cacna1d, Cacna1c, Grin2d, Gria2, Gnas, Ppp3cb, Adcy6, Cacna1a, Slc38a3, Plcb4, Slc1a1*
Dopaminergic synapse	1.70E-08	*Itpr1, Prkcb, Gria1, Ppp1r1b, Grin2b, Plcb1, Mapk10, Adcy5, Grin2a, Ppp1cb, Ppp3ca, Gng7, Ppp2cb, Kif5c, Cacna1d, Mapk14, Camk2a, Cacna1c, Gria2, Gnas, Scn1a, Ppp3cb, Cacna1a, Calm2, Ppp2r2d, Plcb4, Ppp2r1b*
Adrenergic signaling in cardiomyocytes	3.34E-08	*Atp2b2, Cacnb2, Plcb1, Adcy5, Cacng2, Scn7a, Slc8a1, Ryr2, Ppp1cb, Cacna2d4, Cacna2d3, Ppp2cb, Cacna1d, Mapk14, Scn4b, Camk2a, Cacna1c, Atp1a2, Cacnb4, Gnas, Cacng8, Cacnb1, Adcy6, Calm2, Ppp2r2d, Plcb4, Atp1b2, Ppp2r1b*
Amphetamine addiction	5.46E-08	*Prkcb, Gria1, Ppp1r1b, Grin2b, Adcy5, Grin2a, Ppp1cb, Ppp3ca, Ppp3r1, Cacna1d, Camk4, Camk2a, Cacna1c, Grin2d, Gria2, Gnas, Ppp3cb, Calm2*
Circadian entrainment	1.88E-07	*Itpr1, Prkcb, Gria1, Grin2b, Plcb1, Nos1ap, Adcy5, Ryr2, Grin2a, Gng7, Cacna1h, Cacna1d, Camk2a, Cacna1c, Grin2d, Gria2, Gnas, Per1, Adcy6, Calm2, Plcb4*
cGMP-PKG signaling pathway	6.19E-07	*Itpr1, Atp2b2, Rock1, Prkce, Pde2a, Plcb1, Slc8a3, Adcy5, Mef2d, Slc8a1, Ppp1cb, Ppp3ca, Ppp3r1, Slc8a2, Cacna1d, Insr, Gna13, Map2k2, Cacna1c, Atp1a2, Mef2b, Ednra, Ppp3cb, Rock2, Adcy6, Calm2, Plcb4, Atp1b2*
Arrhythmogenic right ventricular cardiomyopathy (ARVC)	7.64E-07	*Cacnb2, Sgcd, Cacng2, Slc8a1, Ryr2, Cacna2d4, Ctnna2, Cacna2d3, Cacna1d, Dag1, Cacna1c, Cacnb4, Itgb8, Cacng8, Cacnb1, Gja1, Itga9*
Calcium signaling pathway	1.29E-06	*Itpr1, Prkcb, Atp2b2, Plcb1, Pde1a, Slc8a3, Htr2c, Slc8a1, Ryr2, Grin2a, Ppp3ca, Ppp3r1, Slc8a2, Cacna1h, Cacna1d, Camk4, Camk2a, Cacna1c, Chrna7, Grin2d, Ednra, Gnas, Ppp3cb, Cacna1a, Calm2, Itpka, Plcb4, Pde1b, Ptk2b*

Cacna2d2 as candidate hnRNP H target for reduced MA-induced behavior and dopamine release in H1 MUT mice

To explore whether the mRNA transcript(s) mediating reduced MA-induced behavior would also show functional changes in expression and/or splicing in response to Treatment and Genotype, in addition to a shift in mRNA-bind, we next sought to determine what the functional consequences of this change in binding were on mRNA transcript levels, and to parse direct effects on bound transcripts from indirect and downstream effects. To integrate striatal hnRNP H binding with gene expression and alternative splicing, we analyzed the transcriptome of striatal tissue from the same samples used in CLIP-seq. We performed both gene- and exon/intron-level transcriptome analysis to identify differentially expressed genes (**Figure A12**) and genes showing evidence for alternative splicing, namely genes showing significant differential exon or intron usage. *Cacna2d2* was the only gene that was identified across all three sets of analysis, including its identification as a binding target of hnRNP H, as a differentially expressed gene (Genotype x Treatment), and as a gene demonstrating differential exon/intron usage (Genotype x Treatment; **Figure 34A**). *Cacna2d2* showed an increase in expression in H1 MUT mice in response to MA and a decrease in WT mice (**Figure 34B**). A total of 19 genes showed a Genotype x Treatment interaction in differential gene expression (**Figure 34B**) with 6 of them (including *Cacna2d2*) overlapping with hnRNP H targets identified in CLIP-seq (circled in red in **Figure 34B** and listed in **Table A11**) – a 30% overlap in binding targets and differential expression is much greater than would be expected by chance (Fisher's exact test p = 6.11E-08). One of these 6 genes was the long noncoding RNA *Malat1* which is involved

in synapse formation and synaptic transmission (Zhang et al., 2017). Interestingly, hnRNP H has been shown to bind to *Malat1* in multiple studies (Uren et al., 2016; Arun et al., 2020; Scherer et al., 2020) and we previously identified a trans-eQTL for *Malat1* that originates within the *Hnrnph1* behavioral QTL for reduced MA-induced locomotor activity (Yazdani et al., 2015). The other overlapping hnRNP H targets and differential expressed genes include *Mir124*, *Gtf2e2*, *Unc13*, and *Camta1* (**Figure 34A-B**). It is possible that one or more of these differentially expressed and spliced mRNA transcript(s) contribute to the reduced MA-induced acute response in H1 MUT mice.

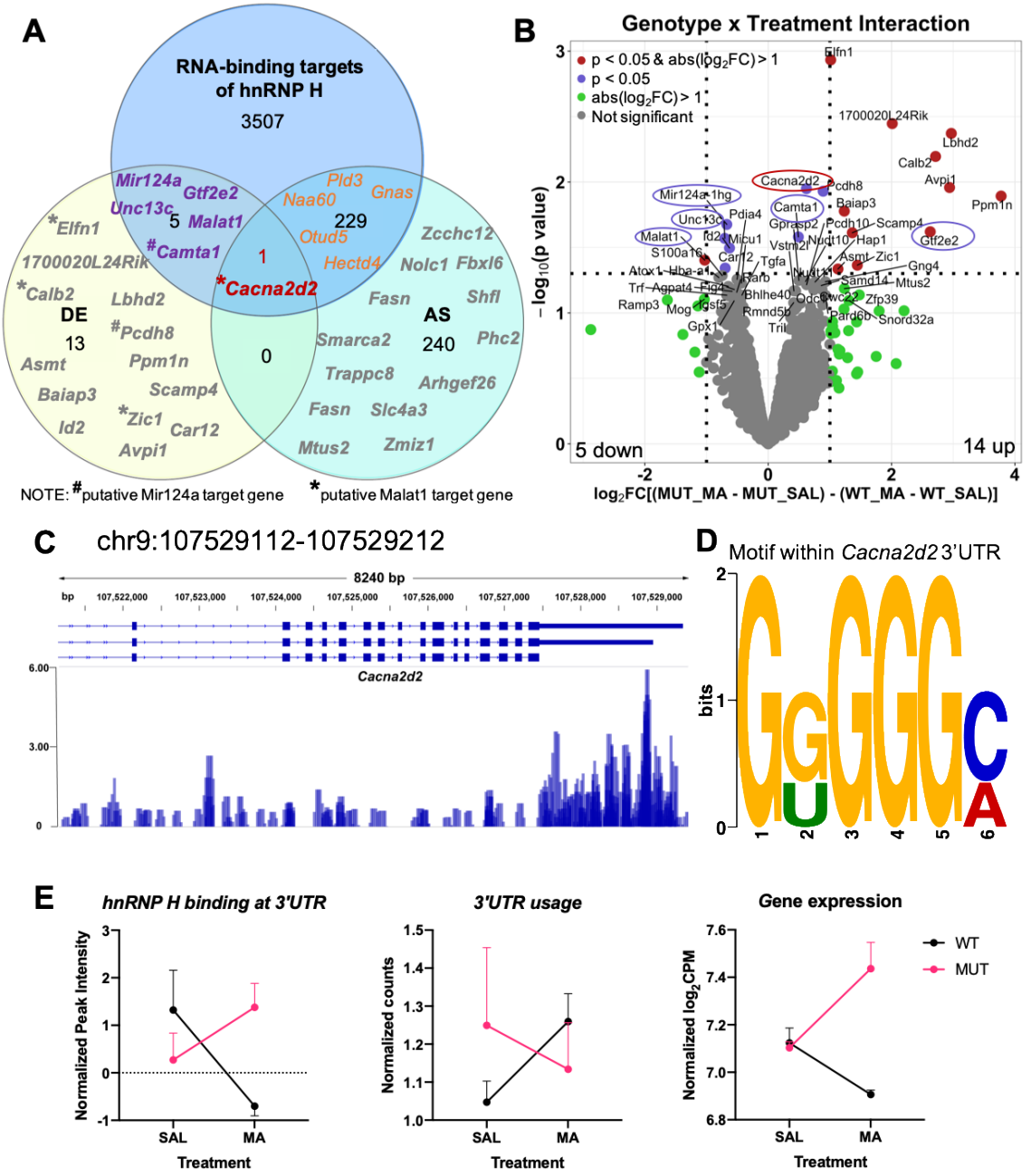

Figure 34. *Cacna2d2* is the only convergent target showing a Genotype x Treatment-induced change in hnRNP H1 binding, gene expression and alternative splicing.
Differential gene expression (DE) for the interaction of Genotype and Treatment [MUT_{MA} – MUT_{SAL}) – (WT_{MA} – WT_{SAL})] was performed using limma (Ritchie et al., 2015) and edgeR (Robinson et al., 2009). Differential exon and intron usage analysis (alternatively spliced; **AS**) for interaction of Genotype and Treatment [MUT_{MA} – MUT_{SAL}) – (WT_{MA} – WT_{SAL})] was performed using Aspli (Mancini et al., 2020). **(A):** Venn diagram comparing RNA-binding targets of hnRNP H with differential gene expression and differential exon or intron usage. The 19 DE genes and 469

AS genes were then compared with the hnRNP H targets that comprised the Genotype x Treatment interactions. *Cacna2d2* is the only RNA-binding target of hnRNP H that was both a DE gene and an AS gene. Only the top overlapping and non-overlapping hnRNP H targets and AS genes are indicated. Out of the 19 DE genes, *Cacna2d2*, *Elfn1*, *Calb2*, and *Zic1* are putative targets of *Malat1* while *Camta1* and *Pcdh8* are putative targets of *Mir124a*. **(B):** Volcano plot of genes showing a Genotype x Treatment interaction between in H1 MUT and WT mice in response to MA The interaction is expressed as $(MUT_{MA} - MUT_{SAL}) - (WT_{MA} - WT_{SAL})$. *Cacna2d2* is circled in red. The five overlapping hnRNP H targets and DE genes are circled in purple. **(C):** hnRNP H preferentially binds to the 3'UTR of *Cacna2d2*. Visualization of reads by Integrative Genome Browser (Thorvaldsdóttir et al., 2013) for the hnRNP CLIP peak at the 3'UTR of *Cacna2d2*. Scale of the plot height is in counts to million (CPM). **(D):** A G-rich motif is detected at the hnRNP H CLIP peak at the 3'UTR of *Cacna2d2*. *De novo* motif discovery of the binding site was performed in MEME (Bailey et al., 2009). **(E):** Interaction plots showing binding of hnRNP H to the 3'UTR of *Cacna2d2* (left), differential usage of the 3'UTR (middle), and differential gene expression of *Cacna2d2* (right) as a function of Genotype and Treatment. The increase in binding of hnRNP H to the 3'UTR of *Cacna2d2* is associated with decreased usage of the 3'UTR and increased gene expression *of Cacna2d2* in the H1 MUT. The interaction plots are generated from CLIP-seq and RNA-seq data showing average values with standard deviation of the means, with n = 3 per condition.

Cacna2d2 codes for the voltage-dependent calcium channel subunit α2δ2. Our CLIP analysis shows that hnRNP H binds to the 3'UTR of *Cacna2d2* and thus could plausibly regulate polyadenylation site selection, mRNA stability at the 3'UTR, and ultimately CACNA2D2 protein levels (**Figure 34C**). Three putative isoforms, harboring different 3'UTR lengths, have been annotated by GENCODE so far. The MEME suite tools (Bailey et al., 2009) identified G-rich motifs (canonical binding motifs for hnRNP H) within the 3'UTR of *Cacna2d2* (**Figure 34D**). Corresponding to this binding was the detection of an alternate usage event at the 3'UTR with a Genotype x Treatment interaction ($\log_2FC = -1.37$, $p = 0.033$). Here, 3'UTR usage is defined as to the number of normalized reads mapped to the 3'UTR portion of *Cacna2d2*. For WT mice, we observed a decrease in hnRNP H binding in response to MA treatment, which was associated with increased 3'UTR usage, and an overall decrease in gene expression (**Figure 34E**). However, in H1

MUT mice, we observed increased binding of hnRNP H which correlated with decreased 3'UTR usage, and an overall increase in gene expression. This identification of *Cacna2d2* implicated calcium signaling as a potential mechanism underlying the reduced MA-induced behavior and dopamine release in the H1 MUT mice. This, interaction of hnRNP H with the 3'UTR implicates a role in translational regulation, perhaps at the level of polyadenylation site selection. **Figure 35** illustrates a putative model of hnRNP H-*Cacna2d2* interaction at the 3'UTR.

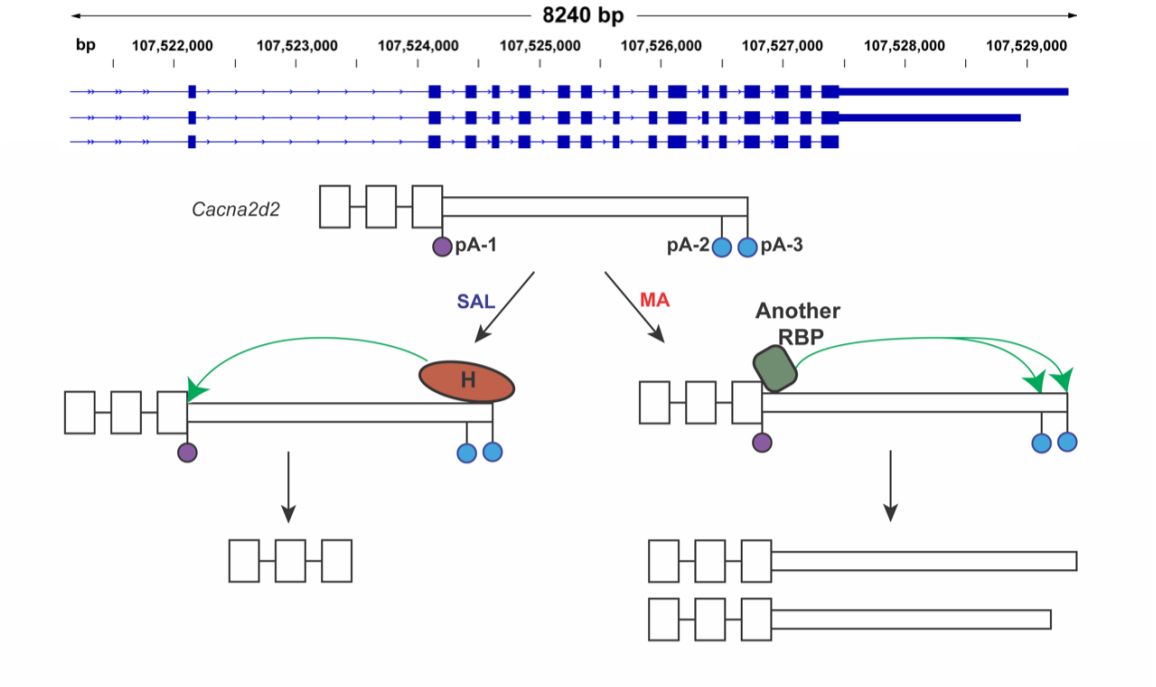

Figure 35. Schematic showing the putative interaction between hnRNP H-mediated selection of polyadenylation site in *Cacna2d2*.
Predicted *Cacna2d2* mRNA isoforms are shown on top (obtained from UCSC Genome Browser). Three polyadenylation sites are present within the 3'UTR of *Cacna2d2* that distinguish isoforms containing 3'UTR of different lengths. We propose that binding of hnRNP H to pA-2 and pA-3 within the 3'UTR of *Cacna2d2* blocks the transcripts from being selected as polyadenylation sites and promotes the usage of pA-1 instead. The interaction of hnRNP H with *Cacna2d2* promotes the generation of the isoform containing a short 3'UTR (or decreased 3'UTR usage as defined in our alternative splicing analysis). In response to acute MA and changes in signaling associated with MA entering the pre-synaptic neurons, there is a shift in binding of hnRNP H to *Cacna2d2*. It is possible that another RBP binds and blocks the usage of pA-1 to favor the selection of pA-2 and pA-3.

DISCUSSION

We identified the genome-wide hnRNP H interactome *in vivo* in the mouse striatum in WT mice (isogenic C57BL/6J), both at baseline and in response to MA treatment. Most of the striatal hnRNP H targets were enriched for pathways and biological functions critical for excitatory synaptic transmission and psychostimulant addiction (**Figures 31 and 32C-D**). The posttranscriptional operon theory proposed by Keene and Tenebaum (2002) states that mRNAs bound by an RBP are often functionally related because these mRNAs shared sequence elements that are recognized by a given RBP and thus, are post-transcriptionally regulated as a group. For hnRNP H, the core motifs in most target mRNAs are G-rich sequences (**Figure 30**), consistent with previous characterization of hnRNP H binding sites (Russo et al., 2010; Lefave et al., 2011; Huelga et al., 2012; Uren et al., 2016). Interestingly, most target mRNAs containing these G-rich motifs code for subunits of pre-synaptic calcium channels (**Figure 30D and Table A8**). In dissecting the binding sites into different gene subregions, many of the 3'UTR targets are involved in psychostimulant-induced pre-synaptic neurotransmitter release and post-synaptic plasticity (**Table 10**). Furthermore, several of the 3'UTR targets showed opposite changes in binding to hnRNP H in response to MA in H1 MUT (decreased 3' UTR binding) versus WT mice (increased 3'UTR binding). The likely regulation of protein levels by hnRNP H binding to 3'UTR targets (e.g., regulation of repression, stability via differential 3'UTR usage, etc.) warrants further investigation. Together, CLIP-seq analysis shows a MA-induced difference in association of hnRNP H with target mRNA transcripts that code for synaptic proteins between the WT and H1 MUT. The opposing changes in MA-induced hnRNP H mRNA interactome

plausibly reflect rapidly regulated proteins that contribute to reduced MA-induced extracellular DA and behavior in H1 MUT mice.

hnRNP H is primarily localized to the nucleus of neurons in adult mice (Kamma et al., 1995; Van Dusen et al., 2010; Ruan et al., 2020a). RBPs binding to 3'UTRs in the nucleus determines cytoplasmic localization and translation of mRNA transcripts (Guramrit et al., 2015). For example, She2p must first bind to the 3'UTR of *ASH1* mRNA in the nucleus before the transcript localizes to the cytoplasm (Niednery et al., 2014). Binding of hnRNP H to 3'UTRs of mRNAs in the nucleus could recruit other proteins necessary for mRNA export to the cytoplasm for translation. We previously discovered that the H1 MUT mice, while showing no change in protein at the total striatal tissue level, showed a robust, two-fold increase in hnRNP H protein in the striatal synaptosome (Ruan et al., 2020a). Here, the H1 MUT genotype affected overall RNA binding in the striatum (**Figure 32**). Thus, differential binding of hnRNP H to its synaptic targets in H1 MUT mice is likely partially explained by the two-fold increase in the overall level of synaptic hnRNP H (Ruan et al., 2020) where it regulates translation of targets via their 3'UTRs, which, in turn would explain the high degree of enrichment of RNA-binding targets related to synaptic function as a function of Genotype (**Figure 32**). Our study demonstrates rapid plasticity of the RBP-mRNA interactome whereby exogenous cellular stimuli, such as acute MA acting on presynaptic terminals and synaptic vesicles, can induce rapid changes in binding of hnRNP H to mRNAs. Several RBPs have been shown to differentially alter their RNA-binding activity in response to arsenite-induced cellular stress, with distinct stress-induced interactomes in the nucleus versus the cytoplasm (Backlund et al., 2020).

Much like these stress-responsive RBPs identified *in vitro*, hnRNP H also showed differential RNA binding to its targets in response to MA treatment *in vivo.*

In agreement with previous studies (Huelga et al., 2012; Uren et al., 2016), our CLIP analysis of hnRNP H identified thousands of RNA-binding targets. Thus, a major challenge is to narrow down the list of targets that functionally contribute to decreased MA-induced extracellular DA level and behaviors in H1 MUT mice. Incorporating parallel transcriptome and spliceome datasets with CLIP targets from the same samples facilitates identification of functional, gene regulatory consequences of RNA binding (Chen and Keleş, 2020; Hwang et al., 2020; Li et al., 2020), that in turn, could modulate the cell biological response. In our final comparative analysis, we triangulated on the dynamic MA-induced interactome with the MA-induced transcriptome and spliceome (**Figure 6**) to associate differential hnRNP H binding with transcriptional regulation in H1 MUT versus WT mice. *Cacna2d2* emerged as an interesting candidate mechanistic target that showed a MA-induced decrease in binding of hnRNP H to 3'UTR, a decrease in 3'UTR usage, and an increase in overall *Cacna2d2* transcript levels in H1 MUT versus WT mice (**Figure 34**). *Cacna2d2* is expressed in the cerebellum, striatum, and hippocampus (Dolphin, 2012). It codes for a pre-protein that is proteolytically processed into the α2 and δ2 subunits of presynaptic, voltage-gated calcium channels (VGCCs) (Dolphin and Lee, 2020). These α2δ2 subunits localize VGCCs to the active zone and promote neurotransmitter release (Dolphin, 2013). Overexpression of α2δ2 subunits decreased presynaptic calcium elevation in response to an action potential, yet somehow increased vesicular release (Hoppa et al., 2012). In addition, overexpression of *Cacna2d2* disrupted both intracellular

calcium signaling and mitochondrial function (Carboni et al., 2003). Changes in intracellular calcium are tightly linked to changes in mitochondrial function as mitochondria can serve to buffer intracellular calcium levels (Rizzuto et al., 2012). Our proteomic analysis of the striatal synaptosome showed opposite changes in mitochondrial protein levels compared in H1 MUT versus WT mice in response to MA (Ruan et al., 2020a). A recent study demonstrated in both cell and slice culture that both intracellular and extracellular calcium contribute to MA-induced DA release in the ventral striatum (Yorgason et al., 2020). Acutely, MA can inhibit calcium entry into L-type and N-type VGCCs, with longer exposure leading to a compensatory upregulation of *Cacna1c* transcript levels in SH-SY5Y cells (Andres et al., 2015), which could potentially mediate calcium-mediated neurotoxicity. Repeated treatment with MA increases mRNA and protein of α2δ subunit in the frontal cortex and limbic forebrain of mice and this upregulation is blocked by DA receptor antagonists (Kurokawa et al., 2010). Our identification of *Cacna2d2* dynamics at multiple levels of analysis following MA administration (3'UTR binding, transcriptional, and usage) suggests that regulation of this calcium channel subunit and others (**Figure 34**) could comprise a rapid, adaptive means for regulation of calcium entry and consequently, DA release and behavior. As an interesting aside, VMAT2 and DAT, the two molecular targets of MA that increase the extracellular level of DA at the synapse (Fleckenstein and Hanson, 2003; Siciliano et al., 2014), were not identified as RNA-binding targets of hnRNP H, which indicates that hnRNP H does not directly modulate their RNA fate.

The precise roles of RBPs in drug-induced synaptic plasticity are largely unexplored. Revelation of the hnRNP H RNA interactome identified a potential novel role for hnRNP H in regulating transport, stability, and/or translation of mRNAs linked to excitatory synapse and psychostimulant-induced synaptic plasticity. Dynamic regulation of synaptic protein synthesis following activation of neurotransmitter receptors, plays a key role in synaptic plasticity (Bramham and Wells, 2007). FMRP is an example of an RBP that localizes to dendrites to regulate mRNA transport and synaptic plasticity (Bassell and Warren, 2008). Loss of FMRP in mice reduced sensitivity to cocaine-induced reward and behavioral sensitization (Smith et al., 2014). Stimulation of the metabotropic glutamate receptors in primary neuronal culture can rapidly dephosphorylate FMRP, leading to a dissociation FMRP from miR-125a and translational activation of PSD-95 mRNA (Muddashetty et al., 2011). DA receptor D1 activation in prefrontal cortical neurons leads to phosphorylation of FMRP and synthesis of synaptic proteins needed for glutamate receptor trafficking (Wang et al., 2008, 2010). Thus, the phosphorylation status of an RBP can affect translational regulation in response to receptor activation. We previously reported that treatment with a D1 DA receptor agonist (but not a D2 agonist) in cultured rat primary cortical neurons induced a D1 antagonist-reversible increase in nuclear immunocytochemical staining of hnRNP H without altering nuclear protein levels (Ruan et al., 2018), suggesting a potential post-translational modification of hnRNP H and/or its protein/RNA complexes. In addition, similar to our findings for hnRNP H RNA-binding targets, the FMRP interactome also revealed target mRNAs encoding proteins linked to synaptic function (Darnell et al., 2011). These targets include ion channels that modulate

neurotransmission, including voltage-gated potassium channels (Gross et al., 2011; Lee et al., 2011), sodium-activated potassium channels (Brown et al., 2010), calcium-activated potassium channels (Deng et al., 2013), and N-type VGCCs (Ferron et al., 2014). The potential transport and localization of *Cacna2d2* (and other VGCC transcripts; **Table A8**) by hnRNP H in response to MA and how this potentially regulates MA-induced DA release warrants further investigation.

To summarize, we provide the first MA-induced RNA interactome study of an RBP in the striatum. Analysis of drug-induced RBP interactomes, especially for drugs of abuse is an understudied approach for understanding rapid, synaptic gene regulation as it relates to cell biological adaptations in neuronal excitability, neurotransmitter release, synaptic plasticity, and behavior. We focused on hnRNP H, given the evidence for its role in MA-induced DA release and behavior (Yazdani et al., 2015; Bryant and Yazdani, 2016; Ruan et al., 2020a, 2020b). We established hnRNP H as a novel gene regulatory link among several target mRNAs coding for proteins that are well-established to mediate psychostimulant-induced neurotransmission and plasticity. Our study design represents a powerful approach for integrating complementary gene sets from different "omic" methods (interactome, transcriptome, and spliceome) that can be broadly applied to the study of drug-induced RBP-RNA dynamics and discovery of functionally relevant RNA-binding targets underlying cell biological responses, adaptations, and organismal phenotypes such as behavioral disorders.

MATERIALS AND METHODS

Mice

H1 MUT were generated via TALENs-mediated induction of a small, 16 bp deletion in the first coding exon as described (Yazdani et al., 2015) and have been deposited to The Jackson Laboratory repository (#033968). A two-fold increase in hnRNP H protein expression was detected in the striatal synaptosome of H1 MUT compared to WT with no change in total tissue level (Ruan et al., 2020a). Mice were generated by mating heterozygous H1 MUT males with C57BL/6J females purchased from The Jackson Laboratory (Bar Harbor, ME USA), yielding offspring that were approximately 50% heterozygotes for H1 MUT and 50% WT for *Hnrnph1*. Both female and male offspring (ranging from 50 – 100 days old at the start of the experiment) from this breeding scheme were used in the study and were genotyped as described (Yazdani et al., 2015). Mice were housed in same-sex groups of 2-5 in standard mouse cages in ventilated racks under standard housing conditions on a 12 h:12 h light:dark schedule with food and water supplied as libidium. All protocols involving mice were in accordance with the Guideline for the Care and Use of Laboratory Animals and were approved by Boston University's IACUC committee.

MA-induced locomotor activity followed by whole striatum harvesting

As described (Yazdani et al., 2015), on Days 1 and 2, all mice received a saline injection (10 ml/kg, i.p.) and were recorded for locomotor activity in Plexiglas chambers (40 cm length x 20 cm width x 45 cm height) for 1 h. On Day 3, mice receive either saline again

or MA (2 mg/kg, i.p.; Sigma Aldrich) and were recorded for locomotor activity for 30 min and the whole striata (left and right sides) were dissected from each mouse at 30 min post-injection (Ruan et al., 2020a). Dissected whole striata were stored in RNAlater (Thermo Fisher Scientific, Cat# AM7020) following manufacturer's instructions to stabilize the RNA and protein followed by CLI library preparation as described below.

CLIP

Striata from four mice were pooled per replicate (3 replicates per Genotype per Treatment). Each replicate used for CLIP-seq and RNA-seq was generated by pooling striata from 4 H1 MUT or WT mice across multiple litters. Each pool consisted of samples from 2 females and 2 males. The striatum was chosen because of its involvement in the MA locomotor stimulant response, reinforcement and reward (Keleta and Martinez, 2012; Lominac et al., 2014). The experimental design and sample size are outlined in **Table A4 and A5**, respectively. Tissue was flash frozen in the mortar-filled liquid nitrogen and crushed into powder with the pestle and kept on dry ice in a 100 mm Petri dish until use. Prior to crosslinking, a portion of the pooled tissue from each replicate was removed and stored in -80°C for later RNA extraction and bulk RNA-seq library preparation. The tissue was kept on dry ice in the dish while crosslinking was performed for three rounds using a 400 mJ/cm^2 dosage of 254 nm ultraviolet radiation. The crosslinked tissue was then homogenized in 1 ml of lysis buffer with a mechanical homogenizer followed by addition of TURBO DNase (2 μl; Thermo Fisher Scientific, Cat# AM2239). The lysate was kept on ice for 30 min followed by the addition of RNAse I$_f$ (125 U/ml; NEB, Cat# M0243L) and

was allowed to incubate in a thermomixer set to 1200 RPM at 37˚C for 3 min. The lysate was then centrifuged at 20,000 x g for 20 mins at 4°C and kept on ice until use.

For RNA-immunoprecipitation, 133.3 µl of MyOne Streptavidin T1 beads (Invitrogen, Cat# 65602) were incubated with 5.8 µl of 1 mg/ml of Pierce™ biotinylated Protein G (Thermo Fisher Scientific, Cat# 29988) and 20 µg of either the hnRNP H antibody (Bethyl; Cat #A300-511A) or the rabbit IgG antibody (EMD Millipore, Cat# 12-370) for 1 h. The antibody-coupled beads were washed five times with 0.5% IgG-free BSA (Jackson ImmunoResearch; Cat# 001-000-162) in 1X PBS, followed by three washes in lysis buffer. The lysate that was clarified by centrifugation was added to the coated and washed beads and incubated with end-to-end rotation at 4°C for 2 h followed by 2X wash with 500 µl of wash buffer (end-over-end rotation at 4°C for 5 min each) and another 2X wash with 500 µl of high salt wash buffer (end-over-end rotation at 4°C for 5 min each). This was followed by another wash with 500 µl each of both wash buffer and high salt wash buffer. The final washes were performed 2X with 500 µl of wash buffer. The rest of the wash buffer was removed and beads resuspended in 20 µl of 1X Bolt LDS non-reducing sample buffer (ThermoFisher Scientific, Cat# B0007). The beads in sample buffer were then heated at 70°C for 10 min prior to SDS-PAGE on a 4-12% gradient NuPAGE Bis/Tris gels (ThermoFisher Scientific, Cat# NP0322BOX) followed by transfer to nitrocellulose membrane (Amersham Protran Premium 0.45 NC; Cat# 10600078) with 10% methanol for 6 hours at constant 150 mA. See below for the components in each buffer:

Lysis buffer
50 mM Tris-HCl pH7.4
100 mM NaCl
1% NP-40 (Igepal CA630)
0.1% SDS
0.5% sodium deoxycholate (protect from light)
Protease and phosphatase inhibitor cocktail (1:100)
Recombinant RNasin Ribonuclease Inhibitor (1 ul/ml)

Wash buffer
20 mM Tris-HCl pH7.4
10 mM $MgCl_2$
0.2% Tween-20
Recombinant RNasin Ribonuclease Inhibitor (1 uL/ml)

High salt wash buffer
50 mM Tris-HCl pH7.4
1M NaCl
1 mM EDTA
1% NP-40
0.1% SDS
0.5% sodium deocxycholate
Recombinant RNasin Ribonuclease Inhibitor (1 uL/ml)

CLIP-seq sequencing library preparation

Following the completion of membrane transfer, the membrane was cut with a clean razor to obtain a vertical membrane slice per lane from 50 kDa (molecular weight of hnRNP H) to 75 kDa, which translates to 30 to 70 nucleotide RNA fragments crosslinked to the protein. RNA was then extracted from the membrane slices following a previously described procedure (Rieger et al., 2018). The same extraction procedure (starting with the addition of 7M urea) was used to isolate RNA from samples previously stored for total RNA-seq. Following RNA extraction, sample concentration was quantified with Agilent Bioanalyzer and approximately 0.2 ng of RNA was used to prepare next-generation sequencing libraries following a published protocol for library preparation (Rieger et al., 2018). Because the

RNA adapter on each sample contained a unique barcode, the cDNA libraries generated from the sample (12 CLIP-seq and 12 RNA-seq libraries) were multiplexed and pooled for increased throughput. A pooled library at a concentration of 10 nM were shipped to University of Chicago Sequencing core and subjected to 100 bp paired-end 2 x 100 sequencing in a single lane on Illumina HiSEQ4000. To increase read coverage for the RNA-seq samples, those 12 cDNA libraries were pooled (10 nM concentration) for sequencing for a second time in one lane using Illumina HiSEQ4000. The read coverage for each sample is shown in **Table A12**.

CLIP-seq Analysis of Multi-Mapped Reads

Reads were trimmed for quality using Trimmomatic (Bolger et al., 2014). Unique Molecular Identifier (UMI) sequences were extracted from Read 2 for removal of PCR amplification duplicates using the 'extract' command in UMI-tools (Smith et al., 2017). After the reads were trimmed and UMI extracted, we used STAR (Dobin et al., 2013) to map reads to mouse genome, version GRCm38/mm10. Even though the samples had gone through the ribosomal RNA (rRNA) depletion prior to library preparation, we used BEDTools (Quinlan and Hall, 2010) to intersect the bam files with the RNA annotation bed file exported from UCSC Table browser (Karolchik et al., 2004) to remove rRNAs and other repetitive RNAs. Using the 'dedup' command in UMI_tools (Smith et al., 2017), PCR duplicates from the rRNA-depleted bam files were removed based on UMI extracted in the previous step. To define the binding sites for hnRNP H for each of the four conditions separately, the deduplicated bam files for the three replicates of each condition were used for peak calling in CLAM (Zhang and Xing, 2017) which stands for **CL**IP-seq **A**nalysis of

Multi-Mapped reads. The BAM file for the CLIP sample and the BAM file for input (corresponding RNA-seq sample) were used as input along with a gene annotation file in Gene Transfer Format downloaded from GENCODE. Following the steps described in CLAM (Zhang and Xing, 2017), in order to allow for peak calling of multi-mapped reads, BAM files were preprocessed first to separate multi-mapped reads and unique mapped reads followed by realigning and then peak calling and peak annotation.

Deduplicated BAM files were merged across all 12 CLIP samples and deduplicated BAM files were merged across all 12 input (bulk RNA-seq) samples to generate two merged BAM files as the input for peak calling in CLAM as described above. The called peaks were then annotated. The file containing all the peaks was formatted into a file in GTF format to be used for strand-specific feature counting in individual BAM files using Subread FeatureCounts (Liao et al., 2014). FeatureCount (Liao et al., 2014) in Subread was used to sum reads under each peak for each of the four conditions. To examine the effect of Genotype, Treatment, and the interactive effects on hnRNP H binding, differential binding sites and peak analysis were performed using limma (Ritchie et al., 2015) and edgeR (Robinson et al., 2009) based on summed counts for each peak derived from Subread FeatureCount. The interaction of Genotype and Treatment is expressed as: I = (MUT_MA – MUT_SAL) – (WT_MA – WT_SAL).

Homer de novo Motif Discovery

To identify the top over-represented motif in the peaks (those peaks with CLIP peak intensity > 1.5) identified in CLAM, the Homer software (Heinz et al., 2010) was used for *de novo* motif discovery by using “findMotifsGenome.pl” function. The input file

comprised a list of hnRNP H associated peaks containing the genomic coordinates. The "annotatePeak.pl" function was then used to identify motif locations to find genes containing a particular motif.

Differential Gene Expression and Exon and Intron Usage

To triangulate the CLIP-seq and RNA-seq data and associate the downstream effect of hnRNP H binding with changes in gene expression and alternative splicing, we used ASpli (Mancini et al., 2020) to analyze differential gene expression as well as differential exon and intron usage. To test that hypothesis that some genes interact with Genotype in their binding or expression response to Treatment, the interaction was expressed as:

I = (MUT_MA – MUT_SAL) – (WT_MA – WT_SAL).

Pathway and Gene Ontology Enrichment Analysis

To examine the biological function of the hnRNP H targets (peak signal value defined by a CLAM value greater than 1.5 for each target), we performed pathway and gene ontology (**GO**) enrichment analysis of those targets in g:Profiler (Raudvere et al., 2019) against the following data sources: Reactome, WikiPathways, GO molecular function, GO cellular component, and GO biological process. The top 10 pathways and GO terms from each these 5 databases (a list of 50 gene sets) were used for network analysis in Cytoscape using the EnrichmentMap module (Merico et al., 2010). Highly redundant gene sets were grouped together as clusters for clear visualization and easy interpretation. The same pathway and GO enrichment analyses were performed in g:Profiler for the hnRNP H targets with Genotype and Treatment interaction to generate an EnrichmentMap (Reimand

et al., 2019). To determine enrichment of the hnRNP H targets for each gene subregion separately, we performed KEGG (Kanehisa et al., 2019) pathway enrichment analysis in WebGestalt (Liao et al., 2019) to examine the biological relevance across each set of targets.

Data and Code Availability

Raw and processed sequencing data from CLIP-seq and RNA-seq can be accessed through NCBI GEO under the accession number GSE160682.

CHAPTER V: Summary & Future Directions

OVERVIEW

The genetic factors underlying risk for psychostimulant addiction remain largely unknown. Our lab mapped and validated *Hnrnph1* as a QTG for reduced MA stimulant sensitivity. Mice with heterozygous deletion of a small region in the first coding exon of *Hnrnph1* also showed reduced MA-induced reward and reinforcement, as well as a decrease in MA-induced extracellular DA in the NAc. The combined results indicate reduced addiction liability in H1 MUT mice. hnRNP H1 is an RNA binding protein that regulates every aspect of RNA metabolism (from the cradle to the grave, as they say). The objective of my dissertation research is to understand the mechanism of hnRNP H1 dysfunction in MA-induced DA release and behavior through multi-omics data integration including proteome, transcriptome, and hnRNP H1 RNA-interactome. The findings from these studies are discussed in detail in Chapters II to IV.

SUMMARY

Chapter II: 5'UTR variants in the quantitative trait gene Hnrnph1 support reduced 5'UTR usage and hnRNP H protein as a molecular mechanism underlying reduced methamphetamine sensitivity

Our lab previously used positioning cloning to identify a 204 kb region containing polymorphisms in two genes, *Hnrnph1* and *Rufy1*, that was necessary for reduced sensitivity to the locomotor stimulant effect of MA. We subsequently showed that congenic mice containing a 114 kb subregion and mutant mice containing a heterozygous frameshift

deletion in *Hnrnph1* also showed reduced MA-induced locomotor activity. These findings supported *Hnrnph1* as the QTG, however, causal variants within or near *Hnrnph1* are not known. Following the discovery of decreased usage of the 5'UTR in *Hnrnph1* in 114 kb congenic mice using exon-level transcriptomic analysis, we validated this decreased 5'UTR usage using qPCR, that in turn, was associated with a two-fold decrease in hnRNP H protein. To determine which of the 4 polymorphic variants within the 5'UTR contribute to the decrease in translation, we cloned the 5'UTR of *Hnrnph1* containing either the individual variants or the combined set of all four variants for fusion to a luciferase reporter for expression analysis in HEK293T and N2A cells. The reporter assay showed that all four variants (but none individually) decreased protein expression. We identified a set of 5'UTR functional variants in *Hnrnph1* that likely comprise the quantitative trait variants underlying decreased hnRNP H protein and likely and decreased MA sensitivity.

Chapter III: A Mutation in Hnrnph1 That Decreases Methamphetamine-Induced Reinforcement, Reward, and Dopamine Release and Increases Synaptosomal hnRNP H and Mitochondrial Proteins

We previously discovered *Hnnrph1* as a QTG for reduced sensitivity to the locomotor stimulant response to MA (Yazdani et al., 2015). We subsequently validated that this reduced MA sensitivity in the H1 MUT mice extends to other addictive properties of MA. H1 MUT showed reduced MA reinforcement and intake and a dose-dependent change in MA reward. In addition, H1 MUT mice showed a decrease in MA-induced extracellular DA in the NAc. However, no genotypic difference was detected between H1 MUT and

WT in baseline extracellular DA, whole tissue striatal DA, DAT, DA uptake, MA striatal metabolite levels, or TH-positive DA neurons. Importantly, a two-fold increase in hnRNP H protein was detected in the striatal synaptosome of H1 MUT mice with no change in whole tissue level, indicating a role of hnRNP H in mRNA localization and/or protein translation at the synapse. Synaptosomal proteomic analysis identified an increased baseline abundance of several mitochondrial complex I and V proteins that rapidly decreased at 30 min after MA administration in H1 MUT mice. In contrast, the much lower level of basal synaptosomal mitochondrial proteins in WT mice showed a rapid increase. Thus, we identified a potential role for hnRNP H in basal and MA-induced changes in mitochondrial function that informs the basal and MA-induced cellular adaptations that could underlie reduced addiction liability in H1 MUT mice.

Chapter IV: The dynamic, methamphetamine-induced hnRNP H interactome reveals synaptic RNA-binding targets associated with reduced dopamine release and behavior

hnRNP H binds to mRNA transcripts and is involved in every aspect of post-translational gene regulation. To understand the mechanism of hnRNP H dysfunction in MA-induced DA release and behavior, we surveyed target RNAs of hnRNP H using CLIP-seq in striatal tissue at baseline and at 30 min post-MA (2 mg/kg, i.p.). To integrate identification of hnRNP H targets with the impact of *Hnrnph1* mutation and MA treatment on downstream gene expression and splicing, we analyzed the transcriptome of the same samples used in CLIP-seq. Analysis of read distribution across transcript subregions revealed enriched binding of hnRNP H in introns, comprising about 70% of the total distribution and

confirming its role in splicing. *De novo* motif discovery of significant hnRNP H-associated binding sites using the Homer database detected the top over-represented motif to be G-rich. Genome-wide identification of hnRNP H targets using CLIP-seq in the mouse striatum of C57BL/6J revealed targets important for synaptic function. MA treatment induced opposite changes in binding of hnRNP H to mRNAs between H1 MUT versus WT mice. More specifically, in response to MA, an RNA target that is more likely to show increased binding to hnRNP H in the H1 MUT is more likely to show decreased binding in WT, demonstrating a negative correlation in hnRNP H binding dynamics between H1 MUT versus WT in response to acute MA. This dominant negative relationship in hnRNP H binding to RNA target was most robust in 3'UTR of the mRNA transcripts encoding for synaptic proteins involved in DA release and psychostimulant-induced excitatory synaptic plasticity. From the transcriptome analysis of parallel samples, a total of 19 genes showed a Genotype x Treatment interaction in differential gene expression, with 6 of these 19 genes (including *Cacna2d2*) overlapping with hnRNP H targets that were identified in CLIP-seq. Two of these six genes were the long non-coding RNA *Malat1* and microRNA *Mir124a*, both of which are involved in regulation of genes important for synapse formation and synaptic transmission. RNA-binding, transcriptome and spliceome analysis triangulated on a potentially critical mechanistic target for MA-induced DA release and behavior, Cacna2d2. Specifically, we observed increased hnRNP H binding to 3'UTR of *Cacna2d2*, an upregulation of *Cacna2d2* transcript, and decreased 3'UTR usage in response to MA in H1 MUT mice. *Cacna2d2* codes for a presynaptic, voltage-gated calcium channel subunit that could plausibly regulate MA-induced DA release and behavior. Interestingly, the

overlapping hnRNP H interactome and transcriptome showing the Genotype x Treatment interaction identified *Unc13c* and *Camta1*, both of which are calcium-responsive genes. Thus, multiple lines of evidence point to the modulation of calcium as likely potential mechanism that links the H1 mutation with MA-induced behavior.

FUTURE DIRECTIONS

Understand the 16-bp deletion in Hnnrph1 in the H1 MUT

The heterozygous 16-bp deletion within the first coding exon (exon 4, UCSC Genome Browser) mediated by transcription activator-like effector molecule in the H1 MUT mice should have theoretically led to a premature stop codon and transcription of a truncated mRNA transcript that should have been degraded. However, with the caveat that there is no specific antibody, we have not detected any decrease in the total level of hnRNP H protein that would indicate protein knockdown. Interestingly, H1 MUT mice showed an increased level of hnRNP H in the striatal synaptosome relative to the WT but no change in total hnRNP H level (Chapter III). This finding prompted us to investigate the synaptosomal proteome and hnRNP H RNA interactome in H1 MUT versus WT mice to further investigate the effect of this mutation on *Hnrnph1* function (Chapters II and III). Both the synaptosome proteome and RNA interactome data detected a genotypic difference in mitochondrial protein level and hnRNP H interaction with mRNAs coding for synaptic proteins involved in psychostimulant-induced synaptic plasticity. Compared to the WT, a higher level of mitochondrial protein is detected with the H1 MUT (Chapter III). CLIP-seq also detected an increase in binding of hnRNP H to the same mRNA transcripts in H1 MUT

compared WT (Chapter IV). Acute treatment MA reversed this genotypic difference in mitochondrial proteins and hnRNP H binding. These findings suggest the heterozygous 16-bp deletion might exert a dominant negative effect on *Hnrnph1* function at baseline steady state. However, in response to MA, there is a reversed effect on *Hnrnph1* function.

This 16-bp deletion is located within the first RRM of *Hnrnph1* that might modify its interaction with mRNA transcripts. It is worth pointing out that there is an alternative start codon downstream of exon 4 where the 16-bp deletion is located. One possibility is that the ribosome skips over the premature stop codon and initiates translation from this other start codon. Both the proteome and CLIP-seq data raise the possibility that H1 MUT mice harbors truncated hnRNP H1 protein that dominates over the function of the WT hnRNP H1 protein. To answer this question, we performed quantitative analysis of protein peptides from hnRNP H co-immunoprecipitation followed by mass spectrometry (Chapter III). Indeed, we detected a decrease in the level of a peptide containing the amino acid residues encoded by the 16-bp deleted region in exon 4 of *Hnrnph1*. However, this decrease did not reach statistical significance. To follow up on this finding, one approach is to clone *Hnrnph1* and use site-directed mutagenesis to delete the same 16 nucleotides. For detection of hnRNP H1 protein, a GFP tag can be added to either the N- or C-term of *Hnrnph1*. In this way, we can determine whether this 16-bp deletion in *Hnrnph1* yields a functional protein or not. The piece of data can help us with better interpretation of future data generated using the H1 MUT mouse model and inform the design of future experiments to further characterize this protein.

Subcellular and Cell-Type Specific hnRNP H1 CLIP-seq

In Chapter IV, we focused on whole tissue analysis of hnRNP H-RNA interaction in the striatum. It is clear from the data that the presynaptic, post-synaptic, cytoplasmic, and nuclear RNA binding events mediated by hnRNP H are not directly identifiable in our whole tissue CLIP. RBPs contribute to stress-induced regulation of RNA fate and function in a nuclear- versus cytoplasmic- specific manner (Backlund et al., 2020). The formation of stress granules is one particular stress response mechanism that requires RBPs to sequester mRNAs from being translated in the cytoplasm (Ivanov et al., 2020). Interestingly, cellular stress induces the accumulation of hnRNP H in the cytoplasm and localization to stress granules (Wall et al., 2020). These findings implicate the ability for hnRNP H to shuttle between the nucleus and cytoplasm to regulate RNA fate and function at the level of splicing (intronic binding or nuclear events) and mRNA stability, localization, and translation (3'UTR binding or cytoplasmic events). In our CLIP-seq analysis, we also identified binding of hnRNP H to the 3'UTR regions of transcripts.

To explore the relationship between nuclear and cytoplasmic functions of hnRNP H, it will be necessary to define hnRNP H-RNA interactions in the nucleus and cytoplasm separately using CLIP-seq. This procedure would be similar to what was done in Chapter IV. After crosslinking the mouse striatum to freeze the RNA-protein complex, the extra step is to sub-fractionate the tissue into nuclear and cytoplasmic fraction prior to the IP and library preparation step. This sub-compartmentalization of hnRNP H-regulated transcripts permits parsing the action of hnRNP H in pre-mRNA versus mature mRNA.

One area worth investigating is the function of hnRNP H at the synapse. While most of the binding regions associated with hnRNP H in our CLIP-seq analyses are intronic, we also identified binding of hnRNP H to 3'UTR of mRNA transcripts found in presynaptic terminal and postsynaptic compartment, such as voltage gated calcium channels, phosphatases, calcium signaling and kinases, transporters, synaptic vesicles, glutamate receptors (Chapter IV). The interactions of hnRNP H at the 3'UTR implicate a role of hnRNP H in mRNA transport and translation at the synapse for new protein synthesis in neurons to respond to cellular stimuli (Holt et al., 2019). Since there is normally a low level of hnRNP H at the synapse, the use of super high-resolution imaging is necessary to define the localization of hnRNP H outside of the nucleus, whether it is predominantly found in the vesicle release site of the presynaptic site or at the postsynaptic density scaffold. Once the synaptic localization of hnRNP H is confirmed, the use of CLIP-seq and RNA-seq on sub-fractionated synaptosomes (pre- versus postsynaptic fraction) will better define the hnRNP H-RNA interactome and hnRNP H-dependent post-transcriptional regulation on these synaptic mRNAs. The differentiation of hnRNP H pre- versus post-synaptic RNA targets would help us determine whether a pre- and/or post-synaptic mechanism links *Hnrnph1* to MA-induced behavior.

Even though *Hnrnph1* is expressed ubiquitously in the brain, our lab has previously established exclusion of *Hnrnph1*expression in glia (Ruan et al., 2020), implicating a cell type-specific function of *Hnrnph1* in regulating RNA expression and processing. Identifying hnRNP H-RNA interactions at cell type resolution (both at steady state and MA-induced) can help us determine the cell type responsible for driving changes in hnRNP

H function in response to acute MA response and the cellular adaptations from repeated MA exposure. The use of cTag-CLIP (Ule et al., 2018) will permit induction of GFP-tagged hnRNP H1 expression in dopaminergic neurons (by crossing to either a DAT-Cre or TH-cre driver mouse line) for cell type specific profiling of hnRNP H 1 targets. This method does not require specific hnRNP H1 antibody but rather a high-affinity GFP antibody to pull down the tagged hnRNP H1. There is also no need for fluorescence-activated cell sorting to isolate DA neurons because the Cre driver line will drive GFP-tagged hnRNP H1 expression in DA neurons which can be readily and specifically isolated using a GFP antibody. The floxed-*Hnnrph1* mouse (which we currently have) crossed to the same Cre driver will serve as a true negative control to narrow down on the high confidence RNA-binding targets. Cell type-specific GFP-tagging of hnRNP H1 is versatile not just for CLIP. This approach can be extended for co-immunoprecipitation to identify functional cooperative and/or competitive interaction between hnRNP H1 with other RBPs in a cell type specific manner in response to MA.

Analysis of hnRNP H regulation of the Cacna2d2 3'UTR Region in a Luciferase Reporter System

As demonstrated in Chapter II, the luciferase reporter assay is highly versatile in the study of noncoding regulatory elements in the untranslated region controlling regulation of gene expression. This assay is adaptable to probe post-transcriptional function of RBPs through their interactions with the UTRs (Sternburg and Karginov, 2020). Our CLIP-seq and RNA-seq analyses indicated that hnRNP H binds to the 3'UTR mRNA transcript of *Cacna2d2*

and induces alternative splicing of the 3'UTR region (Chapter IV). We hypothesize that the interaction of hnRNP H with the 3'UTR of *Cacna2d2* controls polyadenylation selection to generate 3'UTR of varying lengths, which confer differences in mRNA stability and translation efficiency, perhaps in a cell type-specific manner. The luciferase report assay can be applied to test this hypothesis to determine whether hnRNP H exerts a repressive or stabilizing role on *Cacna2d2* expression. This procedure will involve cloning the full length 3'UTR region of *Cacna2d2* into the 3'UTR of a luciferase reporter gene in combination with hnRNP H1 protein level manipulation (knockdown and/or overexpression). There are two output results we can quantify: 1) length of the 3'UTR through qPCR; 2) protein expression through luciferase signal quantification. Besides manipulating expression of hnRNP H1, we can also mutate the hnRNP H1 binding sites found in the 3'UTR of *Cacan2d2* to examine disruption of hnRNP H1 binding and changes in 3'UTR length and protein expression. Through this reporter system, manipulation of *Malat1* and *miR124a* expression can be performed to test for co-regulation of hnRNP H1 with these two noncoding RNAs, which are hnRNP H target RNAs that also show MA-induced and genotypic difference in gene expression in our analyses.

Profiling of mRNAs under Active Translation in the Synaptosome

A genome-wide approach for analyzing the functional consequence of 3'UTR binding by hnRNP H can involve the use of TRAP-seq (Heiman et al., 2008) or RiboTag (Sanz et al., 2009), both of which are common methods for mapping actively translated mRNAs. The key question that can answered is whether or not those 3'UTR targets that show Genotype

x Treatment interaction are also being actively, but differentially translated in response to MA as a function of *Hnrnph1* Genotype. To determine whether hnRNP H plays a role in localized protein synthesis to drive synaptic plasticity in response to MA, TRAP-seq or RiboTag can even be modified to extract ribosome-bound mRNAs from the dendrites. To complement this approach, change in protein synthesis in response to MA in the *Hnrnph1* mutant and WT mice in a temporal manner can be measured using SunSET (Schmidt et al., 2009) or Click-it AHA assay (Rothenberg et al., 2018).

APPENDIX I

Appendix I includes supplemental materials for Chapters II, III, and IV.

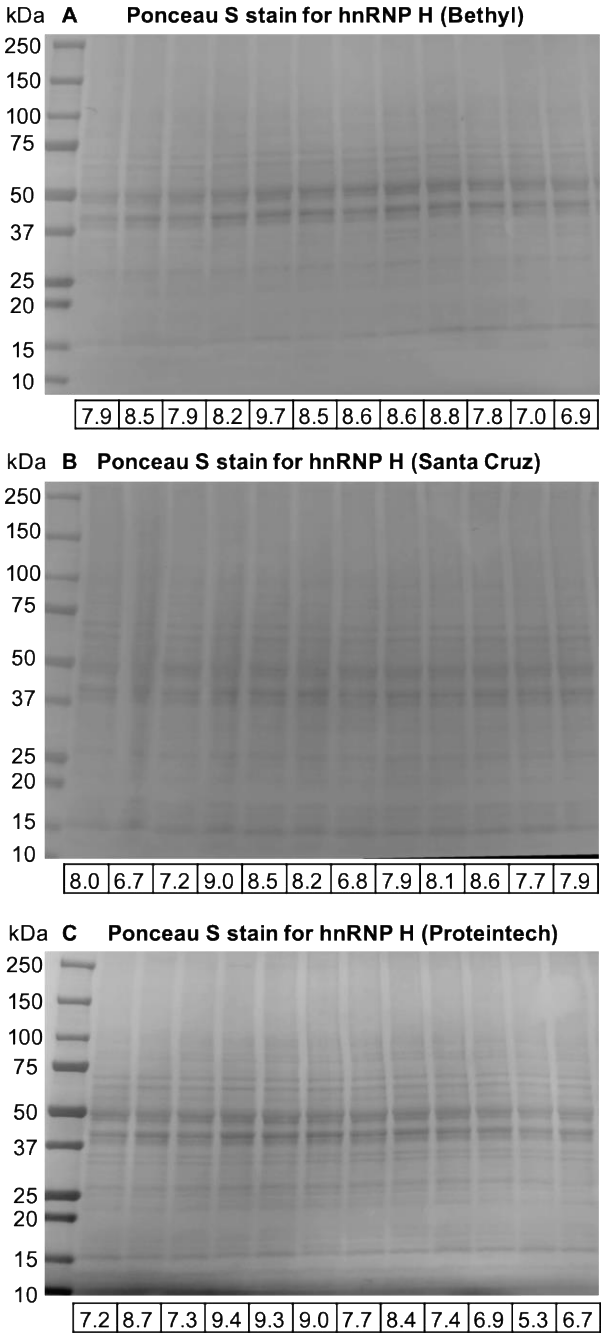

Figure A1. Ponceau S staining for total protein normalization used in immunoblot quantification.
Total protein stains via ponceau S instead of a housekeeping gene were used as loading controls. The densitometry value for the total protein stains in each lane is indicated below each immunoblot. These are the values that were used for normalization. (A-C): Ponceau S total protein staining for quantification hnRNP H protein expression. This figure supports Figure 11.

```
>Chr11: 50,375,375-50,378,330
GCTCCCGTGATCAGATACAGATAGTTACATAGTCCCAGTATTAAGTTAGT 50,375,424
AAGGATTAAAAGAAAGGGAAAGCCCATGTAGTGAAAGTCAGGCGTTTGCA 50,375,474
GCCCTTGTACACAAAAGGATCTTCAAATCCTTCCATTGTTAGAAATTACA 50,375,524
CAAATACTCAGAGCCTTCTGCCAAACAATTGTCCACCAGAAAATCCTCAT 50,375,574
TGCGTGTGGTGGCACACACACTTTAATCCTGTCATTCTGGAGGCGGATGA 50,375,624
TCAAACACTTGAGACCATGCATGACTGCAAGGGGAGTTTGAGGCCGGCCT 50,375,674
GGGATGTGTGCAATCAGGACTCAAAACAATAAGGAAAGGACACAATAAGG 50,375,724
AAAGATAAAAGTTTTTATCTATGATTATACACTGCATTTTTCTCTTACGA 50,375,774
TGGAAAAATAACCTCCCATACAACTAGAATAGAATTTAGAGAAACATCGT 50,375,824
AGGAATGTGGTTGTGTTGTCAGAAGGGAAACATTTCCCCCCCTTCAGGTG 50,375,874
AGAGACCTGGATTGCTAAGTTGCAGTGACTCTCCCATCTCAGCATCTCAA 50,375,924
GTAGATGGGACTACAGGCACATTACTGTGCAAAGTGAAAAAAGATGATTC 50,375,974
AAACAAAAAACGGTGTGTGTGTGTGAAAATATAGTTGAGTGGTAGGACTG 50,376,024
GTTTGCTCAAAGCCTTTCTAGTATGCATTGCTCTTCCCATACATCTAACC 50,376,074
AACGATCGCAGGTCATCTAATAAGTATAGGGCTCTCAAATGGTGTGAATT 50,376,124
AGCTAAAGAAGAGTAATCTTAGTTTCTTGGTAATCAATCTCATGTCCCAA 50,376,174
GACCATGTAGGGGGAAATATACATGTTAAGCAAGCTCTCTACCACTACTA 50,376,224
TTTCTCTTGTCTTCTTTTTGAGACAGGCTTTCAGTAAATTTCCCAGGCTG 50,376,274
CCTTGAACGCACTCTGTTGCTCAGGCAAGTCTTGAAGTTGCAGTTCTCCT 50,376,324
CGGCTGGGCTTGTGTTCTTGCCTTTCACCCACCTCCTGGCCTGGAGACTT 50,376,374
GGGAGTTCTCACTTTTCGATGATCTAAACTAGTGTTTTCTGTCTCCTCTA 50,376,424
GATAGATCCTTTGCAGGTGAGGTCATGTGCAGTTATTCTCCCAGCCTGTC 50,376,474
TCATCCGAGTTTCCCTTACACCTGAAGGTTCACGTTACACAGCTCCTGTT 50,376,524
GCTCTCTTGAAGTCTTGTGATGCCCTTCTACTTAACACCCTTGCGCAGAC 50,376,574
TTAAAAGGTCTGAGTTCTGCACGCAGTCTCTGCACCTTTCCTTTGATGAC 50,376,624
ACCCCCCCCTTTTAAAAAACAAACTGTTCAAACTGGATTTAGCCTCCTCA 50,376,674
ATGTTGCACTTGAAAGAAAAGCGTATTTTTGCCTGTAACCTCTTGTGATG 50,376,724
GCTTTCAGAGGCTTACCAATTGTGGTACCTACCGTGGCACCGCCCAAACA 50,376,774
ATAACTCTTATTGTTAATTTCTAGGGTAGGTCAGTCAGATTCGGAGAAAC 50,376,824
TCGGGACATCATCCGTATTCTGCTATGTTGCAGGAATTCTCTTAAACGTC 50,376,874
ACCCATTTACCTCTGTAAGGGCACACGGGATGACCCGGGCGTGTCTCCAC 50,376,924
CTTGGGAGAGGCCCGTTGGTCGGTCGGGCGCAGCGCTCTGGGGCTGCGTC 50,376,974
CTTCGCGCCCCTGGCAGTCTCAGCCTTCCCTCGCGAGGCGCCGCACACCG 50,377,024
AGCGCCTCTCGTGCAAGGGCGAGGGGTTCGTAGAGTGCGAGTCCGTTAGG 50,377,074
CAAAGTGGGGTACAGGACTAGCTCGGGCACTGGCAGCCCATGTGGGTCGG 50,377,124
GACTGACCCCCTAAAGCGGGCAGGTAAGGGGACTGGTCCCAGGCGCCCCA 50,377,174
CGGAGATCGGGGATTTGGGCGCAGGGGGCGGGGCGGTACCCAGAGGAGGT 50,377,224
TTGGCACAACCCGGCCCTCCAGCTCCTACGCGTTCTGAGGAGAAAGGGCA 50,377,274
TGGCTTCCTTTTCTTCGTGGTGTCTTTCAAAACCGACAGGAGCGCGGATG 50,377,324
AAAAGCTGCGGATTAAGGGTAGAACTACCGCCCCTGCAAACCTGAACGAA 50,377,374
CTCTGGATTACTACCCAGTCCCTGCGGGGAGCTGATTAGCGCCATTCCCC 50,377,424
TCCCCCACTCCGGCGGGTAGGTCTAGAGAACGGTTTGAAGGTAGCCGCAT 50,377,475
GCGCATTAAGTAAAACAAGAAACCGCTGAGACGCCAAGCGCAATAATTGC 50,377,524
AAAAAGGCGCAGGCGCAGAAAGAAAAAAAAAAAACAACCAAAAACACCTC 50,377,574
GGTCAGTTTATGAAGAGGGCTGAGCCCAAACGCATGCGTGTAATAATAGG 50,377,624
ACGGCGGGAGAGAGCTCGGGGTTTCTTAATACGCATGCGTCCAATCTCTC 50,377,674
TGTGACGCAAGTGGGGCGGGGCCGGCAACAGGGTGCGCGTGCGCAGAGCT 50,377,724
TGCTGGAAGGGCTTTATTTAGCCTGCGCAGGCGCCCGCTTATCATTTCTC 50,377,774
CTCAGCCACGCCGAGGCTTTTTGTGGAGGTGAGTGACTTTCCGTCTTCGA 50,377,824
CTGCTGCCCGAGCTCTCCACGGACACCTCTTTGGGTGACGATTGCTTGTC 50,377,874
GCTGAGCTTAGGTTCTAACCTGAGGGGCCGTGGCAGGCGCAGGCTGCCCC 50,377,924
TGGGAGCCGCGAGTGTCTCGCCGGCGTGGCAGCGCCGCCTAGGCCTGCAG 50,377,974
GCCGCGCCGCTTTCTATTGTGTGAGATGTCTGAGGAGGCGGAGCGGAAGC 50,378,024
GGCGGCCGCCATTTCCTCGTCTCAACCGTGGCTGTGGGCCAGGGTCTTAT 50,378,074
TAGCTTGGCGCCTCGGCCCTGGGCGCACTGGGCGGCTTTGGGCATCGGGT 50,378,124
CGCTAGCCGAGGCCGGGTTGCATGCTTGAGTCTCCGGGGCCCAGGCATCC 50,378,174
TGACGGGCGGGACTCGCATGGCGGCGCCCGGTGCCCGCTGTGCGCCGTGA 50,378,224
AGTGGGAGGGCCATTTAAATGCCTGTTTTCTCAGACGCGTTCCTGACCCC 50,378,274
CACCCCCACCCCGCAGCCCCGCAATCTGTGTGGACGCCAGGACCACCGAA 50,378,324
GGGACG                                             50,378,330
```

Figure A2. DNA sequence of the cloned *Hnrnph1* promoter.
The promoter contains the DNA sequence 2956 bp upstream of transcription start site which corresponds to chromosome 11 nucleotide position 50,375,375 to 50,378,330 (mm10). The nucleotides indicated in different colors represent the positions of the SNPs, and the nucleotides indicated in blue represent the positions of the indels. The exons are highlighted in green. This figure supports Figure 12.

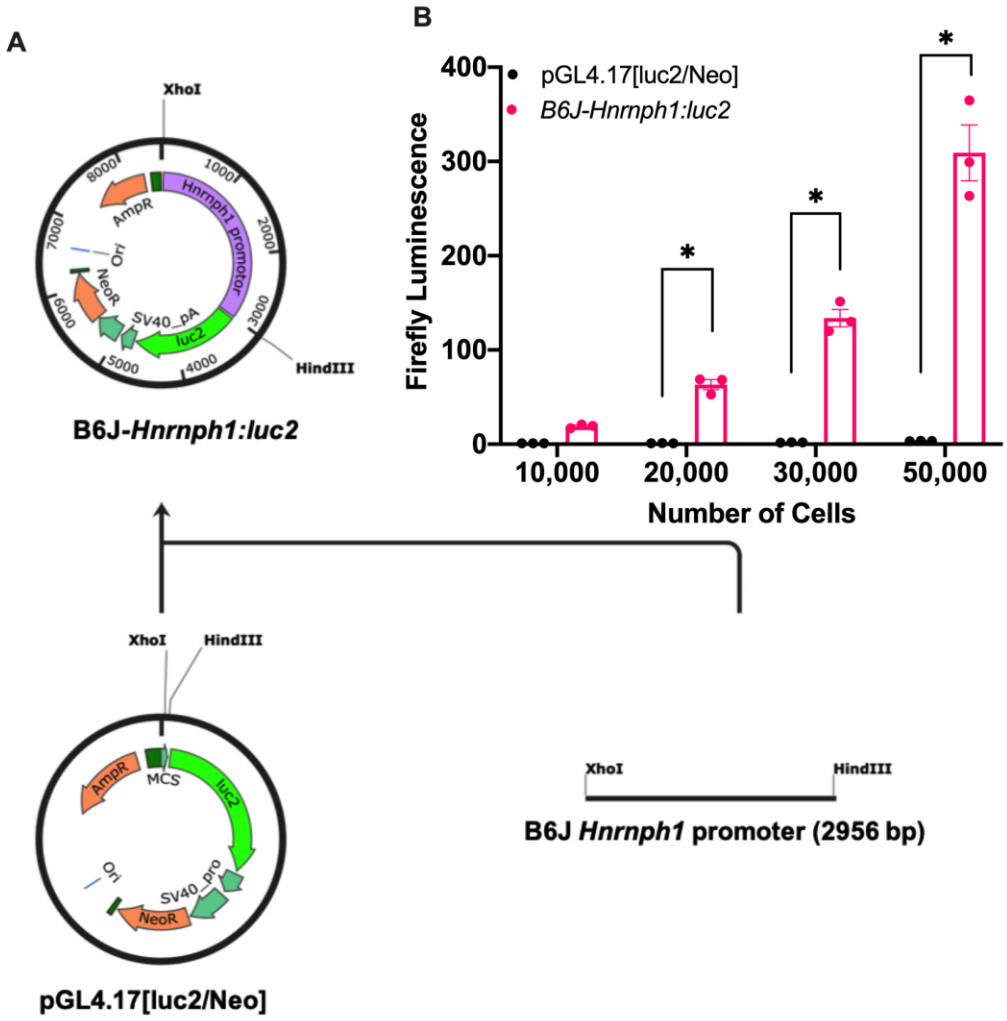

Figure A3. *Hnrnph1:luc2* reporter assay in HEK293T cells.
(A): Schematic representation of the procedure for cloning the *Hnrnph1* promoter into pGL4.17[luc2/Neo]. The promoter region of *Hnrnph1* was PCR-amplified followed by restriction enzyme digest by *XhoI* and *HindIII* for insertion into pGL4.17[luc2/Neo]. *The Hnrnph1* promoter was defined as 2956 bp upstream of the transcriptional start site of *Hnrnph1* and was fused to the firefly luciferase (luc2) to make the *Hnrnph1:luc2* reporter. (B): Different numbers of HEK293T cells were seeded to determine whether the cloned *Hnrnph1* promoter could drive expression of firefly luciferase, *luc2*. Firefly luminescence increased as the cell number increased [two-way ANOVA: $F(3,16) = 64.19$, $p = 3.86E\text{-}09$; Bonferroni's multiple comparison test: $t(16)_{10,000} = 1.15$, $p > 1$; $t(16)_{20,000} = 2.94$, $^*p = 0.005$; $t(16)_{30,000} = 8.35$, $^*p = 1.25e\text{-}6$; $t(16)_{50,000} = 19.36$, $^*p = 6.30e\text{-}12$]. Data are represented as the mean ± S.E.M. This figure supports Figure 13.

Table A1. Primers used for site directed mutagenesis.
This table supports Figures 12 and 13 and Table 7.

Mutation	Position SNP/Indel	Mutagenesis primer Sequences
T7288C	50,377,288	Forward: 5'-tgaaagacaccacgaggaaaaggaagccatgccc-3'
	rs29411274	Reverse: 5'-gggcatggcttccttttcctcgtggtgtctttca-3'
GA7546G	50,377,546	Forward: 5'-gtttttggttgttttttttttctttctgcgcctgcgcctttt-3'
	rs221962608	Reverse: 5'-aaaaggcgcaggcgcagaaagaaaaaaaaaaacaaccaaaaac-3'
T7795G	50,377,795	Forward: 5'-cacctccacacaaagcctcggcgtggctga-3'
	rs29475617	Reverse: 5'-tcagccacgccgaggctttgtgtggaggtg-3'
G7937C	50,377,937	Forward: 5'-cggcgagacagtcgcggctccca-3'
	rs257760362	Reverse: 5'-tgggagccgcgactgtctcgccg-3'
All four mutations (GA7546G:luc2 mutant used as template for multi-site mutagenesis)		Forward1: 5'-gggcatggcttccttttcctcgtggtgtctttca-3'
		Reverse1: 5'-tgaaagacaccacgaggaaaaggaagccatgccc-3'
		Forward2: 5'-tcagccacgccgaggctttgtgtggaggtg-3'
		Reverse2: 5'-cacctccacacaaagcctcggcgtggctga-3'
		Forward3: 5'-tgggagccgcgactgtctcgccg-3'
		Reverse3: 5'-cggcgagacagtcgcggctccca-3'

Table A2. RT-qPCR primers for exon usage.
This table supports Table 6 and Figure 10.

Gene	Targeted exon(s)	Sequences
Hnrnph1	3-4	Forward: 5'-CGCCCGCTTATCATTTCTCC-3'
		Reverse: 5'-CTTCACCACGAAGCCCTCT-3'
Hnrnph1	6-7	Forward: 5'-ACGGCTTAGAGGACTCCCTTT-3'
		Reverse: 5'-CGTACTCCTCCCCTGGAAGT-3'
Hnrnph1	7-8	Forward: 5'-CAGGAAATAGCTGAAAAGGCTCTA-3'
		Reverse: 5'-GCCATAAGTTTTCGTGGTGG-3'
Hnrnph1	3	Forward: 5'-AGCTTGCTGGAAGGGCTT-3'
		Reverse: 5'-ACCTCCACAAAAAGCCTCG-3'
Hnrnph1	4	Forward: 5'-GACCACCGAAGGGACGAT-3'
		Reverse: 5'-AAAAAGCGCTGCACTTCATC-3'
GAPDH	5-6	Forward: 5'-GCCTTCCGTGTTCCTACC-3'
		Reverse: 5'-CCTCAGTGTAGCCCAAGATG-3'

Table A3. Predicted RNA binding proteins (RBPs) associated with the 5'UTR of *Hnrnph1*. The 5'UTR *Hnrnph1* sequence was loaded into RBPDB (Cook et al., 2011) where the sequence was scanned for putative sites for binding of RBPs. A list of RBPs that are predicted to bind to *Hnrnph1* and the binding sites on *Hnrnph1* associated with the RBP are shown. The start and end positions refer to the nucleotide position for the sequence in Figure A2. This table supports Figure 13.

RBP	Start	End	Matching sequence
ZFP36	328	338	AAUAAGGAAAG
ZFP36	344	354	AAUAAGGAAAG
KHSRP	1252	1259	CCCCCCCC
A2BP1	268	273	UGCAUG
A2BP1	2769	2774	UGCAUG
ZRANB2	1772	1777	AGGUAA
HNRNPA1	1422	1427	UAGGGU
ybx2-a	443	448	AACAUC
ybx2-a	443	448	AACAUC
EIF4B	2807	2813	GCGGGAC
NONO	2950	2954	AGGGA
NONO	65	69	AGGGA
NONO	474	478	AGGGA
sap-49	742	747	GUGUGA
sap-49	2619	2624	GUGUGA
sap-49	621	626	GUGUGA
PABPC1	605	609	AAAAA
PABPC1	2151	2155	AAAAA
PABPC1	2180	2184	AAAAA
PABPC1	2173	2177	AAAAA
PABPC1	2179	2183	AAAAA
PABPC1	2190	2194	AAAAA
PABPC1	2178	2182	AAAAA
PABPC1	588	592	AAAAA
PABPC1	587	591	AAAAA
PABPC1	2175	2179	AAAAA
PABPC1	2177	2181	AAAAA
PABPC1	2174	2178	AAAAA
PABPC1	1264	1268	AAAAA
PABPC1	606	610	AAAAA
PABPC1	2176	2180	AAAAA
PABPC1	1265	1269	AAAAA
PABPC1	404	408	AAAAA
RBMY1A1	546	550	CUCAA
RBMY1A1	2671	2675	CUCAA
RBMY1A1	320	324	CUCAA
RBMY1A1	656	660	CUCAA
RBMY1A1	1297	1301	CUCAA
RBMY1A1	734	738	CUCAA

a2bp1	2816	2820	GCAUG
a2bp1	2770	2774	GCAUG
a2bp1	2232	2236	GCAUG
a2bp1	269	273	GCAUG
a2bp1	2097	2101	GCAUG
a2bp1	2283	2287	GCAUG
a2bp1	1898	1902	GCAUG
RBMY1A1	546	550	CUCAA
RBMY1A1	2671	2675	CUCAA
RBMY1A1	320	324	CUCAA
RBMY1A1	656	660	CUCAA
RBMY1A1	1297	1301	CUCAA
RBMY1A1	734	738	CUCAA
EIF4B	449	455	GUAGGAA
PABPC1	150	156	ACAAAUA
RBMY1A1	341	345	CACAA
RBMY1A1	1855	1859	CACAA
RBMY1A1	110	114	CACAA
RBMY1A1	149	153	CACAA
sap-49	1165	1170	UUGUGA
sap-49	1343	1348	UUGUGA
FUS	208	211	GGUG
FUS	2484	2487	GGUG
FUS	2332	2335	GGUG
FUS	2428	2431	GGUG
FUS	1066	1069	GGUG
FUS	497	500	GGUG
FUS	2830	2833	GGUG
FUS	612	615	GGUG
FUS	741	744	GGUG
FUS	1919	1922	GGUG
Pum2	106	109	UGUA
Pum2	77	80	UGUA
Pum2	1334	1337	UGUA
Pum2	806	809	UGUA
Pum2	2239	2242	UGUA
Pum2	1514	1517	UGUA
SNRPA	1303	1309	GUUGCAC
SFRS9	316	320	AGGAC
SFRS9	337	341	AGGAC
SFRS9	1714	1718	AGGAC
SFRS9	2248	2252	AGGAC
SFRS9	2939	2943	AGGAC
SFRS9	644	648	AGGAC
ACO1	523	528	CAGUGA
SFRS9	1888	1892	AGGAG

SFRS9	1844	1848	AGGAG
SFRS9	2633	2637	AGGAG
SFRS9	1938	1942	AGGAG
MBNL1	513	516	UGCU
MBNL1	918	921	UGCU
MBNL1	2351	2354	UGCU
MBNL1	679	682	UGCU
MBNL1	654	657	UGCU
MBNL1	1471	1474	UGCU
MBNL1	2493	2496	UGCU
MBNL1	2452	2455	UGCU
MBNL1	1150	1153	UGCU
MBNL1	2773	2776	UGCU
EIF4B	2355	2358	GGAA
EIF4B	1483	1486	GGAA
EIF4B	452	455	GGAA
EIF4B	476	479	GGAA
EIF4B	2645	2648	GGAA
EIF4B	402	405	GGAA
EIF4B	67	70	GGAA
EIF4B	349	352	GGAA
EIF4B	333	336	GGAA
EIF4B	813	816	GGAA
KHSRP	1786	1789	GUCC
KHSRP	1598	1601	GUCC
KHSRP	181	184	GUCC
KHSRP	32	35	GUCC
KHSRP	2289	2292	GUCC
KHSRP	2018	2021	GUCC
KHSRP	794	797	GUCC
KHSRP	1691	1694	GUCC
YBX1	2021	2026	CCUGCG
YBX1	2372	2377	CCUGCG
MBNL1	2751	2754	CGCU
MBNL1	2608	2611	CGCU
MBNL1	2500	2503	CGCU
MBNL1	1584	1587	CGCU
MBNL1	2386	2389	CGCU
MBNL1	2836	2839	CGCU
MBNL1	2124	2127	CGCU
Vts1	2597	2603	GCAGGCC
YTHDC1	2277	2282	UAAUAC
YTHDC1	2770	2775	GCAUGC
YTHDC1	2232	2237	GCAUGC
YTHDC1	2097	2102	GCAUGC
YTHDC1	2283	2288	GCAUGC

Vts1	2377	2383	GCAGGCG
Vts1	2159	2165	GCAGGCG
Vts1	2533	2539	GCAGGCG
Vts1	1766	1772	GCGGGCA
YBX1	1593	1598	GCUGCG
YBX1	1955	1960	GCUGCG
YTHDC1	1683	1688	GAGUGC
Vts1	2539	2545	GCAGGCU
Vts1	2807	2813	GCGGGAC
Vts1	1828	1834	GCGGGGC
Vts1	2316	2322	GCGGGGC
QKI	2513	2522	UUCUAACCUG
YTHDC1	2337	2342	GCGUGC
RBMX	2937	2940	CCAG
RBMX	893	896	CCAG
RBMX	2015	2018	CCAG
RBMX	1789	1792	CCAG
RBMX	1840	1843	CCAG
RBMX	2689	2692	CCAG
RBMX	1091	1094	CCAG
RBMX	1869	1872	CCAG
RBMX	35	38	CCAG
RBMX	2791	2794	CCAG
RBMX	186	189	CCAG
SFRS13A	335	341	AAAGGAC
SFRS13A	1893	1899	AAAGGGC

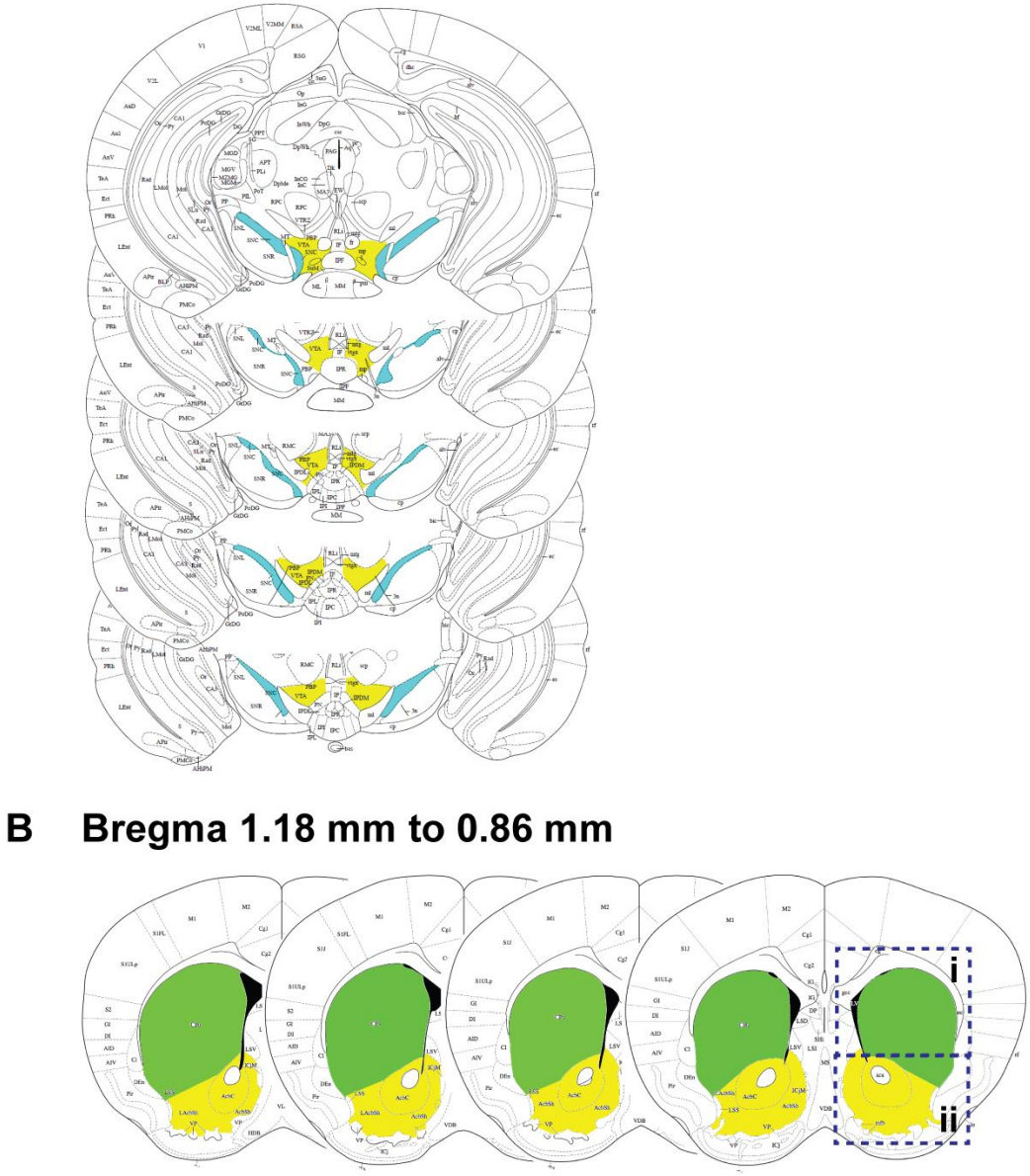

Figure A4. Schematics showing Bregma positions of the brain regions in IHC studies and Western blots.
(A): VTA and SNc of midbrain. Left: schematic showing the ventral midbrain region dissected for Western blot analysis. Right: coronal brain diagrams showing highlighted VTA (yellow) and SNc (teal) for IHC. **(B)**: Coronal brain diagrams showing highlighted dorsal striatum (green) and NAc (yellow) for IHC. This figure supports Figures 21-22.

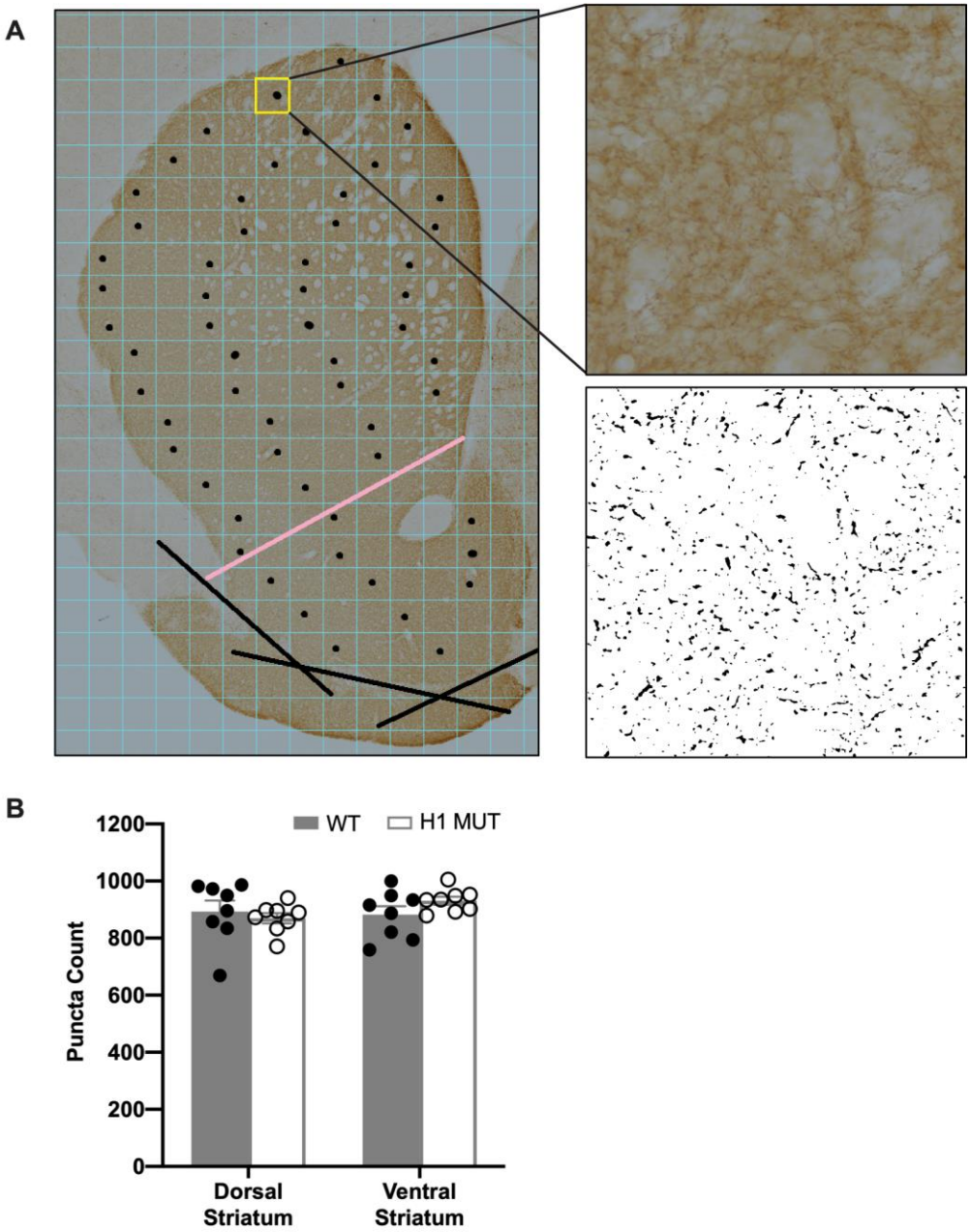

Figure A5. Schematics and puncta count of TH IHC staining in H1 MUT mice.
(A): A 225,000 x 225,000 µm grid was overlaid onto the images in Image J, and every third field (indicated by the black dots) was graded for total number of puncta. Regions of interest were graded by subtracting the background, setting a threshold, creating a binary image, and conducting particle analysis to count total puncta number based on roundness and total size (as indicated by threshold black/white image on bottom right). **(B):** Stereological analysis of the number of TH-positive puncta revealed no genotypic difference on the number of dopaminergic terminals in the dorsal and ventral striatum of H1 MUT versus WT mice (dorsal: $t(14) = 0.55$, $p = 0.588$; ventral: $t(14) = -1.49$, $p = 0.159$). WT: n = 8 and H1 MUT: n = 8. This figure supports Figure 22.

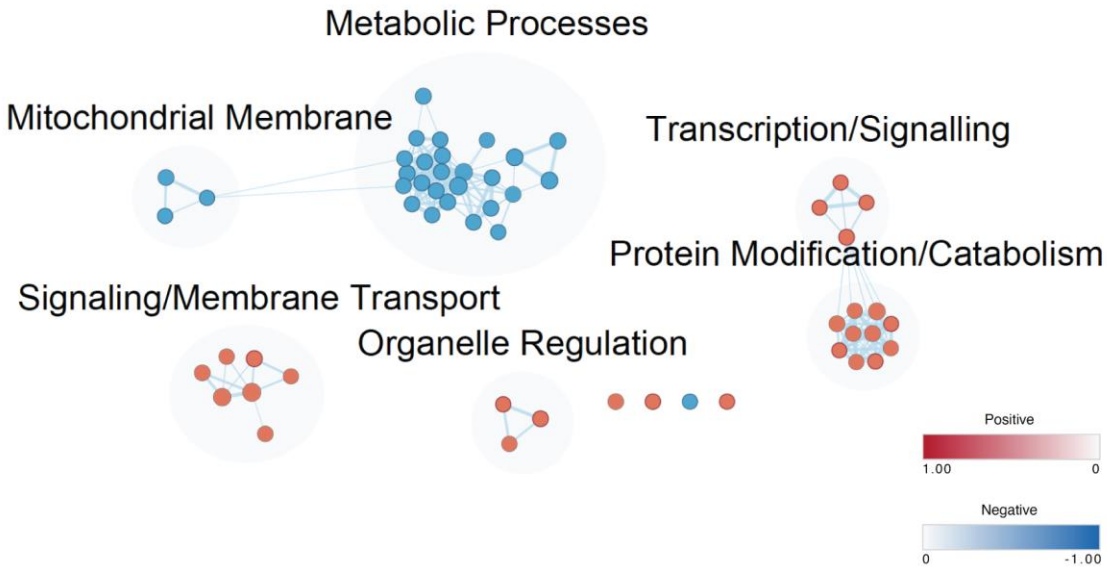

Figure A6. Network and pathway analysis of synaptosomal proteome of H1 MUT versus WT mice treated with MA or SAL [(H1 MUT_{MA} – H1 MUT_{SAL}) – (WT_{MA} – WT_{SAL})].
Enrichment results for the comparisons were visualized using Cytoscape and EnrichmentMap. Pathways were clustered and annotated with themes using AutoAnnotate. Nodes (grey circle) represent the pathways and the size of each node represents the number of proteins. Each circle within each node represents the individual protein (red is up and blue is down relative to WT). An enrichment for metabolic processes was detected in the H1 MUT mice and WT in response to MA in which MA decreased the expression of proteins involved in metabolic processes in the H1 MUT mice. The cut-off for the differential analysis is set to absolute $\log_2FC = 0.2$ and $p < 0.05$. This figure supports Figure 25B.

Table A4. Experimental design.

Drug Treatment	Genotype	IP	# of Animals per replicate	# of replicate(s)	# of animals
SAL	WT	IgG	4	1	4
MA	WT	IgG	4	1	4
SAL	MUT	IgG	4	1	4
MA	MUT	IgG	4	1	4
SAL	WT	Anti-hnRNP H	4	3	12
MA	WT	Anti-hnRNP H	4	3	12
SAL	MUT	Anti-hnRNP H	4	3	12
MA	MUT	Anti-hnRNP H	4	3	12
					64

This table supports Figure 29.

Table A5. Sample size.

Type of Experiment	Conditions
CLIP-seq	WT_SAL (IgG): n = 1 WT_MA (IgG): n = 1 MUT_SAL (IgG): n = 1 MUT_MA (IgG): n = 1 WT_SAL (anti-hnRNP H IP): n = 3 WT_MA (anti-hnRNP H IP): n = 3 MUT_SAL (anti-hnRNP H IP): n = 3 MUT_MA (anti-hnRNP H IP): n = 3
RNA-seq	WT_SAL: n = 1+ 3 WT_MA: n = 1 + 3 MUT_SAL: n = 1 + 3 MUT_MA: n = 1 + 3

This table supports Figure 29.

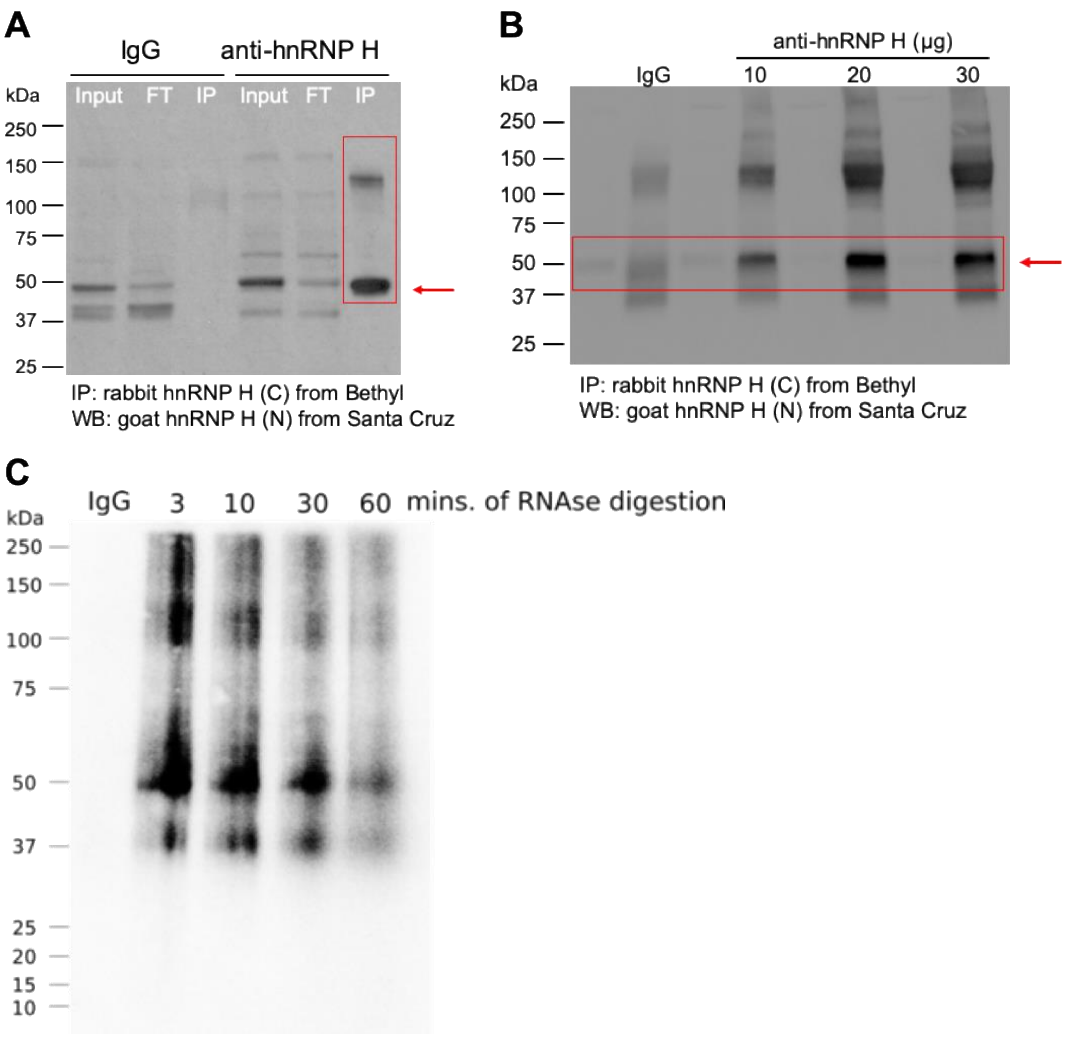

Figure A7. Optimization of the CLIP conditions for hnRNP H.
(A): Immunoblot shows the IP condition using the anti-hnRNP H antibody. No nonspecific bands were detected in the rabbit IgG pulldown. In the hnRNP H IP, a band of 50 kDa corresponding to the size of hnRNP H was detected. **(B):** Immunoblot showing IP condition using different concentrations of hnRNP H antibody. A total of 20 ug of antibody was chosen for the IP. **(C):** CLIP and ^{32}P labeling of bound RNA under different duration of RNase I_f digestion. Three min was chosen as the optimal length of digestion. This figure supports Figure 30A.

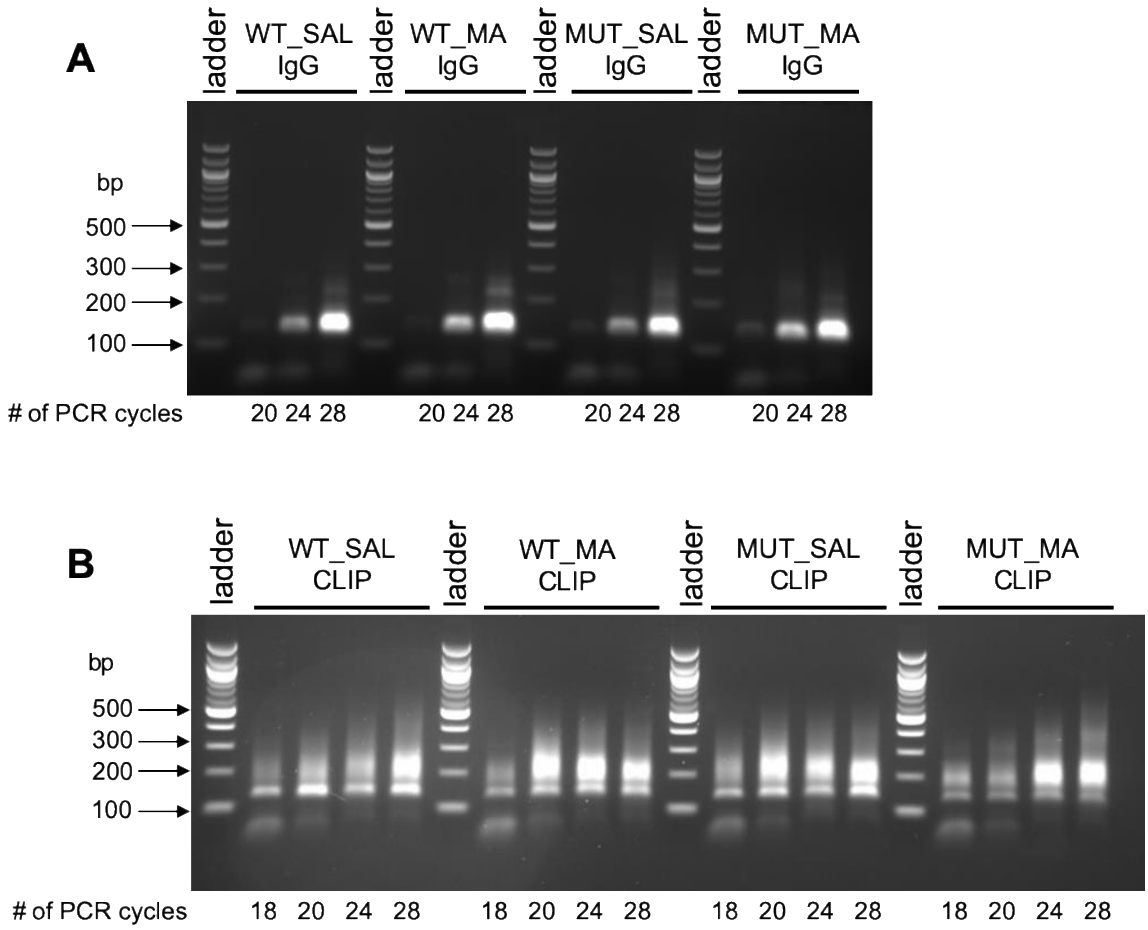

Figure A8. cDNA libraries generation followed by visualization with DNA gel electrophoresis. (A): No cDNA library was generated from IgG mock IP**.** Even after 28 cycles, no cDNA library (which should be > 200 bp) was detected. For this reason, these four samples were not subjected to RNA-seq. **(B):** In contrast with CLIP cDNA libraries, DNA bands > 200 bp were detected after 20 PCR cycles. This figure supports Figure 30A.

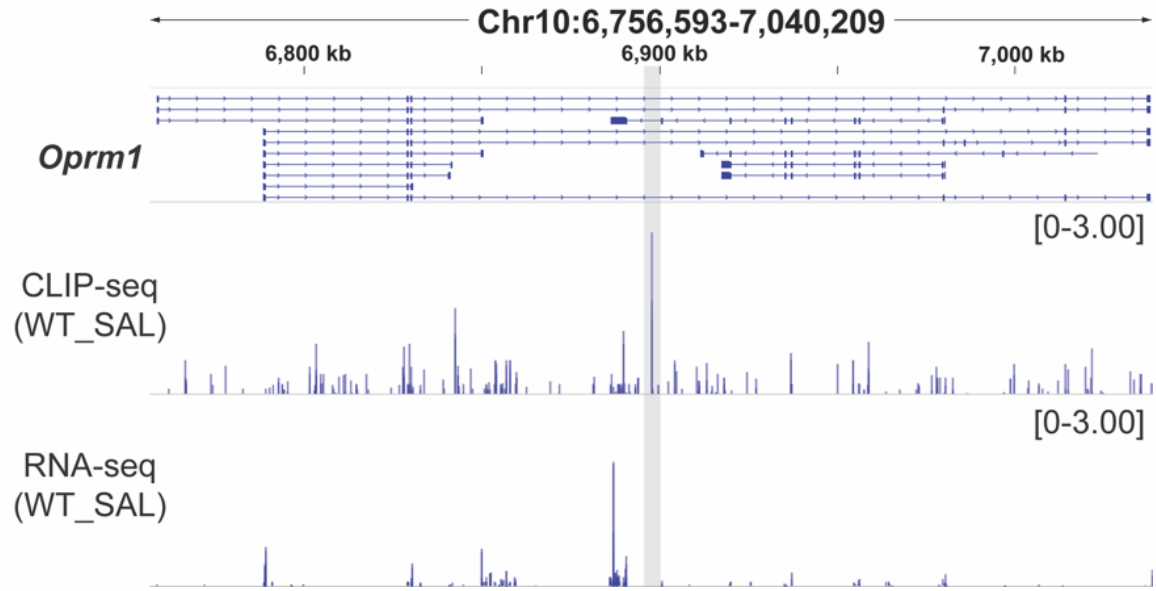

Figure A9. Visualization of read density by Integrative Genomics Viewer (Thorvaldsdóttir et al., 2013) **on top hnRNP H associated target, Oprm1.**
Scale of track height in CPM is the same for both tracks. Top track represents reads from CLIP-seq. Bottom track represents reads from RNA-seq. This figure supports Figure 30.

Table A6. hnRNP H motif by genomic region in untreated saline WT mice.
The top 3 Homer de novo motif results are shown for each genomic region type (5'UTR, CDS, intron and 3'UTR). The motif discovery was performed in Homer (Heinz et al., 2010). This table supports Figure 30C.

Genomic Region Type	Motif	p value	% of Target
5'UTR		1e-20	5.57%
		1e-16	23.49%
		1e-14	10.87%
CDS		1e-122	18.76%
		1e-75	15.00%
		1e-70	18.36%
Intron		1e-47	12.19%
		1e-34	9.88%
		1e-34	7.75%
3'UTR		1e-54	15.74%
		1e-47	9.85%
		1e-42	30.08%

Table A7. Top 10 pathways enriched in hnRNP H-associated targets with G-rich motif in WT_SAL.

Pathway	Database	Adjusted p	RNA targets
Presynaptic depolarization and calcium channel opening	pathway_Reactome	9.52E-05	*Cacna1a, Cacnb4, Cacna1e, Cacng4, Cacna1b, Cacng2, Cacnb2*
Phase 1 - inactivation of fast Na+ channels	pathway_Reactome	0.0225	*Kcnd3, Kcnip3, Kcnip2, Kcnd2*
LGI-ADAM interactions	pathway_Reactome	6.95E-04	*Dlg4, Adam23, Stx1b, Lgi4, Cacng4, Cacng2, Adam22*
Unblocking of NMDA receptors, glutamate binding and activation	pathway_Reactome	1.85E-04	*Gria1, Dlg4, Dlg2, Grin2a, Gria3, Camk2d, Grin2b, Actn2, Camk2a*
Interaction between L1 and Ankyrins	pathway_Reactome	0.0186	*Sptbn4, Ank3, Ank2, Ank1, Sptb*
CREB phosphorylation through the activation of CaMKII	pathway_Reactome	2.86E-04	*Dlg4, Creb1, Dlg2, Grin2a, Calm1, Camk2d, Grin2b, Actn2, Camk2a*
Ras activation upon Ca2+ influx through NMDA receptor	pathway_Reactome	4.41E-04	*Rasgrf1, Dlg4, Dlg2, Grin2a, Calm1, Camk2d, Grin2b, Actn2, Camk2a*
Reduction of cytosolic Ca++ levels	pathway_Reactome	0.0096	*Atp2a2, Atp2b2, Slc8a2, Atp2b1, Calm1, Slc8a1*
Rap1 signaling	pathway_Reactome	0.0096	*Rap1gap, Ywhaz, Prkg1, Rasgrp2, Rap1gap2, Rasgrp1*
Hypothetical Network for Drug Addiction	pathway_Wikipathway	1.76E-05	*Cacna1a, Cacnb4, Cacna1e, Cacng4, Cacna1b, Cacng2, Cacnb2*

This table supports Figure 30D.

Table A8. hnRNP H binding sites on the 7 targets enriched for "presynaptic depolarization and calcium channel opening."

RNA-binding Target	Peak Position(s)	Genomic Region Type
Cacna1a	chr8: 84611302-84611402	Intron
Cacnb4	chr8: 52629320- 52629420 chr8: 52560620- 52560720 chr8: 52472520- 52472620	Intron Intron Intron
Cacna1e	chr1:154446931- 154447031	Intron
Cacng4	chr11:107794366- 107794466	5'UTR or CDS depending on the mRNA isoform
Cacna1b	chr2: 24608087- 24608187 chr2: 24606587-24606687	CDS or intron depending on the mRNA isoform CDS
Cacng2	chr15: 78045548 - 78045548 chr15: 78103948- 78104048	Intron Intron
*Cacnb2**	Chr2: 14762588- 14762688 Chr2:14685188- 14685288 Chr2: 14622788- 14622888	Intron Intron Intron

*only 3 out of 9 peaks lists

This table supports Figure 30D and Table A7.

Table A9. Chi-square tests comparing difference in proportion of hnRNP H associated binding regions.

Given the binding events associated with hnRNP H detected in WT_SAL, the proportions of 3'UTR and intron targets in the other three conditions are significantly differently as depicted by the p values calculated in chi square test. This table supports Figure 32A.

Subregion	Comparison to WT_SAL		
	WT_MA vs WT_SAL	MUT_SAL vs WT_SAL	MUT_MA vs WT_SAL
3'UTR	0.0008 (***)	< 0.0001 (****)	< 0.0001 (****)
distal intron	< 0.0001 (****)	< 0.0001 (****)	< 0.0001 (****)
proximalx500_intron	< 0.0001 (****)	< 0.0001 (****)	< 0.0001 (****)
proximax200_intron	< 0.0001 (****)	0.453	< 0.0001 (****)
other_exon	0.42	0.864	0.226
CDS	0.208	0.714	< 0.0001 (****)
5'UTR	0.237	0.88	0.0008 (***)

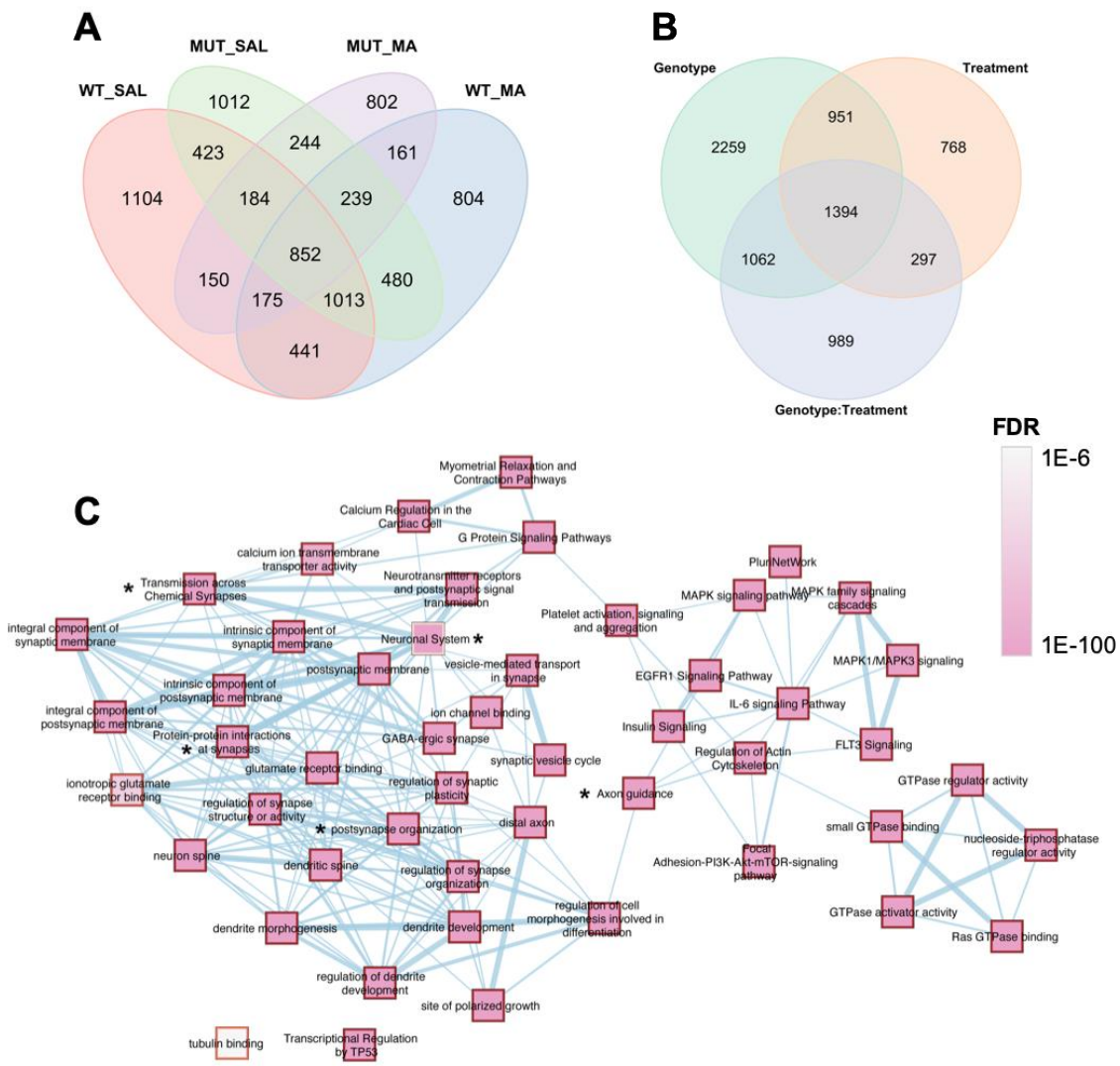

Figure A10. hnRNP H RNA-binding targets showing Genotype x Treatment interactions are enriched in pathways and gene ontology involved in drug-induced synaptic plasticity.
(A): Venn diagram shows distinct and overlapping hnRNP H targets identified in each of the four conditions. **(B):** Venn diagram shows distinct and overlapping hnRNP H targets as a function of Genotype, Treatment, or Genotype x Treatment interaction. Peak calling was performed using CLAM to identify peaks based on merged bam files across all conditions. Individual bam files were then used to count reads against the identified peaks. Differential peak analysis for Genotype x Treatment interaction was performed using limma/edgeR. The Genotype x Treatment interaction is expressed as $(MUT_{MA} - MUT_{SAL}) - (WT_{MA} - WT_{SAL})$. **(C):** Pathway analysis of the hnRNP H targets that showed a Genotype x Treatment interaction. The EnrichmentMap Cytoscape App (Merico et al., 2010) was used to build a network of the top 10 gene ontology and pathways enrichment results. Each square (or node) represents a gene set and edge represents mutual overlaps. A majority of gene sets are involved in synaptic function. This figure supports Figure 32B.

Table A10. KEGG pathways and GO cellular components enriched for hnRNP H-associated RNA targets with Genotype x Treatment interaction.
Only those pathways or cellular components that are significantly enriched are shown. This table supports Figure 32C.

(A): KEGG Pathway	
Gene Set	**RNA targets**
Amphetamine addiction	*Adcy5, Arc, Cacna1c, Calm2, Camk2a, Camk2b, Camk4, Creb3, Gnas, Gria1, Gria2, Grin2b, Ppp1cc, Ppp1ccb, Ppp1r1b, Ppp3ca, Ppp3r1*
Long-term potentiation	*Adcy1, Braf, Cacna1c, Calm2, Camk2a, Camk2b, Camk4, Ep300, Gnaq, Gria1, Gria2, Grin1, Grin2b, Grin2c, Grm1, Grm5, Hras, Map2k2, Ppp1cc, Ppp1ccb, Ppp3ca, Ppp3r1, Prkacb, Raf1, Rap1a*
Alcoholism	*Adcy5, Braf, Calm2, Camk4, Creb3, Gnas, Gnb1, Gng7, Grin2b, H3f3b, Hdac11, Hdac5, Hras, Ntrk2, Pkia, Ppp1cc, Ppp1ccb, Ppp1r1b*
Dopaminergic synapse	*Adcy5, Akt3, Cacna1a, Cacna1c, Calm2, Camk2a, Camk2b, Creb3, Gnaq, Gnas, Gnb1, Gng7, Gria1, Gria2, Grin2b, Gsk3b, Ppp1cc, Ppp1ccb, Ppp1r1b, Ppp2r1b, Ppp2r2a, Ppp2r5b, Ppp3ca*
(B): GO: Cellular Component	
Gene Set	**RNA targets**
ATPase complex	*Actl6b, Anp32e, Appl1, Arid1a, Arid1b, Atp1a3, Atp1b1, Atp1b2, Atp2a2, Bicra, Bicral, Brd8, Chd4, Chd5, Dpf1, Ep400, Gatad2b, Kat5, Mta1, Rbbp7, Ruvbl2, Smarca4, Smarcc2, Smarcd1, Srcap*
neuron spine	*Anks1b, Arc, Arhgap32, Arhgap33, Arrb1, Asic2, Atp2b1, Baiap2, Camk2a, Cdk5r1, Dgki, Dlg4, Dlgap3, Dnm1, Fus, Gria1, Grin2b, Grm5, Gsk3b, Hspa8, Itpka, Kcna4, Map1b, Myh10, Nrgn, Ntrk2, Pde4b, Ppp1cc, Ppp1r1b, Ppp1r9b, Ppp3ca, Pten, Rgs7bp, Sez6, Shisa7, Shisa9, Sipa1l1, Strn4, Syne1*
myelin sheath	*Aco2, Actg1, Aldoa, Atp1a3, Atp1b1, Atp5b, Atp5c1, Atp6v1a, Atp6v1b2, Car2, Cltc, Dlat, Dnm1, Eef1a1, Eef1a2, Eno1, Gjc2, Gjc3, Glul, Gnb1, Gsn, Gstm1, Hrh3, Hspa8, Hspa9, Mbp, Mog, Napb, Ncam1, Ndrg1, Nefm, Pdcd6ip, Pdia3, Pebp1, Pkm, Plp1, Pten, Rap1a, Slc25a3, Stxbp1, Syn2, Tppp, Tspan2, Vdac1, Ywhag*
nuclear chromatin	*Actl6b, Aldoa, Anp32e, Appl1, Arid1a, Arid1b, Bicra, Bicral, Brd4, Brd8, Cenpb, Chd4, Chd5, Clock, Cpsf6, Dpf1, Enc1, Ep400, Gatad2b, H1f0, H2afy, Jun, Kat2a, Kat5, Mef2d, Mta1, Nsmf, Polr2a, Ppp1r10, Rbbp7, Rcc1, Ruvbl2, Sfr1, Sin3b, Smad4, Smarca4, Smarcc2, Smarcd1, Srcap, Stat3, Suds3, Tbp, Tcf4, Trnp1, Zfp385a, Zfp57*

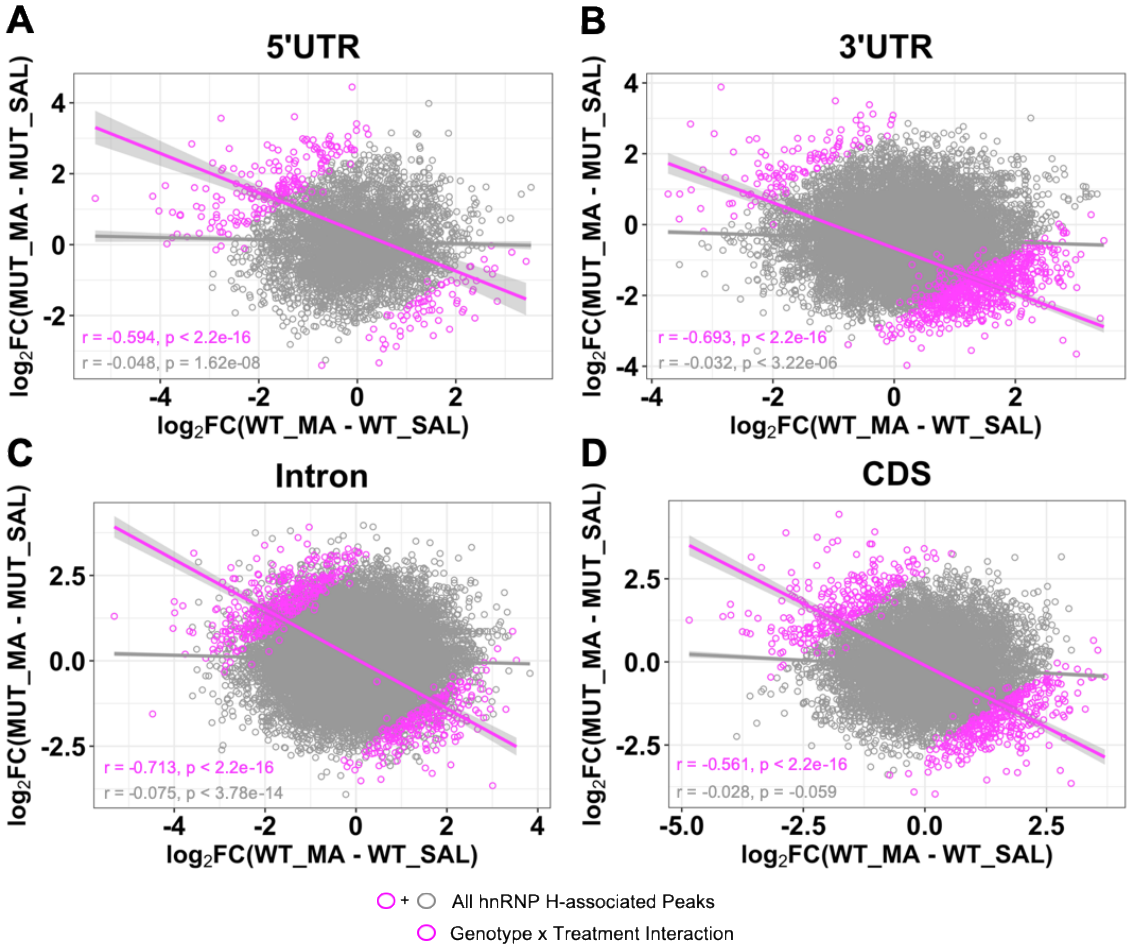

Figure A11. A strong negative correlation is detected between hnRNP H RNA-binding dynamic in the WT and MUT in response MA in the 3'UTR (A), introns (B), CDS (C), and 5'UTR (D).

The data points highlighted in magenta are those that show significant Genotype x Treatment interaction. The plots supportt the findings displayed in Figures 32B and 33.

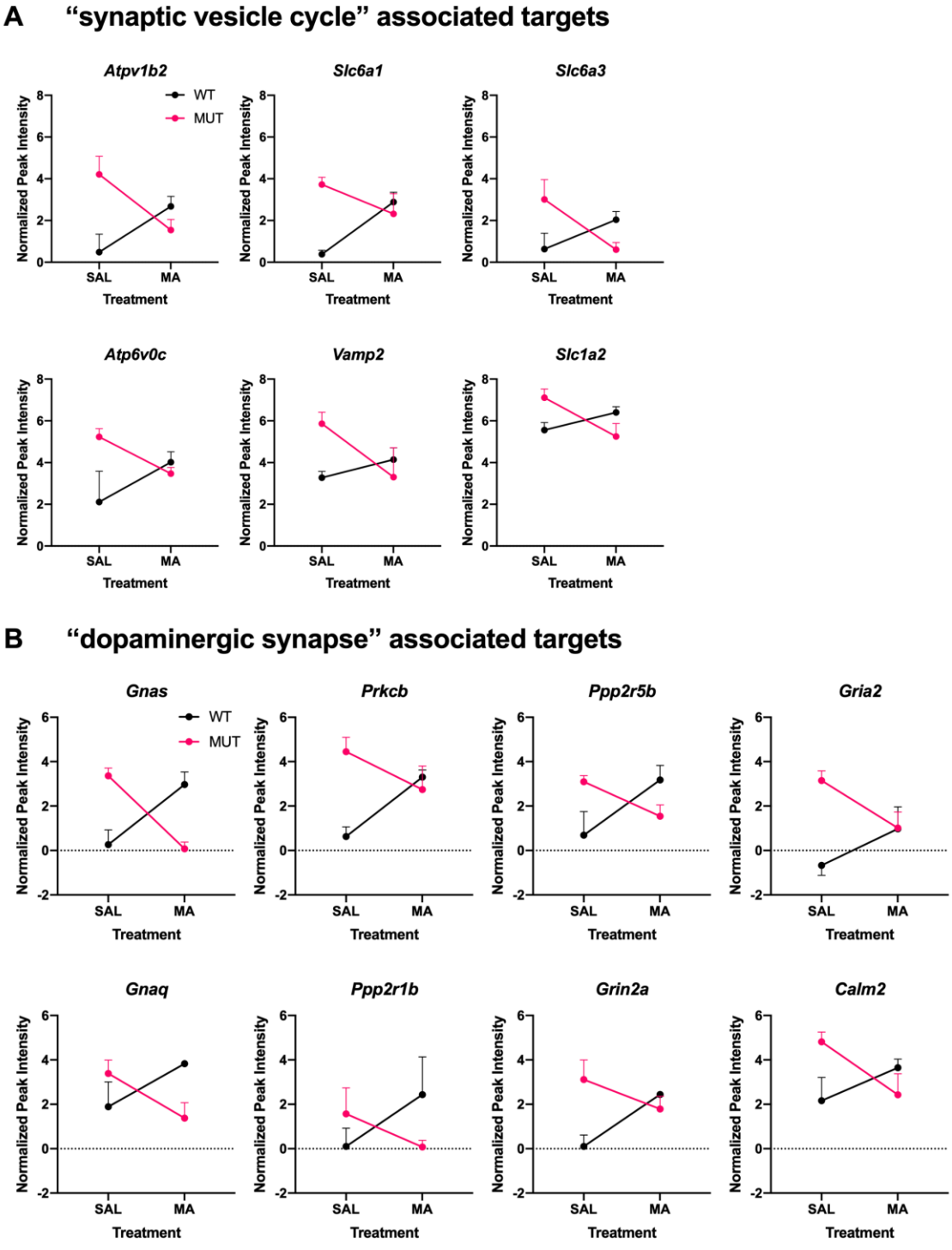
A "synaptic vesicle cycle" associated targets
Atpv1b2
Slc6a1
Slc6a3
Atp6v0c
Vamp2
Slc1a2
WT
MUT
Normalized Peak Intensity
SAL
MA
Treatment
B "dopaminergic synapse" associated targets
Gnas
Prkcb
Ppp2r5b
Gria2
Gnaq
Ppp2r1b
Grin2a
Calm2

Figure A12. 3'UTR targets show significant enrichment for both pre- and post-synaptic function.
Interaction plots for 3'UTR targets with significant Genotype by Treatment interaction that are enriched for **(A)** synaptic vesicle cycle and **(B)** dopaminergic synapse.The interaction plots are generated from CLIP-seq data showing average values with standard deviation of the means, with n = 3 per condition. This figure supports Table 10.

Table A11. Differential expressed genes overlapping with hnRNP H targets with Genotype by Treatment interaction.

Gene	Expression		Peak Intensity		Peak Location	
	logFC	p value	logFC	p value	Coordinate	Type
Cacna2d2	0.619	0.011	3.078	0.032	chr9:107529112-107529212	3'UTR or intron
Mir124a-1hg	-0.672	0.021	-4.020	0.004	chr14:64592731-64592831	Other exon
			-3.306	0.019	chr14:64592631-64592731	Other exon
			-3.062	0.030	chr14:64593631-64593731	Other exon
Gtf2e2	2.627	0.024	3.737	0.008	chr8:33774733-33774833	Intron
			3.102	0.035	chr8:33759333-33759433	Intron
Camta1	0.488	0.026	4.781	2.985E-04	chr4:151134622-151134722	Intron
			3.223	0.022	chr4:151107922-151108022	Intron
			-2.994	0.033	chr4:151717622-151717722	Intron
			-2.997	0.036	chr4:151060922-151061022	3UTR
			2.830	0.041	chr4:151510022-151510122	Intron
Unc13c	-0.705	0.027	3.343	0.018	chr9:73765622-73765722	Intron
			2.858	0.037	chr9:73509222-73509322	Intron
*Malat1**	-1.029	0.040	-2.381	2.155E-04	ch19:5801590-5801690	Intron
			-2.296	2.603E-04	chr19:5798090-5798190	Other exon
			-1.872	7.208E-04	chr19:5797290-5797390	Intron or other exon
			-1.774	8.040E-04	chr19:5797390-5797490	Intron or other exon
			-2.093	0.001	chr19:5797990-5798090	Other exon

*5 out of 48 peaks shown
This table supports Figure 34A.

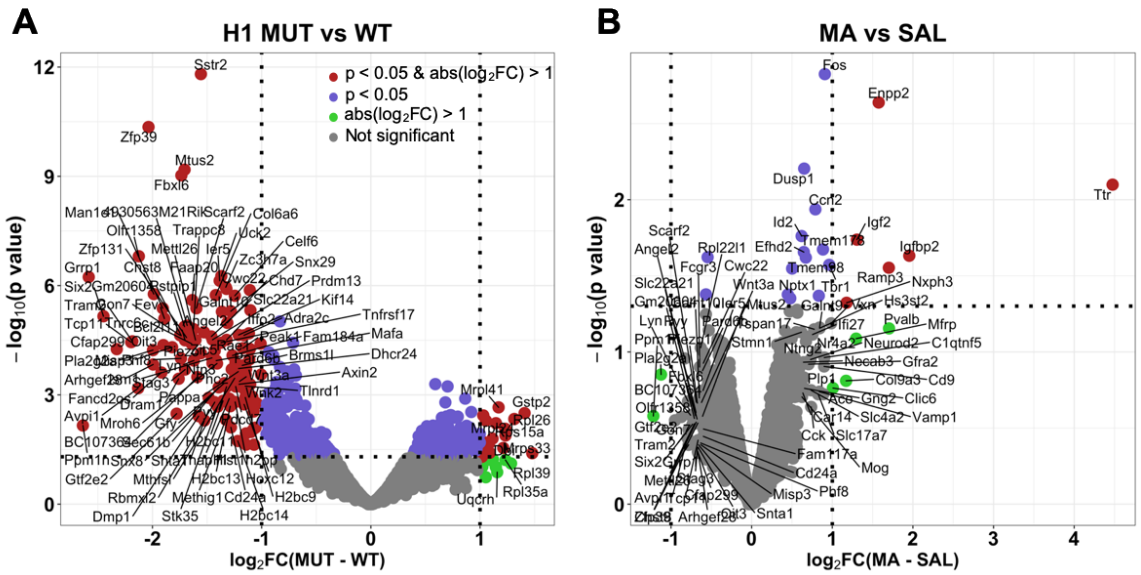

Figure A13. The main effect of Genotype is more significant than the main effect of Treatment.

Differential gene expression for interaction of Genotype (MUT – WT) or Treatment (MA – SAL) was performed using limma (Ritchie et al., 2015) and edgeR (Robinson et al., 2009). (A): Volcano plot showing genes that are differentially expressed between H1 MUT and WT. (B): Volcano plot showing genes that are differential expressed between MA and SAL condition. This figure supports Figure 34B.

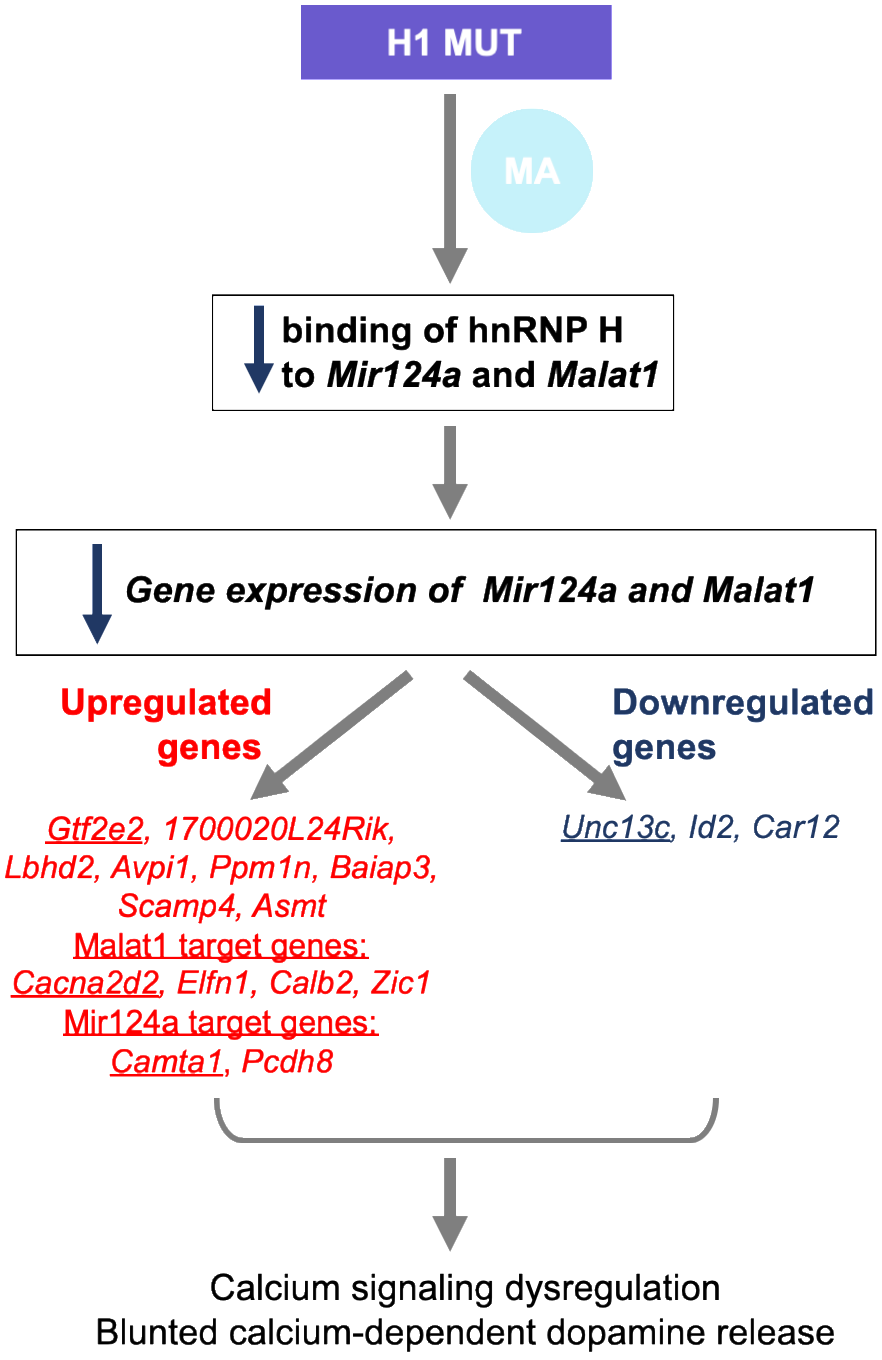

Figure A14. Putative model for *Mir124a*- and *Malat1*-mediated transcriptional regulation that could underlie blunted MA-induced DA release observed in H1 MUT mice.
CLIP-seq and transcriptome analysis indicated that hnRNP H showed decreased binding of hnRNP H to *Mir124a* and *Malat1* which we propose leads to a subsequent downregulation of both *Mir124a* and *Malat1* at the gene *level* after acute MA exposure in the H1 MUT relative to WT control. The suppression in *Mir124a* and *Malat1* levels that is induced by MA in the H1 MUT leads to an increase in expression of *Cacna2d2* (a putative Malat1 target gene), *Camta1* (a putative Mir124a

target gene), and *Getf2e2*, and other genes, and a decrease in expression of *Unc13c* and other genes. Out of the 19 significant differentially expressed genes showing a Genotype x Treatment interaction, 16 genes showed an increase in expression after MA treatment in H1 MUT versus WT mice, implicating that a reduction in expression of the two noncoding RNAs, *Mir124a* and *Malat1* leads to an increase in expression of genes that are involved in calcium-regulated DA release induced by MA (e.g., *Cacna2d2* and *Camta1*). The underlined genes are RNA-binding targets of hnRNP H. H1 MUT mice show markedly blunted MA-induced DA release (Ruan et al., 2020a). Interestingly, the overlapping hnRNP H interactome and transcriptome that represents the Genotype x Treatment interaction revealed *Unc13c* (**Figure 34A-B**) as a differential, MA-induced hnRNP H binding target in H1 MUT (decrease) versus WT mice (increase) (**Figure 34B**). Unc13 or Munc-13 couples calcium entry through VGCC and synaptic vesicle fusion to plasma membrane, triggered by calcium binding to sensor proteins (Eggermann et al., 2012; Dittman and Ryan, 2019). Unc13 activates the SNARE complex and docks synaptic vesicles close to VGCCs and recruits/positions VGCCs to the active zone to couple calcium influx with neurotransmitter release (Südhof, 2013; Böhme et al., 2018; Kusch et al., 2018; Dittman, 2019). Unc13 activity at the active zone is tightly associated with synaptic vesicle release dynamics. In turn, calcium and calmodulin binding modulates the activity of Unc13 (Lipstein et al., 2012). The calmodulin-binding transcription factor, *Camta1*, was also identified as a differential expressed gene that showed a MA-induced increase in expression in H1 MUT relative to WT mice (**Figure 34A-B**). Our previous transcriptome analysis in drug-naïve mice indicated differential splicing of *Ppp3ca* in the H1 MUT compared to WT (Ruan et al., 2020b). *Ppp3ca* codes for the α catalytic subunit of calcineurin, which is a calcium/calmodulin-response protein phosphatase involved in dopamine receptor signaling and behavioral responses to psychostimulants (Oliver and Shenolikar, 1998). Thus, multiple lines of evidence point to perturbations in calcium signaling as likely potential mechanism linking blunted MA-induced dopamine release observed in the H1 MUT mice. Convergent analysis of the hnRNP H interactome and transcriptome also identified non-coding RNAs, *miR-124a* and *Malat1* as showing differential binding to hnRNP H between H1 MUT and WT in response to MA (**Figure 34A-B**). Both non-coding RNAs showed a MA-induced decrease in expression in H1 MUT versus WT (**Table A11**). Drug-induced synaptic plasticity requires changes in gene expression and post-transcriptional regulation (McClung and Nestler, 2008; Nestler, 2008), which can be orchestrated by microRNAs (miRs) and long noncoding RNAs (lncRNAs). miRs like miR-124a that suppress mRNA translation by targeting the 3'UTR (Lipovich et al., 2012). lncRNAs like Malat1 serve as precursors to small RNAs and regulate RNA processing, transcriptional and post-transcriptional modulation of gene expression(Mercer et al., 2009; Xie et al., 2014). Malat1 can promote neuronal cell apoptosis by sequestering miR-124a in models of Parkinson's Disease (Liu et al., 2017). Changes in ventral striatal gene expression after repeated MA exposure depend on miRNAs and lncRNAs (Zhu et al., 2016). Multiple studies show evidence for a downregulation of miR-124 in response to psychostimulants and concomitant upregulation of genes involved in drug-induced plasticity (Guo et al., 2016; Cabana-Domínguez et al., 2018; Liu et al., 2019). For example, MA treatment in cultured astrocytes decreased MIR-124 expression and *SIGMAR1* by alleviating translational repression of MIR-124 at the 3'UTR (Huang et al., 2017). Also, striatal overexpression of *miR-124* overexpression inhibited cocaine-mediated locomotor hyperactivity (Periyasamy et al., 2018). Binding of hnRNP H to both *miR-124* and *Malat1* and the subsequent genotype-interactive effect on MA-induced gene expression could impact transcriptional and posttranscriptional regulation of their downstream targets. Accordingly, the miRNA-target (TargetScan, 134) and lncRNA-target (LncRRIsearch, 135) algorithms predicted *Camta1* as putative target of miR-124 and *Cacna2d2* as putative target of *Malat1*, respectively. This figure supports Figure 34A.

Table A12. Read Coverage in CLIP-seq and input RNA-seq samples.

Sample Name	Type	Genotype	Treatment	Replicate	Barcode Sequence	Read Counts
CLIP_WT_SAL_1	CLIP-seq	WT	SAL	1	ACAGTG	16,446,905
CLIP_WT_SAL_2	CLIP-seq	WT	SAL	2	GATCAG	12,440,933
CLIP_WT_SAL_3	CLIP-seq	WT	SAL	3	AGTCAA	22,826,085
CLIP_WT_MA_1	CLIP-seq	WT	MA	1	GCCAAT	24,419,809
CLIP_WT_MA_2	CLIP-seq	WT	MA	2	TAGCTT	16,402,702
CLIP_WT_MA_3	CLIP-seq	WT	MA	3	AGTTCC	13,376,067
CLIP_MUT_SAL_1	CLIP-seq	MUT	SAL	1	CAGATC	25,759,157
CLIP_MUT_SAL_2	CLIP-seq	MUT	SAL	2	GGCTAC	27,432,645
CLIP_MUT_SAL_3	CLIP-seq	MUT	SAL	3	ATGTCA	25,812,360
CLIP_MUT_MA_1	CLIP-seq	MUT	MA	1	ACTTGA	17,903,276
CLIP_MUT_MA_2	CLIP-seq	MUT	MA	2	CTTGTA	16,116,861
CLIP_MUT_MA_3	CLIP-seq	MUT	MA	3	CCGTCC	12,899,100
INPUT_WT_SAL_1	RNA-seq	WT	SAL	1	GTTTCG	44,421,956
INPUT_WT_SAL_2	RNA-seq	WT	SAL	2	ACTGAT	48,930,085
INPUT_WT_SAL_3	RNA-seq	WT	SAL	3	CAACTA	53,470,359
INPUT_WT_MA_1	RNA-seq	WT	MA	1	CGTACG	53,843,037
INPUT_WT_MA_2	RNA-seq	WT	MA	2	ATGAGC	55,822,205
INPUT_WT_MA_3	RNA-seq	WT	MA	3	CACGAT	44,088,258
INPUT_MUT_SAL_1	RNA-seq	MUT	SAL	1	GAGTGG	43,697,136
INPUT_MUT_SAL_2	RNA-seq	MUT	SAL	2	ATTCCT	45,817,909
INPUT_MUT_SAL_3	RNA-seq	MUT	SAL	3	CACTCA	42,147,542
INPUT_MUT_MA_1	RNA-seq	MUT	MA	1	GGTAGC	37,184,152
INPUT_MUT_MA_2	RNA-seq	MUT	MA	2	CAAAAG	39,745,547
INPUT_MUT_MA_3	RNA-seq	MUT	MA	3	CAGGCG	33,706,973

This table supports Tables A4.

BIBLIOGRAPHY

Adinoff B (2004) Neurobiologic processes in drug reward and addiction. Harvard Review of Psychiatry 12:305–320.

Agarwal V, Bell GW, Nam JW, Bartel DP (2015) Predicting effective microRNA target sites in mammalian mRNAs. eLife 4:1–38.

Alarcon JM, Hodgman R, Theis M, Huang YS, Kandel ER, Richter JD (2004) Selective modulation of some forms of Schaffer collateral-CA1 synaptic plasticity in mice with a disruption of the CPEB-1 gene. Learning & Memory11:318–327.

Aldridge GM, Podrebarac DM, Greenough WT, Weiler IJ (2009) The use of total protein stains as loading controls: an alternative to high-abundance single protein controls in semi-quantitative immunoblotting Georgina. Journal of Neuroscience Methods 172:250–254.

Anders S, Pyl PT, Huber W (2015) HTSeq-A Python framework to work with high-throughput sequencing data. Bioinformatics 31:166–169.

Anders S, Reyes A, Huber W (2012) Detecting differential usage of exons from RNA-seq data. Genome Research 22:2008–2017.

Andres MA, Cooke IM, Bellinger FP, Berry, MJ, Zaporteza M, Rueli RH, Barayuga SM, Chang L (2015) Methamphetamine acutely inhibits voltage-gated calcium channels but chronically upregulates L-type channels. Journal of Neurochemistry 134:56–65.

Annepu J, Ravindranath V (2000) 1-Methyl-4-phenyl-1,2,3,6-tetrahydropyridine-induced complex I inhibition is reversed by disulfide reductant, dithiothreitol in mouse brain. Neuroscience Letters 289:209–212.

Araujo PR, Yoon K, Ko D, Smith AD, Qiao M, Suresh U, Burns SC, Penalva LOFF (2012) Before it gets started: Regulating translation at the 5′UTR. Comparative and Functional Genomics 2012.

Arhin GGK, Boots M, Bagga PPS, Milcarek C, Wilusz J (2002) Downstream sequence elements with different affinities for the hnRNP H/H' protein influence the processing efficiency of mammalian polyadenylation signals. Nucleic Acids Research 30:1842–1850.

Arun G, Aggarwal D, Spector DL (2020) MALAT1 Long Non-Coding RNA: Functional Implications. Non-Coding RNA 6:22.

Atkins CM, Davare MA, Oh MC, Derkach V, Soderling TR (2005) Bidirectional regulation of cytoplasmic polyadenylation element-binding protein phosphorylation by Ca2+/calmodulin-dependent protein kinase II and protein phosphatase 1 during hippocampal long-term potentiation. Journal of Neuroscience 25:5604–5610.

Aulas A, Velde C Vande (2015) Alterations in stress granule dynamics driven by TDP-43 and FUS: A link to pathological inclusions in ALS? Frontiers in Cellular Neuroscience 9:1–13.

Backlund M, Stein F, Rettel M, Schwarzl T, Perez-Perri JI, Brosig A, Zhou Y, Neu-Yilik G, Hentze MW, Kulozik AE (2020) Plasticity of nuclear and cytoplasmic stress responses of RNA-binding proteins. Nucleic Acids Research 48:4725–4740.

Bailey TL, Boden M, Buske FA, Frith M, Grant CE, Clementi L, Ren J, Li WW, Noble WS (2009) MEME Suite: Tools for motif discovery and searching. Nucleic Acids Research 37:202–208.

Bain JM, Cho MT, Telegrafi A, Wilson A, Brooks S, Botti C, Gowans G, Autullo LA, Krishnamurthy V, Willing MC, Toler TL, Ben-Zev B, Elpeleg O, Shen Y, Retterer K, Monaghan KG, Chung WK (2016) Variants in HNRNPH2 on the X Chromosome Are Associated with a Neurodevelopmental Disorder in Females. American Journal of Human Genetics 99:1–7.

Bassell GJ, Warren ST (2008) Fragile X Syndrome: Loss of Local mRNA Regulation Alters Synaptic Development and Function. Neuron 60:201–214.

Bateup HS, Svenningsson P, Kuroiwa M, Gong S, Heintz N, Greengard P (2008) Cell-type specific regulation of DARPP-32 phosphorylation by psychostimulant and antipsychotic drugs. Nature Neuroscience 11:932–939.

Baumann MH, Ayestas MA, Sharpe LG, Lewis DB, Rice KC, Rothman RB (2002) Persistent antagonism of methamphetamine-induced dopamine release in rats pretreated with GBR12909 decanoate. Journal of Pharmacology and Experimental Therapeutics 301:1190–1197.

Beaulieu J-M, Gainetdinov RR (2011) The Physiology, Signaling, and Pharmacology of Dopamine Receptors. Pharmacological Reviews 63:182–217.

Beaulieu JM, Sotnikova TD, Marion S, Lefkowitz RJ, Gainetdinov RR, Caron MG (2005) An Akt/β-arrestin 2/PP2A signaling complex mediates dopaminergic neurotransmission and behavior. Cell 122:261–273.

Beer SM, Taylor ER, Brown SE, Dahm CC, Costa NJ, Runswick MJ, Murphy MP (2004) Glutaredoxin 2 catalyzes the reversible oxidation and glutathionylation of mitochondrial membrane thiol proteins: Implications for mitochondrial redox

regulation and antioxidant defense. Journal of Biological Chemistry 279:47939–47951.

Beninger RJ (1983) The role of dopamine in locomotor activity and learning. Brain Research Reviews 6:173–196.

Bernheim A, See RE, Reichel CM (2016) Chronic methamphetamine self-administration disrupts cortical control of cognition. Neuroscience & Biobehavioral Reviews 69:36–48.

Bernier FP et al. (2012) Haploinsufficiency of SF3B4, a component of the pre-mRNA spliceosomal complex, causes nager syndrome. American Journal of Human Genetics 90:925–933.

Béthune J, Jansen RP, Feldbrügge M, Zarnack K (2019) Membrane-Associated RNA-Binding Proteins Orchestrate Organelle-Coupled Translation. Trends in Cell Biology 29:178–188.

Black DL (1992) Activation of c-src neuron-specific splicing by an unusual RNA element in vivo and in vitro. Cell 69:795–807.

Böhme MA, Grasskamp AT, Walter AM (2018) Regulation of synaptic release-site Ca2+ channel coupling as a mechanism to control release probability and short-term plasticity. Federation of European Biochemical Societies (FEBS) Letters 592:3516–3531.

Bolger AM, Lohse M, Usadel B (2014) Trimmomatic: A flexible trimmer for Illumina sequence data. Bioinformatics 30:2114–2120.

Bosch PJ, Peng L, Kivell BM (2015) Proteomics analysis of dorsal striatum reveals

changes in synaptosomal proteins following methamphetamine self-administration in rats. Public Library of Science (PLOS) One 10:1–17.

Bottini S, Pratella D, Grandjean V, Repetto E, Trabucchi M (2017) Recent computational developments on CLIP-seq data analysis and microRNA targeting implications. Briefings in Bioinformtics:1–12.

Bourdy R, Sánchez-Catalán MJ, Kaufling J, Balcita-Pedicino JJ, Freund-Mercier MJ, Veinante P, Sesack SR, Georges F, Barrot M (2014) Control of the nigrostriatal dopamine neuron activity and motor function by the tail of the ventral tegmental area. Neuropsychopharmacology 39:2788–2798.

Bramham CR, Wells DG (2007) Dendritic mRNA: Transport, translation and function. Nature Reviews Neuroscience 8:776–789.

Brown JM, Quinton MS, Yamamoto BK (2005) Methamphetamine-induced inhibition of mitochondrial complex II: Roles of glutamate and peroxynitrite. Journal of Neurochemistry 95:429–436.

Brown MR, Kronengold J, Gazula V, Chen Y, John G, Sigworth FJ, Navaratnam D, Kaczmarek LK (2010) FMRP regulates gating of Na+ activated K+ channel Slack. Nature Neuroscience 13:819–821.

Bryant CD (2011) The blessings and curses of C57BL/6 substrains in mouse genetic studies HHS Public Access Author manuscript. Annals of the New York Academy of Sciences 1245:31–33.

Bryant CD, Graham ME, Distler MG, Munoz MB, Li D, Vezina P, Sokoloff G, Palmer AA (2009) A Role for Casein Kinase 1 Epsilon in the Locomotor Stimulant

Response to Methamphetamine. Psychopharmacology 203:703–711.

Bryant CD, Parker CC, Zhou L, Olker C, Chandrasekaran RY, Wager TT, Bolivar VJ, Loudon AS, Vitaterna MH, Turek FW, Palmer AA (2012) Csnk1e is a genetic regulator of sensitivity to psychostimulants and opioids. Neuropsychopharmacology 37:1026–1035.

Bryant CD, Smith DJ, Kantak KM, Nowak TS, Williams RW, Damaj MI, Redei EE, Chen H, Mulligan MK (2020) Facilitating Complex Trait Analysis via Reduced Complexity Crosses. Trends in Genetics 36:549–562.

Bryant CD, Yazdani N (2016) RNA binding proteins, neural development and the addictions. Genes, Brain and Behavior 15:169–186.

Burke RE, Lud Cadet J, Kent JD, Karanas AL, Jackson-Lewis V (1990) An assessment of the validity of densitometric measures of striatal tyrosine hydroxylase-positive fibers: relationship to apomorphine-induced rotations in 6-hydroxydopamine lesioned rats. Journal of Neuroscience Methods 35:63–73.

Burrows KB, Gudelsky G, Yamamoto BK (2000) Rapid and transient inhibition of mitochondrial function following methamphetamine or 3,4-methylenedioxymethamphetamine administration. European Journal of Pharmacology 398:11–18.

Cabana-Domínguez J, Arenas C, Cormand B, Fernàndez-Castillo N (2018) MiR-9, miR-153 and miR-124 are down-regulated by acute exposure to cocaine in a dopaminergic cell model and may contribute to cocaine dependence. Translational Psychiatry 8:1–8.

Carboni GL, Gao B, Nishizaki M, Xu K, Minna JD, Roth JA, Ji L (2003) CACNA2D2-mediated apoptosis in NSCLC cells is associated with alterations of the intracellular calcium signaling and disruption of mitochondria membrane integrity. Oncogene 22:615–626.

Carninci P, Kasukawa T, Katayama S, Gough J, Frith, M. C., Maeda, N., Oyama, R., Ravasi, T., Lenhard, B., Wells, C., Kodzius, R., Shimokawa, K., Bajic, V. B., Brenner, S. E., Batalov, S., Forrest, A. R. R., Zavolan, M., Davis, M. J., Wilming, L. G and RGERG and GSG (Genome NPCG (2005) The transcriptional landscape of the mammalian genome. Science 309:1559–1563.

Chakrabarti A, Haberman N, Praznik A, Luscombe N, Ule J (2017) Data Science Issues in Understanding Protein-RNA Interactions. The Preprint Server for Biology bioRxiv: 208124.

Chandra R et al. (2017) Drp1 mitochondrial fission in D1 neurons mediates behavioral and cellular plasticity during early cocaine abstinence. Neuron 96:1327–1341.

Chatterjee S, Pal JK (2009) Role of 5′- and 3′-untranslated regions of mRNAs in human diseases. Biology of the Cell 101:251–262.

Chen EY, Tan CM, Kou Y, Duan Q, Wang Z, Meirelles G V., Clark NR, Ma'ayan A (2013) Enrichr: Interactive and collaborative HTML5 gene list enrichment analysis tool. BioMed Central (BMC) Bioinformatics 14:1–14.

Chen F, Keleş S (2020) SURF: integrative analysis of a compendium of RNA-seq and CLIP-seq datasets highlights complex governing of alternative transcriptional regulation by RNA-binding proteins. Genome Biology 21:1–23.

Chi L, Reith MEA (2003) Substrate-Induced Trafficking of the Dopamine Transporter in Heterologously Expressing Cells and in Rat Striatal Synaptosomal Preparations. Journal of Pharmacology and Experimental Therapeutics 307:729–736.

Chick JM, Munger SC, Simecek P, Huttlin EL, Choi K, Gatti DM, Raghupathy N, Svenson KL, Churchill GA, Gygi SP (2016) Defining the consequences of genetic variation on a proteome-wide scale. Nature 534:500–505.

Chin MH, Qian WJ, Wang H, Petyuk VA, Bloom JS, Sforza DM, Laćan G, Liu D, Khan AH, Cantor RM, Bigelow DJ, Melega WP, Camp DG, Smith RD, Smith DJ (2008) Mitochondrial dysfunction, oxidative stress, and apoptosis revealed by proteomic and transcriptomic analyses of the striata in two mouse models of Parkinson's disease. Journal of Proteome Research 7:666–677.

Choi SY, Lopez-Gonzalez R, Krishnan G, Phillips HL, Li AN, Seeley WW, Yao WD, Almeida S, Gao FB (2019) C9ORF72-ALS/FTD-associated poly(GR) binds Atp5a1 and compromises mitochondrial function in vivo. Nature Neuroscience 22:851-862.

Chou M-Y, Rooke N, Turck CW, Black DL (1999) hnRNP H Is a Component of a Splicing Enhancer Complex That Activates a c-src Alternative Exon in Neuronal Cells. Molecular and Cellular Biology 19:69–77.

Comery TA, Harris JB, Willems PJ, Oostra BA, Irwin SA, Weiler IJ, Greenough WT (1997) Abnormal dendritic spines in fragile X knockout mice: Maturation and pruning deficits. Proceedings of the National Academy of Sciences of the United States of America 94:5401–5404.

Conlon EG, Manley JL (2017) RNA-binding proteins in neurodegeneration: Mechanisms

in aggregate. Genes & Development 31:1509–1528.

Cook KB, Kazan H, Zuberi K, Morris Q, Hughes TR (2011) RBPDB: A database of RNA-binding specificities. Nucleic Acids Research 39:301–308.

Costall B, Naylor RJ (1975) The Behavioural Effects Of Dopamine Applied Intracerebrally To Areas Of The Mesolimbic System. European Journal of Pharmacology 32:87–92.

Cruickshank CC, Dyer KR (2009) A review of the clinical pharmacology of methamphetamine. Addiction 104:1085–1099.

Czaplinski K (2014) Understanding mRNA trafficking: Are we there yet? Seminars in Cell & Developmental Biology 32:63–70.

Darnell JC, Driesche SJ Van, Zhang C, Hung KYS, Mele A, Fraser CE, Stone EF, Chen C, Fak JJ, Chi SW, Licatalosi DD, Richter JD, Darnell RB (2011) FMRP stalls ribosomal translocation on mRNAs linked to synaptic function and autism. Cell 146:247–261.

Darnell RB (2013) RNA Protein Interaction in Neurons. Annu Rev Neurosci 36:243–270.

Dassi E (2017) Handshakes and fights: The regulatory interplay of RNA-binding proteins. Frontiers in Molecular Biosciences 4:1–8.

Daubner SC, Le T, Wang S (2011) Tyrosine hydroxylase and regulation of dopamine synthesis. Archives of Biochemistry and Biophysics 508:1–12.

Dawson TM, Dawson VL (2017) Mitochondrial mechanisms of neuronal cell death: Potential the rapeutics. Annual Reviews of Pharmacology and Toxicology 57:437–454.

de Guglielmo G, Conlisk DE, Barkley-Levenson AM, Palmer AA, George O (2018) Inhibition of Glyoxalase 1 reduces alcohol self-administration in dependent and nondependent rats. Pharmacology Biochemistry and Behavior 167:36–41.

De Mei C, Ramos M, Iitaka C, Borrelli E (2009) Getting specialized: presynaptic and postsynaptic dopamine D2 receptors. Current Opinion in Pharmacology 9:53–58.

de Wit H, Phillips TJ (2012) Do initial responses to drugs predict future use or abuse? Neuroscience & Biobehavioral Reviews 36:1565–1576.

Deminiere JM, Piazza P V., Le Moal M, Simon H (1989) Experimental approach to individual vulnerability to psychostimulant addiction. Neuroscience & Biobehavioral Reviews 13:141–147.

Deng P-Y, Rotman Z, Blundon JA, Cho Y, Cui J, Cavalli V, Zakharenko SS, Klyachko VA (2013) FMRP Regulates Neurotransmitter Release and Synaptic Information Transmission by Modulating Action Potential Duration via BK channels. Neuron 77:696–711.

Devine MJ, Kittler JT (2018) Mitochondria at the neuronal presynapse in health and disease. Nature Review Neuroscience 19:63–80.

DeYoung DZ, Heinzerling KG, Swanson AN, Tsuang J, Furst BA, Yi Y, Wu YN, Moody DE, Andrenyak DM, Shoptaw SJ (2016) Safety of intravenous methamphetamine administration during ibudilast treatment. Journal of Clinical Psychopharmacology 36:347–354.

Di Chiara G, Imperato A (1988) Drugs abused by humans preferentially increase synaptic dopamine concentrations in the mesolimbic system of freely moving rats.

Proceedings of the National Academy of Sciences of the United States of America 85:5274–5278.

Dickson PE, Miller MM, Calton MA, Bubier JA, Cook MN, Goldowitz D, Chesler EJ, Mittleman G (2015) Systems genetics of intravenous cocaine self-administration in the BXD recombinant inbred mouse panel. Psychopharmacology 233(4):701-714.

Distler MG, Gorfinkle N, Papale LA, Wuenschell GE, Escayg A, Winawer MR, Palmer AA (2014) Glyoxalase 1 and its substrate methylglyoxal are novel regulators of seizure susceptibility. Epilepsia 54:649–657.

Distler MG, Plant LD, Sokoloff G, Hawk AJ, Aneas I, Wuenschell GE, Termini J, Meredith SC, Nobrega MA, Palmer AA (2012) Glyoxalase 1 increases anxiety by reducing GABA A receptor agonist methylglyoxal. Journal of Clinical Investigation 122:2306–2315.

Dittman JS (2019) Unc13: a multifunctional synaptic marvel. Current Opinion in Neurobiology 57:17–25.

Dittman JS, Ryan TA (2019) The control of release probability at nerve terminals. Nature Review Neuroscience 20:177–186.

Divakaruni SS, Van Dyke AM, Chandra R, LeGates TA, Contreras M, Dharmasri PA, Higgs HN, Lobo MK, Thompson SM, Blanpied TA (2018) Long-Term Potentiation Requires a Rapid Burst of Dendritic Mitochondrial Fission during Induction. Neuron 100:860-875.e7.

Dobin A, Davis CA, Schlesinger F, Drenkow J, Zaleski C, Jha S, Batut P, Chaisson M, Gingeras TR (2013) STAR: Ultrafast universal RNA-seq aligner. Bioinformatics

29:15–21.

Dolphin AC (2012) Calcium channel auxiliary α2δ and β subunits: Trafficking and one step beyond. Nature Review Neuroscience 13:542–555.

Dolphin AC (2013) The α2δ subunits of voltage-gated calcium channels. Biochimica Biophysica Acta - Biomembranes 1828:1541–1549.

Dolphin AC, Lee A (2020) Presynaptic calcium channels: specialized control of synaptic neurotransmitter release. Nature Review Neuroscience 21:213–229.

Dominguez C, Allain FHT (2006) NMR structure of the three quasi RNA recognition motifs (qRRMs) of human hnRNP F and interaction studies with Bcl-x G-tract RNA: A novel mode of RNA recognition. Nucleic Acids Research 34:3634–3645.

Doyle M, Kiebler MA (2011) Mechanisms of dendritic mRNA transport and its role in synaptic tagging. Eureopean Molecular Biology Organization Journal 30:3540–3552.

Drago J, Padungchaichot P, Accili D, Fuchs S (1998) Dopamine Receptors and Dopamine Transporter in Brain Function and Addictive Behaviors: Insight frim Targeted Mouse Mutants. Developmental Neuroscience 20:188-203.

Dreyfuss G, Matunis MJ, Pinol-Roma S, Burd CG (1993) hnRNP Proteins and the Biogenesis of mRNA. Annual Review Biochemistry 62:289–321.

Du L, Richter JD (2005) Activity-dependent polyadenylation in neurons. RNA 11:1340–1347.

Ducci F, Goldman D (2012) The Genetic Basis of Addictive Disorders. Psychiatric Clinics of North America 35:495–519.

Dunkley PR, Jarvie PE, Robinson PJ (2008) A rapid percoll gradient procedure for preparation of synaptosomes. Nature Protocols 3:1718–1728.

Dvir S, Velten L, Sharon E, Zeevi D, Carey LB, Weinberger A, Segal E (2013) Deciphering the rules by which 5′-UTR sequences affect protein expression in yeast. Proceedings of the National Academy of Sciences of the United States of America 110:E2792–E2801.

Eggermann E, Bucurenciu I, Goswami SP, Jonas P (2012) Nanodomain coupling between Ca 2+ channels and sensors of exocytosis at fast mammalian synapses. Nature Review Neuroscience 13:7–21.

Ehlers MD, Tingley WG, Huganir RL (1995) Regulated Subcellular Distribution of the NR1 Subunit of the NMDA Receptor. Science 269 (5231):1734–1737.

Eliyahu E, Pnueli L, Melamed D, Scherrer T, Gerber AP, Pines O, Rapaport D, Arava Y (2010) Tom20 Mediates Localization of mRNAs to Mitochondria in a Translation-Dependent Manner. Molecular and Cellular Biology 30:284–294.

Faul F, Erdfelder E, Lang A-G, Buchner A (2007) G*Power 3: A flexible statistical power analysis program for the social, behavioral, and biomedical sciences. Behavior Research Methods 39:175–191.

Faure JJ, Hattingh SM, Stein DJ, Daniels WM (2009) Proteomic analysis reveals differentially expressed proteins in the rat frontal cortex after methamphetamine treatment. Metabolic Brain Disease 24:685–700.

Fernandez-Moya SM, Bauer KE, Kiebler MA (2014) Meet the players: Local translation at the synapse. Frontiers in Molecular Neuroscience 7:1–6.

Fernández E, Rajan N, Bagni C (2013) The FMRP regulon: From targets to disease convergence. Frontiers in Molecular Neuroscience 7:1–9.

Ferron L, Nieto-Rostro M, Cassidy JS, Dolphin AC (2014) Fragile X mental retardation protein controls synaptic vesicle exocytosis by modulating N-type calcium channel density. Nature Communication 5:1–14.

Fillebeen C, Wilkinson N, Pantopoulos K (2014) Electrophoretic mobility shift assay (EMSA) for the study of RNA-protein interactions: The IRE/IRP example. Journal Visualized Experiments 7:1–9.

Fisette JF, Toutant J, Dugré-Brisson S, Desgroseillers L, Chabot B (2010) hnRNP A1 and hnRNP H can collaborate to modulate 5′ splice site selection. RNA 16:228–238.

Fish EW, Krouse MC, Stringfield SJ, DiBerto JF, Robinson JE, Malanga CJ (2013) Changes in Sensitivity of Reward and Motor Behavior to Dopaminergic, Glutamatergic, and Cholinergic Drugs in a Mouse Model of Fragile X Syndrome. Public Library of Science (PLOS) One 8:1–14.

Fleckenstein AE, Hanson GR (2003) Impact of psychostimulants on vesicular monoamine transporter function. European Journal of Pharmacology 479:283–289.

Fleckenstein AE, Volz TJ, Riddle EL, Gibb JW, Hanson GR (2007) New Insights into the Mechanism of Action of Amphetamines. Annual Review of Pharmacology and Toxicology 47:681–698.

Fogger SA (2019) Methamphetamine Use: A New Wave in the Opioid Crisis? Journal of Addictions Nursing 30:219–223.

Fu XD, Ares M (2014) Context-dependent control of alternative splicing by RNA-

binding proteins. Nature Review Genetics 15:689–701.

Fukuda T, Naiki T, Saito M, Irie K (2009) hnRNP K interacts with RNA binding motif protein 42 and functions in the maintenance of cellular ATP level during stress conditions. Genes to Cells 14:113–128.

Fukunaga T, Iwakiri J, Ono Y, Hamada M (2019) Lncrrisearch: A web server for lncRNA-RNA interaction prediction integrated with tissue-specific expression and subcellular localization data. Frontiers in Genetics 10:1–6.

Fulks JL, Obryhim BE, Wenzel SK, Fowler SC, Vorontsova E, Pinkston JW, Ortiz AN, Johnson MA (2010) Dopamine release and uptake impairments and behavioral alterations observed in mice that model fragile X mental retardation syndrome. American Chemical Soceity Chemical Neuroscience 1:679–690.

Gagliardi M, Matarazzo MR (2016) RIP: RNA Immunoprecipitation. In Methods in Molecular Biology, pp 73–86.

Galbraith N (2015) The methamphetamine problem. BJPsych Bulletin 39:218–220.

García-Rodríguez LJ, Gay AC, Pon LA (2007) Puf3p, a Pumilio family RNA binding protein, localizes to mitochondria and regulates mitochondrial biogenesis and motility in budding yeast. Journal of Cell Biology 176:197–207.

Gardner EL, Ashby CR (2000) Heterogeneity of the mesotelencephalic dopamine fibers: Physiology and pharmacology. Neuroscience & Biobehavioral Reviews 24:115–118.

Gehrke S, Wu Z, Klinkenberg M, Sun Y, Auburger G, Guo S, Lu B (2015) PINK1 and Parkin Control Localized Translation of Respiratory Chain Component mRNAs on

Mitochondria Outer Membrane Stephan. Cell Metabolism 21:95–108.

Gelernter J, Sherva R, Koesterer R, Almasy L, Zhao H, Kranzler HR, Farrer L (2014) Genome-wide association study of cocaine dependence and related traits: FAM53B identified as a risk gene. Molecular Psychiatry 19:717–723.

Gerber AP, Herschlag D, Brown PO (2004) Extensive association of functionally and cytotopically related mRNAs with Puf family RNA-binding proteins in yeast. Public Library of Science (PLOS) Biology 2:0342–0354.

Geuens T, Bouhy D, Timmerman V (2016) The hnRNP family: insights into their role in health and disease. Human Genetics 135:851–867.

Gilda JE, Gomes A V. (2013) Stain Free Total Protein Staining is a Superior Loading Control to β-Actin for Western Blots. Analytical Biochemistry 440:1–6.

Glisovic T, Bachorik JL, Yong J, Dreyfuss G (2008) RNA-binding proteins and post-transcriptional gene regulation. Federation of European Biochemical Sociesties (FEBS) Letters 582:1977–1986.

Glock C, Heumüller M, Schuman EM (2017) mRNA transport & local translation in neurons. Current Opinion in Neurobiology 45:169–177.

Goldberg LR, Kirkpatrick SL, Yazdani N, Babbs RK, Jenkins DF, Johnson WE, Bryant CD (2017) Casein kinase 1-epsilon deletion increases mu opioid receptor-dependent behaviors and binge eating. Genes, Brain and Behavior:1–14.

Goldman D, Oroszi G, Ducci F (2005) The genetics of addictions: uncovering the genes. Nature Review Genetics 6:521–532.

Grammatikakis I, Zhang P, Mattson MP, Gorospe M, Grammatikakis I, Zhang P, Mattson

MP, Gorospe M (2016a) The long and the short of TRF2 in neurogenesis Ioannis. Cell Cycle 15:3026–3032.

Grammatikakis I, Zhang P, Panda AC, Kim J, Maudsley S, Abdelmohsen K, Yang X, Martindale JL, Motino O, Hutchison ER, Mattson MP, Gorospe M (2016b) Alternative Splicing of Neuronal Differentiation Factor TRF2 Regulated by HNRNPH1/H2. Cell Reports 15:1–9.

Gross C, Yao X, Pong DL, Jeromin A, Bassell GJ (2011) Fragile X mental retardation protein regulates protein expression and mRNA translation of the potassium channel Kv4.2. Journal of Neuroscience 31:5693–5698.

Gudz TI, Schneider TE, Haas TA, Macklin WB (2002) Myelin proteolipid protein forms a complex with integrins and may participate in integrin receptor signalling in oligodendrocytes. Journal of Neuroscience 22:7398–7407.

Guil S, Long JC, Cáceres JF (2006) hnRNP A1 Relocalization to the Stress Granules Reflects a Role in the Stress Response. Molecular and Cell Biology 26:5744–5758.

Guo ML, Periyasamy P, Liao K, Kook YH, Niu F, Callen SE, Buch S (2016) Cocaine-mediated downregulation of microglial miR-124 expression involves promoter DNA methylation. Epigenetics 11:819–830.

Guramrit S, Gabriel P, Gene W. Y, Melissa J. M (2015) The Clothes Make the mRNA: Past and Present Trends in mRNP Fashion. Annual Review of Biochemistry:229–262.

Haberman N, Huppertz I, Attig J, König J, Wang Z, Hauer C, Hentze MW, Kulozik AE, Le Hir H, Curk T, Sibley CR, Zarnack K, Ule J (2017) Insights into the design and

interpretation of iCLIP experiments. Genome Biology 18:1–21.

Han K, Yeo G, An P, Burge CB, Grabowski PJ (2005) A combinatorial code for splicing silencing: UAGG and GGGG motifs. Public Library of Science (PLOS) Biology 3:0843–0860.

Han SP, Tang YH, Smith R (2010) Functional diversity of the hnRNPs: past, present and perspectives. Biochemical Journal 430:379–392.

Harkness JH, Shi X, Janowsky A, Phillips TJ (2015) Trace Amine-Associated Receptor 1 Regulation of Methamphetamine Intake and Related Traits. Neuropsychopharmacology 40:2175–2184.

Harris JJ, Jolivet R, Attwell D (2012) Synaptic Energy Use and Supply. Neuron 75:762–777.

Harvey RF, Smith TS, Mulroney T, Queiroz RML, Pizzinga M, Dezi V, Villenueva E, Ramakrishna M, Lilley KS, Willis AE (2018) Trans-acting translational regulatory RNA binding proteins. Wiley Interdisciplinary Reviews: RNA 9:1–19.

Hassan SF, Wearne TA, Cornish JL, Goodchild AK (2016) Effects of acute and chronic systemic methamphetamine on respiratory, cardiovascular and metabolic function, and cardiorespiratory reflexes. The Journal Physiology 594:763–780.

Haughey HM, Fleckenstein AE, Metzger RR, Hanson GR (2002) The Effects of Methamphetamine on Serotonin Transporter Activity. Journal of Neurochemistry 75:1608–1617.

Hedegaard H, Miniño AM, Warner M (2020) Drug Overdose Deaths in the United States, 1999-2018. National Center for Health Statistics Data Brief:1–8.

Hedges DM, Obray JD, Yorgason JT, Jang EY, Weerasekara VK, Uys JD, Bellinger FP, Steffensen SC (2018) Methamphetamine Induces Dopamine Release in the Nucleus Accumbens Through a Sigma Receptor-Mediated Pathway. Neuropsychopharmacology 43:1405–1414.

Heiman M, Schaefer A, Gong S, Peterson JD, Day M, Ramsey KE, Suárez-Fariñas M, Schwarz C, Stephan DA, Surmeier DJ, Greengard P, Heintz N (2008) A Translational Profiling Approach for the Molecular Characterization of CNS Cell Types. Cell 135:738–748.

Heinz S, Benner C, Spann N, Bertolino E, Lin YC, Laslo P, Cheng JX, Murre C, Singh H, Glass CK (2010) Simple combinations of lineage-determining transcription factors prime cis-regulatory elements required for macrophage and B cell identities. Molecular Cell 38:576–589.

Hentze MW, Castello A, Schwarzl T, Preiss T (2018) A brave new world of RNA-binding proteins. Nature Reviews Molecular Cell Biology 19:327–341.

Hobson GM, Huang Z, Sperle K, Sistermans E, Rogan PK, Garbern JY, Kolodny E, Naidu S, Cambi F (2006) Splice-site contribution in alternative splicing of PLP1 and DM20: Molecular studies in oligodendrocytes. Human Mutation 27:69–77.

Holt CE, Martin KC, Schuman EM (2019) Local translation in neurons: visualization and function. Nature Structural & Molecular Biology 26:557–566.

Hong WC, Amara SG (2013) Differential targeting of the dopamine transporter to recycling or degradative pathways during amphetamine-or PKC-regulated endocytosis in dopamine neurons. The Federation of American Societies for

Experimental Biology (FASEB) Journal 27:2995–3007.

Honoré B (2000) The hnRNP 2H9 gene, which is involved in the splicing reaction, is a multiply spliced gene. Biochimica Biophysica Acta - Gene Structure and Expression 1492:108–119.

Honoré B, Rasmussen HH, Vorum H, Dejgaard K, Liu X, Gromov P, Madsen P, Gesser B, Tommerup N, Celis JE (1995) Heterogeneous nuclear ribonucleoproteins H, H′, and F are members of a ubiquitously expressed subfamily of related but distinct proteins encoded by genes mapping to different chromosomes. Journal of Biological Chemistry 270:28780–28789.

Honore B, Vorum H, Baandrup U (1999) hnRNPs H, H' and F behave differently with respect to posttranslational cleavage and subcellular localization. The Federation of European Biochemical Societies (FEBS) Letters 456:274–280.

Hooks MS, Jones GH, Smith AD, Neill DB, Justice JB (1991) Individual differences in locomotor activity and sensitization. Pharmacology Biochemistry and Behavior 38:467–470.

Hoppa MB, Lana B, Margas W, Dolphin AC, Ryan TA (2012) α2δ Expression Sets Presynaptic Calcium Channel Abundance and Release Probability. Nature 486:122–125.

Hörnberg H, Holt C (2013) RNA-binding proteins and translational regulation in axons and growth cones. Frontiers in Neuroscience 7:1–9.

Hovatta I, Tennant RS, Helton R, Marr RA, Singer O, Redwine JM, Ellison JA, Schadt EE, Verma IM, Lockhart DJ, Barlow C (2005) Glyoxalase 1 and glutathione

reductase 1 regulate anxiety in mice. Nature 438:662–666.

Howell LL, Negus SS (2014) Monoamine transporter inhibitors and substrates as treatments for stimulant abuse. Advances in Pharmacology 69:129–176.

Huang R, Zhang Y, Han B, Bai Y, Zhou R, Gan G, Chao J, Hu G, Yao H (2017) Circular RNA HIPK2 regulates astrocyte activation via cooperation of autophagy and ER stress by targeting MIR124–2HG. Autophagy 13:1722–1741.

Huang Y-S, Jung M-Y, Sarkissian M, D.Richter J (2002) N-methyl-D-aspartate receptor signaling results in Aurora kinase-catalyzed CPEB phosphorylation and CaMKII mRNA polyadenylation at synapses. European Molecular Biology Organization (EMBO) Journal 21:2139–2148.

Huber KM, Gallagher SM, Warren ST, Bear MF (2002) Altered synaptic plasticity in a mouse model of fragile X mental retardation. Proceedings of the National Academy of Sciences of the United States of America 99:7746–7750.

Huelga SC, Vu AQ, Arnold JD, Liang TD, Liu PP, Yan BY, Donohue JP, Shiue L, Hoon S, Brenner S, Ares M, Yeo GW (2012) Integrative Genome-wide Analysis Reveals Cooperative Regulation of Alternative Splicing by hnRNP Proteins. Cell Reports 1:167–178.

Hutson CB, Lazo CR, Mortazavi F, Giza CC, Hovda D, Chesselet M-F (2011) Traumatic Brain Injury in Adult Rats Causes Progressive Nigrostriatal Dopaminergic Cell Loss and Enhanced Vulnerability to the Pesticide Paraquat. Journal of Neurotrauma 28:1783–1801.

Hwang H-W, Saito Y, Park CY, Blachère NE, Tajima Y, Fak JJ, Zucker-Scharff I,

Darnell RB (2017) cTag-PAPERCLIP reveals alternative polyadenylation promotes cell-type specific protein diversity and switches Araf isoforms with microglia activation. Neuron 95:1334–1349.

Hwang JY, Jung S, Kook TL, Rouchka EC, Bok J, Park JW (2020) rMAPS2: an update of the RNA map analysis and plotting server for alternative splicing regulation. Nucleic Acids Research 48:300–306.

Hyman SE, Malenka RC, Nestler EJ (2006) Neural Mechanisms of Addiction: The Role of Reward-Related Learning and Memory. Annual Review of Neuroscience 29:565–598.

Iakoubova OA, Olsson CL, Dains KM, Ross DA, Andalibi A, Lau K, Choi J, Kalcheva I, Cunanan M, Louie J, Nimon V, Machrus M, Bentley LG, Beauheim C, Silvey S, Cavalcoli J, Lusis AJ, West DB (2001) Genome-tagged mice (GTM): Two sets of genome-wide congenic strains. Genomics 74:89–104.

Ivanov P, Kedersha N, Anderson P (2020) Stress Granules and Processing Bodies in Translational Control. Cold Spring Harbor Perspectives in Biology 11:1–26.

Iwazaki T, Matsumoto I, McGregor IS (2007) Protein expression profile in the striatum of rats with methamphetamine-induced behavioral sensitization. Proteomics 7:1131–1139.

Iwazaki T, McGregor IS, Matsumoto I (2006) Protein expression profile in the striatum of acute methamphetamine-treated rats. Brain Research 1097:19–25.

Jackson RJ, Hellen CUT, Pestova T V (2010) The mechanism of eukaryotic translation initiation and principles of its regulation. Nature Reviews Molecular Cell Biology

11:113–127.

Jensen KP (2016) A Review of Genome-Wide Association Studies of Stimulant and Opioid Use Disorders. Molecular Neuropsychiatry 2:37–45.

Joffe ME, Grueter CA, Grueter BA (2014) Biological substrates of addiction. Wiley Interdisciplinary Reviews: Cognitive Science 5:151–171.

Johnson LA, Furman CA, Zhang M, Guptaroy B, Gnegy ME (2005) Rapid delivery of the dopamine transporter to the plasmalemmal membrane upon amphetamine stimulation. Neuropharmacology 49:750–758.

Juarez B, Han M-HH (2016) Diversity of Dopaminergic Neural Circuits in Response to Drug Exposure. Neuropsychopharmacology 41:2424–2446.

Kahlig KM, Lute BJ, Wei Y, Loland CJ, Gether U, Javitch JA, Galli A (2006) Regulation of dopamine transporter trafficking by intracellular amphetamine. Moleclar Pharmacology 70:542–548.

Kamma H, Portman DSDS, Dreyfuss G (1995) Cell Type-Specific Expression of hnRNP Proteins. Experimental Cell Research 221:187–196.

Kanehisa M, Sato Y, Furumichi M, Morishima K, Tanabe M (2019) New approach for understanding genome variations in KEGG. Nucleic Acids Research 47:D590–D595.

Karolchik D, Hinrichs AS, Furey TS, Roskin KM, Sugnet CW, Haussler D, Kent WJ, Center (2004) The UCSC Table Browser data retrieval tool. Nucleic Acids Research 32:D493–D496.

Katz Y, Wang ETT, Airoldi EMM, Burge CBB (2010) Analysis and design of RNA

sequencing experiments for identifying isoform regulation. Nature Methods 7:1009–1015.

Keene JD, Tenenbaum SA (2002) Eukaryotic mRNPs may represent posttranscriptional operons. Molecular Cell 9:1161–1167.

Keleta YB, Martinez JL (2012) Brain Circuits of Methamphetamine Place Reinforcement Learning: The Role of the Hippocampus-VTA Loop. Brain and Behavior 2:128–141.

Kim H-J, Song EJ, Lee K-J (2002) Proteomic analysis of protein phosphorylations in heat shock response and thermotolerance. Journal of Biological Chemistry 277:23193–23207.

Kim N, Lee JO, Lee HJ, Lee SK, Moon JW, Kim SJ, Park SH, Kim HS (2014a) AMPKα2 translocates into the nucleus and interacts with hnRNP H: Implications in metformin-mediated glucose uptake. Cellular Signalling 26:1800–1806.

Kim Y, Lee G, Jeon E, Sohn EJ, Lee Y, Kang H, Lee DW, Kim DH, Hwang I (2014b) The immediate upstream region of the 5'-UTR from the AUG start codon has a pronounced effect on the translational efficiency in Arabidopsis thaliana. Nucleic Acids Research 42:485–498.

Kirkpatrick SL, Bryant CD (2015) Behavioral architecture of opioid reward and aversion in C57BL / 6 substrains. Frontiers in Behavioral Neuroscience 8:1–11.

Kish SJ (2008) Pharmacologic mechanisms of crystal meth. Canadian Medical Association Journal 178:1679–1682.

Kivell B, Uzelac Z, Sundaramurthy S, Rajamanickam J, Ewald A, Chefer V, Jaligam V,

Bolan E, Simonson B, Annamalai B, Mannangatti P, Prisinzano TE, Gomes I, Devi LA, Jayanthi LD, Sitte HH, Ramamoorthy S, Shippenberg TS (2014) Salvinorin A regulates dopamine transporter function via a kappa opioid receptor and ERK1/2-dependent mechanism. Neuropharmacology 86:228–240.

Klein ME, Monday H, Jordan BA (2016) Proteostasis and RNA Binding Proteins in Synaptic Plasticity and in the Pathogenesis of Neuropsychiatric Disorders. Neural Plasticity 2016.

Koob GF (1992) Neural Mechanisms of Drug Reinforcement. Annals of the New York Academy of Sciences 654:171–191.

Kuleshov M V, Jones MR, Rouillard AD, Fernandez NF, Duan Q, Wang Z, Koplev S, Jenkins SL, Jagodnik KM, Lachmann A, Mcdermott MG, Monteiro CD, Gundersen W, Ma A (2016) Enrichr : a comprehensive gene set enrichment analysis web server 2016 update. Nucleic Acids Research 44:W90-97.

Kumar V, Kim K, Joseph C, Kourrich S, Yoo SH, Huang HC, Vitaterna MH, Villena FP De, Bonci A, Takahashi JS (2015) C57BL/6N mutation in Cytoplasmic FMR interacting protein 2 regulates cocaine response. Science 342:1508–1512.

Kurokawa K, Shibasaki M, Ohkuma S (2010) Methamphetamine-induced up-regulation of α2/δ subunit of voltage-gated calcium channels is regulated by DA receptors. Synapse 64:822–828.

Kusch V, Bornschein G, Loreth D, Bank J, Jordan J, Baur D, Watanabe M, Kulik A, Heckmann M, Eilers J, Schmidt H (2018) Munc13-3 Is Required for the Developmental Localization of Ca 2+ Channels to Active Zones and the

Nanopositioning of Ca v 2.1 Near Release Sensors. Cell Reports 22:1965–1973.

Lapointe CP, Wilinski D, Saunders HAJ, Wickens M (2015) Protein-RNA networks revealed through covalent RNA marks Christopher. Nature Methods 12:1163–1170.

LaVoie MJ, Hastings TG (1999) Dopamine quinone formation and protein modification associated with the striatal neurotoxicity of methamphetamine: Evidence against a role for extracellular dopamine. Journal of Neuroscience 19:1484–1491.

Lee FCY, Ule J (2018) Advances in CLIP Technologies for Studies of Protein-RNA Interactions. Molecular Cell 69:354–369.

Lee FJS, Pei L, Moszczynska A, Vukusic B, Fletcher PJ, Liu F (2007) Dopamine transporter cell surface localization facilitated by a direct interaction with the dopamine D2 receptor. European Molecular Biology Organization (EMBO) Journal 26:2127–2136.

Lee HY, Ge W, Huang W, He Y, Wang GX, Smith SJ, Jan YN, Jan LY (2011) Bidirectional regulation of voltage gated K+ channels by FMRP. Neuron 72:630–642.

Lefave C V, Squatrito M, Vorlova S, Rocco GL, Brennan CW, Holland EC, Pan Y, Cartegni L (2011) Splicing factor hnRNPH drives an oncogenic splicing switch in gliomas. European Molecular Biology Organization (EMBO) Journal 30:4084–4097.

Lein ES et al. (2007) Genome-wide atlas of gene expression in the adult mouse brain. Nature 445:168–176.

Levey AI, Hersch SM, Rye DB, Sunaharat RK, Niznikt HB, Kitt CA, Price DL, Maggio1

R, Brann Ii MR, Ciliax BJ (1993) Localization of D1 and D2 dopamine receptors in brain with subtype-specific antibodies. Neurobiology 90:8861–8865.

Li M, Shin J, Risgaard RD, Parries MJ, Wang J, Chasman D, Liu S, Roy S, Bhattacharyya A, Zhao X (2020) Identification of FMR1-regulated molecular networks in human neurodevelopment. Genome Research 30:361–374.

Li X, Song J, Yi C (2014) Genome-wide Mapping of Cellular Protein-RNA Interactions Enabled by Chemical Crosslinking. Genomics, Proteomics & Bioinformatics 12:72–78.

Li Z, Okamoto KI, Hayashi Y, Sheng M (2004) The importance of dendritic mitochondria in the morphogenesis and plasticity of spines and synapses. Cell 119:873–887.

Liao PC, Kuo YM, Hsu HC, Cherng CG, Yu L (2005) Local proteins associated with methamphetamine-induced nigrostriatal dopaminergic neurotoxicity. Journal of Neurochemistry 95:160–168.

Liao Y, Smyth GK, Shi W (2014) FeatureCounts: An efficient general purpose program for assigning sequence reads to genomic features. Bioinformatics 30:923–930.

Liao Y, Wang J, Jaehnig EJ, Shi Z, Zhang B (2019) WebGestalt 2019: gene set analysis toolkit with revamped UIs and APIs. Nucleic Acids Research 47:W199–W205.

Licatalosi DD, Mele A, Fak JJ, Ule J, Kayikci M, Chi SW, Clark TA, Schweitzer AC, Blume JE, Wang X, Darnell JC, Darnell RB (2008) HITS-CLIP yields genome-wide insights into brain alternative RNA processing. Nature 456:464–469.

Limanaqi F, Gambardella S, Biagioni F, Busceti CL, Fornai F (2018) Epigenetic effects

induced by methamphetamine and methamphetamine-dependent oxidative stress. Oxidative Medicine and Cellular Longevity 2018:1-28.

Lin C, Miles WO (2019) Survey and summary beyond ClIp: Advances and opportunities to measure RBP-RNA and RNA-RNA interactions. Nucleic Acids Research 47:5490–5501.

Lindgren N, Usiello A, Goiny M, Haycock J, Erbs E, Greengard P, Hokfelt T, Borrelli E, Fisone G (2003) Distinct roles of dopamine D2L and D2S receptor isoforms in the regulation of protein phosphorylation at presynaptic and postsynaptic sites. Proceedings of the National Academy of Sciences of the United States of America 100:4305–4309.

Lines MA et al. (2012) Haploinsufficiency of a spliceosomal GTPase encoded by EFTUD2 causes mandibulofacial dysostosis with microcephaly. American Journal of Human Genetics 90:369–377.

Lipari RN, Park-Lee E, Van Horn S (2016) America's Need for and Receipt of Substance Use Treatment in 2015. National Survey on drug Use and Health: The CBHSQ Report.

Lipovich L, Dachet F, Cai J, Bagla S, Balan K, Jia H, Loeb JA (2012) Activity-dependent human brain coding/noncoding gene regulatory networks. Genetics 192:1133–1148.

Lipstein N, Schaks S, Dimova K, Kalkhof S, Ihling C, Kolbel K, Ashery U, Rhee J, Brose N, Sinz A, Jahn O (2012) Nonconserved Ca2+/Calmodulin Binding Sites in Munc13s Differentially Control Synaptic Short-Term Plasticity. Molecular and Cellular Biology 32:4628–4641.

Liu D, Zhu L, Ni T, Guan F lin, Chen Y jiong, Ma D liang, Goh ELK, Chen T (2019) Ago2 and Dicer1 are involved in METH-induced locomotor sensitization in mice via biogenesis of miRNA. Addiction Biology 24:498–508.

Liu W, Zhang Q, Zhang J, Pan W, Zhao J, Xu Y (2017) Long non-coding RNA MALAT1 contributes to cell apoptosis by sponging miR-124 in Parkinson disease. Cell & Bioscience 7:1–9.

Livak KJ, Schmittgen TD (2001) Analysis of relative gene expression data using real-time quantitative PCR and the 2-ΔΔCT method. Methods 25:402–408.

Loftis JM, Lasarev M, Shi X, Lapidus J, Janowsky A, Hoffman WF, Huckans M (2019) Trace amine-associated receptor gene polymorphism increases drug craving in individuals with methamphetamine dependence. Public Library of Science (PLOS) One 14:1–15.

Lominac KD, McKenna CL, Schwartz LM, Ruiz PN, Wroten MG, Miller BW, Holloway JJ, Travis KO, Rajasekar G, Maliniak D, Thompson AB, Urman LE, Phillips TJ, Szumlinski KK (2014) Mesocorticolimbic monoamine correlates of methamphetamine sensitization and motivation. Frontiers in Systems Neuroscience 8:1–19.

Lominac KD, Quadir SG, Barrett HM, Mckenna CL, Schwartz LM, Ruiz PN, Wroten MG, Campbell RR, Miller BW, Holloway JJ, Travis KO, Rajasekar G, Maliniak D, Thompson AB, Urman LE, Kippin TE, Phillips TJ, Szumlinski KK (2016) Prefrontal glutamate correlates of methamphetamine sensitization and preference. European Journal of Neuroscience 43:689–702.

Lüscher C (2013) Drug-evoked synaptic plasticity causing addictive behavior. Journal of Neuroscience 33:17641–17646.

Luscher C, Malenka RC (2011) Drug-evoked synaptic plasticity in addiction: from molecular changes to circuit remodeling. Neuron 69:650–663.

Mancini E, Rabinovich A, Iserte J, Yanovsky M (2020) ASpli: Analysis of alternative splicing using RNA-Seq. R Packag version 1140.

Markmiller S, Soltanieh S, Server KL, Mak R, Jin WJ, Fang MY, Luo E-C, Krach F, Yang D, Sen A, Fulzele A, Yeo GW, Wozniak JM, Gonzalez DJ, Kankel MW, Gao F-B, Bennett EJ, Lécuyer E (2018) Context-Dependent and Disease-Specific Diversity in Protein Interactions within Stress Granules. Cell 172:590–604.

Martinez-Contreras R, Cloutier P, Shkreta L, Fisette JF, Revil T, Chabot B (2007) Chapter 8: hnRNP proteins and splicing control. In: Advances in Experimental Medicine and Biology, pp 123–147.

Martinez-Contreras R, Fisette JF, Nasim FUH, Madden R, Cordeau M, Chabot B (2006) Intronic binding sites for hnRNP A/B and hnRNP F/H proteins stimulate pre-mRNA splicing. Public Library of Science (PLOS) Biology 4:172–185.

Massoulié J, Anselmet A, Bon S, Krejci E, Legay C, Morel N, Simon S (1998) Acetylcholinesterase: C-terminal domains, molecular forms and functional localization. Journal of Physiology - Paris 92:183–190.

Matunis MJ, Xing J, Dreyfuss G (1994) The hnRNP F protein: Unique primary structure, nucleic acid-binding properties, and subcellular localization. Nucleic Acids Research 22:1059–1067.

Mayr C (2017) Regulation by 3 -Untranslated Regions. Annual Reviews 51:171–194.

McBride SMJ, Choi CH, Wang Y, Liebelt D, Braunstein E, Ferreiro D, Sehgal A, Siwicki KK, Dockendorff TC, Nguyen HT, McDonald T V., Jongens TA (2005) Pharmacological rescue of synaptic plasticity, courtship behavior, and mushroom body defects in a Drosophila model of Fragile X syndrome. Neuron 45:753–764.

McClung CA, Nestler EJ (2008) Neuroplasticity mediated by altered gene expression. Neuropsychopharmacology 33:3–17.

McMahon AC, Rahman R, Jin H, Shen JL, Fieldsend A, Luo W, Rosbash M (2016) TRIBE: Hijacking an RNA-Editing Enzyme to Identify Cell-Specific Targets of RNA-Binding Proteins. Cell 165:742–753.

McMurray KMJ, Du X, Brownlee M, Palmer AA (2016) Neuronal overexpression of Glo1 or amygdalar microinjection of methylglyoxal is sufficient to regulate anxiety-like behavior in mice. Behavioural Brain Research 2016 301:119–123.

McMurray KMJ, Ramaker MJ, Barkley-Levenson AM, Sidhu PS, Elkin PK, Reddy MK, Guthrie ML, Cook JM, Rawal VH, Arnold LA, Dulawa SC, Palmer AA (2018) Identification of a novel, fast-acting GABAergic antidepressant. Molecular Psychiatry 23:384–391.

McMurray KMJ, Sidhu PS, Cook JM, Arnold LA, Palmer AA (2017) Genetic and pharmacological manipulation of Glyoxalase 1 regulates voluntary ethanol consumption in mice. Addiction Biology 22:381–389.

Mercer TR, Dinger ME, Mattick JS (2009) Long non-coding RNAs: insights into functions. Nature Review Genetics 10:155–159.

Merico D, Isserlin R, Stueker O, Emili A, Bader GD (2010) Enrichment map: A network-based method for gene-set enrichment visualization and interpretation. Public Library of Science (PLOS) One 5(11):e13984.

Mimaki M, Wang X, McKenzie M, Thorburn DR, Ryan MT (2012) Understanding mitochondrial complex I assembly in health and disease. Biochimica Biophysica Acta - Bioenergetics 1817:851–862.

Min H, Chan RC, Black DL (1995) The generally expressed hnRNP F is involved in a neural-specific pre-mRNA splicing event. Genes & Development 9:2659–2671.

Min H, Turck CW, Nikolic JM, Black DL (1997) A new regulatory protein, KSRP, mediates exon inclusion through an intronic splicing enhancer. Genes & Development 11:1023–1036.

Miner NB, Elmore JS, Baumann MH, Phillips TJ, Janowsky A (2017) Trace amine-associated receptor 1 regulation of methamphetamine-induced neurotoxicity. Neurotoxicology 63:57–69.

Mirisis AA, Carew TJ (2019) The ELAV family of RNA-binding proteins in synaptic plasticity and long-term memory. Neurobiology of Learning and Memory 161:143–148.

Missale C, Nash RS, Robinson SW, Jaber M, Caron MG (1998) Dopamine Receptors: From Structure to Function. Physiological Reviews 78:189–225.

Mu Y, Otsuka T, Horton AC, Scott DB, Ehlers MD (2003) Activity-dependent mRNA splicing controls ER export and synaptic delivery of NMDA receptors. Neuron 40:581–594.

Muddashetty RS, Nalavadi VC, Gross C, Yao X, Xing L, Laur O, Warren ST, Bassell GJ (2011) Reversible Inhibition of PSD-95 mRNA Translation by miR-125a, FMRP Phosphorylation, and mGluR Signaling. Molecular Cell 42:673–688.

Mulligan MK, Abreo T, Neuner SM, Parks C, Watkins CE, Houseal MT, Shapaker TM, Hook M, Tan H, Wang X, Ingels J, Peng J, Lu L, Kaczorowski CC, Bryant CD, Homanics GE, Williams RW (2019) Identification of a functional non-coding variant in the GABAA receptor α2 subunit of the C57BL/6J mouse reference genome: Major implications for neuroscience research. Frontiers in Genetics 10:1–15.

Nagy J, Lee T, Seeman P, HC F (1978) Direct evidence for presynaptic and postsynaptic dopamine receptors in brain. Nature 274:278–281.

Nazim M, Masuda A, Rahman MA, Nasrin F, Takeda J, Ohe K, Ohkawara B, Ito M, Ohno K (2016) Competitive regulation of alternative splicing and alternative polyadenylation by hnRNP H and CstF64 determines acetylcholinesterase isoforms. Nucleic Acids Research:1–14.

Nechay M, Kleiner RE (2020) High-throughput approaches to profile RNA-protein interactions. Current Opinion in Chemical Biology 54:37–44.

Nelson EC et al. (2016) Evidence of CNIH3 involvement in opioid dependence. Molecular Psychiatry 21:608–614.

Nestler EJ (2001) Molecular basis of long-term plasticity underlying addiction. Nature Review Neuroscience 2:119–128.

Nestler EJ (2008) Transcriptional mechanisms of addiction: role of FosB. Philosophical

Transactions of the Roayl Society B Biological Sciences 363:3245–3255.

Niednery A, Edelmanny FT, Niessing D (2014) Of social molecules: The interactive assembly of ASH1 mRNA-transport complexes in yeast. RNA Biology 11:998–1009.

Nimchinsky EA, Oberlander AM, Svoboda K (2001) Abnormal development of dendritic spines in FMR1 knock-out mice. Journal of Neuroscience 21:5139–5146.

Nishi A, Kuroiwa M, Shuto T (2011) Mechanisms for the Modulation of Dopamine D1 Receptor Signaling in Striatal Neurons. Frontiers in Neuroanatomy 5:1–10.

Nordahl TE, Salo R, Leamon M (2003) Neuropsychological effects of chronic methamphetamine use on neurotransmitters and cognition: A review. Journal of Neuropsychiatry and Clinical Neuroscience 15:317–325.

Oettinghaus B, Schulz JM, Restelli LM, Licci M, Savoia C, Schmidt A, Schmitt K, Grimm A, Morè L, Hench J, Tolnay M, Eckert A, D'adamo P, Franken P, Ishihara N, Mihara K, Bischofberger J, Scorrano L, Frank S (2016) Synaptic dysfunction, memory deficits and hippocampal atrophy due to ablation of mitochondrial fission in adult forebrain neurons. Cell Death & Differentiation 23:18–28.

Oliver CJ, Shenolikar S (1998) Physiologic importance of protein phosphatase inhibitors. Frontiers in Bioscience 3:961–972.

Pan Q, Shai O, Lee LJ, Frey BJ, Blencowe BJ (2008) Deep surveying of alternative splicing complexity in the human transcriptome by high-throughput sequencing. Nature Genetics 40:1413–1415.

Park CY, Zhou J, Wong AK, Chen KM, Theesfeld CL, Darnell RB, Troyanskaya OG

(2020) Genome-wide landscape of RNA-binding protein dysregulation reveals a major impact on psychiatric disorder risk. The Preprint Server for Biology bioRxiv:2020.05.19.102319.

Parker CC, Cheng R, Sokoloff G, Palmer AA (2012) Genome-wide association for methamphetamine sensitivity in an advanced intercross mouse line. Genes, Brain and Behavior 11:52–61.

Paxinos G, Franklin KBJ (2001) Paxinos and Franklin's the Mouse Brain in Stereotaxic Coordinates, 2nd ed. Academic Press.

Periyasamy P, Liao K, Kook YH, Niu F, Callen SE, Guo ML, Buch S (2018) Cocaine-Mediated Downregulation of miR-124 Activates Microglia by Targeting KLF4 and TLR4 Signaling. Molecular Neurobiology 55:3196–3210.

Piazza PV, Deminière J-M, Moal M Le, Simon H (1989) Factors that Predict Individual Vulnerability to Amphetamine Self-Administration. Science (80-) 245:1511–1513.

Pierce RC, Fant B, Swinford-Jackson SE, Heller EA, Berrettini WH, Wimmer ME (2018) Environmental, genetic and epigenetic contributions to cocaine addiction. Neuropsychopharmacology 43:1471–1480.

Pilch J, Koppolu AA, Walczak A, Murcia Pienkowski VA, Biernacka A, Skiba P, Machnik-Broncel J, Gasperowicz P, Kosińska J, Rydzanicz M, Emich-Widera E, Płoski R (2018) Evidence for HNRNPH1 being another gene for Bain type syndromic mental retardation. Clinical Genetics 94:381–385.

Prus AJ, James JR, Rosecrans JA (2009) Conditioned Place Preference. In: Methods of Behavior Analysis in Neuroscience, 2nd edition.

Quinlan AR, Hall IM (2010) BEDTools: A flexible suite of utilities for comparing genomic features. Bioinformatics 26:841–842.

Rankin ML., HAZELWOOD LA, FREE RB, NAMKUNG Y, REX EB, ROOF RA, SIBLEY DR (2009) Molecular Pharmacology of the Dopamine Receptors. Molecular Pharmacology 17:61–87.

Raudvere U, Kolberg L, Kuzmin I, Arak T, Adler P, Peterson H, Vilo J (2019) G:Profiler: A web server for functional enrichment analysis and conversions of gene lists (2019 update). Nucleic Acids Research 47:W191–W198.

Reed C, Baba H, Zhu Z, Erk J, Mootz JR, Varra NM, Williams RW,

Phillips TJ (2018) A spontaneous mutation in Taar1 impacts methamphetamine-related traits exclusively in DBA/2 mice from a single vendor. Frontiers in Pharmacology 8:1–18.

Reichert SC et al. (2020) HNRNPH1-related syndromic intellectual disability: Seven additional cases suggestive of a distinct syndromic neurodevelopmental syndrome. Clinical Genetics 98:91–98.

Reimand J, Isserlin R, Voisin V, Kucera M, Tannus-Lopes C, Rostamianfar A, Wadi L, Meyer M, Wong J, Xu C, Merico D, Bader GD (2019) Pathway enrichment analysis and visualization of omics data using g:Profiler, GSEA, Cytoscape and EnrichmentMap. Nature Protocols 14:482–517.

Reineke LC, Neilson JR (2019) Differences between acute and chronic stress granules, and how these differences may impact function in human disease. Biochemical Pharmacology 162:123–131.

Rieger MA, King DM, Cohen BA, Dougherty JD (2018) CLIP-Seq and massively parallel functional analysis of the CELF6 RNA binding protein reveals a role in destabilizing synaptic gene mRNAs through interaction with 3'UTR elements in vivo. The Prepring Server for Biology bioRxiv:401604.

Riley KJ, Steitz JA (2013) The "Observer Effect" in Genome-Wide Surveys of Protein-RNA Interactions. Molecular Cell 49:601–604.

Ritchie ME, Phipson B, Wu D, Hu Y, Law CW, Shi W, Smyth GK (2015) Limma powers differential expression analyses for RNA-sequencing and microarray studies. Nucleic Acids Research 43:e47.

Rizzuto R, De Stefani D, Raffaello A, Mammucari C (2012) Mitochondria as sensors and regulators of calcium signalling. Nature Reviews Molecular Cell Biology 13:566–578.

Robertson SD, Matthies HJG, Galli A (2009) A closer look at amphetamine-induced reverse transport and trafficking of the dopamine and norepinephrine transporters. Molecular Neurobiology 39:73–80.

Robinson MD, McCarthy DJ, Smyth GK (2009) edgeR: A Bioconductor package for differential expression analysis of digital gene expression data. Bioinformatics 26:139–140.

Rossoll W, Bassell GJ (2019) Crosstalk of Local Translation and Mitochondria: Powering Plasticity in Axons and Dendrites. Neuron 101:204–206.

Rothenberg DA, Taliaferro JM, Huber SM, Begley TJ, Dedon PC, White FM (2018) A Proteomics Approach to Profiling the Temporal Translational Response to Stress

and Growth. iScience 9:367–381.

Rothman RB, Baumann MH, Dersch CM, Romero D V., Rice KC, Carroll FI, Partilla JS (2001) Amphetamine-type central nervous system stimulants release norepinephrine more potently than they release dopamine and serotonin. Synapse 39:32–41.

Ruan QT et al. (2020a) A mutation in hnRNPH1 that decreases methamphetamine-induced reinforcement, reward, and dopamine release and increases synaptosomal hnRNP H and mitochondrial proteins. Journal of Neuroscience 40:107–130.

Ruan QT, Yazdani N, Beierle JA, Hixson KM, Hokenson KE, Apicco DJ, Luttik KP, Zheng K, Maziuk BF, Ash PEA, Szumlinski KK, Russek SJ, Wolozin B, Bryant CD (2018) Changes in neuronal immunofluorescence in the C- versus N-terminal domains of hnRNP H following D1 dopamine receptor activation. Neuroscience Letters 684:109–114.

Ruan QT, Yazdani N, Reed ER, Beierle JA, Peterson LP, Luttik KP, Szumlinski KK, Johnson WE, Ash PEA, Wolozin B, Bryant CD (2020b) 5′ UTR variants in the quantitative trait gene Hnrnph1 support reduced 5′ UTR usage and hnRNP H protein as a molecular mechanism underlying reduced methamphetamine sensitivity. The Federation of American Societies for Experimental Biology (FASEB) Journal 34:9223-9244.

Rueden CT, Schindelin J, Hiner MC, DeZonia BE, Walter AE, Arena ET, Eliceiri KW (2017) ImageJ2: ImageJ for the next generation of scientific image data. BioMed Central Bioinformatics 18:1–26.

Russo A, Siciliano G, Catillo M, Giangrande C, Amoresano A, Pucci P, Pietropaolo C,

Russo G (2010) hnRNP H1 and intronic G runs in the splicing control of the human rpL3 gene. Biochimica et Biophysica Acta - Gene Regulatory Mechanisms 1799:419–428.

Sanford JR, Coutinho P, Hackett JA, Wang X, Ranahan W, Caceres JF (2008) Identification of nuclear and cytoplasmic mRNA targets for the shuttling protein SF2/ASF. Public Library of Science (PLOS) One 3(10):e3369.

Sanz E, Yang L, Su T, Morris DR, McKnight GS, Amieux PS (2009) Cell-type-specific isolation of ribosome-associated mRNA from complex tissues. Proceedings of the National Academy of Sciences of the United States of America 106:13939–13944.

Saunders C, Ferrer J V., Shi L, Chen J, Merrill G, Lamb ME, Leeb-Lundberg LMF, Carvelli L, Javitch JA, Galli A (2000) Amphetamine-induced loss of human dopamine transporter activity: An internalization-dependent and cocaine-sensitive mechanism. Proceedings of the National Academy of Sciences of the United States of America 97:6850–6855.

Schatton D, Rugarli EI (2018) A concert of RNA-binding proteins coordinates mitochondrial function. Critical Reviews in Biochemistry and Molecular Biology 53:652–666.

Scherer M, Levin M, Butter F, Scheibe M (2020) Quantitative proteomics to identify nuclear rna- binding proteins of malat1. International Journal of Molecular Sciences 21:1–12.

Schmidt EK, Clavarino G, Ceppi M, Pierre P (2009) SUnSET, a nonradioactive method to monitor protein synthesis. Nature Methods 6:275–277.

Schmittgen TD, Livak KJ (2008) Analyzing real-time PCR data by the comparative CT method. Nature Protocols 3:1101–1108.

Schuman EM (1999) mRNA trafficking and local protein synthesis at the synapse. Neuron 23:645–648.

Schuman EM, Dynes JL, Steward O (2006) Synaptic regulation of translation of dendritic mRNAs. Journal of Neuroscience 26:7143–7146.

Segal DS, Kuczenski R (1997) Repeated binge exposures to amphetamine and methamphetamine: behavioral and neurochemical characterization. Journal of Pharmacology and Experimental Therapeutics 282:561–573.

Sephton CF, Yu G (2015) The function of RNA-binding proteins at the synapse: Implications for neurodegeneration. Cell and Molecular Life Sciences 72:3621–3635.

Shabani S, Mckinnon CS, Reed C, Cunningham CL, Phillips TJ (2011) Sensitivity to rewarding or aversive effects of methamphetamine determines methamphetamine intake. Genes, Brain and Behavior 10:625–636.

Sharma LK, Lu J, Bai Y (2009) Mitochondrial Respiratory Complex I: Structure, Function and Implication in Human Diseases. Current Medicinal Chemistry 16:1266–1277.

Shi X, Walter NAR, Harkness JH, Neve KA, Williams RW, Lu L, Belknap JK, Eshleman AJ, Phillips TJ, Janowsky A (2016) Genetic polymorphisms affect mouse and human trace amine-associated receptor 1 function. Public Library of Science (PLOS) One 11:1–14.

Shimosato K, Nagao N, Watanabe S, Kitayama S (2003) Suppressive effects of trihexyphenidyl on methamphetamine-induced dopamine release as measured by in vivo microdialysis. Synapse 49:47–54.

Shin EJ, Dang DK, Tran TV, Tran HQ, Jeong JH, Nah SY, Jang CG, Yamada K, Nabeshima T, Kim HC (2017) Current understanding of methamphetamine-associated dopaminergic neurodegeneration and psychotoxic behaviors. Archives of Pharmacal Research 40:403–428.

Si K, Giustetto M, Etkin A, Hsu R, Janisiewicz AM, Miniaci MC, Kim JH, Zhu H, Kandel ER (2003) A Neuronal Isoform of CPEB Regulates Local Protein Synthesis and Stabilizes Synapse-Specific Long-Term Facilitation in Aplysia. Cell 115:893–904.

Siciliano CA, Calipari ES, Ferris MJ, Jones SR (2014) Biphasic mechanisms of amphetamine action at the dopamine terminal. Journal of Neuroscience 34:5575–5582.

Slawon M, Taccogno J, Foltz R, Moody DE (2002) Quantitative Analysis of Selegiline and Three Metabolites (N-Desmethylselegiline, Methamphetamine, and Amphetamine) in Human Plasma by High Performace Liquid Chromatography-Atmospheric Pressure Chemical Ionization-Tandem Mass Spectrometry. Journal of Analytical Toxicology 26:430–437.

Smith LN, Jedynak JP, Fontenot MR, Hale CF, Dietz KC, Taniguchi M, Thomas FS, Zirlin BC, Birnbaum SG, Huber M, Thomas MJ, Cowan CW, Smith LN, Jedynak JP, Fontenot MR (2014) Fragile X mental retardation protein regulates synaptic and

behavioral plasticity to repeated cocaine administration. Neuron 82:645–658.

Smith T, Heger A, Sudbery I (2017) UMI-tools: Modelling sequencing errors in Unique Molecular Identifiers to improve quantification accuracy. Genome Research 27: 491-499.

Smyth GK, Michaud J, Scott HS (2005) Use of within-array replicate spots for assessing differential expression in microarray experiments. Bioinformatics 21:2067–2075.

Sokoloff P, Diaz J, Foll B Le, Guillin O, Leriche L, Bezard E, Gross C (2006) The dopamine D3 receptor : A therapeutic target for the treatment of Neuropsychiatric disorders. CNS & Neurological Disorders - Drug Targets 5:25–43.

Song KY, Choi HS, Law P-Y, Wei L-N, Loh HH (2012) Post-transcriptional regulation of mu-opioid receptor: role of the RNA-binding proteins heterogeneous nuclear ribonucleoprotein H1 and F. Cell and Molecular Life Sciences 69:599–610.

Song KY, Choi HS, Law PY, Wei LN, Loh HH (2017) Post-Transcriptional Regulation of the Human Mu-Opioid Receptor (MOR) by Morphine-Induced RNA Binding Proteins hnRNP K and PCBP1. Journal of Cellular Physiology 232:576–584.

Soreq H, Seidman S (2001) Acetylcholinesterase - new roles for an old actor. Nature Reviews Neuroscience 2:294–302.

Sorkina T, Doolen S, Galperin E, Zahniser NR, Sorkin A (2003) Oligomerization of dopamine transporters visualized in living cells by fluorescence resonance energy transfer microscopy. Journal of Biological Chemistry 278:28274–28283.

Spellman R, Smith CWJ (2006) Novel modes of splicing repression by PTB. Trends in Biochemical Sciences 31:73–76.

Staal RGW, Ray S, Sulzer D (2007) Terminals Amperometric Detection of Dopamine Exocytosis from Synaptic Introduction to Dopamine Neurotransmission. In: Electrochemical Methods for Neuroscience.

Stafford AM, Reed C, Baba H, Walter NAR, Mootz JRK, Williams RW, Neve KA, Fedorov LM, Janowsky AJ, Phillips TJ (2019) Taar1 gene variants have a causal role in methamphetamine intake and response and interact with Oprm1. eLife 8:1–28.

Steri M, Idda ML, Whalen MB, Orrù V (2018) Genetic variants in mRNA untranslated regions. Wiley Interdisciplinary Reviews: RNA 9:1–36.

Sternburg EL, Karginov F V. (2020) Global Approaches in Studying RNA-Binding Protein Interaction Networks. Trends in Biochemical Sciences 45:593–603.

Südhof TC (2013) Neurotransmitter release: The last millisecond in the life of a synaptic vesicle. Neuron 80:675–690.

Sulzer D, Sonders MS, Poulsen NW, Galli A (2005) Mechanisms of neurotransmitter release by amphetamines: A review. Progress in Neurobiology 75:406–433.

Surmeier DJ, Ding J, Day M, Wang Z, Shen W (2007) D1 and D2 dopamine-receptor modulation of striatal glutamatergic signaling in striatal medium spiny neurons. Trends in Neurosciences 30:228–235.

Swiss VA, Nguyen T, Dugas J, Ibrahim A, Barres B, Androulakis IP, Casaccia P (2011) Identification of a gene regulatory network necessary for the initiation of oligodendrocyte differentiation. Public Library of Science (PLOS) One 6(4):e18088.

Szostak E, Gebauer F (2013) Translational control by 3'-UTR-binding proteins. Briefings

in Functional Genomics 12:58–65.

Szumlinski KK, Lominac KD, Campbell RR, Cohen M, Fultz EK, Brown CN, Miller BW, Quadir SG, Martin D, Thompson AB, Jonquieres G von, Klugmann M, Phillips TJ, Kippin TE (2017) Methamphetamine addiction vulnerability: The glutamate, the bad and the ugly. Biological Psychiatry 81:959–970.

Thalhammer A, Jaudon F, Cingolani LA (2020) Emerging Roles of Activity-Dependent Alternative Splicing in Homeostatic Plasticity. Frontiers in Cellular Neuroscience 14:1–9.

Thelen MP, Kye MJ (2020) The Role of RNA Binding Proteins for Local mRNA Translation: Implications in Neurological Disorders. Frontiers in Molecular Biosciences 6:1–13.

Thomson DW, Bracken CP, Goodall GJ (2011) Experimental strategies for microRNA target identification. Nucleic Acids Research 39:6845–6853.

Thorvaldsdóttir H, Robinson JT, Mesirov JP (2013) Integrative Genomics Viewer (IGV): High-performance genomics data visualization and exploration. Briefings in Bioinformatics 14:178–192.

Tiruchinapalli DM, Ehlers MD, Keene JD (2008) Activity-dependent expression of RNA binding protein HuD and its association with mRNAs in neurons. RNA Biology 5:157–168.

Todorova V, Blokland A (2017) Mitochondria and Synaptic Plasticity in the Mature and Aging Nervous System. Current Neuropharmacology 15:166–173.

Tolino M, Kohrmann M, Kiebler MA (2012) RNA-binding proteins involved in RNA

localization and their implications in neuronal diseases. European Journal of Neuroscience 35:1818–1836.

Tomkins DM, Sellers EM (2001) Addiction and the brain : role of neurotransmitters in the cause and traitement of drug dependance. Canadian Medical Association Journal 164:817–821.

Trapnell C, Roberts A, Goff L, Pertea G, Kim D, Kelley DR, Pimentel H, Salzberg SL, Rinn JL, Pachter L (2012) Differential gene and transcript expression analysis of RNA-seq experiments with TopHat and Cufflinks. Nature Protocols 7:562–578.

Uhl GR, Drgonova J, Hall FS (2014) Curious cases: Altered dose-response relationships in addiction genetics. Pharmacology & Therapeutics 141:335–346.

Uhl M, Houwaart T, Corrado G, Wright PR, Backofen R (2017) Computational analysis of CLIP-seq data. Methods 118–119:60–72.

Ule J, Darnell RB (2006) RNA binding proteins and the regulation of neuronal synaptic plasticity. Current Opinion in Neurobiology 16:102–110.

Ule J, Hwang HW, Darnell RB (2018) The future of cross-linking and immunoprecipitation (CLIP). Cold Spring Harbor Perspectives in Biology 10:1–12.

Ule J, Jensen K, Mele A, Darnell RB (2005a) CLIP: A method for identifying protein-RNA interaction sites in living cells. Methods 37: 376-386.

Ule J, Ule A, Spencer J, Williams A, Hu JS, Cline M, Wang H, Clark T, Fraser C, Ruggiu M, Zeeberg BR, Kane D, Weinstein JN, Blume J, Darnell RB (2005b) Nova regulates brain-specific splicing to shape the synapse. Nature Genetics 37:844–852.

Uramura K, Yada T, Muroya CAS, Shioda S, Shiratani T, Takigawa M (2000)

Methamphetamine induces cytosolic Ca2+ oscillations in the VTA dopamine neurons. Neuropharmacology 11:1057–1061.

Uren PJ, Bahrami-Samani E, de Araujo PR, Vogel C, Qiao M, Burns SC, Smith AD, Penalva LOF (2016) High-throughput analyses of hnRNP H1 dissects its multi-functional aspect. RNA Biology:1–12.

Usiello a, Baik JH, Rougé-Pont F, Picetti R, Dierich a, LeMeur M, Piazza P V, Borrelli E (2000) Distinct functions of the two isoforms of dopamine D2 receptors. Nature 408:199–203.

Van Dusen CM, Yee L, McNally LM, McNally MT (2010) A glycine-rich domain of hnRNP H/F promotes nucleocytoplasmic shuttling and nuclear import through an interaction with transportin 1. Molecular and Cellular Biology 30:2552–2562.

Van Ende R, Balzarini S, Geuten K (2020) Single and Combined Methods to Specifically or Bulk-Purify RNA-Protein Complexes. Biomolecules 10(8):1160.

Van Nostrand EL, Pratt GA, Shishkin AA, Gelboin- C, Fang MY, Sundararaman B, Blue SM, Thai B, Surka C, Elkins K, Stanton R, Rigo F, Yeo GW, Jolla L, Program C, Jolla L, Jolla L, California J, Engineering B (2016) Robust transcriptome-wide discovery of RNA binding protein binding sites with enhanced CLIP (eCLIP). Nature Methods 13:508–514.

Vogel C, De Sousa Abreu R, Ko D, Le SY, Shapiro BA, Burns SC, Sandhu D, Boutz DR, Marcotte EM, Penalva LO (2010) Sequence signatures and mRNA concentration can explain two-thirds of protein abundance variation in a human cell line. Molecular Systems Biology 6:1–9.

Volkow ND, Wang GJ, Fowler JS, Tomasi D, Telang F, Baler R (2010) Addiction: Decreased reward sensitivity and increased expectation sensitivity conspire to overwhelm the brain's control circuit. BioEssays 32:748–755.

Vos M, Lauwers E, Verstreken P (2010) Synaptic mitochondria in synaptic transmission and organization of vesicle pools in health and disease. Frontiers in Synaptic Neuroscience 2:1–10.

Wall ML, Bera A, Wong FK, Lewis SM (2020) Cellular stress orchestrates the localization of hnRNP H to stress granules. Experimental Cell Research 394:112111.

Wang E, Aslanzadeh V, Papa F, Zhu H, de la Grange P, Cambi F (2012) Global Profiling of Alternative Splicing Events and Gene Expression Regulated by hnRNPH/F. Public Library of Science (PLOS) One 7:1–10.

Wang E, Dimova N, Cambi F (2007) PLP/DM20 ratio is regulated by hnRNPH and F and a novel G-rich enhancer in oligodendrocytes. Nucleic Acids Research 35:4164–4178.

Wang E, Huang Z, Hobson GM, Dimova N, Sperle K, McCullough A, Cambi F (2006) PLP1 alternative splicing in differentiating oligodendrocytes: Characterization of an exonic splicing enhancer. Journal of Cellular Biochemistry 97:999–1016.

Wang H, Kim SS, Zhuo M (2010) Roles of fragile X mental retardation protein in dopaminergic stimulation-induced synapse-associated protein synthesis and subsequent α-amino-3-hydroxyl-5-methyl-4-isoxazole-4-propionate (AMPA) receptor internalization. Journal of Biological Chemistry 285:21888–21901.

Wang H, Wu LJ, Kim SS, Lee FJS, Gong B, Toyoda H, Ren M, Shang YZ, Xu H, Liu F, Zhao MG, Zhuo M (2008) FMRP Acts as a Key Messenger for Dopamine Modulation in the Forebrain. Neuron 59:634–647.

Wang T, Xiao G, Chu Y, Zhang MQ, Corey DR, Xie Y (2015) Design and bioinformatics analysis of genome-wide CLIP experiments. Nucleic Acids Research 43:5263–5274.

Wang Z, Grabowski PJ (1996) Cell- and stage-specific splicing events resolved in specialized neurons of the rat cerebellum. RNA 2:1241–1253.

Williams CC, Jan CH, Weissman JS (2014) Targeting and plasticity of mitochondrial proteins revealed by proximity-specific ribosome profiling. Science 346:748–751.

Williams R, Lim JE, Harr B, Wing C, Walters R, Distler MG, Teschke M, Wu C, Wiltshire T, Su AI, Sokoloff G, Tarantino LM, Borevitz JO, Palmer AA (2009) A common and unstable copy number variant is associated with differences in Glo1 expression and anxiety-like behavior. Public Library of Science (PLOS) One 4(3):e4649.

Wise RA (2004) Dopamine, learning and motivation. Nature Reviews Neuroscience 5:483–494.

Wise RA, Bozarth MA (1987) A Psychomotor Stimulant Theory of Addiction. Psychological Review 94:469–492.

Witten JT, Ule J (2011) Understanding splicing regulation through RNA splicing maps. Trends in Genetics 27:89–97.

Wolf ME, Roth RH (1990) Autoreceptor Regulation of Dopamine Synthesis. Annals of the New York Academy of Sciences 604:323–343.

Wolozin B, Ivanov P (2019) Stress granules and neurodegeneration. Nature Reviews Neuroscience 20:649–666.

Won S, Hong RA, Shohet R V., Seto TB, Parikh NI (2013) Methamphetamine-associated cardiomyopathy. Clinical Cardiology 36:737–742.

Wu CW, Ping YH, Yen JC, Chang CY, Wang SF, Yeh CL, Chi CW, Lee HC (2007) Enhanced oxidative stress and aberrant mitochondrial biogenesis in human neuroblastoma SH-SY5Y cells during methamphetamine induced apoptosis. Toxicology and Applied Pharmacology 220:243–251.

Wurtz T, Kiseleva E, Nacheva G, Alzhanova-Ericcson A, Rosén A, Daneholt B (1996) Identification of two RNA-binding proteins in Balbiani ring premessenger ribonucleoprotein granules and presence of these proteins in specific subsets of heterogeneous nuclear ribonucleoprotein particles. Molecular and Cellular Biology 16:1425–1435.

Xie C, Yuan J, Li H, Li M, Zhao G, Bu D, Zhu W, Wu W, Chen R, Zhao Y (2014) NONCODEv4: Exploring the world of long non-coding RNA genes. Nucleic Acids Research 42:98–103.

Xu J et al. (2014) A Heroin Addiction Severity-Associated Intronic Single Nucleotide Polymorphism Modulates Alternative Pre-mRNA Splicing of the Opioid Receptor Gene OPRM1 via hnRNPH Interactions. Journal of Neuroscience 34:11048–11066.

Yagi T (1994) Src Family Kinases Control Neural Development and Function. Development, Growth & Differentiation 36:543–550.

Yalcin B, Flint J (2012) Association studies in outbred mice in a new era of full-genome

sequencing. Mammalian Genome 23:719–726.

Yamamoto DJ, Nelson AM, Mandt BH, Larson GA, Rorabaugh JM, Ng CMCC, Barcomb KM, Richards TL, Allen RM, Zahniser NR (2013) Rats classified as low or high cocaine locomotor responders: A unique model involving striatal dopamine transporters that predicts cocaine addiction-like behaviors. Neuroscience & Biobehavioral Reviews 37:1738–1743.

Yazdani N, Parker CC, Shen Y, Reed ER, Guido MA, Kole LA, Kirkpatrick SL, Lim JE, Sokoloff G, Cheng R, Johnson WE, Palmer AA, Bryant CD (2015) Hnrnph1 Is A Quantitative Trait Gene for Methamphetamine Sensitivity. Public Library of Science (PLOS) Genetics 11:e1005713.

Yeo G, Holste D, Kreiman G, Burge CB (2004) Variation in alternative splicing across human tissues. Genome Biology 5:1–15.

Yoon Y, McKenna MC, Rollins DA, Song M, Nuriel T, Gross SS, Xu G, Glatt CE (2013) Anxiety-associated alternative polyadenylation of the serotonin transporter mRNA confers translational regulation by hnRNPK. Proceedings of the National Academy of Sciences of the United States of America 110:11624–11629.

Yorgason JT, Hedges DM, Obray JD, Jang EY, Bills KB, Woodbury M, Williams B, Parsons MJ, Andres MA, Steffensen SC (2020) Methamphetamine increases dopamine release in the nucleus accumbens through calcium-dependent processes. Psychopharmacology (Berlin) 237:1317–1330.

Zaniewska M, Filip M, Przegaliński E (2015) The involvement of norepinephrine in behaviors related to psychostimulant addiction. Current Neuropharmacology

13:407–418.

Zhang W, Liu H, Han K, Grabowski PJ (2002) Region-specific alternative splicing in the nervous system: Implications for regulation by the RNA-binding protein NAPOR. RNA 8:671–685.

Zhang X, Hamblin MH, Yin KJ (2017) The long noncoding RNA Malat1: Its physiological and pathophysiological functions. RNA Biology 14:1705–1714.

Zhang Z, Xing Y (2017) CLIP-seq analysis of multi-mapped reads discovers novel functional RNA regulatory sites in the human transcriptome. Nucleic Acids Research 45:9260–9271.

Zhou Y, Dong F, Mao Y (2018) Control of CNS functions by RNA-binding proteins in neurological diseases. Current Pharmacology Reports 4:301–313.

Zhou Z, Karlsson C, Liang T, Xiong W, Kimura M, Tapocik JD, Yuan Q, Barbier E, Feng A, Flanigan M, Augier E, Enoch MA, Hodgkinson CA, Shen PH, Lovinger DM, Edenberg HJ, Heilig M, Goldman D (2013) Loss of metabotropic glutamate receptor 2 escalates alcohol consumption. Proceedings of the National Academy of Sciences of the United States of America 110:16963–16968.

Zhu J, Mayeda A, Krainer AR (2001) Exon identity established through differential antagonism between exonic splicing silencer-bound hnRNP A1 and enhancer-bound SR proteins. Molecular Cell 8:1351–1361.

Zhu J, Reith MEA (2008) Role of the dopamine transporter in the action of psychostimulants, nicotine, and other drugs of abuse. CNS & Neurological Disorders - Drug Targets 7:393–409.

Zhu L, Li J, Dong N, Guan F, Liu Y, Ma D, Goh ELK, Chen T (2016) mRNA changes in nucleus accumbens related to methamphetamine addiction in mice. Scientific Reports 6:36993.

CURRICULUM VITAE